Constructing a Toolbox of Geochemical Indicators of Community Composition Shifts in Coral Reef Ecosystems Under Stress

Isaiah W. Bolden

A dissertation

submitted in partial fulfillment of the

requirements for the degree of

Doctor of Philosophy

University of Washington

2020

Reading Committee:

Alexander C. Gagnon, Chair

Julian P. Sachs

Jodi N. Young

Program Authorized to Offer Degree:

Oceanography

University of Washington

Abstract

Constructing a Toolbox of Geochemical Indicators of Community Composition Shifts in Coral Reef Ecosystems Under Stress

Isaiah W. Bolden

Chair of the Supervisory Committee:
Alexander C. Gagnon
Assistant Professor
School of Oceanography

Modern coral reef ecosystems house 25% of the planet's entire marine biodiversity in ~ 0.1% of the surface area cover of the ocean and provide numerous ecosystem services for human populations. Unfortunately, these marine rainforests are known to be in a global state of decline, largely due to the impacts of sea-surface warming, ocean acidification, pollution, disease, and other direct human impacts. Numerous studies have proposed that as these stressors increase in reef environments, a pronounced shift from precipitation to dissolution of calcium carbonate ($CaCO_3$) substrates will induce the collapse of habitat-forming coral structures and lead to dominance of macroalgae. Together, these changes lend themselves to a decline in the overall biodiversity of marine organisms hosted in today's reef ecosystems in addition to major losses to global fisheries, erosion of coastal protection, and dissolution of the foundations of many tropical islands. As a

means to improve future reef management and adaptation strategies, there has been a recent push for the development of new tools for monitoring the health of coral reefs under environmental stressors. My research follows a forensic geochemistry approach to understand ecological shifts within and between reef ecosystems in the age of anthropogenic climate change. Specifically, I combine discrete and continuous measurements of seawater composition in coral reef environments, mathematical modeling, and high-resolution mass spectrometry to determine the most effective geochemical proxies for changes in reef metabolism and community composition under stress. Here, I will report on (1) the limitations of exploring variability in modern reef metabolism through assumptions of canonical relationships between carbon and oxygen budgets, (2) the development of a high-precision method for detecting variability in the seawater dissolved strontium-to-calcium (Sr/Ca_{sw}) ratio and its potential as an indicator of calcifier community composition, and (3) variability in the stable carbon isotope ($\delta^{13}C$) composition of seawater dissolved inorganic carbon (DIC) on reefs as a potential proxy for benthic primary producer community composition. With the current unprecedented decline of coral reef ecosystems, the ultimate goal of my research is to construct a sophisticated and quantitative toolkit for detecting ecological transitions within these dynamic marine habitats.

TABLE OF CONTENTS

LIST OF FIGURES

LIST OF TABLES

ACKNOWLEDGEMENTS

This work for this thesis could not have been completed without the guidance, support, and mentorship of a small village-worth of people. First, to my advisor Alex, thank you for (1) unwavering support in my pursuit of knowledge, (2) ample opportunities to grapple with difficult analytical and numerical topics in geoscience research, and (3) the chance to conduct field research in a location that would eventually be visited by President Obama. To the small team of Avengers that is my supervisory committee (Julian, Steve, Parker, Terrie, and Jodi), thank you for your helpful feedback on my research and my career aspirations as well as your patience in dealing with my tendency to schedule committee meetings at the last possible minute. At least I'm not afraid of you all anymore… I don't think. Steve, maybe. To my lab group and the graduate student community in the UW School of Oceanography – I could not have asked for a better group of friends with whom to suffer through a Ph.D. Thank you to Sasha (my P.I.C.), Ann (6^{th} year – Stoneway Hardware), Robert, Zac, Claire, Rosalind, Marta, Elisa, Mary Margaret, Dan, Amy, Andrew, and my entire Oceans 11 cohort for being amazing. I owe a particular debt of gratitude to Tamas Ugrai in the UW TraceLab facility and Dr. Aaron Satkoski at the University of Texas at Austin for assistance in data collection. The research presented in this thesis would also not be possible without the generous financial support of Jim and Marsha Seeley. I am also grateful for the logistical support provided by the Tetiaroa Society and the Brando Resort in French Polynesia, collaborators at the Australian National University, One Tree Island Research Station, and the UW Oceanography Stable Isotope Lab. Additional graduate support supplied by the University of Washington-hosted NSF IGERT Program on Ocean Change (AN: 1068839), the NSF Graduate Research Fellowship Program, the Social Science Research Council Graduate Studies

Enhancement Grant, the Mellon-Mays Travel and Research Grant (Andrew. W Mellon Foundation), and the Achievement Rewards for College Scientists Fellowship.

DEDICATION

For my mother, Phyllis, and late father, Paul. With love, “The Best Boy in the World.”

Chapter 1. INTRODUCTION

Coral reef ecosystems are known to be in a global state of decline, largely attributed to the impacts of sea-surface warming, ocean acidification, pollution, disease, and direct human impacts. The impending loss of these environments could translate to major losses in marine biodiversity, erosion of coastal protection, stress on major fisheries, and contributions to the dissolution of the foundations of many low-lying tropical islands e.g. (Bryant et al., 1998; Hoegh-Guldberg et al., 2007; Doney et al., 2009). As a means to improve future reef management and adaptation strategies, there has been a recent push for the development of geochemical tools that can be used as proxies for monitoring the health of coral reefs under environmental stressors. Many previous studies have developed and/or applied tools that have focused on quantifying the rate of ecosystem level metabolism, inclusive of net ecosystem productivity (NEP) and calcification (NEC), for many reefs throughout the world. In addition to providing baseline values of ecosystem metabolism, these integrated studies of both NEP and NEC can also elucidate complex interactions between calcification and productivity that govern chemical variability within the ecosystem. For example, results from a recent study in Bermuda indicate that the productivity/calcification interactions of temperate, reef-dwelling organisms may work to partially offset changes in global ocean pH and carbonate saturation state (Ω) associated with ocean acidification (Andersson et al., 2014). Additional investigations of interactions between productivity and calcification dynamics on reefs have led to the proposal of the NEC/NEP ratio as an indicator of the extent of trophic level transitions from dominance of stony corals to fleshy macroalgae that may be observed in coming decades as stressors on reefs increase (Andersson and Gledhill, 2013). However, if this ratio of metabolic output on reefs is to

have any significant meaning for future management strategies, it is essential that the methods of determining NEP and NEC are valid and result in accurate and precise estimates of ecosystem level metabolism. Errors associated with invalid assessments of NEP and NEC could lead to trophic mischaracterization and eventual mishandling of monitoring and adaptation strategies within and between reef ecosystems.

On the topic of trophic characterizations, assessments of reef ecosystem health and trophic transitions under stress could benefit from the development of geochemical proxies that capture more nuanced, community-level details of calcification and productivity dynamics within these dynamic environments. For example, while calcification within coral reefs results in the production of calcium carbonate ($CaCO_3$) minerals, the mineral polymorph and the solubility of that polymorph can vary depending upon the calcifying community responsible for precipitation (Burton and Walter, 1987; Andersson et al., 2008; Ries, 2010). The ability to capture trends in $CaCO_3$ solubility within reef seawater and relate those changes to trends in calcifier community composition would allow for community-specific, quantitative assessments of NEC and the ability to monitor trophic-level calcification dynamics on reefs as stressors increase. Additionally, with the compounding effects of stressors, many coral reef ecosystems are expected to experience a community shift away from calcifiers altogether to a state dominated by the presence of photosynthesizing fleshy macroalgae (Maliao et al., 2008; Fabricius et al., 2011; Agostini et al., 2018). A geochemical indicator of ecosystem productivity on reefs that responds to slight nuances of community composition differences could be developed into a proxy for quantifying the state of this predicted transition. Overall, attempts to improve assessments of metabolism on reefs in these ways would also greatly improve the ability

to detect and compare changes in the biogeochemical cycling of neighboring reef ecosystems in cases where differences in net metabolic rates may be small.

My dissertation makes use of discrete bottle and autonomous instrumentation measurements of coral reef biogeochemistry, quantitative decomposition models of biogeochemical fluxes within reefs, and high-resolution mass spectrometry to investigate the practicability of various geochemical proxies for changes in reef metabolism and community composition under stress. In Chapter 2, I use data from a four-year and ongoing field campaign to decompose reef carbon and oxygen budgets and empirically determine net productivity quotients for a pristine, French Polynesian atoll (Bolden et al., 2019). Productivity quotients have been used as a stoichiometric workaround for obtaining net ecosystem metabolic rates in studies of reefs that are limited to measurements of pH and O_2. Many of these previous studies assume stoichiometric unity between carbon and oxygen during photosynthesis and respiration; I show that the value of this ratio is highly variable over multiple timescales, and associated errors in estimated NEP and NEC rates can be greater than 100% when assuming unity.

In Chapter 3, I propose and develop a method for investigating diel variability in seawater Sr/Ca ratios on coral reefs as a geochemical tool for monitoring and comparing community level calcification dynamics, particularly under increasing warming and ocean acidification. The Sr/Ca ratio in seawater (Sr/Ca_{sw}) is sensitive to calcification rates and differences between partition coefficients of polymorphs of calcium carbonate ($CaCO_3$). In Chapter 2, I use a modified version of isotope dilution thermal ionization mass spectrometry (ID-TIMS) to develop a method of measuring accurate Sr/Ca_{sw} with high precision. I also apply this method to discrete diel samples of seawater from reefs in French Polynesia and Australia, each with a different balance of organisms that precipitate different $CaCO_3$ polymorphs, to quantify

and characterize the identity of the community of calcifiers responsible for fluxes of calcification and dissolution that comprise integrated values of NEC.

In Chapter 4, I attempt to develop measurements of temporal variability in the seawater stable carbon isotope composition of DIC ($\delta^{13}C_{DIC}$) on coral reefs into a proxy for benthic photosynthesizer community composition. Marine primary producers employ a variety of carbon transport pathways for photosynthesis, with each carrying a unique net organic matter fractionation factor (ε_{org}). I use measurements of $\delta^{13}C_{DIC}$ to solve for dusk, dawn, and average daily ε_{org} – each of which should be directly related to the dominant carbon concentrating mechanism of community productivity and serves as a metric for how these mechanisms and the overall benthic producer community will shift as a function of environmental stressors.

Through the investigation and development of the geochemical proxies presented here, the goal of this dissertation is ultimately to improve the ability to detect shifts in reef biogeochemistry for reef ecosystems across the planet.

Chapter 2. NON-CANONICAL PRODUCTIVITY QUOTIENTS ARE OBSERVED IN CORAL REEF ENVIRONMENTS (REPRODUCED FROM BOLDEN ET AL., 2019 – MARINE CHEMISTRY)

2.1 INTRODUCTION

Coral reefs are ecosystems where pH, oxygen saturation, and other biogeochemical parameters can vary dramatically over short temporal scales, e.g. (Hofmann et al. 2011; Shamberger et al. 2011; Koweek et al. 2015a; b; Gruber et al. 2017). This dynamic variability both sets the habitat for reef-dwelling organisms and acts as an indicator of ecosystem function.

Specifically, the periodic variability of reef seawater chemistry, termed the "heartbeat" of the reef (Cyronak et al., 2018), is a result of the combined metabolic processes of productivity, respiration, calcification, and dissolution as well as physical processes like advection and gas exchange. Reef metabolism studies harness the information encoded in this chemical signal to isolate key parameters like net ecosystem productivity (NEP) and calcification (NEC). This is typically done through discrete measurements of two carbonate system parameters, such as total alkalinity (TA) and dissolved inorganic carbon (DIC), together with independent knowledge of advection and gas transfer rates (Frankignoulle et al., 1996; Gattuso et al., 1996; Bates, 2002; Falter et al., 2008; Drupp et al., 2013; Gruber et al., 2017). A graphical representation of how NEP and NEC are calculated from seawater measurements of TA and DIC is shown in Figure 2.1. On such plots, transitioning from one DIC + TA point to another requires a unique combination of NEP and NEC vectors. The application of this approach has been instrumental in establishing ecosystem-scale metabolic rates on contemporary reefs from which the impacts of stressors like ocean acidification and sea-surface warming can be monitored (Wei et al., 2009; Pandolfi et al., 2011; Silverman et al., 2012; Silverman et al., 2014; Albright et al., 2018).

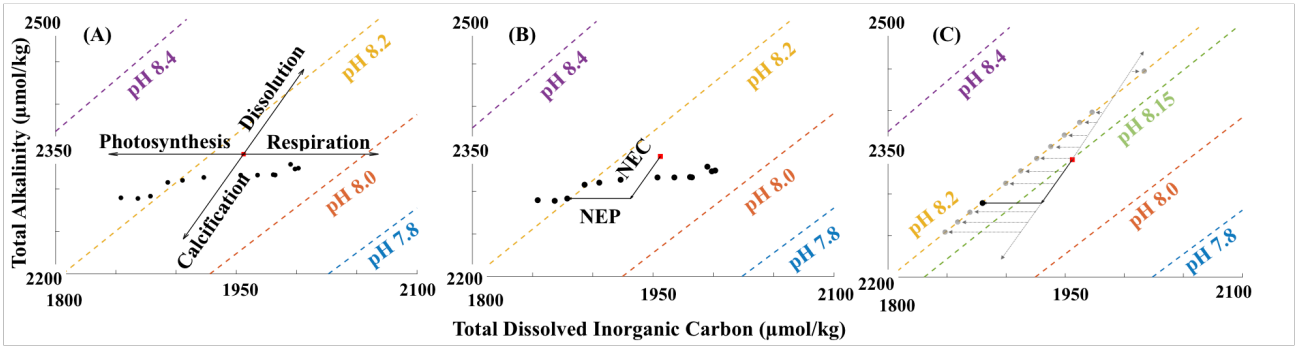

Figure 2.1. A graphical representation of the ways that net ecosystem productivity (NEP) and calcification (NEC) are determined from seawater measurements. In each plot, DIC and TA data represent typical diel measurements from May 2014 on Tetiaroa Atoll (circles). Contours of constant pH values plot as lines in this space. A: The metabolic processes of

calcification/dissolution and photosynthesis/respiration can be represented as vectors because they affect DIC and TA in known, constant proportions. B: Moving from one point (open ocean conditions, red square) to any given condition on a reef requires a unique combination of calcification/dissolution (2:1 change for TA:DIC) and photosynthesis/respiration (assumed to change only DIC). This means that NEP and NEC can be calculated if the DIC and TA of samples are known, together with corrections for gas exchange and advection. C: If, however, only knowledge of a final pH and starting condition pH (with an assumed DIC/ TA) is known, then the carbonate system is under-constrained, leading to infinite possibilities of NEP and NEC vectors (gray dashed lines). Using an assumed stoichiometric relationship between productivity-driven O2 and DIC (Q), variability in O_2 is turned into a NEP vector, which results in a unique solution and a unique corresponding NEC value.

However, the requirement to collect discrete seawater samples for carbonate chemistry analysis makes extended time series and high temporal resolution records of biogeochemical variability on reefs logistically challenging, even when supported by autonomous water sampling systems (Albright et al., 2013). Overcoming this logistical challenge to higher frequency sampling would allow for ecosystem characterizations that provide richer information on tidal, seasonal, and decadal scales, making it easier to separate secular trends from higher frequency variability. High-resolution, continuous sampling of reef ecosystem metabolism would also facilitate the characterization of biogeochemical variability under local and global environmental stressors for a much larger number of reefs around the world. Though under development, instruments for collecting autonomous pCO_2, DIC and TA are not yet widely available for mass deployment in reef ecosystems (Spaulding et al., 2014; Fassbender et al., 2015; McMahon et al., 2018; Terlouw et al., 2019). In contrast, instrumentation for frequent autonomous measurements of pH and O_2 are widely available, accurate, and can be deployed for extended periods of time in

harsh reef environments (Martz et al., 2003; Martini et al., 2007; Seidel et al., 2008; Hoeke et al., 2009; Price et al., 2012; Gray et al., 2012; DeCarlo et al., 2017).

To calculate metabolic rates from oxygen and pH, oxygen fluxes are converted into estimates of NEP using an assumed net productivity quotient (Q). This NEP is then combined with pH and an estimated TA to invert for other metabolic fluxes, like NEC (Fig. 1c). In effect, the oxygen data are used to correct the pH signal for the impacts of productivity. The remaining pH change is then interpreted as calcification. This approach is both commonly used, (e.g. Barnes, 1983; Gattuso et al., 1999b; Takeshita et al., 2016), and allows for the application of powerful, new techniques of measuring benthic fluxes, such as eddy covariance methods (Long et al., 2013). However, the accuracy of this approach is crucially dependent on the selection of an appropriate value of Q.

Early studies of Q suggested an average global ocean value of -138/106 ($\Delta O_2/\Delta DIC$, ≅ -1.3), largely based on the stoichiometry of marine metabolic processes (Redfield et al., 1963; Falkowski, 1998). However, there have since been a number of studies reporting a large degree of geographic variability in Q, both in the open ocean and in coral reef ecosystems (Smith and Marsh, 1973; Kinsey, 1979; Barnes, 1983; Kinsey, 1985; Takahashi et al., 1985; Hedges et al., 2002; Carpenter and Williams, 2007; Taddei et al., 2008). The extent to which this documented spatial variability in Q is itself temporally variable within a single reef ecosystem has also been the subject of investigation; however, these studies have heretofore focused on the seasonal variability of sedimentary processes within a reef environment (Taddei et al., 2008) or daily variability along a fixed transect within a reef environment (Smith and Marsh, 1973; Kinsey, 1985). A more comprehensive and extended survey of temporal variability in ecosystem-level Q within a particular reef would aid in determining the limitations and associated errors of applying

assumed or empirically-measured Q values to records of pH and O_2 on reefs across a range of timescales.

Using data from a three-year field campaign on Tetiaroa Atoll, French Polynesia, I combined discrete measurements of DIC and TA with more frequent, co-located sensor measurements of O_2 and pH. The combined data allow us to calculate an empirically-determined net stoichiometric relationship (Q) for marine organic matter produced/consumed within the coral reef ecosystem. These values of Q are compared with canonical and previously applied values in reef ecosystems, and the sources of variability and uncertainty in estimates of Q are explored with simple models. I first decompose our reef data using a single, well-mixed box model, an approach that has been applied to a number of other studies of reef metabolism (Frankignoulle et al., 1996; Bates, 2002; Falter et al., 2008). I then detail how reefs often differ from this ideal case and explore the impacts that more realistic models of water flow on reefs has on inversions of metabolism. The dataset allows us to determine NEP and NEC in two independent manners: (1) using the carbonate system parameters DIC and TA and (2) using O_2, pH, and a value of Q. I compare these different estimates of NEC and NEP to evaluate the impact that observed variability in Q could have on biogeochemical studies when reef metabolism is derived from measurements of pH and O_2 alone.

2.2 METHODS

2.2.1 *Study Site*

Historically devoid of significant human presence and influence, Tetiaroa Atoll (17.0ºS, 149.5ºW) is located ~53 km north of the island of Tahiti in the Windward Islands of French Polynesia (Figure 2.2). The atoll has an area of approximately 6 km^2 and is composed of 13 carbonate islets (locally termed “motus”) surrounded by a reef flat that encloses a central lagoon. Sampling campaigns, consisting of discrete seawater sampling and simultaneous analysis by

instruments, were conducted in May 2014, November 2014, October 2015, and March 2017 on a sand patch on the reef flat of the southwest islet of Onetahi. The sampling site (17.0168ºS, 149.5943ºW) was located ~0.5 km east of the reef crest in a location where benthic coverage, estimated from satellite measurements, is ~21% scleractinian corals and ~79% carbonate sands (see Supplementary Materials). Tides at this location are diurnal yet small in amplitude, with an average tidal range of 0.2 meters compared with a typical water depth of 1 meter (Jeanson et al., 2014). Circulation patterns on Tetiaroa, as indicated by dye releases and acoustic doppler current profiles (ADCP) and Surface Wave Instrument Float with Tracking (microSWIFT, Thomson 2012) deployments, are characteristic of a seasonally-dominant westward flow of surface waters, with significant seasonal ocean swell form the southeast to southwest from March-October and northwest to north from November-February. At the sampling location, water typically flows northward alongshore.

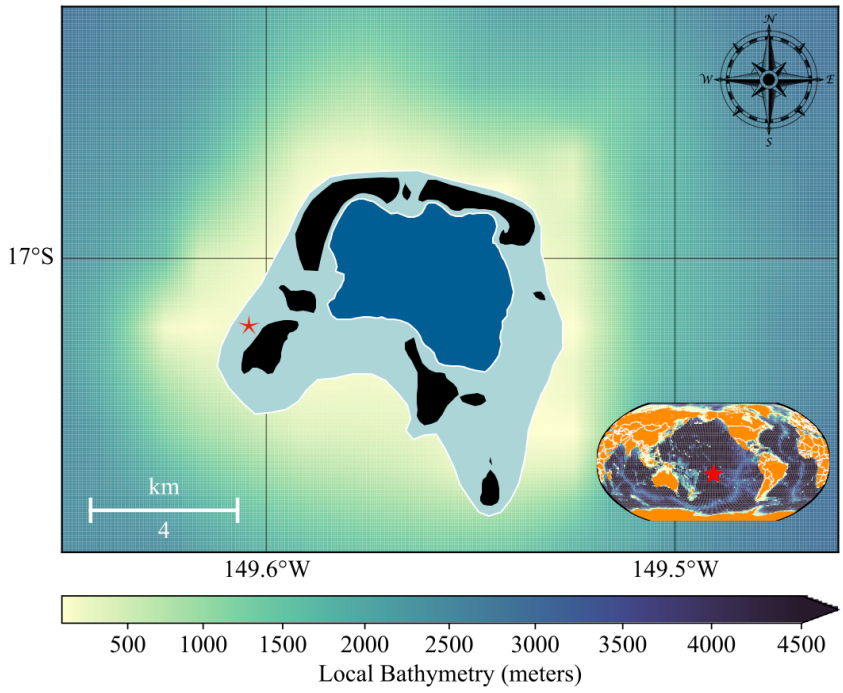

Figure 2.2. Map of Tetiaroa Atoll. On Tetiaroa, black shapes represent individual islets (locally termed “motus”). The shaded lighter blue region represents the reef flat of the atoll

(average water depth ≅ 1 m), while the darker blue shaded region is the central lagoon (average water depth ≅ 15 m). The sampling location for this study (red star) is directly to the west of motu Onetahi. Water that overtops the reef crest and enters the reef flat on the west side of Onetahi generally travels towards shore and then northward along shore. On Onetahi's southwest, water typically flows towards shore and southward along shore.

2.2.2 *Sampling*

During each field campaign, samples for DIC and TA analyses were collected at a frequency of 2 hours for a duration of 24-36 hours using hand-triggered Niskin bottles. Sampling followed the standard operating procedures of Dickson et al. (2007). Briefly, samples were transferred from the Niskin without exposure to the atmosphere into 300 mL borosilicate glass BOD bottles. All water samples were poisoned onsite with 150 µL of a saturated solution of the biocide mercuric chloride ($HgCl_2$) for later offsite analyses. At the same location as bottle sampling, complementary diel variability in pH and O_2 for each field campaign were measured every 15-30 minutes using a SAMI-pH (SunBurst Sensors, LLC) coupled with an SBE 16plus V2 SeaCAT CTD Recorder fit with an SBE 63 oxygen optode (Sea-Bird Electronics). Temperature (± 0.005ºC) and salinity (± 0.005) were obtained for each diel cycle at the 15-30 minute resolution of the CTD. Salinity corrections to the CTD+optode pair as well as to the SAMI-pH results were applied during data processing. Since DIC and TA are sufficient to characterize the complete carbonate system, measuring pH is redundant. However, pH data are still included here because higher frequency pH measurements provide context for the less frequent bottle measurements. For the November 2014 field campaign, optode O_2 measurements were calibrated against discrete samples subject to Winkler titrations. The two techniques agree to within ± 4 µmol O_2/kg (2σ std. dev.; n = 14).

2.2.3 *DIC and TA Analyses*

Carbonate system measurements follow the methods of Dickson et al. (2007). Briefly, TA (µmol/kg) was determined through open-cell automated titration (876 Dosimat plus, Metrohm AG) with a solution of 0.1M hydrochloric acid (HCl) + 0.6M sodium chloride (NaCl). Total DIC (µmol/kg) was obtained through coulometric determination (VINDTA 3D, Marianda with UIC coulometer). Certified reference materials for TA and DIC obtained from Andrew Dickson (Scripps Institution of Oceanography) were run in conjunction with seawater samples as a calibration standard and to monitor precision. Long-term precision on DIC and TA based on repeated measurements of CRM materials was ± 3.7 µmol/kg (n = 46; 2σ std. dev.) and ± 4.3 µmol/kg (n = 41; 2σ std. dev.), respectively. The accuracy and precision for instrumentally-determined pH was compared to pH values calculated from simultaneous discrete measurements of DIC and TA as inputs into CO2SYS v2.1 for Microsoft Excel using the total pH scale with carbonate equilibrium constants refit from Mehrbach et al. (1973) by Dickson and Millero (1987); borate alkalinity was calculated using the boron/chlorinity (salinity) relationship provided by Uppström (1974) and equilibrium constants from Dickson (1990). Across all diel sampling campaigns, SAMI-pH averaged a 0.021 ± 0.019 unit offset from discrete DIC/TA-based pH. Given the instrumental precision of DIC and TA versus the variability observed within instrumental pH measurements, all pH values reported and used in calculations here are derived from DIC and TA using CO2SYS. Where appropriate, O_2, TA, and DIC values used in subsequent calculations are salinity-normalized ([nO_2], [nTA] and [nDIC]) to a mean open ocean salinity value of 35.4.

2.2.4 *Modeling Approach and Quantitative Biogeochemical Decomposition*

A biogeochemical modeling framework is required to translate chemical measurements from a sampling site on the reef into metabolic fluxes of NEP and NEC and to further isolate these fluxes from other physical processes like advection and gas exchange. I use three different model geometries to decompose chemical measurements into fluxes and to calculate empirical values of Q (Figure 2.3). The use of multiple models allows us to evaluate the extent to which empirical values of Q are robust to model topology. The model geometries explored here, a single box model, a non-dispersive flow model, and an Eulerian inverse model, capture much of the diversity of previous quantitative biogeochemical decomposition studies on reefs.

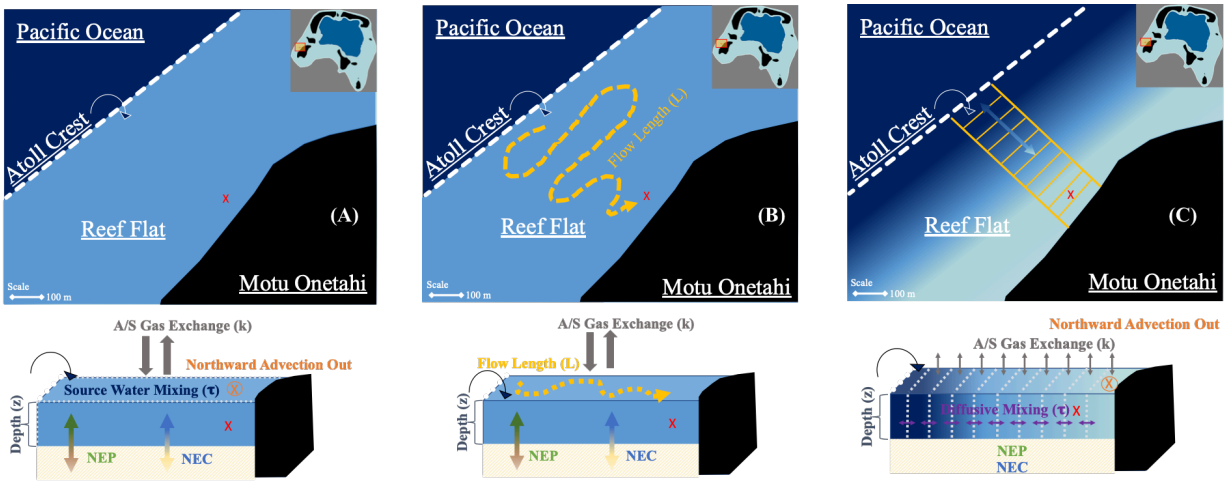

Figure 2.3. Three model geometries are used in this study to separate community metabolism and calcification from gas exchange and advection. A: A well-mixed single box model assumes homogenous chemical distribution for the entire reef flat, such that measurements at the sampling location are representative of this entire portion of the atoll (sampling site marked with an X). B: A non-dispersive mixing model that integrates the impacts of benthic fluxes of NEP and NEC and gas exchange along flow path of length L. C: A multi-box, Eulerian inverse model assumes that water from the open ocean overtops the atoll reef crest, and then seawater chemistry is modified within a series of discretized boxes from crest to the shore each subject to homogenous benthic fluxes of productivity and calcification, wind driven gas exchange using a

homogenous wind field, and eddy-driven mixing. The gradient in chemical parameters from reef crest to shore in this model matches the pattern of oxygen concentrations measured during high spatial resolution kayak-based sampling.

2.2.5 *Single, Well-Mixed Box Model*

For a single well-mixed box subject to the fluxes described in Figure 2.3a, the governing differential equations for the evolution of nTA, nDIC, and nO_2 concentrations on the reef are (Equations 2.1 – 2.3):

$$\frac{d[nTA]}{dt} = \frac{1}{\tau}([TA]_{sw} - [nTA]) + 2\frac{NEC}{z\rho} \qquad (2.1)$$

$$\frac{d[nDIC]}{dt} = \frac{1}{\tau}([DIC]_{sw} - [nDIC]) + \frac{NEP_{DIC}}{z\rho} + \frac{NEC}{z\rho} + \frac{k_{CO2}}{z}([CO_2]_{sat} - [CO_2]) \qquad (2.2)$$

$$\frac{d[nO_2]}{dt} = \frac{1}{\tau}([O_2]_{sw} - [nO_2]) + \frac{NEP_{O2}}{z\rho} + \frac{k_{O2}}{z}([O_2]_{sat} - [O_2]) \qquad (2.3)$$

These equations can be rearranged to solve for NEC, NEP_{DIC}, and NEP_{O2} as follows:

$$NEC = \frac{1}{2}z\rho\left(\frac{d[nTA]}{dt} - \frac{1}{\tau}([TA]_{sw} - [nTA])\right) \quad (2.4)$$

$$NEP_{DIC} = z\rho\left(\frac{d[nDIC]}{dt} - \frac{1}{\tau}([DIC]_{sw} - [nDIC])\right) - \rho k_{CO2}([CO_2]_{sat} - [CO_2]) - NEC \qquad (2.5)$$

$$NEP_{O2} = z\rho\left(\frac{d[nO_2]}{dt} - \frac{1}{\tau}([O_2]_{sw} - [nO_2])\right) - \rho k_{O2}([O_2]_{sat} - [O_2]) \qquad (2.6)$$

The quantities $[TA]_{sw}$, $[DIC]_{sw}$, and $[O_2]_{sw}$ represent the endmember composition of seawater, normalized to a salinity value of 35.4, that is advected from the open ocean onto the reef through swell and wind-driven waves (Falter et al., 2004; Monismith, 2007; Lowe et al., 2009; Zhang et al., 2012; Falter et al., 2013). This advective process leads to a characteristic residence time (τ, or e-folding time) of water in the model domain, measured in hours. The endmember values of $[TA]_{sw}$, $[DIC]_{sw}$, and $[O_2]_{sw}$ is set by our direct sampling of nearby offshore waters along with

data from the CLIVAR Repeat Section P16 hydrography cruises. These data additionally indicate that nearby offshore waters are near saturation with respect to O_2 and contain an average 1978 µmol/kg DIC and 2332 µmol/kg TA (Talley et al., 2015; Cross et al., 2017). Repeat occupations of this region indicate seasonal variability in offshore DIC and TA on the order of ±12 and ±17 µmol/kg, respectively (Feely et al., 2006). The parameter z is the ratio of the box volume to the benthic surface area and is effectively equivalent to the average depth of the box, which is set to 1 m. The term ρ is an assumed average seawater density of 1025 kg/m^3. Actual densities at the field location ranged between 1022 – 1024 kg/m^3. Air/sea gas exchange follows a gas-specific piston velocity, k_{CO2} and k_{O2}, in $m*hr^{-1}$.

I define the quantities NEP and NEC for a particular part of the reef as the net fluxes of carbon (in $moles*m^{-2}*hr^{-1}$) due to production-respiration and calcification-dissolution, respectively. I normalize NEC and NEP to square meters of seafloor rather than trying to estimate the complicated surface area of reef structures. This choice follows the typical convention used by other reef studies (UNESCO, 1982), facilitates extrapolation to larger reef areas, and makes the benthic surface area equivalent to the surface area of the air-water interface, simplifying our calculations. However, this choice also means that the calculated NEC and NEP values are somewhat specific to reefs with similar structure and benthic coverage. These net ecosystem quantities include both benthic and water column processes, which does not affect our calculations but is important if our fluxes are compared with other reefs. Since the typical water depth of the reef flat at our study site does not differ significantly from 1 m, and I make an additional assumption of vertical homogeneity due to high flow rates over rough topography, the relative importance of water column vs. benthic processes is likely constant across the reef.

Piston velocity is calculated for all of the models in our study using the updated parameterization provided by Wanninkhof (2014) and hourly wind speed data from a weather station deployed on Tetiaroa within 150 m of the study site (height ≅ 3 m above the ground; ≅ 10 m above sea level). I acknowledge that there is much discussion on the appropriateness of applying piston velocity parameterizations that are solely dependent on wind speeds in shallow reef environments and coastal locations where current interactions with benthic topography may influence gas exchange with the atmosphere (Ho et al., 2011; Ho et al., 2018). As described below, the main results of our study do not differ if I use gas exchange parameterizations developed for the open ocean or for shallow systems (Wanninkhof, 1992; Cole and Caraco, 1998; Ho et al., 2006; Wanninkhof, 2014; Ho et al., 2016). Note that the criteria of a well-mixed box are not strictly necessary for equations 2.1 – 2.6 to be true if [nTA], [nDIC], and [nO_2] represent mean concentrations. However, a well-mixed box is a necessary assumption if measurements at a single sensor package location are interpreted as whole box values, as done here. For the specific case of a single box that is not in steady state, the quantities d[nTA]/dt, d[nDIC]/dt, and d[nO_2]/dt are measured between successive time points. Together with endmember seawater concentrations and calculated values for the residence time and piston velocity, it is then possible to solve equations 3-6 for NEC, NEP, and empirical values of Q.

2.2.6 *Seawater Residence Time on the Tetiaroa Reef Flat*

Values of τ were estimated from salinity recovery after rainfall events on Tetiaroa. Within the framework of the single box model, this involved fitting CTD-derived salinity records to the following equation (Equation 2.7):

$$Sal(t) = e^{\frac{-t}{\tau}}\left(Sal_o - Sal_{final}\right) + Sal_{final} \quad (2.7)$$

where t is equal to the time in hours of a salinity record that captured a rain event; Sal_o is equal to the salinity value at the point that the rain event stops, and is typically the lowest salinity value in a time series; and Sal_{final} is the value of salinity following the recovery. The impact of evaporation on salinity recovery events and residence time estimates was found to be negligible in this location on diel timescales and was estimated using evaporative heat flux of vaporization estimates from local temperature and salinity measurements in accordance with the hfbulktc.m MATLAB script (ver. 2.0, 1999) and the MIT Thermophysical Properties of Seawater function toolbox for MATLAB (Sharqawy et al., 2010; Nayar et al., 2016). Rainfall amounts for each diel dataset, estimated from the NASA Tropical Rainfall Measuring Mission (TRMM 2011), ranged between 5 – 20 mm, with resultant salinity anomalies ranging between 0.1 – 0.6 (see Supplementary Materials). These rainfall amounts somewhat act as an independent check on model geometry. Comparing the magnitude of the initial salinity anomaly with the amount of rainfall for each diel field campaign, and assuming a well-mixed reservoir, implies an average box depth of 1.4 m for the entire reef flat, which compares relatively favorably with the measured depth of 1 m at the sampling location. While the magnitudes of NEP and NEC may scale with this difference in estimated box depths, values of Q, expressed as the quotient NEP_{O2}/NEP_{DIC}, are robust to choice of "z" (changes are insignificant compared to signals). Using the salinity recovery approach, residence times at the sampling location were estimated to range between 2.75 and 8.75 hours for different field campaigns presented here. The implications of uncertainties in residence times is discussed in more detail below (see 2.3.3 *Sources of Error in Empirical Q Determinations*).

2.2.7 *Biogeochemistry of Steady, Non-Dispersive Flow*

Instead of a single well-mixed box, dynamics on the reef flat can also be modeled from the perspective of individual parcels of water. By the time a parcel of water reaches a specific sampling location on the reef, it has already traversed some (possibly complicated) path across the reef flat that extends back to the open ocean (Figure 2.3b). If a parcel travels some distance "L" along this path, and if I neglect horizontal mixing (dispersion) along this path, then the acquired chemical anomaly is a result of the path-integrated fluxes (Equations 2.8 – 2.10):

$$TA(L) = TA_{sw} - 2\int_0^L \frac{NEC(\ell)}{z\rho}\frac{1}{flow(\ell)}d\ell \qquad (8)$$

$$DIC(L) = DIC_{sw} - \int_0^L \frac{1}{2}\frac{NEP(\ell)}{z\rho}\frac{1}{flow(\ell)}d\ell - \int_0^L \frac{NEC(\ell)}{z\rho}\frac{1}{flow(\ell)}d\ell + \int_0^L \frac{k_{CO2}}{z}\Delta CO_2(\ell)\frac{1}{flow(\ell)}d\ell \quad (9)$$

$$O_2(L) = O_{2_{sw}} + \int_0^L Q(\ell)\frac{NEP(\ell)}{z\rho}\frac{1}{flow(\ell)}d\ell + \int_0^L \frac{k_{O2}}{z}\Delta O_2(\ell)\frac{1}{flow(\ell)}d\ell \qquad (10)$$

Equations 8-10 reduce to a familiar set of tracer anomaly equations that have been applied to solve NEC and NEP in several previous reef studies (Equations 2.11 - 2.13, Gattuso et al. 1996; Silverman et al. 2007a, 2009; Falter et al. 2008; Shamberger et al. 2011; Koweek et al. 2015b):

$$NEC = \frac{z\rho}{2}\frac{flow}{L}\Delta TA \qquad (2.11)$$

$$NEP_{DIC} = z\rho\frac{flow}{L}\Delta DIC - NEC + k_{CO2}\rho(CO_2 - CO_{2_{sat}}) \qquad (2.12)$$

$$NEP_{O2} = z\rho\frac{flow}{L}\Delta O_2 + k_{O2}\rho(O_2 - O_{2_{sat}}) \qquad (2.13)$$

where Q = NEP_{O2}/NEP_{DIC}. Using equations 2.11 – 2.13 requires careful site selection because they are only valid when the following simplifying assumptions are true: (1) steady and non-dispersive flow ($d\ell/dt$ = flow(ℓ) = constant), which may apply for channel-like flow within some reefs, (2) average benthic fluxes and Q are all homogenous and time invariant ($dNEP(\ell)/d\ell$ = $dNEC(\ell)/d\ell$ = $dQ(\ell)/d\ell$ = 0), which may be appropriate when flow paths are integrated over

large reef areas and if flow is fast with respect to temporal variability, and (3) constant [O_2] and [CO_2] along the path. While flow on a reef is unlikely to obey all of these assumptions, this approach is relevant because it may represent a more realistic picture of reef circulation than a well-mixed box, and it is included here because it has been applied to previous reef studies. Even with the assumptions made about this model type, this approach still differs from the geometry of a single, well-mixed box. The inclusion of a time rate-of-change term in the single box model framework juxtaposes the path-dependent integrated approach applied in the non-dispersive flow model and results in properties of water being phase shifted relative to each other in different ways between model types. Note that dynamics are driven by the term flow/L, which has units of hr^{-1} and is an indication of the typical transit time or age for a parcel of water (Monsen et al., 2002). Where approximate fluxes are reported using this model, mean water mass ages were estimated to be consistent with the salinity-derived residence time from rain events for each diel experiment.

2.2.8 *Multi-box Eulerian Inverse Model*

This model assumes that open-ocean source waters enter the reef flat at the reef crest and then evolve through a series of discretized, area-normalized boxes along a 560-meter path toward the shore (Figure 2.3c). The geometry of this 1-D model allows for a chemical gradient normal to the reef crest. In other words, chemical composition evolves towards shore but is invariant in a direction parallel to the reef crest. While this 1-D treatment is a simplification, the geometry is consistent with the fact that oxygen concentration data evolve along the reef crest-shore axis without much change in the axis parallel to the shore (described below). The last box in the model corresponds to the sampling location in our study, consistent with its approximate distance of 0.5 km away from the reef crest. Water movement and chemical exchange between the boxes

is assumed to be driven by eddy mixing parameterized with a Fickian-like diffusion term. The same constant mixing parameter is applied throughout the model domain. The value of this mixing term is tuned inversely to generate a salinity recovery profile in the last box that matches real observations following precipitation events. While still simpler than a "real" reef, this model shares many of the components of more sophisticated treatments of reef flow (Falter et al., 2004; Falter et al., 2008; Falter et al., 2012; Falter et al., 2013).

After initialization of each box with open ocean seawater values and accounting for short-term spin-up time of the model, the concentrations of nO_2, nDIC, and nTA in each discretized box at any given moment are solved through the calculation of the instantaneous contributions of air-sea gas exchange through the top of the box in response to a homogenous wind field, the mixing of O_2, DIC, and TA between boxes, and the prescription of area-normalized benthic fluxes corresponding to net productivity and net calcification. In short, Equations 2.4 – 2.6 are applied to each box. The benthic fluxes of productivity are assumed to be homogenous across the entire reef flat but vary in time as hyperbolic tangent functions of photosynthetically active radiation (PAR), consistent with physiological parameterizations of coral reef metabolism (Equations 2.14 – 2.15, Atkinson and Grigg 1984; Langdon and Atkinson 2005; Bouman et al. 2018):

$$NEP_{O2} = (Pmax_{O2} \tanh\left(\frac{PAR*\alpha}{Pmax_{O2}}\right) - R_{O2}) \quad (2.14)$$

$$NEP_{DIC} = (Pmax_{DIC} \tanh\left(\frac{PAR*\alpha}{Pmax_{DIC}}\right) - R_{DIC}) \quad (2.15)$$

P_{max} is the maximum rate of net photosynthesis in units of mol O_2 or DIC * m^{-2} * hr^{-1}, α is the sensitivity of net production at light levels close to zero (mol O_2 or DIC * m^{-2} * hr^{-1} * μmol photons^{-1} * m^{-2} * sec^{-1}), and R is a constant respiration rate of O_2 or DIC (mol O_2 or DIC * m^{-2} * hr^{-1}). Sub-hourly PAR data was provided from the local weather station on Onetahi.

Fluxes of net calcification were modeled using a modified version of the Platt et al. (1980) power function, which governs calcification as a function of PAR (Equation 2.16, Egilsdottir et al. 2016):

$$NEC = (C_{Max}\left(1 - e^{-\alpha_{CD}*\frac{PAR}{C_{Max}}}\right) + C) \qquad (2.16)$$

where C_{Max} is the maximum rate of net calcification in units of mol $CaCO_3$ * m^{-2} * hr^{-1}, α is the sensitivity of net calcification under low light (mol $CaCO_3$ * m^{-2} * hr^{-1} * µmol $photons^{-1}$ * m^{-2} * sec^{-1}), and C is a constant rate of dark calcification/dissolution. For each diel dataset, a single value of P_{max}, C_{max}, α, α_{CD}, R, and C were tuned by minimizing the sum of the square of the residuals between the modeled values of nDIC, nTA, and nO_2 within the last box as compared with the measured values of these parameters over the sampling period. A summary of the optimal parameters corresponding for each diel dataset is presented in the Supplemental Materials. Following model spin-up and inversion, the instantaneous Q for every time point within the day is the quotient of Equations 2.14 and 2.15, which equals NEP_{O2}/NEP_{DIC}.

2.3 Results and Discussion

In every diel campaign dataset presented here, minima in nDIC correspond with maxima in nO_2 in the late afternoon and vice versa near dawn. The amplitude of this inverse relationship, relative to changes in nTA, implies that productivity rather than calcification is the dominant metabolic process driving diel cycles in nDIC at our reef site (Figure 2.4, Barnes 1983; Barnes and Lazar 1993). Additionally, nTA variations followed a similar daytime trend as nDIC variations, an observation consistent with light-enhanced calcification in reef ecosystems (Falkowski et al., 1984; Gattuso, Allemand, et al., 1999; Cohen et al., 2016).

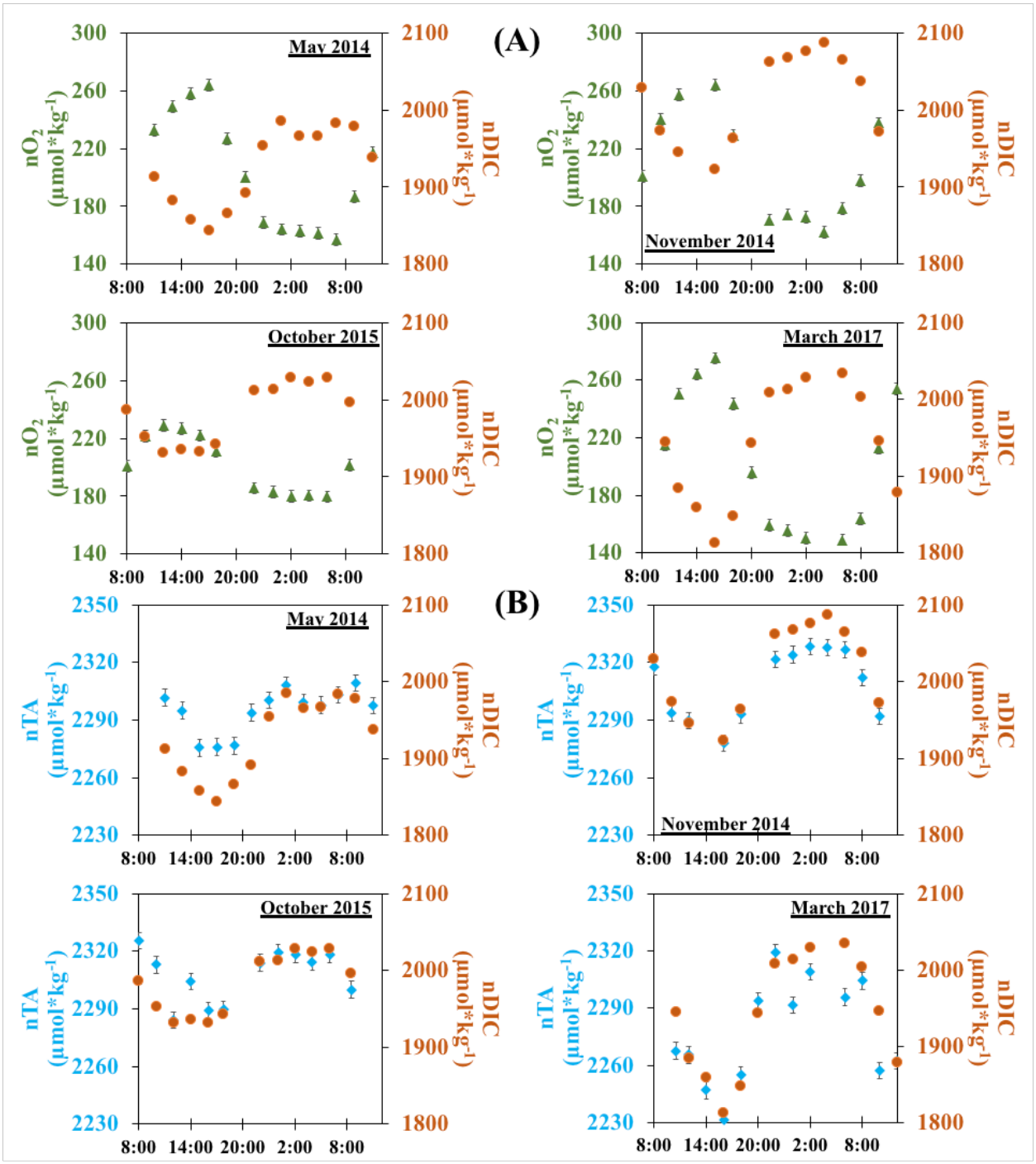

Figure 2.4. A) Values of nDIC (brown, circles) and nO_2 (green, triangles) measured at the reef-flat sampling location vary inversely during every field campaign, consistent with a productivity-dominated system. (B) Values of nTA (blue, diamonds) and nDIC are also tightly coupled, but with a positive correlation, indicative of the impact of carbonate precipitation/ dissolution and consistent with light-enhanced calcification during the day. Differences in the

magnitude, mean, and pattern of these chemical parameters between field campaigns are interpreted as the result of differences in residence time, gas exchange, and benthic fluxes as a function of tidal or seasonal cycles, swell intensity or direction, and weather. The field measurements summarized here are the primary data used to calculate NEC, NEP, and Q.

2.3.1 *Determination of NEC, NEP, and Q for a Single Box*

For the well-mixed single box model, estimates of daily NEP (range = -66 – 312 mmol DIC * m^{-2} * day^{-1}) are indicative of either net daily heterotrophy or autotrophy on the reef flat depending on the sampling day, while NEC values (range = 43 – 90 mmol $CaCO_3$ precipitated * m^{-2} * day^{-1}) indicate net calcification during all field campaigns. Uncertainties in the residence time calculations between field campaigns (i.e flow regimes) are the most likely cause for the range of observed values in metabolic fluxes; however, the values themselves are similar to those reported from nearby Mo'orea (Gattuso et al., 1993; Gattuso et al., 1997).

One additional method of visualizing these metabolic results is a plot of the hourly fluxes of NEP_{DIC} (Eqns. 2.5, 2.12, and 2.15) vs NEP_{O2} (Eqns. 2.6, 2.13, and 2.16; Figure 2.5). On this plot, the y-coordinate and x-coordinate of a single point can be ratioed to reveal the instantaneous hourly Q for that time, while the slope of the relationship between all points can be interpreted as an estimate of "net" daily Q (Q_{net}) for a given dataset with the assumption that the residence time on the reef flat within a particular diel cycle is invariant. Note that if reef metabolism was governed by canonical stoichiometry, instantaneous and daily net values of Q should reduce to values of -1.45 or -1. Scatter around a line of constant slope implies temporal variability in Q associated with uncertainties in measurements, additional metabolic biochemical reactions with non-canonical photosynthesis/respiration stoichiometries between carbon and oxygen, and/or missing advective or gas exchange processes (discussed in more detail below). Non-zero values for the y-intercept imply non-steady state water chemistry behavior on the

timescale of days (i.e. the concentrations of DIC, TA, and O_2 do not return to the same "starting" values at the beginning of each day). Additional uncertainty in intercepts may arise from the assumption that open ocean endmember values of DIC, TA, and O_2 from the P16 repeat hydrography cruise are appropriate for all field campaigns.

Empirical values of Q change throughout the day as does Q_{net} (i.e., slope of the linear regressions of NEP_{O2} vs NEP_{DIC}) for each field campaign ($-0.86 \leq Q_{net} \leq -0.57$; Figure 2.5). This variability is observed between field campaign datasets as well (Table 2.1). Empirical values of Q also differ from the canonical Redfield-Hedges value of -1.45 (Hedges et al., 2002) and the value of -1 (Sargent and Austin, 1949; Sargent and Austin, 1954; Odum and Odum, 1955; Kohn and Helfrich, 1957; Smith and Marsh, 1973; Kinsey, 1979; Kinsey, 1985; Gattuso, Frankignoulle, et al., 1999; Takeshita et al., 2016) measured or often assumed for tropical reef ecosystems. Large variability (≥ 0.2 units) in Q between successive samples and times of day with significant deviations from Q = -1.45 or Q = -1 are observed during all four diel experiments. These key observations about Q are true whether or not Q is averaged across a 24-hr period, calculated for each time point independently, or only calculated when successive measurements imply a steady rate of change (i.e. periods of time within a diel cycle when d[nTA]/dt, d[nDIC]/dt, and $d[nO_2]/dt$ are all constant; see Supplementary Materials).

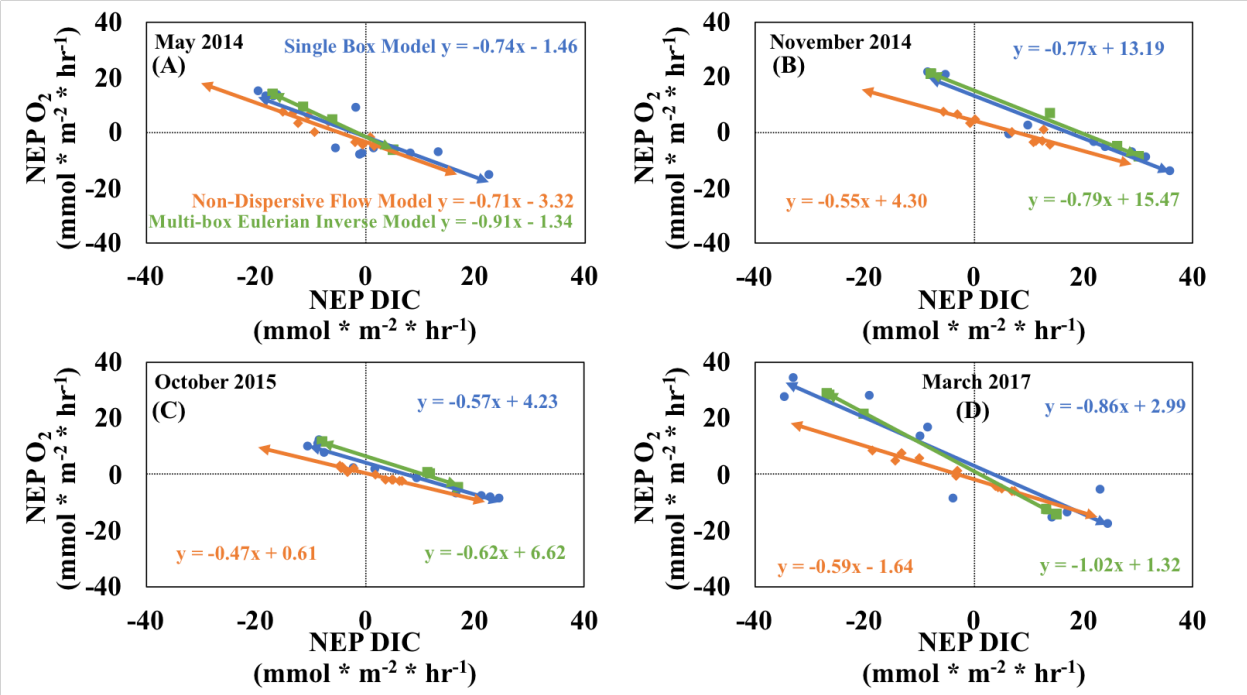

Figure 2.5. Hourly fluxes of NEP_{O2} vs NEP_{DIC}, where the slope of the regression line through this data = net daily $\Delta O2/\Delta DIC = Q_{net}$, show large hourly and net daily variability in empirically-determined Q both within and between field campaigns (A: May 2014, B: November 2014, C: October 2015, and D: March 2017). Fluxes of NEP have been corrected for the hourly contributions of calcification (applicable to DIC only), mixing, and gas exchange. Colors of linear regression lines and equations are representative of Q vectors that best describe data decomposed using the single box model (blue, circles), the non-dispersive flow model (orange, diamonds), and the multi-box Eulerian inverse model (green, squares). The variability in y-intercepts of regression lines between field campaigns may be an indicator of non-steady state chemical variability on the timescale of days as well as differences between open ocean concentrations of DIC, TA, and O_2 (due to changes in seasonal circulation patterns, for example).

Table 2.1. Summary of temporal variability in Q_{net} and daily NEP and NEC for the field campaigns conducted on Tetiaroa Atoll.

Time	Single Box Model	Non-Dispersive Flow Model	Multi-box Inverse Model
May 2014 Campaign			
5:00	-0.91	8.13	-1.20
11:00	-0.76	-0.61	-0.82
17:00	13.40	-0.52	-0.85
23:00	-0.52	1.70	-1.20
Daily Q_{net}	-0.74	-0.71	-0.91
Daily NEP (mmol DIC*m^{-2}*day^{-1})	-66	-132	-110
Daily NEC (mmol $CaCO_3$*m^{-2}*day^{-1})	43	81	44
November 2014 Campaign			
6:00	-0.10	0.09	0.51
12:00	-3.05	-2.26	-2.69
18:00	-0.21	-4.25	-0.18
0:00	-0.28	-0.25	-0.28
Daily Q_{net}	-0.77	-0.55	-0.79
Daily NEP (mmol DIC*m^{-2}*day^{-1})	312	110	292
Daily NEC (mmol $CaCO_3$*m^{-2}*day^{-1})	55	48	66
October 2015 Campaign			
6:15	1.05	-0.44	0.09
12:00	-0.97	-0.69	-1.44
17:45	-0.15	-0.34	0.04
0:04	-0.35	-0.36	-0.26
Daily Q_{net}	-0.57	-0.47	-0.62
Daily NEP (mmol DIC*m^{-2}*day^{-1})	141	12	131
Daily NEC (mmol $CaCO_3$*m^{-2}*day^{-1})	75	46	66
March 2017 Campaign			
6:00	2.21	-0.78	-0.93
12:00	-1.48	-0.58	-1.07
18:00	-0.24	-0.35	-0.92
0:00	-1.07	-1.02	-0.93
Daily Q_{net}	-0.86	-0.59	-1.02
Daily NEP (mmol DIC*m^{-2}*day^{-1})	2	-56	-49
Daily NEC (mmol $CaCO_3$*m^{-2}*day^{-1})	90	118	74

2.3.2 *Determination of NEC, NEP, and Q for Other Models*

The above scenario treated the reef as a single well-mixed box in order to build a simple model of coral reef biogeochemistry. A more realistic characterization of the reef would acknowledge the presence of chemical variations and gradients on various space and time scales (Cooper et al., 2007; Falter et al., 2012; Manzello et al., 2012). For example, regions of less chemically-evolved water might be found near the reef crest, which would be chemically more similar to the open ocean than older parcels of water on the back reef. Indeed, high spatial-resolution (~10 m) dissolved O_2 measurements from the Tetiaroa reef flat, taken by kayak in the mid-afternoon (between 2 PM and 4 PM on 02 April 2017), when productivity fluxes are the largest and thus easiest to observe, revealed a strong chemical gradient with concentrations generally increasing from the reef crest toward the shore (see Supplementary Materials). A multi-box Eulerian inverse model that faithfully reproduces both the trend in the mapped spatial gradient in dissolved oxygen and diel chemistry was used to test whether Q still differed from canonical or assumed values in a more realistic model.

As the implied NEP fluxes for DIC (Eq. 2.15) and oxygen (Eq. 2.16) are solved independently, they can be used to calculate hourly and daily net values of Q for each diel cycle. Again, hourly Q was found to be variable within each dataset and different from canonical values ($-1.02 \leq Q_{net} \leq -0.62$; Table 2.1, green squares in Figure 2.5). Daily NEP and NEC estimates differ between the modeling frameworks but the trends and magnitudes are similar, with daily NEP ranging from -110 – 292 mmol DIC * m^{-2} * day^{-1} (still indicative of potential daily net heterotrophy) and NEC suggestive of net daily calcification with a range of 44 – 74 mmol $CaCO_3$ precipitated * m^{-2} * day^{-1}. Additionally, I tested steady non-dispersive flow models for

decomposition (Eq. 8-13) and still found hourly values of Q to be variable, although the range of daily Q_{net} values shifted to $-0.71 \leq Q_{net} \leq -0.47$ (Table 2.1, Figure 2.5).

In summary, empirically measured values of Q are different from canonical values even when reef biogeochemistry is modeled in very different ways. Furthermore, single box, steady flow, and multi-box models all imply that Q can vary from hour to hour. These are robust results of our study that imply true variations in Q within and between diel datasets in one reef location.

2.3.3 *Sources of Error in Empirical Q Determinations*

The rapid exchange of O_2 with the atmosphere as compared with CO_2 is a well-known feature of chemical oceanography that stems from differences in kinetic constraints between O_2 and equilibrium reactions between dissolving CO_2 and the oceans' large reservoir of bicarbonate and carbonate ions (Emerson and Hedges, 2008). It can lead to variations in apparent Q if gas exchange is not accurately accounted for. For example, the e-folding times for gas exchange of O_2 and CO_2 between the atmosphere and a 1-m-deep column of water are 20 hours and > 160 days, respectively, using the typical wind speeds observed in this study. As previously mentioned, there is much discussion surrounding the appropriate parameterization of gas exchange in shallow, coastal reef environments, with slight nuances between different approaches, such as variability in equation constants and specific considerations of surface rugosity, potentially resulting in significant differences in wind speed-derived piston velocities (Ho et al., 2011; Ho et al., 2018). However, the results of a simple sensitivity analysis using the single box model suggested that even if piston velocities for each discrete measurement across all field campaigns were increased 4x and subjected to the analytical uncertainties of nDIC, nTA, and nO_2 measurements, per-hour Q values show similar patterns of hourly variability, and $-1.52 \leq$ Daily $Q_{net} \leq -0.71$ (Supplemental Information). The $Q_{net} = -1.52$ value (March 2017), although

closer to that predicted for Redfield-like stoichiometry, implies sustained windspeeds in excess of 12 m * s^{-1} throughout the day, which is inconsistent with measured wind speed data. This result implies that reasonable uncertainties in gas exchange errors alone cannot explain the deviation from canonical Redfield stoichiometric closing of metabolic carbon and oxygen budgets observed here.

I further investigated the impact of a range of piston velocities (0 – 0.6 m * hr^{-1}) and water residence times (0.5 – 12 hrs) on the overall biogeochemical decomposition of metabolic data. Using a Monte Carlo approach, I tested whether the measured data at each time point in a given diel dataset were consistent with the canonical (-1.45) or commonly assumed (-1) values of Q (Fig. 6). This exercise explored 5000 iterations of the aforementioned ranges of k and τ along with normally-distributed random errors on nDIC, nTA, and nO_2 measurements. Note that the explicit treatment of error in this Monte Carlo approach appropriately deemphasizes departures of empirical Q from canonical Q when the values are very uncertain (i.e. dawn and dusk). To understand why dawn and dusk may show large variability in empirical Q, even if "true" Q were constant, consider that empirical Q is the ratio between NEP_{O2}, calculated using oxygen, divided by the NEP_{DIC}, determined from DIC and TA. During dusk and dawn, when the reef switches between net photosynthesis and net respiration, both NEP values approach zero, thus the relative uncertainty in NEP (and by extension, Q) is highest at these times. In contrast, during the middle of the day or night, NEP fluxes are large, more certain, and result in relatively smaller errors for Q. The fact that Q diverges from canonical values even during the middle of the day and night is further support that our findings are robust.

From the results of our Monte Carlo analysis, it is possible to find time intervals where there are combinations of τ and k such that the null hypothesis, that empirical Q equals canonical

Q, cannot be rejected at the 95 % level of confidence (LOC; Figure 2.6 and Supplementary Materials). However, there is no single choice of τ and k such that the empirical Q is within error of canonical Q for all time intervals. Nor do the changing combinations of τ and k necessary to yield a canonical value for Q match other field observations of these parameters. For example, in Figure 2.6, which is representative of the October 2015 diel field campaign, values of Q = -1 and -1.45 can be rejected at the 95% LOC unless wind speeds approach or exceed 15 m/s. Yet measured wind speeds during this field campaign rarely exceeded 5 m/s and never exceeded 8 m/s ($k \cong 0.2$ m/hr). Furthermore, the values of τ and k necessary to produce the canonical value of Q at one time interval can be very different from the necessary combinations of τ and k in subsequent time intervals. While some changes in wind speed and water residence time are reasonable, maintaining a constant value of canonical Q can imply physically unreasonable shifts in reef conditions. For example, the parameter space for maintaining a value of Q that is within the 95% LOC of Q = -1 shifts between 6 PM and 10 PM in the October 2015 data, such that sustained wind speeds would have had to increase to nearly 20 m/s and residence times would have to increase by at least 1.5 hours (Figure 2.6). Considering the results from this single box error propagation analysis, I can reject the null hypothesis that Q is constant and equal to canonical or assumed values throughout the day if wind speeds and water residence are assumed to fall within their observed range or, if outside that range, assume they cannot shift by physically improbable amounts from hour to hour.

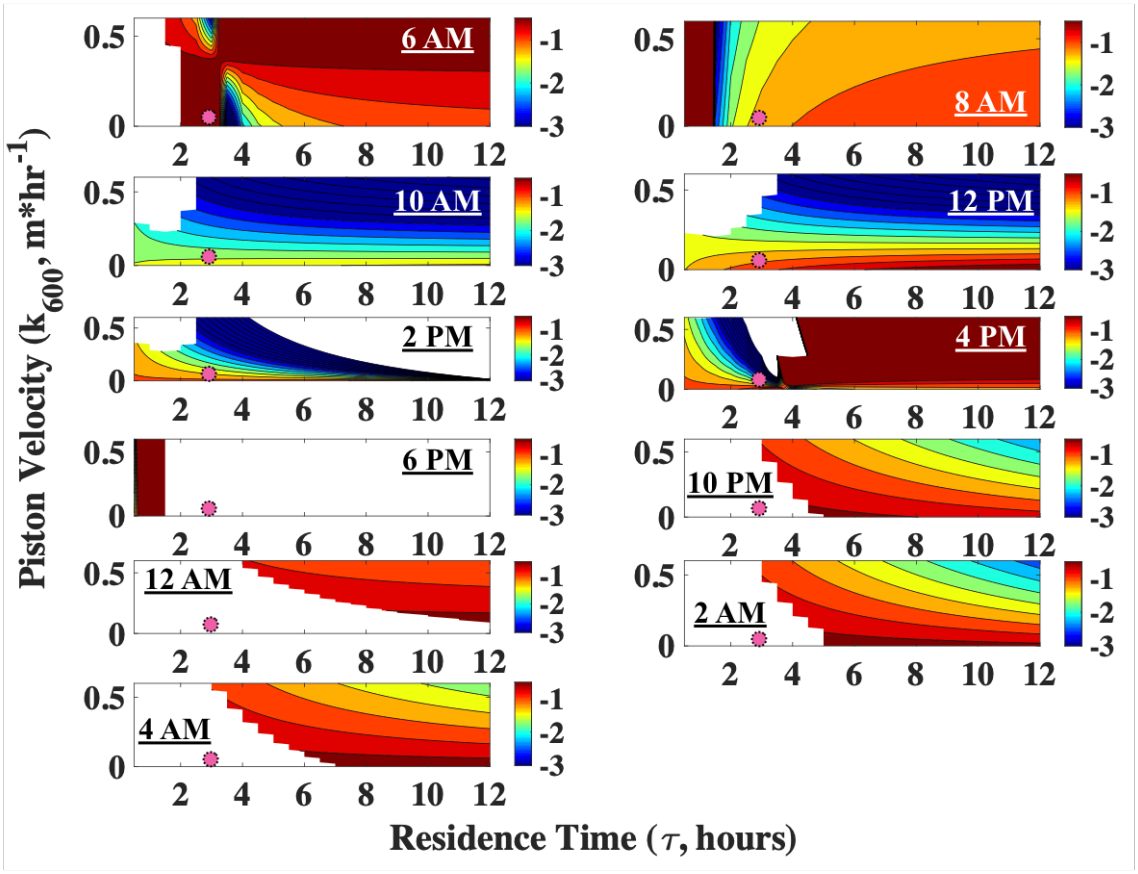

Figure 2.6. Variations of Q across a range of possible gas exchange rates (k_{600}) and water residence times (τ) during the October 2015 field campaign. Even when a large range of piston velocities and residence times are explored, there is no single choice of τ and k such that the empirical Q is within error of canonical Q for all hours of the day. Furthermore, many of the implied hourly shifts in k and τ between time points imply physical shifts in flow and/or wind speed that do not match other observations about the reef. Shaded regions correspond to values of Q where a value of −1 cannot be statistically excluded at 95% C.I. when considering analytical uncertainty on DIC, TA, and O_2 measurements errors over 5000 Monte Carlo iterations of Q inversions. Individual color contours within each panel represent values of Q calculated at each time point from empirically measured DIC, TA, and O_2. White, unshaded regions are indicative of combinations of k and tau where Q = −1 can be rejected at 95% C.I. when subjected to measurement uncertainties for nDIC, nTA, and nO_2. The pink circle in each panel indicates the values for k and tau based on measured wind speed and salinity anomaly-derived residence time, where gas exchange parameterization followed results of Wanninkhof,

2014. Data shown is from the October 2015 field campaign, with similarly unpredictable trends observed in datasets from other campaign datasets (see Supplementary Materials).

2.3.4 *Implications for Monitoring Reef Biogeochemistry Using pH and O_2*

The impact of variable values of Q on estimates of daily NEP and NEC was investigated using the data generated from the Eulerian inverse model. This is the most conservative dataset because this model architecture results in empirical Q values that are the closest to the canonical value. Applying Q = -1 to productivity fluxes of O_2 results in errors in rates of daily net productivity no less than 40% and at times exceeding 160%. NEC estimates using Q = -1, pH, and O_2 data to solve for instantaneous calcification fluxes result in errors between 60% and 235%, with two estimates shifting from implied net calcification to net dissolution (see Supplementary Materials). These NEC estimates employed the analytical scheme described graphically in Figure 2.1 and are algebraically identical to the approach of Barnes (1983), which itself has been applied in more recent reef metabolism investigations that relied on coupled pH and O_2 measurements (Gattuso et al., 1999b; Takeshita et al., 2016). The large error in NEC rates determined using Q = -1 also assume perfect information about values of TA_o at the time each sensor-based pH and O_2 measurement was made. Errors in NEC are magnified by the use of a constant value of TA_o, which is the approach used in previous determinations of metabolism on reefs using Q (Barnes, 1983; Gattuso, Frankignoulle, et al., 1999; Takeshita et al., 2016). Given the promising recent proposal of NEC/NEP ratios as indicators of community composition changes on reefs under environmental stressors (Andersson and Gledhill, 2013), the errors associated with choosing an inappropriate value for Q may also ultimately lead to mischaracterizations of the ratio of calcifiers to macroalgae within and between reef ecosystems, if these measurements are based on pH and O_2. Our data and analysis imply that inaccurate Q

values can have major implications for reef metabolism studies. The variability in Q throughout the day further implies that Q has to be measured regularly to overcome these issues, which places limits on the utility of autonomous pH and O_2 measurements for determining reef metabolism.

2.3.5 *Potential Causes of Low Productivity Quotients*

If daily benthic fluxes of photosynthesis/respiration on the reef flat are truly governed by canonical Redfield-Hedges stoichiometry between O_2 and DIC, a missing net flux of oxygen or carbon must exist. When put in terms of O_2, this flux generally follows a pattern of being a missing sink of oxygen in the day and a missing source at night, although the mean value of the flux switches to imply a missing source throughout both day and night in the Nov. 2014 experiment (Figure 2.7). I chose to focus on explaining these trends from the perspective of O_2 because most processes that I consider primarily operate on oxygen rather than DIC. Where this is not the case, the inverse pattern applies to DIC. The results of our previous analysis (2.3.3 *Sources of Error in Empirical Q Determinations*) indicate that error in gas exchange parameterizations cannot adequately account for this pattern. I therefore evaluated additional potential explanations for the missing fluxes based on whether they can explain the overall low magnitude of empirically-determined Q, as well as the timing of departures from expected Q values observed in Figure 2.7.

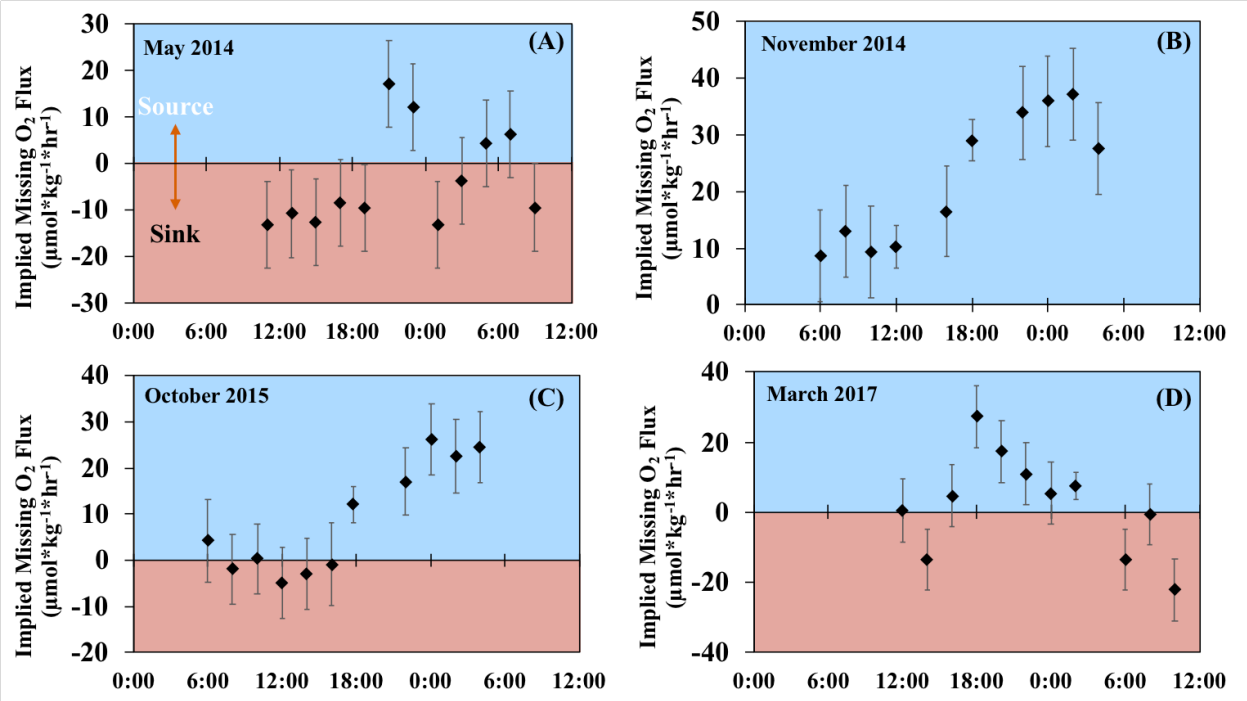

Figure 2.7. The implied missing hourly O_2 flux assuming productivity on the reef follows a canonical value of Q (−1.45) generally indicates a missing O_2 sink during the day and a missing O_2 source at night (A: May 2014, B: November 2014, C: October 2015, and D: March 2017). One possible explanation of this pattern is loss of O_2 into captive biologically-driven bubbles during the day, with subsequent dissolution at night supplying additional O_2. The patterns seem reproducible across all diel field campaigns. Missing fluxes are calculated using the single well mixed box model. Error bars represent 95% LOC on per hour missing flux based on uncertainties in instrumental precision.

2.3.6 *Oxidation State of Organic Matter*

The change in dissolved oxygen due to either metabolizing or synthesizing different organic substrates depends on the oxidation state of the atoms within each compound. For example, aerobic respiration of glucose ($C_6H_{12}O_6$) leads to a theoretical Q of -1, while respiration of formic acid (HCO_2H) corresponds to a value of Q = -0.5. Other processes that result in low magnitude Q values include the formation and respiration of certain amino acids, ribonucleoside monophosphates (such as RNA), and deoxyribonucleoside monophosphates (such as DNA) in

the presence of ammonia (Laws, 1991). This is because the direct assimilation of ammonia consumes less oxygen than the assimilation of nitrate. The production of these biomolecules from ammonia result in $-0.92 \leq Q \leq -0.75$, similar to average daily values on Tetiaroa. Thus, it is possible to drive true Q to lower than the canonical values if the organic matter on the reef is more oxidized than typical marine organic matter, or if primary production is supported primarily by ammonia rather than nitrate. However, it is inconsistent with our knowledge of typical cellular components to assume that most of the organic matter on a reef, including living biomass, is composed of such highly oxidized compounds. Previous studies indicate that the dominant dissolved organic carbon (DOC) compounds in coral reef environments include the glycerol ($C_3H_8O_3$) and the amino acid alanine ($C_3H_7NO_2$), and the fixation/remineralization of these biomolecules in the presence of ammonia results in $-1.16 \leq Q \leq -1$ (Muscatine et al., 1981; Falkowski et al., 1984; Laws, 1991). Therefore, while it is possible that ammonia assimilation coupled with the assimilation, production, and respiration of oxidized organic compounds contributes in some part to the observed deviations from canonical Q observed here, it is unlikely to be the main source of this signal.

2.3.7 *Photorespiration*

Photorespiration, the wasteful binding of O_2 to RuBisCO in plants and algae and the subsequent recycling of the resulting metabolic products, *consumes* O_2 to produce CO_2 in a roughly 2:1 ratio (Voet and Voet, 2011). Thus, photorespiration acts on O_2 and CO_2 in the opposite direction as photosynthesis even though they occur at the same time. Because of the $\sim 2O_2{:}1CO_2$ stoichiometry, photorespiration acts to reduce O_2 production due to photosynthesis more than it reduces the CO_2 consumption from photosynthesis. In net, this means less O_2 production relative to CO_2 consumption and lower values of Q when photorespiration is

occurring. While the low Q values that I observe can be explained through the effects of photorespiration, the pattern in time cannot be explained through this process alone. As observed in Figure 2.5 and Table 2.1, both daytime and nighttime productivity quotients show significant deviations from Redfield-Hedges or that typically assumed for reef environments (Q = -1), with nighttime values often smaller in magnitude than those observed during daylight hours. If photorespiration were driving the observed variability in Q, then the empirical Q would diverge during the day only. It is therefore unlikely that this process alone is responsible for the observed variability in productivity ratios.

2.3.8 *Metabolic Processes in the Sediment*

Microbially-mediated, anaerobic redox reactions can decouple oxygen and dissolved inorganic carbon. Specifically, denitrification consumes organic matter and produces inorganic carbon without directly affecting oxygen. It is possible that this process could contribute to low magnitude Q values, particularly at night when dissolved O_2 concentrations decrease dramatically (Figure 2.4). Denitrification in the carbonate sediments of reefs have previously been shown to contribute meaningfully to biogeochemical cycling on coral reefs (Entsch et al., 1983; Alongi, 1989; Santos et al., 2012; Erler et al., 2014). Hermatypic corals are known to be extremely efficient in the cycling of organic and inorganic nitrogen, with some studies suggesting a balance of nitrification/denitrification necessary to maintain net autotrophy in such oligotrophic environments (Siboni et al., 2008; Rädecker et al., 2015).

To support significant denitrification fluxes on the reef, several conditions are necessary: (1) a carbon source, (2) a nitrate or nitrite source, and (3) an anoxic environment. A high abundance of holothurians or “sea cucumbers”, which are deposit feeders, near our sampling location implies a source of particulate organic carbon in or on the sediments, even if the

carbonate sediments appear to have a low standing stock of organic matter. At some other atoll and reef locations, the degradation of coral mucus within reef sediments has also been shown to cause large enough gradients in shallow sediment oxygenation to fuel sulfate reduction, which also increases DIC without changing *in situ* O_2 (Wild et al., 2004). In the context of increased mucus supply to sediments, Wild et al. reported values of net productivity quotients at Heron Island on Australia's Great Barrier Reef of $-0.64 \leq Q \leq -0.48$, similar to net daily and nighttime values of Q on Tetiaroa. Organic matter respiration sufficient to generate anoxic conditions like those observed by Wild et al. (2004) or sufficient to support denitrification, would also be expected to lower pore water pH and lead to sediment dissolution. However, Eyre et al. (2018) conducted sediment incubations elsewhere on Tetiaroa, as part of a study on carbonate sediment dissolution on reefs under the stress of ocean acidification, and found no sign of net nighttime sediment dissolution. This lack of sediment dissolution and associated anoxic conditions is consistent with the fact that the sediments near our study site are thin, with only a few centimeters of sediments covering a hard carbonate basement. These shallow sediments are likely well-ventilated by strong water flow. The likely absence of strongly anoxic sediments, the limited supply of nitrogen containing species in the oligotrophic waters of Tetiaroa Atoll, and the fact that Q is shifted from canonical values throughout the diel cycle and not just during the night, all indicate that denitrification and other sediment redox processes, while possibly influential, are probably not the main mechanisms that lead to low Q.

2.3.9 *Mixing*

nDIC and nTA are two measured quantities that are subject to conservative mixing in seawater; nO_2, however, is not, because of gas exchange. This difference in mixing behavior can affect the ratio of oxygen to DIC in the mixture, which shifts the apparent Q. I conducted a

simple synthetic mixing experiment to explore how apparent Q varies when real reef waters are mixed. The values of nO_2, nDIC, and nTA measured during one diel experiment were combined with the nO_2, nDIC, and nTA values corresponding to the same time of day, but from a different diel experiment. This simulates the mixing of two authentic water masses from the reef, even if they differ in time rather than space. For all time points, the mixing ratio between the end members was kept constant, although different instances of this thought experiment were also explored where the mixing ratio of every time point was changed to a new value. The resulting set of mixed nO_2, nDIC, and nTA were then decomposed within the single well-mixed box framework, representing the idealized case of no mixing. Diel experiments with similar residence times were chosen to make the choice of τ in the subsequent decomposition clear.

The results of this thought experiment show that apparent Q can be modified as a result of mixing, but the extent of this modification largely falls close to or between the Q values associated with each endmember. For example, mixing waters sampled at 10 PM local time from the November 2014 field campaign (hourly Q = -0.25) with waters sampled at the same time from the October 2015 campaign (hourly Q = -0.40) results in a range of potential values of Q $-0.41 \leq Q \leq -0.25$. This result is consistent when mixing parcels of water from other times of day. This exercise implies that mixing is an important factor for apparent Q and that it should be considered when inverting biogeochemical fluxes, but that it typically results in intermediate rather than divergent values of Q. Furthermore, the role of mixing at our site is probably small. Water that overtops the reef crest and enters the reef flat near our study site generally travels towards shore and then *northward* along shore. To the south of our study site, water typically flows towards shore and *southward* along shore. This divergence tends to isolate our study site from mixing with other reef water masses.

2.3.10 *Effect of Captive Bubbles on Apparent Q*

Low magnitude values of Q have previously been observed on Pacific reefs that are dominated by either algal flats, or heterotrophs and filter-feeders (Kinsey, 1985). In the case of algal flats, the loss of O_2 to the atmosphere through photoautrotrophic bubble formation is hypothesized as a key missing flux. Due to differences in solubility between oxygen and CO_2, these bubbles have a much larger impact on O_2 than on DIC. Additionally, bubble loss would only result in a missing O_2 sink during the day and could not explain the implied O_2 source typically observed on Tetiaroa during the night. However, the potential for productivity-driven *captive* bubble formation could lead to smaller magnitude Q values throughout a 24 hour diel cycle (Bastviken, 2009; Koschorreck et al., 2017; Howard et al., 2018). The formation of captive bubbles, which are abundant on the surface of algae as well as the undersides of coral on Tetiaroa's reef flat during the day (Figure 2.8), represent a temporary gaseous oxygen reservoir that acts like a missing oxygen sink. If these bubbles shrink and eventually re-dissolve at night, consistent with nighttime images of the reef, then they would act as a gaseous oxygen source at night. This cycle would act to lower the magnitude of Q over a 24-hour period, consistent with our observations.

Integrating the per hour missing oxygen fluxes represented by Figure 2.7, accounting for this missing oxygen entirely with captive bubbles, and assuming that the gas inside captive bubbles is in equilibrium with surrounding water, implies a maximum daily bubble volume between 0 and 5 L * m^{-2} (Supplemental Material). Based on the images of bubbles from Tetiaroa, a reasonable bubble diameter is 4 mm, with a typical corresponding gas volume of 0.03 mL. Because the missing sink during the day exceeds the missing source at night by up to 50%, up to a 50% fraction of the bubble volume formed during the day may escape to the atmosphere.

Accounting for this bubble loss mechanism reduces the maximum size of this reservoir, implying a range of 0 – 160,000 bubbles * m^{-2}. This implied number of bubbles is large but may be reasonable given the sheer magnitude of bubbles associated with a single head of coral from Tetiaroa during the day (Figure 2.8). From this image of algae-covered *Porites* colonies at 10 AM local time, the 0.05 m^2 area represented by the photo includes ~3000-5000 bubbles. Reefs are characterized by complex shapes, with extensive vertical surfaces, which provide a large effective surface area per square meter of seafloor that could boost the bubble density. The presence of large bubbles trapped under overhangs, which I commonly observe on Tetiaroa, could also contribute to the bubble volume. Taken together, this analysis implies that captive bubbles can act as a missing O_2 flux in an otherwise Redfield-governed reef system. However, the fact that 1 diel campaign (October 2015) implies a consistent missing source of O_2 throughout the 24-hour cycle is evidence that some processes in addition to captive bubbles must be affecting variability in Q. Because these bubbles affect oxygen at the surface of reef primary producers, the resulting non-canonical Q values would impact sensors placed anywhere in the water column.

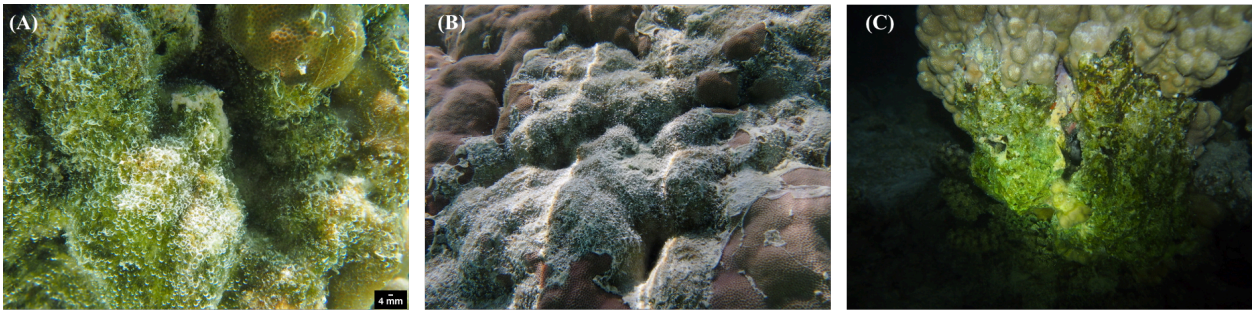

Figure 2.8. Photographic evidence of numerous captive bubbles on coral colonies and algal turf recorded on Tetiaroa's reef flat near the sampling location. A and B: Bubble presence on algae-covered Porites colonies (10 AM local time). C: Same location as left panel; bubbles shrink and disappear at night (10:30 PM local time). Typical bubble size estimated using a Porites polyp diameter of 4 mm, which resulted in an average bubble volume of 0.03 mL. At this

size, there would need to be 0–160,000 bubbles * m^{-2} to account for the missing implied reservoir of O_2.

2.4 CONCLUSIONS

Our results indicate that productivity quotients on coral reefs have a smaller magnitude than open ocean values and exhibit large temporal variability within and between diel sampling campaigns. These observations are robust to changes in the complexity and design of the biogeochemical models used to assimilate the data. They can be explained, in part, from captive bubbles with possible additional contributions from mixing, sediment denitrification, and ammonium-fueled primary productivity. Assumptions of canonical, Redfield-like or other ratios of oxygen to carbon in a shallow reef ecosystem, may neglect the contributions of these key processes and may result in significant inaccuracies in NEP and NEC calculations in shallow reef ecosystems. Because the significant limitations of this approach appear to come from oxygen variability, I indicate that metabolic studies of reefs should be based on spatially and temporally distributed measurements of carbonate chemistry rather than O_2 and pH. However, approaches that rely on eddy covariance-derived metabolism on reefs could still prove fruitful in locations where Q is empirically characterized and/or is temporally stable over the duration of the study. Furthermore, the role of captive bubbles may impact other dissolved gases and should be considered during future biogeochemical analysis of coral reefs.

Chapter 3. SEAWATER Sr/Ca RATIOS – A POTENTIAL PROXY FOR COMMUNITY CALCIFIER COMPOSITION DYNAMICS WITHIN CORAL REEF ECOSYSTEMS

3.1 INTRODUCTION

The interactive impacts of environmental stressors (warming, ocean acidification, hypoxia, eutrophication, and other local impacts) within coral reef environments could translate to large reductions in rates of net ecosystem calcification (NEC) amongst communities of marine calcifiers (Pandolfi, 2003; Pandolfi et al., 2011; Altieri et al., 2017; Baird et al., 2018; Kealoha, 2019; Kealoha et al., 2019). The ecological structure and stability of modern reef ecosystems at this community level is still unclear, particularly under increasing rates of ocean acidification. Within a reef, coral polyps work colonially to calcify immense and elaborate physical structures of $CaCO_3$ that serve as habitats for other marine organisms. Many additional genera of marine calcifiers (crustose coralline algae, non-coralline calcifying algae, gastropods, bivalves, etc.) can be found on reefs but do not themselves form community-supporting structures. Therefore, should highly sensitive coral species be replaced by more acid-tolerant corals as acidification increases (i.e. Camp et al., 2017), then future reef ecosystems may behave similarly to current reefs. Conversely, if ocean acidification leads to an overall shift from corals to non-reef building communities, then these habitats could become structurally destabilized (i.e. Kuffner et al., 2008; Fabricius et al., 2011; Hamylton, 2014). New forensic geochemical tools that are capable of detecting regime shifts from corals to other calcifiers could increase our ability to identify the

early signs of this transition, quantify the rate of this shift where it occurs and help manage the impacts of ocean acidification in reef ecosystems.

3.1.1 *Sr/Ca Partitioning in Calcifying Environments*

Conventional measurements of TA and DIC quantify the amount of calcification/dissolution on reef ecosystems (see Chapter 2) but do so without identifying *what* is calcifying. The signature of calcifying organisms is recorded in seawater, however, making it theoretically possible to distinguish the organisms undergoing calcification or dissolution through their distinct geochemical fingerprints. Specifically, Sr uptake from seawater into a carbonate mineral defines an empirical partition coefficient ($K_{D\text{-}Sr}$), which represents the exchange reaction of Sr and Ca ions between solution and mineral phases (Equation 3.1, Morse and Bender, 1990):

$$K_{D-Sr} = \frac{Sr/Ca_{mineral}}{Sr/Ca_{seawater}} \qquad (3.1)$$

Experimentally, $K_{D\text{-}Sr}$ differs between polymorphs of $CaCO_3$ precipitating from seawater, with most aragonites displaying values near seawater ($K_{D\text{-}Sr} \sim 0.9 – 1.3$) as compared to high- and low-Mg calcites ($K_{D\text{-}Sr} \sim 0.05 – 0.45$) which selectively reject Sr from the mineral form. Table 3.1 summarizes the diversity of observed Sr/Ca partitioning between seawater, inorganic $CaCO_3$, and many different calcifying marine taxa often found in reef environments (Kinsman and Holland, 1969; Weber, 1973; Carpenter and Lohmann, 1992; Elderfield et al., 2000; Stoll et al., 2002; Dietzel et al., 2004; Rosenheim et al., 2005; Gaetani and Cohen, 2006; Tang et al., 2008; Hetzinger et al., 2011; Gagnon et al., 2013; Steiner et al., 2014; Müller et al., 2014; Steiner et al., 2018). Additionally, the 0.5 unit or greater $K_{D\text{-}Sr}$ difference between most aragonite-precipitating and calcite-precipitating organisms is maintained despite temperature dependent relationships that govern biogenic and inorganic precipitation of aragonite ($\Delta K_{D\text{-}Sr} \sim 0.004$ -

0.005 per ºC; Kinsman and Holland, 1969; Dietzel et al., 2004; Gaetani and Cohen, 2006; Müller et al., 2014).

Table 3.1. A summary of Sr/Ca partition coefficients for many $CaCO_3$-precipitating marine organisms. *indicates studies that explored temperature dependence of $K_{D\text{-}Sr}$ from 10 – 25ºC. **indicates studies that explored the temperature dependence of $K_{D\text{-}Sr}$ from 0 – 80ºC. ***indicates a study that explored the temperature dependence of $K_{D\text{-}Sr}$ from 5 – 50ºC.

$CaCO_3$ Polymorph	**Media**	**Reported $K_{D\text{-}Sr}$**	**Reference**
Low-Mg Calcite (LMC)	Inorganic precipitation	0.05 – 0.17	Tang et al., 2008
LMC	Core-top planktonic forams	0.15	Elderfield et al., 2000
LMC	Cultured coccolithophores	0.28 – 0.45*	Müller et al., 2014
High-Mg Calcite (HMC)	Crustose coralline algae (*C. compactum* and *C. nereostratum*)	0.38 – 0.40	Calculated from Hetzinger et. al, 2011
Aragonite	Pteropods	0.12	Steiner et al., 2018
Aragonite	73 coral genera	0.82 – 1.1	Weber, 1973
Aragonite	Inorganic precipitation	0.9 – 1.15**	Kinsman and Holland, 1969
Aragonite	Inorganic precipitation	1.1 – 1.3***	Dietzel et al., 2004
Aragonite	Coral cores (*P. lobata*)	1.04	Steiner et al., 2014 (calculated from Corrège, 2006)
Aragonite	Inorganic precipitation	0.85 – 1.25**	Gaetani and Cohen, 2006

Aragonite	Cultured corals (*S. pistillata*)	1.04	Gagnon et al., 2013
Aragonite	Sclerosponges (*C. nicholsoni*)	1.1 – 1.2	Calculated from Rosenheim, Swart, and Thorrold, 2005

With $K_{D\text{-}Sr}$ values often slightly greater than 1, most aragonitic organisms will cause the seawater Sr/Ca ratio (Sr/Ca_{sw}) to decrease slightly as result of calcification and increase slightly as a result of dissolution. Alternatively, calcification of calcitic organisms and pteropods will cause Sr/Ca_{sw} increase, while dissolution will cause Sr/Ca_{sw} to decrease. This conceptually implies that in coral reefs and other calcifier-dominated environments, neither Sr nor Ca are biologically conservative, but they covary with one another as a function of (1) the magnitude of calcification/dissolution (NEC) *and* (2) the relative proportions of aragonite and calcite within the environment. Steiner et al. (2014; 2018) utilized this conceptual framework to develop Sr/Ca_{sw} into a tool to separate the calcification signals of coral from pelagic algae on a basin-wide scale in the Red Sea, a unique location where very large spatial gradients in calcification are observed ($\Delta nTA = 200\ \mu mol*kg^{-1}$ and aragonite calcification contributions range from 0 – 20%). If this tool can be adapted to detect the subtler changes in Sr/Ca_{sw} within and between coral reef environments on spatial and temporal scales, it would complement carbonate chemistry estimates of NEC across diel and seasonal cycles by quantifying community percent contributions to calcification budgets. Sr/Ca_{sw} could then be used as a proxy for monitoring the rate at which calcification regimes may change with time as ambient acidity and other stressors increase. Such a tool would be particularly timely, as the high-Mg calcites of coralline algae are often the “glue” that provides structural stability to coral skeletal frameworks but have been

shown to be much more soluble in acidifying conditions than reef-building corals (Burton and Walter, 1987; Andersson et al., 2008; Ries, 2010).

3.1.2 *Single Box Estimates of Sr/Ca_{sw} Variability within Coral Reef Ecosystems*

Given that rates of NEC, calculated from hourly changes in TA (see Chapter 2), change systematically over the course of a diel cycle in calcifying environments like coral reefs, it can be expected that patterns of temporal variability will be similar for Sr/Ca_{sw}. However, the expected signals and gradients are small in these locations when compared to previous studies focusing on basin scale variability. I designed a single-box model that uses hourly salinity-normalized alkalinity (nTA) variability from the March 2017 diel field campaign on Tetiaroa Atoll (see Chapter 2), assumed $K_{D\text{-}Sr}$ of 1.1 (aragonite) and 0.35 (calcite), and a Rayleigh fractionation systematic to predict how changes in total alkalinity impact theoretical magnitudes of diel variability of Sr/Ca_{sw} within coral reef ecosystems. Note that because total alkalinity is a component of salinity, it is necessary to salinity-normalize TA data to correct for the impacts of evaporation and/or rainfall that work to concentrate/dilute both TA and salinity.

My model assumes that hour-to-hour changes in nTA are equal to 2x the change in Ca due to NEC (ΔCa_{sw}, Equation 3.2):

$$\Delta Ca_{sw} = \frac{\Delta nTA}{2} \qquad (3.2)$$

Given a particular value for $K_{D\text{-}Sr}$ and an assumed global Sr/Ca_{sw} of 8.53 mmol/mol (de Villiers et al., 1994), values of NEC_{Ca} can be translated into changes in the dissolved Sr concentration of seawater (ΔSr_{sw}, Equation 3.3):

$$\Delta Sr_{sw} = \Delta Ca_{sw} * K_{D-Sr} * \left(\frac{Sr}{Ca}\right)_{sw} \qquad (3.3)$$

In each of these equations, I assume a global seawater dissolved Ca concentration (Ca_o) of 10.2 mmol*kg^{-1} (Emerson and Hedges, 2008). Together with global Sr/Ca_{sw}, these assumptions indicate a dissolved Sr concentration (Sr_o) equal to 87 µmol*kg^{-1}. To investigate the temporal evolution of Sr/Ca_{sw}, ΔSr_{sw} and ΔCa_{sw} can be used to calculate the new concentrations of Ca ($[Ca]_t$), Sr ($[Sr]_t$), and the Sr/Ca ratio ($[Sr/Ca]_t$) in seawater following a period of calcification (Equations 3.4 – 3.6):

$$[Ca]_t = \Delta Ca_{sw} + [Ca]_{sw} \quad (3.4)$$

$$[Sr]_t = \Delta Sr_{sw} + [Sr]_{sw} \quad (3.5)$$

$$[Sr/Ca]_t = {[Sr]_t}/{[Ca]_t} \quad (3.6)$$

Note that Equations 3.3 – 3.6 indicate that the evolution of Sr and Ca concentrations in seawater from initial concentrations (Sr_o and Ca_o) within coral reef environments can be described by a Rayleigh fractional distillation mechanism, where $K_{D\text{-}Sr}$ is the primary control of the magnitude of partitioning between solid and solution phases over the observed temporal or spatial gradient in Sr and Ca concentrations (Equations 3.7 – 3.9, derived from Elderfield et al., 1996):

$$\int_{Sr_o}^{Sr} \left(\frac{\Delta Sr}{Sr_{sw}}\right) = K_{D-Sr} * \int_{Ca_o}^{Ca} \left(\frac{\Delta Ca}{Ca_{sw}}\right) \quad (3.7)$$

$$\ln\left(\frac{Sr}{Sr_o}\right) = K_{D-Sr} * \ln\left(\frac{Ca}{Ca_o}\right) \quad (3.8)$$

$$\left(\frac{Sr}{Sr_o}\right) = \left(\frac{Ca}{Ca_o}\right)^{K_{D-Sr}} \quad (3.9)$$

Equation 3.9 can then be rearranged into a form that reflects the evolution of Sr/Ca_{sw} over an observed gradient as a function of measured and initial Ca concentrations and $K_{D\text{-}Sr}$ (Equation 3.10):

$$\frac{Sr}{Ca} = \left(\frac{Sr}{Ca}\right)_o * \left(\frac{Ca_{measured}}{Ca_{source}}\right)^{K_{D-Sr}-1} \quad (3.10)$$

However, outside of model parameters, any given coral reef likely contains a heterogenous community of calcitic and aragonitic marine calcifiers. I therefore hypothesize that Sr/Ca partitioning during NEC follows a Rayleigh fractionation from seawater that is governed by the "net" partition coefficient ($K_{D\text{-}Sr,\ Net}$) of the reef ecosystem. Based on Equations 3.4 – 3.6, the value of $K_{D\text{-}Sr,\ Net}$ can be used to calculate ΔSr_{sw} as a function of the global Sr/Ca_{sw} ratio, values of ΔCa_{sw} due to aragonite and calcite calcification/dissolution, and their respective polymorph $K_{D\text{-}Sr}$ (Equation 3.11):

$$\Delta Sr_{sw} = \left(\frac{Sr}{Ca}\right)_{sw} * \left(\Delta Ca_{sw-Aragonite} * K_{D-Sr,Aragonite} + \Delta Ca_{sw-Calcite} * K_{D-Sr,Calcite}\right) \quad (3.11)$$

Using the value of ΔCa_{sw} (instead of $\Delta Ca_{sw\text{-}Aragonite}$ and $\Delta Ca_{sw\text{-}Calcite}$), Equation 3.8 further implies that $K_{D\text{-}Sr,\ Net}$ is simply the sum of the relative contribution of aragonitic and calcitic $K_{D\text{-}Sr}$ relative to their fractional distribution or coverage within the ecosystem (Equation 3.12 – 3.13):

$$\Delta Sr_{sw} = \left(\frac{Sr}{Ca}\right)_{sw} * \Delta Ca_{sw} * \left(K_{D-Sr,Aragonite} * X_{Aragonite} + K_{D-Sr,Calcite} * (1 - X_{Aragonite})\right) \quad (3.12)$$

$$K_{D-Sr.Net} = K_{D-Sr,Calcite} * (X_{Calcite}) + K_{D-Sr,Aragonite} * \left(1 - X_{Aragonite}\right) \quad (3.13)$$

where "X" is equal to the fractional contribution of aragonitic $CaCO_3$ precipitation/dissolution. Additionally, because this single box Rayleigh fractionation framework relies on changes in Sr/Ca_{sw} relative to initial starting conditions, any observed variability within coral reefs over daily, seasonal, and interannual timescales should be relatively robust to characterizations of residence time – an issue that has plagued studies of metabolism and elemental cycling in these dynamic environments on numerous occasions (see Chapter 2).

The results of this modeling exercise, based on a maximum measured diel $\Delta nTA = 88$ $\mu mol*kg^{-1}$ and the aforementioned assumptions, implies reef Sr/Ca_{sw} would display a maximum

offset from open ocean seawater of -0.05% if all calcification could be attributed to aragonite precipitation ($K_{D\text{-}Sr}$ = 1.1; Figure 3.1) and +0.3% if all calcification could be attributed to high-Mg calcite precipitation ($K_{D\text{-}Sr}$ = 0.35; Figure 3.2). Thus, in a regime with a similar diel ΔnTA, the analytical precision on measurements of Sr/Ca_{sw} would need to be much better than 0.3% to resolve signals of calcifier community contributions to NEC. This ability to resolve relative percent contributions of aragonite and calcite to budgets of NEC scales linearly with precision in Sr/Ca_{sw} measurements (Figure 3.3). For example, a method that maintains 0.01% RSD or better external precision in Sr/Ca_{sw} should be capable of resolving single digit percent contributions of different $CaCO_3$ polymorphs to NEC budgets. Note that over the course of a full diel cycle, the offsets between reef and open ocean Sr/Ca_{sw} can decrease to tens to hundreds of parts-per-million (relative difference); thus, as external precision increases, so does the ability to distinguish differences in community calcifier contributions on hourly timescales.

I also acknowledge that there are a range of potential values of $K_{D\text{-}Sr}$ for both calcitic and aragonitic organisms (as shown in Table 3.1) and that the assumed values applied in this modeling exercise may not be the most representative of real-world conditions within any given reef ecosystem. When this model is used to explore the range of previously published values of $K_{D\text{-}Sr}$ listed in Table 3.1, 100% domination of NEC by either calcite or aragonite still results in unique partitioning behaviors of Sr/Ca_{sw} – even when differences between $K_{D\text{-}Sr}$ values are at their smallest (minimum $\Delta K_{D\text{-}Sr}$ between calcite and aragonite = 0.37). This finding indicates that measurements of Sr/Ca_{sw} should be capable of resolving changes in calcification dynamics *between* communities of calcitic and aragonitic organisms despite the apparent spread of potential $K_{D\text{-}Sr}$ values for each $CaCO_3$ polymorph. Said another way, the assumption of $K_{D\text{-}Sr}$ = 1.1 for aragonitic communities and $K_{D\text{-}Sr}$ = 0.35 for calcitic communities are valid in this

framework for distinguishing these two polymorph communities from one another. However, given the significant overlap in observed values of $K_{D\text{-}Sr}$ *within* communities of high- and low-Mg calcitic organisms (and in the case of pteropods, aragonitic organisms), empirical measurements of the molar Sr/Ca ratio of benthic carbonates may be necessary complements to measurements of Sr/Ca_{sw} to constrain calculations of $K_{D\text{-}Sr}$.

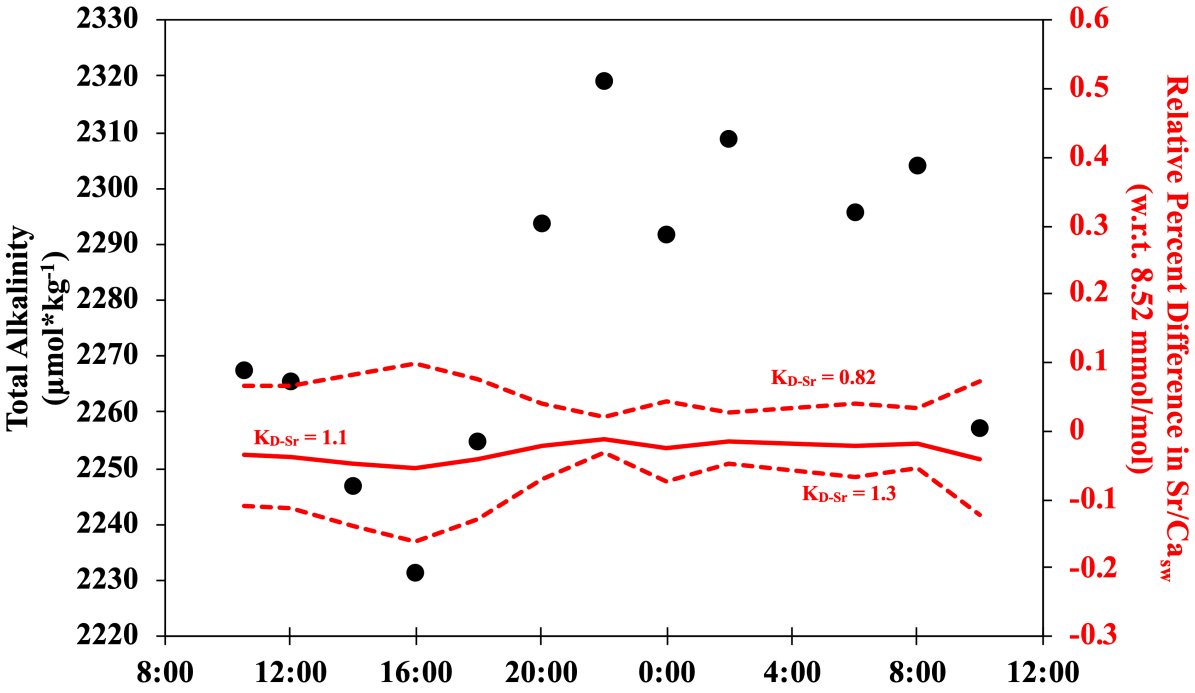

Figure 3.1. Modeled diel variability in relative Sr/Ca_{sw} differences assuming an aragonitic $K_{D\text{-}Sr}$ = 1.1 (solid red line) and nTA variability (black dots) from March 2017 diel cycle on Tetiaroa Atoll (see Chapter 2). Modeled data implies a maximum -0.05% (-0.004 mmol/mol) Sr/Ca_{sw} offset from seawater under an aragonitic calcification regime with this $K_{D\text{-}Sr}$ value. Dashed red lines indicate projected envelopes of Sr/Ca_{sw} variability based on the range of previously published values of $K_{D\text{-}Sr}$ for inorganic and biogenic aragonite. Sr/Ca_{sw} data is with reference to an assumed open ocean value of 8.52 mmol/mol.

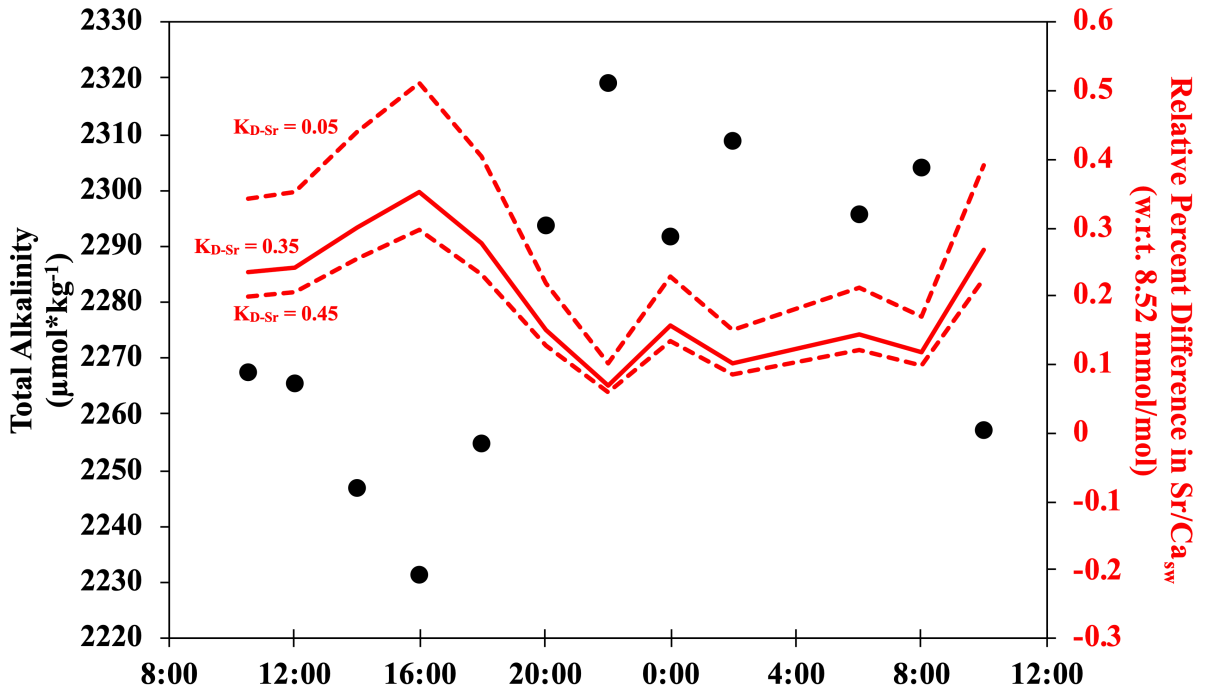

Figure 3.2. Modeled diel variability in relative Sr/Ca_{sw} differences assuming a calcitic $K_{D\text{-}Sr}$ = 0.35 (solid red line) and nTA variability (black dots) from March 2017 diel cycle on Tetiaroa Atoll (see Chapter 2). Modeled data implies a maximum +0.3% (0.026 mmol/mol) Sr/Ca_{sw} offset from seawater under calcification regime with this $K_{D\text{-}Sr}$ value. Dashed red lines indicate projected envelopes of Sr/Ca_{sw} variability based on previously published values of $K_{D\text{-}Sr}$ for inorganic and biogenic calcite. Sr/Ca_{sw} data is with reference to an assumed open ocean value of 8.52 mmol/mol.

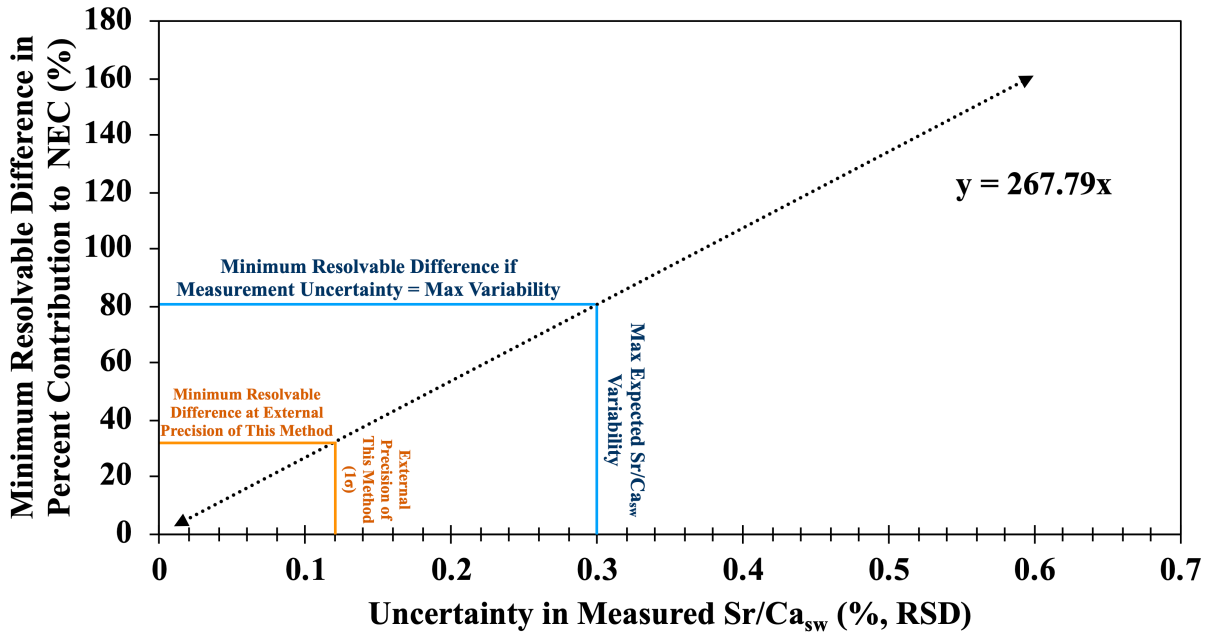

Figure 3.3. Error in the ability to resolve percent contributions to measured NEC values should scale linearly with the relative error on measured Sr/Ca_{sw}. Data is the result of a modeling exercise in which hourly variability in NEC from the March 2017 field campaign on Tetiaroa Atoll was coupled with assumed $K_{D\text{-}Sr} = 0.35$ (for calcite) and $K_{D\text{-}Sr} = 1.1$ (for aragonite). Using a single box model approach, the percent contributions of aragonite to each hourly calculation of NEC were increased from 0 – 100% (where calcite percent coverage = 1 – aragonite percent coverage), and the percent change in Sr/Ca_{sw} per percent increase aragonite contribution for each hour were tabulated. Results indicate that the analytical method developed and explored here should be capable of resolving differences in calcifier community composition of ± 27% given the calculated March 2017 diel rates of NEC (orange lines). Data shown here is reported with respect to the 2σ standard deviation of % percent change in Sr/Ca_{sw} per percent increase aragonite contribution at the hour with the highest offset from open ocean Sr/Ca_{sw}. It is therefore the "best case scenario" in error based on the data from this particular diel cycle and assumed $K_{D\text{-}Sr}$ behaviors.

It is also worth noting the Sr/Ca_{sw} may be uniquely suited to addressing these kinds of questions of community calcifier composition relative to other commonly measured elemental ratios (i.e. Mg/Ca). Given that open ocean Sr concentrations are nearly two orders of magnitude lower than Ca *and* that partition coefficients for Sr and Ca into different polymorphs of $CaCO_3$

are similarly distant, this elemental ratio (or others that follow similar characteristics) provides users with optimal opportunities for quantification in calcifying environments. Conversely (for example), Mg is 5x more concentrated than Ca in seawater with partition coefficients into calcite/aragonite from seawater similarly offset from one another (Zhong and Mucci, 1989; Dietzel et al., 2004; Gaetani and Cohen, 2006; Gagnon et al., 2007; Gagnon, 2010; Hetzinger et al., 2011). This results in virtually indistinguishable differences between community calcifier regimes when attempting to apply Equations 3.2 – 3.13 to Mg/Ca_{sw} variability in reef environments.

3.1.3 *Achieving Target Precision: Sources of Error during Sr/Ca_{sw} Analysis*

The extent to which an external reproducibility target of 0.05 – 0.3% 1σ RSD in Sr/Ca_{sw} measurements can be achieved by previously published methodologies is not immediately clear for two key reasons: (1) there are only a handful of studies in the literature that have reported Sr/Ca_{sw} values throughout the global ocean, and (2) each of these studies reports measurement error, uncertainty, and/or reproducibility using slightly different terminology (Table 3.2). For the goals of this project, it is important to distinguish the differences and nuances between sources of internal, external, and replicate precision on Sr/Ca_{sw} measurements. Doing so will elucidate key methodological details that could greatly assist in attempts to improve previous methods for future investigations of Sr/Ca_{sw} with the target precision. I define the internal precision of a particular analytical technique to be the tolerance of the method's ability to reproduce the same value of Sr/Ca_{sw} *during* the analysis of a single sample. As such, internal precision is governed primarily by sources of instrumental error during sample analyses and provides a fundamental minimum limit on the external precision of the overall method. External precision includes any uncertainties due to internal precision but also captures predicted long-term tolerance of the

method's ability to reproduce the same value of Sr/Ca_{sw} *across* analyses of different samples – inclusive of sources of error that manifest during the preparation of samples for analysis. Replicate precision captures components of internal and external sources of error and is a measure of a method's ability to return a constant value for Sr/Ca_{sw} for a single sample analyzed multiple times within or between analytical runs. Given the importance of contributions of internal error to external and replicate precision, I choose to focus primarily on identifying and minimizing sources of internal error during Sr/Ca_{sw} analyses.

Table 3.2. Summary table of previously reported methodologies for obtaining Sr/Ca_{sw} values and their associated reported measurement precisions in the context of the current study. Note – the discussion of internal and external precision in previously published studies is variable and not standardized. Here, I choose to describe the internal and external precision of the method, as well as the precision on measurements of replicate samples.

Method	**Isotope Dilution?**	**Reported Sr/Ca_{sw} Precision**	**Reference**
Thermal Ionization Mass Spectrometry (TIMS)	Yes; ^{42}Ca-^{44}Ca-^{84}Sr Mixed Spike	± 0.082% (2σ RSD on replicate filaments, n = 3)	de Villiers et al., 1994; de Villiers, 1999
TIMS	Yes; ^{42}Ca-^{44}Ca-^{84}Sr Mixed Spike	± 0.055% (2σ RSD on replicate filaments, n = 3)	Shen et al., 1996
Multicollector Inductively Coupled Plasma Mass Spectrometry (MC-ICP-MS)	Yes; ^{43}Ca-^{87}Sr Mixed Spike	± 0.09% (2σ RSD on replicate standard injections within a single run, n = 6)	Fernandez et al., 2010
Inductively Coupled Plasma Optical Emission Spectrometry (ICP-OES)	No	± 0.6% (2σ RSD, internal precision)	Steiner et al., 2014
ICP-OES	No	± 0.24 (2σ RSD; unreported details)	Steiner et al., 2018

ICP-OES	No	± 0.2 – 0.8% (2σ RSD on duplicate injections, n = 33)	Lebrato et al., 2020
TIMS	Yes; ^{43}Ca-^{48}Ca-^{84}Sr-^{87}Sr Double Mixed Spike	Long-Term Precision of the Method: ± 0.22% (2σ RSD on identically-processed internal standards, n = 8) Internal Precision of the Method: ± 0.003% (2σ RSE across all TIMS cycles of identically-processed internal standards) Replicate Filaments: ± 0.03%	This Study

As shown in Table 3.2, previous investigations of Sr/Ca_{sw} have relied on thermal ionization mass spectrometry (TIMS), multicollector inductively coupled plasma mass spectrometry (ICP-MS), or ICP optical emission spectrometry (ICP-OES) as the primary instrument of analysis, with TIMS methods being among the most precise techniques (de Villiers et al., 1994; Shen et al., 1996; de Villiers, 1999). Potential sources of internal error on Sr/Ca_{sw} measurements using any of these instruments can arise from the considerable spectral (isobaric mass interferences) and non-spectral influences of the high salt content (matrix effects) during analyses (Søndergaard et al., 2015). This is particularly the case with ICP-MS and ICP-OES, where spectral, chemical, and physical interferences caused by the high salt matrix of seawater combines with sample introduction effects, space-charge effects, and plasma variability within

the instrument to cause significant signal drift, signal suppression, and differences in ionization efficiencies between elements when attempting to measure concentrations of a particular analyte outright (Wilschefski and Baxter, 2019). The detrimental impacts of the matrix can often be isolated and removed through purification of the sample with chromatographic columns, where analytes of interest are pre-concentrated before being subjected to spectrometric analyses. However, this step does little else to combat the remaining sources of internal variability with ICP-MS and ICP-OES analyses of seawater and can itself be a potential source of external error if the pre-concentration techniques are not quantitative in their recovery of analytes of interest.

Fortunately, for ICP-MS and TIMS methods of concentration analyses, matrix removal can be coupled with a technique known as isotope dilution (ID) to combat issues associated with ionization efficiencies for elements that are not monoisotopic (Fassett and Paulsen, 1989; Heumann, 1992). In ID experiments, a sample is enriched or "spiked" with an isotope of the analyte of interest. The isotope ratio of the resultant mixture (R_m) is what is ultimately measured by the mass spectrometer, and the isotope mixing equation for R_m (Equation 3.14) can be rearranged and solved for the concentration of the analyte in the original sample at the relative precision and accuracy of isotope ratio measurements (Equation 3.15; Fassett and Paulsen, 1989; Heumann, 1992):

$$R_m = \frac{total\ moles\ of\ isotope\ A}{total\ moles\ of\ isotope\ B} = \frac{A_x C_x M_x + A_s C_s M_s}{B_x C_x M_x + B_s C_s M_s} \qquad (3.14)$$

$$C_x = \left(\frac{C_s M_s}{M_x}\right)\left(\frac{A_s - R_m B_s}{R_m B_x - A_x}\right) \qquad (3.15)$$

where "A" or "B" is the relative abundance (mole fraction) of isotope A or B in the analyte of interest, "C" is the concentration of the element of interest (mol*L^{-1}), "M" is the measured mass (kg), and "X" or "S" is the sample or spike index, respectively. Note that the internal precision of isotope dilution concentration determinations arises from uncertainties that propagate through R_m

(inclusive of errors due to counting statistics, spike weighing, and stability of isotope ratio measurements). In particular, under- or over-spiking a sample with enriched isotopes risks biasing the measurement of R_m toward that of the pure sample or pure spike, respectively. The amount that instrumental uncertainty scales with the isotope dilution approach can be represented by an Error Amplification Factor (EAF, Equation 3.16):

$$EAF = \frac{\sigma_{Cx}}{\sigma_{Rm}} = \left|\frac{R_m*(R_x - R_s)}{(R_m - R_x)*(R_s - R_m)}\right| \quad (3.16)$$

where "R_x" is equal to the true isotope ratio of the sample of interest and "R_s" is the true isotope ratio of the spike solution. This error function reaches a minimum when R_m is roughly equivalent to the geometric mean of R_x and R_s (Equation 3.17):

$$\frac{\partial EAF}{\partial R_m} = 0 \; when \; R_m = \sqrt{R_x * R_s} \quad (3.17)$$

Equations 3.14 – 3.17 therefore allow for the mathematical optimization of a target spike composition that minimizes uncertainties associated with the ID method. Additionally, previous ID-TIMS determinations of Sr/Ca_{sw} benefited from the use of a *mixed* isotope spike, where samples were enriched in isotopes of both Ca *and* Sr (Table 3.2; de Villiers et al., 1994; Shen et al., 1996; de Villiers, 1999). This method of ID normalizes errors associated with spike weighing during the calculation of the Sr/Ca_{sw} of a particular sample, since the Sr/Ca ratio of a particular mixed spike blend is a constant.

Despite the potential improvements in precision offered by ID methods, all ICP-MS and TIMS instruments can display significant mass bias during the analysis of isotope ratios within and between samples as a function of isotope fractionation within the instrument (Russell, 1971; Albarède and Beard, 2004; Albarède et al., 2015). This process, known as instrumental mass fractionation or IMF, is believed to be more stable during TIMS analyses compared to ICP methods of mass spectrometry. However, because this fractionation can vary significantly within

and between the analysis of a single sample, it is also more difficult to characterize and control than ICP methods which can benefit from standard-sample bracketing techniques to normalize the impacts of IMF (Carlson, 2014; Wilschefski and Baxter, 2019). As previously mentioned, internal precision and accuracy of the ID method propagates primarily through the ability to measure R_m. Since IMF directly influences the stability of isotope ratio measurements during and between sample analyses, it can be a significant source of error during ID experiments.

An isotope dilution method known as double spike (DS) can be used to address and correct for the influences of IMF in TIMS if the analyte of interest has four or more naturally occurring isotopes. This technique assumes that mass bias within the instrument follows and exponential rate law and that the mass fractionation factors (β) for all isotopes of a single element within a particular sample are equal (Equation 3.18; Dodson, 1963; Albarède and Beard, 2004; Rudge et al., 2009):

$$R_{AB}^{Measured} = R_{AB}^{True} * \left(\frac{MW_A}{MW_B}\right)^{-\beta} \qquad (3.18)$$

where "R_{AB}" is the ratio of isotopes A and B within a sample, and "MW" is the molecular weights of those isotopes. Note that a similar exponential law is used to define the isotopic composition of any given sample with reference to fractionation (α) from a standard of known composition (Equation 3.19):

$$R_{AB}^{Sample} = R_{AB}^{Standard} * \left(\frac{MW_A}{MW_B}\right)^{\alpha} \qquad (3.19)$$

For systems with radiogenic, naturally occurring isotopes (like Sr), Equation 3.19 is typically used to correct for IMF through normalization to a particular isotope ratio value. A graphic illustrating the steps involved in double spike isotope dilution experiments is provided in Figure 3.4. To create the double spike mixture, two single spikes, each enriched in a particular isotope of the analyte of interest, are combined in a particular mixing ratio. The isotope composition of

resultant solution is then calibrated before being added to a sample to form a sample+spike blend for analysis (see below). The fractional contribution of a reference isotope from the spike to the overall mixture (mixing ratio, "X_{DS}") is treated as an unknown along with β and α (Equation 3.20):

$$X_{DS} = \frac{moles\ reference\ isotope\ contributed\ from\ spike}{total\ moles\ reference\ isotope\ in\ spike{+}sample\ mixture} \quad (3.20)$$

Given the isotopic composition of the spike solution, the measured composition of the sample+spike blend, and the composition of a standard, the "true" isotopic compositions of the sample+spike blend and the original sample can be determined as solutions to the system of Equations 3.18 – 3.20, which govern the behavior of X_{DS}, β, and α. Three independently measured isotope ratios are needed as initial inputs to solve these equations, hence why DS experiments only work for systems with four or more naturally occurring isotopes. In addition to sources of internal error during normal ID experiments, factors influencing the precision and accuracy of measurements using the double spike technique arise from the optimization of the sample+spike blend, uncertainties associated with the numerical inversion, and, in the case of elemental systems with more than four naturally occurring isotopes, the choice of isotopes used in the inversion. Fortunately, an error minimization toolbox for double spike analysis exists for use on a number of isotope systems, and much work has previously been done to optimize the spike blend for the high precision determinations of α, β, or a particular isotope ratio of interest (Krabbenhöft et al., 2009; Rudge et al., 2009; Raddatz et al., 2013). However, the extent to which optimizing a double spike solution results in increased precision on seawater concentrations of Sr and Ca and Sr/Ca_{sw} remains to be seen. Previously published ID-TIMS methods of measuring Sr/Ca_{sw}, as observed in Table 3.2, report the use of a mixed isotope dilution spike that is enriched in *two* isotopes for Ca but not Sr. Thus, the potential improvements

in internal and (by extension) external precision on Sr/Ca_{sw} from the inclusion of both Sr and Ca in a double mixed spike ID-TIMS method is worth further investigation. Combining the benefits of TIMS, isotope dilution (ID), double spike (DS), and mixed spike (MS) techniques could potentially provide the best path toward achieving the 0.05 – 0.3% 1σ RSD or better precision in Sr/Ca_{sw} necessary to quantify community calcifier dynamics within coral reef environments.

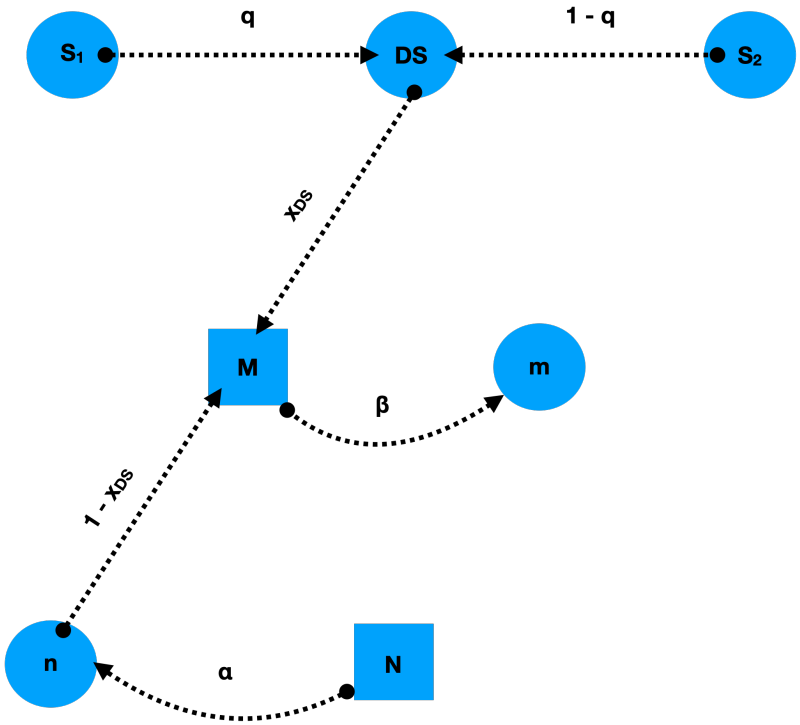

Figure 3.4. A diagram illustrating the steps involved in a typical double spike isotope dilution experiment (adapted from Rudge et al., 2009). First, two separate isotope spikes, S_1 and S_2, are combined in mixing ratios q and 1-q to make the double spike solution, DS. n is the isotopic composition of the sample of interest. The composition of this sample is some measure of fractionation, α, away from a natural abundance standard, N (Equation 3.19). Combining this sample with the double spike solution produces mixture, M, whose isotopic composition is reflected by mixing ratio X_{DS} (X_{DS} = mole contribution of reference isotope from the spike in the spike+sample mixture, Equation 3.20). Measurements of mixture M through TIMS produces isotope ratios, m, that have been subjected to instrumental mass fractionation (IMF) by some measure β (Equation 3.18). However, the measured ratios of m and the composition of DS are used to invert the values of α, β, and X_{DS}. Initial guesses of these values are made and used to

iteratively generate synthetic values of mixture m. The optimal values of α, β, and X_{DS} are those that minimize the sum of the square of the residuals between these synthetic values of m and the true values of m. The inverted α values are then used in Equation 3.19 to correct the mixture ratios back to the true isotope composition of n.

In this chapter, I optimize a double mixed spike isotope dilution thermal ionization mass spectrometry (DMS-ID-TIMS) approach to develop a method for measuring variability in Sr/Ca_{sw} with high levels of precision (~0.003% internal RSE, 1σ; ~0.1% external RSD, 1σ; 0.03% on replicate filaments). With the outcomes of this optimization, I apply this method to the analysis of seawater samples collected and processed from two coral reef environments, Tetiaroa Atoll, French Polynesia and One Tree Island, Australia, to report observable trends in the diel variability of stable Ca ($\delta^{44/40}Ca$) and Sr ($\delta^{88/86}Sr$) isotopes, dissolved Ca and Sr concentrations, and Sr/Ca_{sw}. I apply the single-box, Rayleigh modeling framework detailed in *Section 3.1.2.* to decompose Sr/Ca_{sw} into measurements of $K_{D\text{-}Net,\ Sr}$ for both ecosystems and further propose the application of this method as a tool that complements measurements of NEC in calcifying environments. Lastly, I place the long-term precision of this method in the context of potential applications to outstanding paleoceanographic, paleoclimatological, and modern ecological research questions.

3.2 METHODS

In order to apply a DMS-ID-TIMS method to measurements of Sr/Ca_{sw}, an enriched mixed isotope spike solution must be prepared and calibrated such that its own isotopic composition is known. It is then added to seawater samples, Sr and Ca are chromatographically purified using ion-specific resins, and these isolated fractions are analyzed separately for their isotopic composition via TIMS. Here, I describe each of these methodological steps in detail to

show how I account for and attempt to minimize sources of error in the development and application of this method of Sr/Ca_{sw} analysis.

3.2.1 *Spike Design*

As mentioned in *Section 3.1.3*, numerical toolboxes exist for designing double spike experiments that optimize the composition of single spikes in the double spike mixture (the molar ratio of q and 1-q in Figure 3.4) and the molar mixing ratio of the double spike solution in the sample+spike mixture (X_{DS} in Figure 3.4) to minimize internal error in α, β, or a particular isotope ratio of interest. The framework of these toolboxes needs to be modified to optimize the spike composition of a *mixed* double spike (enriched in isotopes of both Sr and Ca) for the inversion of the molar Sr/Ca ratio of any sample at high precision. Using a numerical modeling approach based on Rudge et al. (2009) and the governing double spike equations detailed above (Equations 3.18 – 3.20), I designed a MATLAB script that iteratively optimizes the best choices of single isotope spikes and values of q and X_{DS} for both Sr and Ca that minimize internal error in inverted molar Sr/Ca ratios (see Appendix B). Briefly, this script assumes a particular double mixed spike composition, makes synthetic mixtures between this spike and a typical sample of fixed Ca and Sr molar and isotopic composition, and uses the double spike algorithm from Figure 3.4 to invert the values of α, β, and X_{DS} for the original sample. This analysis includes a Monte Carlo error propagation exercise featuring 1000 iterations of simulated internal errors on isotope ratio measurements that result from Johnson Noise and counting statistics within the mass spectrometer. Note that this modeled assessment of precision is based entirely on *theoretical* limits of internal error; experimental internal and external error may include the numerous factors discussed in *Section 3.1.3* and detailed below.

In optimizing the spike composition and double spike approach for high precision Sr/Ca measurements, more focus is placed on the internal measurement precision of X_{DS}. This is because the ratio of moles of any particular reference isotope (for both Sr and Ca) in the sample of interest versus moles of reference isotope in the spike can be expressed as F_{ref} (Equation 3.21):

$$\frac{1-X_{DS}}{X_{DS}} = F_{Ref} \quad (3.21)$$

Values for F_{Ref} can easily be translated into the ratio of total moles of an analyte in the sample of interest versus total moles of analyte in the spike given the calculated abundances of the reference isotopes in both solutions (Equation 3.22):

$$F_{Tot} = F_{Ref} * \left(\frac{A_S}{A_x}\right) \quad (3.22)$$

Thus, F_{Tot} for Sr ($F_{Tot, Sr}$) and Ca ($F_{Tot, Ca}$) and the molar Sr/Ca ratio of the mixed double spike solution can be used calculate the total molar Sr/Ca ratio of any particular sample without needing to meticulously measure keep track of weights used during the experiment (Equation 3.23):

$$\left(\frac{Sr}{Ca}\right)_x = \left(\frac{F_{Tot,Sr}}{F_{Tot,Ca}}\right) * \left(\frac{Sr}{Ca}\right)_S \quad (3.23)$$

Note, however, that if notes are kept of volumes and weights used during the double mixed spike solution, then $F_{Ref, Sr}$ and $F_{Ref, Ca}$ can be used to solve for the individual concentrations of Sr and Ca within a sample (Equation 3.24 shown for Ca with Sr analogue):

$$[Ca] = \frac{F_{Ref} * [Ca]_S * M_S * A_S}{A_X M_X} \quad (3.24)$$

This series of equations implies that relative error in F_{Ref} (and by extension F_{Tot}) simply propagates into Sr/Ca ratio error through the following equation (Equation 3.25):

$$\sigma_{Sr/Ca} = \sqrt{\left(\frac{\sigma_{FTot,Sr}}{F_{Tot,Sr}}\right)^2 + \left(\frac{\sigma_{FTot,Ca}}{F_{Tot,Ca}}\right)^2} \quad (3.25)$$

Precision in F_{Ref} is therefore essential for interpreting data that result from the application of the double mixed spike method developed here, and I chose to optimize the double spike composition and spike-to-sample ratio such that precision in F_{Ref} is optimized.

The results of my script indicate that, when using ^{88}Sr and ^{44}Ca as reference isotopes, an $^{84\text{-}87}Sr + {}^{43\text{-}48}Ca$ double mixed spike typically maintains internal precisions on F_{Ref} better than 100 ppm (0.01%) when the target molar contribution of the ^{43}Ca (^{48}Ca) spike to the total Ca in this solution was 0.58 (0.42) and the target molar contribution of ^{84}Sr (^{87}Sr) spike to the total dissolved Sr was 0.27 (0.73). Additionally, this script implies that the ideal values of $X_{DS,\,Ca} = 0.19$ and $X_{DS,\,Sr} = 0.22$. This information as well as the ideal theoretically-optimized isotopic and molar composition of the double mixed spike solution are listed in Table 3.3 and Table 3.4.

Table 3.3. Summary of Ca and Sr isotope spikes used in this study and target mixing ratios for double mixed spike isotope dilution thermal ionization mass spectrometry (DMS-ID-TIMS). Spikes were procured from Oak Ridge National Laboratory (ORNL, Oak Ridge, TN, USA).

ORNL Isotope Spike	Batch #	Target Mixing Ratio in Double Spike	Target X_{DS}
$^{43}CaCO_3$	169191	0.58	0.19
$^{48}CaCO_3$	219801	0.42	
$^{84}SrCO_3$	163191	0.27	0.22
$^{87}SrCO_3$	136990	0.73	

Table 3.4. Target Ca (w.r.t. ^{44}Ca) and Sr (w.r.t. ^{88}Sr) isotope and molar ratios in the double mixed spike solution based on the results of my modified numerical optimization of the double spike inversion toolbox.

Isotope Ratio	Target Composition in Double Mixed Spike Solution
$^{40}Ca/^{44}Ca$	2.2790
$^{42}Ca/^{44}Ca$	0.15598
$^{43}Ca/^{44}Ca$	16.4192

$^{48}Ca/^{44}Ca$	13.8710
$^{84}Sr/^{88}Sr$	2.4285
$^{86}Sr/^{88}Sr$	0.1750
$^{87}Sr/^{88}Sr$	7.3296
Molar Sr/Ca Ratio	0.13

As alluded to in *Section 3.1.3*, amplification of internal error during isotope dilution experiments scales with uncertainty in the sample+spike blend. At the optimal choice of single spikes in the double mixed spike solution, X_{DS} values span a range of potential mixing choices for Sr and Ca for which relative internal error on $F_{Ref, Sr}$ and $F_{Ref, Ca}$ is less than 0.01% (1σ RSD). This provides some range of allowable uncertainty in sample spiking without major sacrifices to predicted precision. For example, at the "ideal" ^{84}Sr proportion (0.27), better than 0.001% relative error (1σ RSD) in $F_{Ref, Sr}$ is predicted for the 0.08 – 0.74 range of X_{DS} values (Figure 3.5). In the Ca system, at the "ideal" ^{43}Ca proportion (0.58), better than 0.001% relative error (1σ RSD) in $F_{Ref, Ca}$ is predicted for the 0.06 – 0.50 range of X_{DS} values (Figure 3.6). As mentioned, the design of the DMS-ID-TIMS method for inverting molar Sr/Ca ratios at high precision normalizes errors associated with weighing during ID experiments; as such, in the context of EAF, reasonable uncertainty in X_{DS} should not error propagation much.

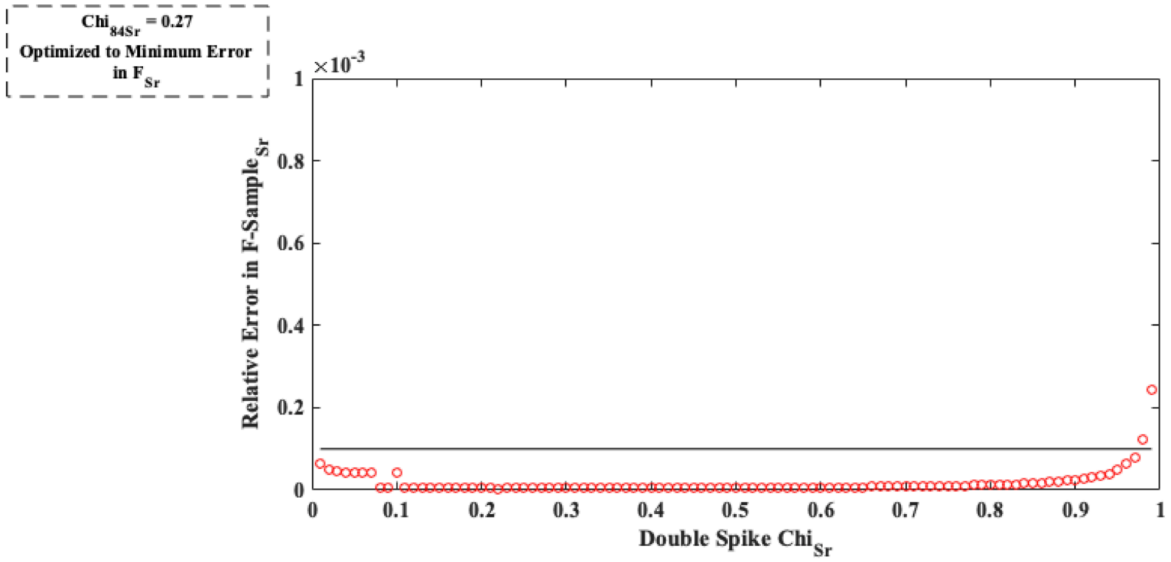

Figure 3.5. The results of an error propagation and spike optimization exercise using an $^{84+87}$Sr double spike indicate internal precision on $F_{Ref.\ Sr}$ is below 100 ppm RSD (0.01%, 1σ RSD) across a wide range of potential X_{DS} values.

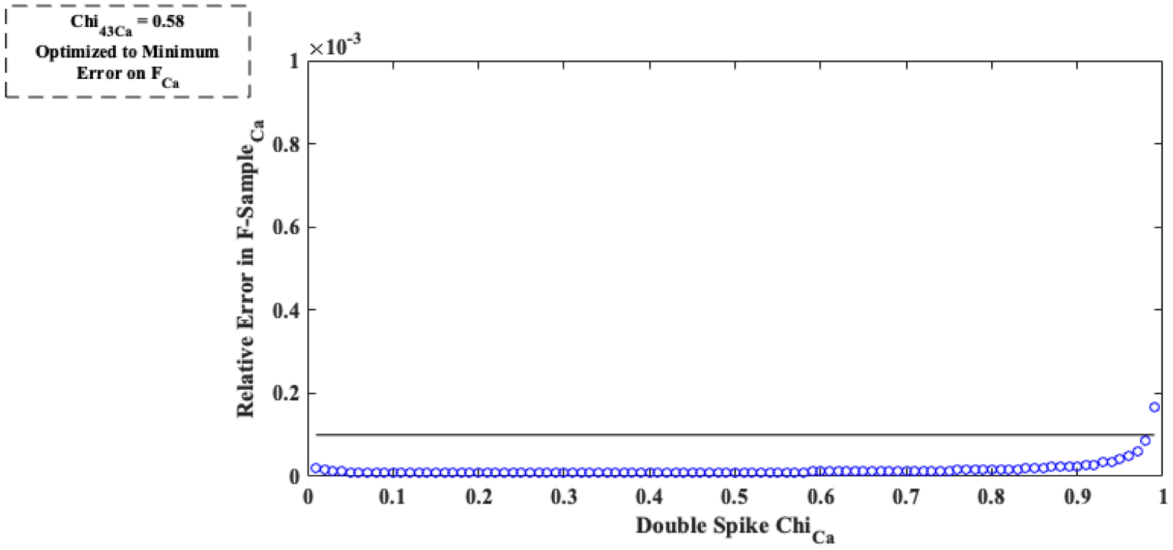

Figure 3.6. The results of an error propagation and spike optimization exercise using an $^{43+48}$Ca double spike indicate internal precision on $F_{Ref.\ Ca}$ is below 100 ppm RSD (0.01%, 1σ RSD) across a wide range of potential X_{DS} values.

Enriched aliquots of $^{43}CaCO_3$ (Batch #169191), $^{48}CaCO_3$ (Batch #219801), $^{84}SrCO_3$ (Batch #163191), and $^{87}SrCO_3$ (Batch #136990) were obtained from Oak Ridge National

Laboratory (ORNL, Oak Ridge, TN USA), gravimetrically weighed and dissolved in 2M Optima HNO_3 before being diluted and mixed at the appropriate, numerically determined single spike mixing ratios to form the double mixed spike solution. At the composition and target mixing ratios tabulated in Table 3.3 and Table 3.4, 120 mg of seawater, representative of ~50 µg Ca and ~1 µg Sr, should be spiked with 78 mg of the double mixed spike solution to practically obtain the precision limits discussed above.

3.2.2 *Spike Calibration*

Once gravimetrically mixed, empirically calibrating the composition of the double mixed spike solution is a crucially important step since the *true* isotopic and molar composition are needed as inputs to solve the spike inversion for the Sr/Ca ratio of any given sample. Previous studies on the double spike TIMS method have alluded to difficulties involved in spike calibration being a fundamental control on both the precision and accuracy of isotope ratio determinations using this technique (Heuser et al., 2002; Rudge et al., 2009; John, 2012; Elhamel, 2014; Coath et al., 2017; Mondal and Chakrabarti, 2018). Two commonly used means of spike calibration are explored (with varying degrees of success): (1) measuring multiple mixtures of a *single* natural abundance standard of known isotopic *and* concentration information at multiple X_{DS} and (2) defining the intersection of mixing lines between multiple standards of known isotopic composition spiked at multiple X_{DS} (Dodson, 1963; Rudge et al., 2009). The nature of both of these numerical spike optimization algorithms involves solving a multi-dimensional, unconstrained system of equations which could result in finding *local* rather than *global* optimized spike compositions. Additionally, the graphical intersection method works best when choosing standards of known composition that plot as distant from each other as possible from one another in isotope ratio space – that is, the value of α between the two standards is

relatively large, resulting in drastically different isotopic compositions of the spike+standard mixtures. Furthermore, precision of the graphical method is improved if fractionation by α and β as well as mixing influences of X_{DS} move data points along surfaces that are as orthogonal to one another as possible. It is also worth noting that the graphical approach bundles the impacts of β with accuracy errors associated with the graphical inversion of spike composition. This is further complicated by the likelihood that each data point that defines the mixing lines for each TIMS cycle would have different values for β, despite all theoretically having the same values for α.

To my knowledge, there are not many Sr or Ca interlaboratory standards or certified reference materials with a known isotopic *and* concentration composition. Therefore, for the use cases of the double spike method explored here, calibrating the spike through the use of a single standard does not seem feasible. However, separate standards of known/calibrated Sr and Ca isotopic composition and the overall molar Sr/Ca ratio do exist but are not significantly fractionated from each other in ways that lead to the viability of the graphical method of spike calibration. This raises the question of how to best empirically calibrate the composition of the double mixed spike solution developed here.

I chose to calibrate the isotopic and molar composition of the double mixed spike solution using a modified multi-standard numerical approach and the following interlaboratory standards and certified reference materials: IAPSO seawater, AIST JCp-1 (Coral $CaCO_3$), NIST SRM 915a ($CaCO_3$), and NIST SRM 987 ($SrCO_3$). IAPSO and NIST standard samples were used as isotope reference materials, while JCp-1 was included because of its interlaboratory calibrated molar Sr/Ca ratio (8.838 $mmol*mol^{-1}$; Okai et al., 2002; Hathorne et al., 2013). Given the importance of the Sr/Ca ratio of the double mixed spike solution in the inversion of the

original Sr/Ca of a spiked sample (Equation 3.23), the inclusion of JCp-1 served as an additional molar (versus isotopic) accuracy check on the composition of the spike solution.

For the IAPSO and NIST standards, aliquots of each, representative of 40 µg Ca (IAPSO and SRM915a) and 1 µg Sr (IAPSO and SRM987), were spiked at values of X_{DS} ranging from 0.1 – 0.6. Spiked IAPSO and SRM987 samples were further chemically purified for separate Sr and Ca fractions before being subjected to TIMS analysis (see *Sections 3.2.6* and *3.2.7*) and subjected to the double mixed spike inversion script to calculate their original stable isotope composition (corrected for the influences of IMF). For Ca, initial guesses of spike composition isotope ratios were iteratively tuned until the $\delta^{44/40}$Ca value of each inverted SRM 915a and IAPSO X_{DS} experiment fell to within ~0.1‰ of the commonly accepted value of -0.97‰ (SRM 915a) and 1.1‰ (IAPSO) with respect to Bulk Silicate Earth (BSE, $^{44}Ca/^{44}Ca = 47.153 \pm 0.003$, Russell et al., 1978; DePaolo, 2004; Nielsen et al., 2012). Similarly, for Sr, initial guesses of spike composition isotope ratios were iteratively tuned until the $\delta^{88/86}$Sr value of each inverted SRM 987 ($^{88}Sr/^{86}Sr = 8.37861 \pm 0.00325$) and IAPSO X_{DS} experiment fell to within ~0.1‰ of the commonly accepted value of 0‰ (SRM 987, by definition) and 0.386‰ (IAPSO, Krabbenhöft et al., 2009).

Furthermore, as an independent check on the stable Ca and Sr isotopic composition of the double mixed spike solution and to provide an idea of initial starting points from which to begin the tuning process, an aliquot of the raw double spike solution was subjected to analysis using an ELEMENT 2 high resolution double-focusing magnetic sector ICP-MS at the University of Washington. For stable Ca analyses, ^{42}Ca, ^{43}Ca, ^{44}Ca, and ^{48}Ca were collected in medium resolution (MR) counting mode using the electric scan (EScan). Because ^{40}Ar is used as a carrier gas with the ELEMENT 2, measurements of ^{40}Ca are not possible in this method of analysis.

Doubly-charged ^{87}Sr and ^{47}Ti were also monitored for peak interferences on Ca isotopes. Aliquots of unspiked SRM915a and JCp-1 were used in a standard-sample bracketing scheme to correct the measured isotope ratios for the influences of IMF. This correction followed a time-weighted linear model to interpolate the impacts of IMF on measured spike and JCp-1 values between bracketing SRM915a measurements (Equation 3.26, Gagnon, 2010):

$$f_{t=s} = \left(\frac{f_{t=1}}{t_s - t_1} + \frac{f_{t=2}}{t_2 - t_s}\right) \Big/ \left(\frac{1}{t_s - t_1} + \frac{1}{t_2 - t_s}\right) \qquad (3.26)$$

where f = (True Ratio) / (Measured Ratio). For stable Sr analyses, ^{84}Sr, ^{86}Sr, ^{87}Sr, and ^{88}Sr were also collected in MR counting mode using the EScan, with ^{83}Kr and ^{85}Rb being monitored for peak interferences on Sr isotopes. Here, SRM987 and JCp-1 were used in the IMF-correcting standard-sample bracketing scheme of Equation 3.26.

For spike and sample molar ratio accuracy determination, an aliquot of JCp-1, representative of 40 µg Ca and 1 µg Sr, was spiked at the *ideal* target molar X_{DS} (~0.2) and subjected to chemical purification of Sr and Ca fractions before being subjected to TIMS analysis (see *Sections 3.2.6* and *3.2.7*). To calibrate the value of Sr/Ca_s, I tuned the isotopic composition of the spike using the methods and standards detailed above and then further tuned the value of Sr/Ca_s used in the double spike inversion algorithm until the sum of the square of the residuals between the true value of JCp-1's Sr/Ca and the calculated value based on the iterative composition of the spike was minimized. Given an initial JCp-1 aliquot, the value of Sr/Ca_s can be accurately determined (Equation 3.27):

$$\left(\frac{Sr}{Ca}\right)_s = \frac{\left(\frac{Sr}{Ca}\right)_{JCp-1} * M_{JCp-1}}{\left(\frac{F_{Tot,Sr}}{F_{Tot,Ca}}\right)_{JCp-1} * M_s} \qquad (3.27)$$

Note – the standards presented here each have different radiogenic Sr isotope signatures ($^{87}Sr/^{86}Sr$) from the decay of ^{87}Rb. This issue is explicitly handled in two ways in this study. First, the $^{87}Sr/^{88}Sr$ and $^{86}Sr/^{88}Sr$ ratios of each standard were independently measured using the ID-DMS-TIMS method, allowing for the calculation of the true, unnormalized $^{87}Sr/^{86}Sr$ ratios of IAPSO and SRM987. Furthermore, this method is optimized for the typical sample being a seawater matrix. Given the 1,000-year circulation time of the global ocean and the average millennial scale residence times of Sr in the open ocean, I assume that the $^{87}Sr/^{86}Sr$ ratio of the seawater samples analyzed here is roughly equal to the measured IAPSO value of 0.71048. A summary of the assumed isotope ratios of the standards used in spike calibration can be found in Table 3.5.

Table 3.5. Summary of standards and reference materials and their assumed absolute Ca and Sr isotope ratios. SRM 915a and IAPSO Ca isotope ratios were calculated using Equation 3.7, BSE ratios, data from Nielsen et al., (2012). Similarly, the Ca isotope ratios for JCp-1 were calculated using Equation 3.7, SRM 915a ratios, and data from Mondal and Chakrabarti (2018). IAPSO and JCp-1 Sr ratios were calculated using Equation 3.7, SRM 987 ratios, and data from Krabbenhöft et al., (2009). *Note – $^{87}Sr/^{86}Sr$ is prone to radiogenic influences from the decay of ^{87}Rb.

Reference Material	**$^{40}Ca/^{44}Ca$**	**$^{42}Ca/^{44}Ca$**	**$^{43}Ca/^{44}Ca$**	**$^{48}Ca/^{44}Ca$**	**$^{84}Sr/^{86}Sr$**	**$^{87}Sr/^{86}Sr$***	**$^{88}Sr/^{86}Sr$**
Bulk Silicate Earth (BSE)	47.153 ± 0.003	0.31221 ± 0.00002	0.06486 ± 0.00001	0.08871 ± 0.00002	-	-	-
SRM 915a	47.199	0.31236	0.06488	0.08863	-	-	-
SRM 987	-	-	-	-	0.05655 ± 0.00014	0.71034 ± 0.00026	8.37861 ± 0.00325
IAPSO Seawater	47.147	0.31219	0.06486	0.08872	0.05653	0.71048	8.38184

AIST JCp -1	47.159	0.31222	0.06486	0.08870	0.05654	0.71041	8.38026

3.2.3 *Seawater Sample Collection*

The Sr/Ca ratios of additional samples of seawater were analyzed here as part of a broader investigation of the application of the ID-DMS-TIMS method to quantify offsets in net community values of $K_{D\text{-}Sr}$ within and between reef environments. These samples, seven from the reef flat of Tetiaroa Atoll in French Polynesia and two from the reef flat of One Tree Island in Australia, were collected during field campaigns in March 2017 and December 2017, respectively. Furthermore, the Tetiaroa samples correspond to complementary and concurrent carbonate chemistry samples collected between 12:00 and 12:00 local time as part of the diel exploration of productivity quotients on reefs (see Chapter 2).

On Tetiaroa, the sampling site (17.0ºS, 149.5ºW) was located ~0.5 km east of the reef crest in an area where benthic coverage, estimated from satellite measurements, is ~21% scleractinian aragonitic corals and ~79% carbonate sands. Note that benthic coverage does not necessarily correspond to the contribution of corals or other organisms to calcification. Samples for Sr/Ca_{sw} were collected by hand into a 1 L, acid-leached LDPE bottle at a frequency of 2 hours for 24 – 36 hours. This was done to capture diel patterns in the metal ratio associated with temporal variability in alkalinity due to calcification/dissolution fluxes. For each sampling, the 1 L bottle was rinsed with seawater three times before being submerged and capped underwater to avoid contributions of bubbles. All samples were processed in the field while taking the following steps to maintain cleanliness and avoid sample contamination: a vacuum filtration apparatus and 0.2 µm pore size plastic Whatman filter (pre-leached in 2% HNO_3) was rinsed with 60 mL of high-purity MilliQ water. The 1 L sample bottle was then gradually filtrated for

particulates using the vacuum apparatus into duplicate 30 or 60 mL acid-leached LDPE bottles. Each LDPE bottle was rinsed 2-3x with the filtered sample before final collection took place. All samples were then acidified to pH 2 using Optima/Aristar Ultra 12M HCl to maintain elemental solubility. Here, I focus on presenting the results from the analysis of a subset of samples collected at 12:00 and 12:00 local time, which should be representative of the diel variability in salinity-normalized (S = 35.4) alkalinity values highlighted in Figure 2.4 (Bolden et al., 2019). I also collected, filtered, and analyzed an offshore, open ocean seawater sample from between Tetiaroa Atoll and Tahiti (17.3ºS, 149.57ºW) as a constraint on the Sr/Ca_{sw} of source waters supplying the study location using the aforementioned collection/processing methods.

On One Tree Island, primary sampling of the terraced reef flat took place 0.1 km north of the reef crest (23.5ºS, 152.1ºE) using a 0.01 cubic meter Perspex dome connected to a pump chamber fitted with pH, temperature, and O_2 probes. The dome was placed over a benthic community of ≥ 90% *Porolithon onkodes*, a high-Mg calcite precipitating species of coralline algae that is dominant in many tropical reef environments, and discretely sampled for metal content, pH and TA at an hourly frequency for ± 3 hours on either side of the afternoon and early morning low tide. Sampling under this regime continued for two weeks in order to construct a diel cycle of metal content, pH, TA, and O_2 for the sampling location. Similar to the Tetiaroa samples, we focus on presenting the results from the analysis of two samples collected at 05:00 and 18:10 local time, which correspond to the times of highest (2366 $\mu mol*kg^{-1}$) and lowest (~2226 $\mu mol*kg^{-1}$) salinity normalized (S = 35) measured dissolved alkalinity concentrations observed over a diel cycle (Silverman et al., 2012 and unpublished data). All samples for Sr/Ca_{sw} analyses were collected using 60 ml virgin plastic Luer-Lock syringes (BD Syringe) and filtered

through 0.22 µm BioFil filters into duplicate 5 mL virgin plastic pipette tubes. Samples were then acidified to pH 2 using Optima/Aristar Ultra 12M HCl.

3.2.4 *Reef Seawater Consistency Standard*

Although many of the studies listed in Table 3.2 focus on replicate/duplicate methodological precision as the primary error assessment, an arguably more useful and nuanced assessment of error tests the ability of a method to reproduce a value for Sr/Ca_{sw} for identically-prepared but separate aliquots of a standard with a similar composition as a typical sample. When precision is assessed in this way, it can be used to clearly distinguish the impacts of internal (instrumental) and external (sample preparation) sources of error given that the actual composition of the standard is invariant across all aliquots. In addition to the standards for spike calibration and seawater offset samples, I also designed and calibrated the stable Ca and Sr isotope composition and Sr/Ca_{sw} ratio of a Reef Seawater Consistency Standard (RSCS) as a check on the external reproducibility of measured Sr/Ca_{sw} values derived from the method presented here. This solution is a mixture of seawater samples collected from the reef flat of Tetiaroa Atoll in January 2016 (using similar procedures as other samples from this region mentioned above) and carries an implied (calculated from components of the mixture), salinity-normalized alkalinity value of 2280 $\mu mol*kg^{-1}$ (S = 35.4). This standard is not meant to represent reef conditions but instead acts as a large volume of homogenous reef seawater that can be used to evaluate the reproducibility of our Sr/Ca method.

3.2.5 *Typical Sample Spiking*

To prepare the reef seawater, open ocean seawater, and RSCS samples for elemental and isotopic analyses, a 120 mg aliquot of each sample, representative of ~50 µg Ca and ~1 µg Sr,

was spiked with 78 mg of the double mixed spike solution, evaporated to dryness, and reconstituted in 2M Aristar Optima HNO_3. Note that the amount of spike added corresponds with the target, error-minimizing X_{DS}, which is the contribution of spike-derived ^{44}Ca and ^{88}Sr in the sample+spike mixture of total Ca and Sr.

3.2.6 *Column Chemistry*

As mentioned above in *Section 3.1*, elemental analysis of seawater through mass spectrometry is often prone to numerous spectral and other matrix-based interferences that result from the high salt content in the sample. These interferences can increase uncertainties in isotope ratio measurements and ultimately concentration and/or elemental ratio inversions. For Sr and Ca analysis, spectral interferences can arise from doubly-charged SO_4 (mass-to-charge ratio = 48) and doubly-charged Sr (mass-to-charge ratios = 42 – 44) ions overlapping with Ca isotopes. Furthermore, isotopes of Rb (^{85}Rb and ^{87}Rb) can cause spectral interferences on ^{86}Sr and ^{87}Sr. For these reasons, I targeted a two-stage chromatographic separation and purification of Ca and Sr (Figure 3.7). The goal of this staggered separation was to purify both Sr and Ca first from the seawater matrix and then from each other. I designed sets of hand-pulled, 250 µL PFA columns that contained Eichrom (Lisle, IL USA) DGA or SrSpec resins and fit with a porous, 35 µm hydrophilic PTFE frit. At the beginning of any chromatographic separation, DGA and SrSpec columns were both cleaned with 2 mL of 0.05M HNO_3. Reconstituted spiked samples were then loaded onto a DGA column, and the sample matrix was separated from Ca and Sr by washing the column with 2 mL of 2M HNO_3. The combined Ca and Sr fractions were eluted off of the column with 2 mL of 8M HNO_3. After loading this resultant mixture onto a SrSpec column, the Ca fraction was eluted with 2 mL of 8M HNO_3; the purified Sr fraction was eluted by subsequently washing the column with 2 mL of 0.05M HNO_3. The recovery and separation of

this procedure was tested using unspiked, natural abundance seawater. The resulting fractions were then analyzed using an ICAP-Q quadrapole ICP-MS (Thermo Scientific, Bremen, Germany) at the University of Washington to measure Ca, Sr, and other elements. The recovery is near-quantitative, and column blanks appear to be on the order of 0.4 µg Ca (1% of expected Ca load) and 0.65 ng Sr (0.065% of expected Sr load, Figure 3.8). This is important to note; as mentioned in *Section 3.1.3*, chromatographic purification of samples can itself be a source of methodological external error (fractionation of isotopes on column, irregularities in resin-binding, etc.) if yield off of columns is non-quantitative. Spiked SRM 915a samples were not subjected to column chemistry; these samples were only used to quantify and calibrate the Ca isotope composition of the double mixed spike solution and contain a negligible amount of Sr relative to Ca in the spiked 915a mixtures.

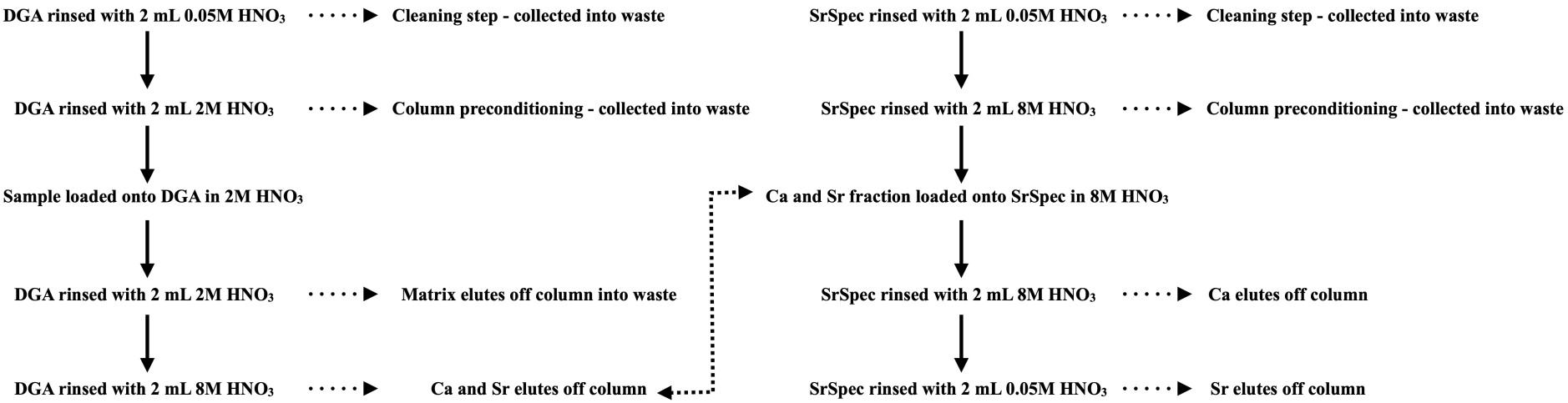

Figure 3.7. Systematic of chromatographic purification of Ca and Sr from analyzed samples using Eichrom DGA and SrSpec resins and 250 µL PTFE microcolumns.

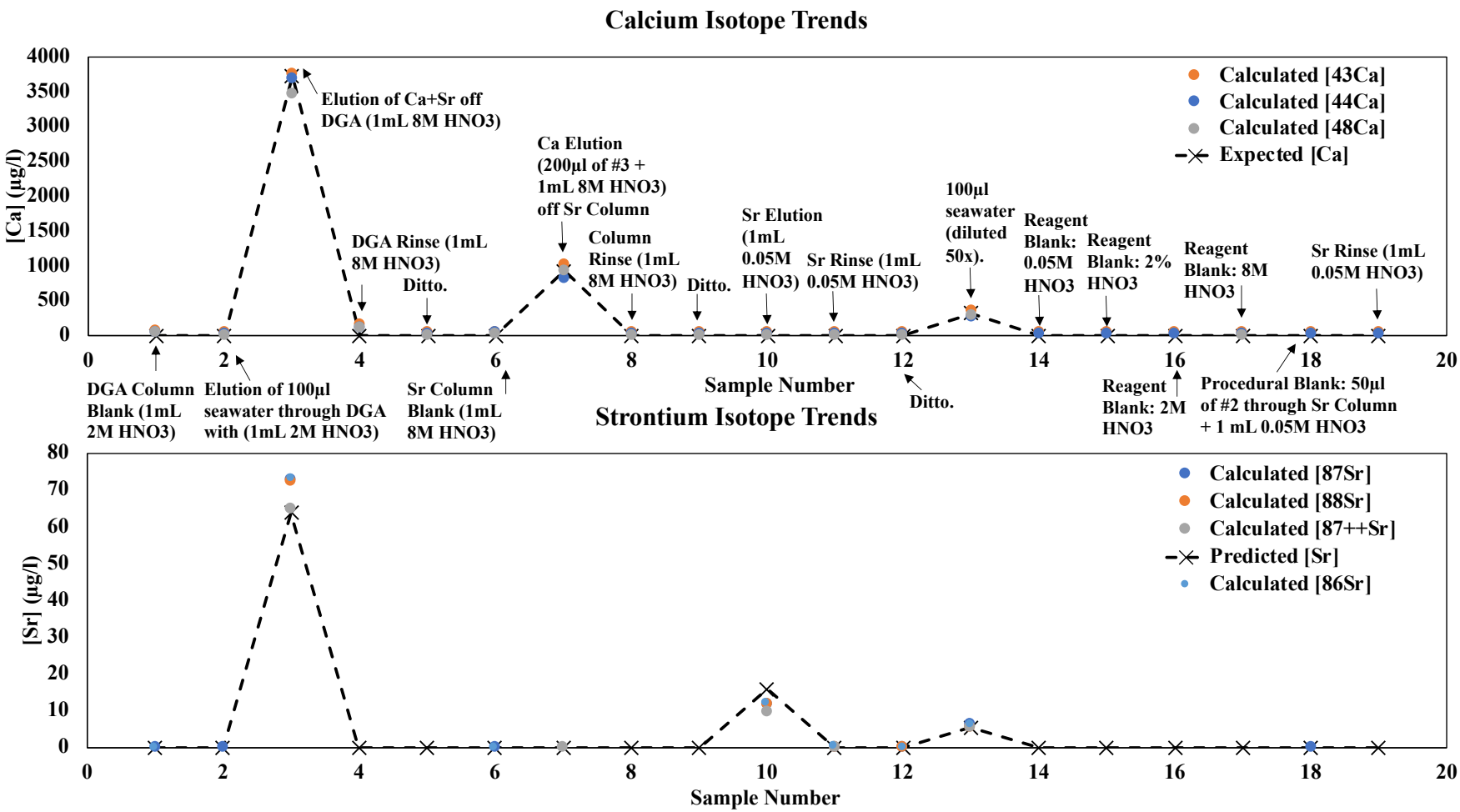

Figure 3.8. Procedural recovery of Ca (top panel) and Sr (bottom panel) using the column chemistry methods detailed in *Section 3.2.6*. Sample used is unspiked NOAA Ocean Station Papa (50.1°N, 144.9°W) seawater with assumed [Ca] = 10.21 mM and [Sr] = 87.81 µM (assumptions used to calculated black reference lines in both panels). Column yields indicate that after 2 mL rinse steps between elution steps, recovery of Ca and Sr appears near-quantitative, and column blanks appear to be on the order of 0.4 µg Ca (1%

of expected Ca load) and 0.65 ng Sr (0.065% of expected Sr load). Data collected using ThermoScientific iCAP-Q Quadrupole Inductively Coupled Plasma Mass Spectrometer at the University of Washington.

3.2.7 *Thermal Ionization Mass Spectrometry (TIMS)*

After column separation, purified fractions of Sr and Ca were evaporated to dryness, re-dissolved, and loaded as 3 – 5 µg Ca or 300 – 700 ng Sr in 10% HNO_3 directly onto rhenium (Re) ribbon single filaments in preparation for multicollector TIMS analysis. One µL of 1M phosphoric acid (H_3PO_4) was then added to each filament with the sample, and filaments were once heated to evaporation at a current of ~2 A.

Sr and Ca isotope measurements were carried out at the University of Texas at Austin Isotope Geochemistry Facility using a TRITON multicollector thermal ionization mass spectrometer (ThermoFisher, Bremen, Germany). The instrument operated in positive ion mode with a 10 kV acceleration voltage and 10^{11} Ω (ohm) resistors for the nine moveable Faraday cups. For Ca analyses, the instrument was configured to use a multi-dynamic method, with the first sequence collecting ^{40}Ca (L3), ^{42}Ca (C), ^{43}Ca (H1), ^{44}Ca (H2) and ^{48}Ca (H4). The second sequence collected ^{44}Ca (L1) such that m/z = 45 occupied the center (C) position. The sample was tuned to target a ^{40}Ca voltage of ~10 V. Each Ca filament was analyzed for a total of 100 cycles, with 10 cycles per block, roughly 40 seconds per cycle, and ~1.8 hours total per sample. For Sr analyses, the instrument's configuration was changed to collect for ^{84}Sr (L1), ^{85}Rb (ion counter), ^{86}Sr (H1), ^{87}Sr (H2), and ^{88}Sr (H4) and tuned to target an ^{87}Sr voltage of ~4 V. Each Sr filament was analyzed for a total of 160 cycles, with 20 cycles per block, roughly 10 seconds per cycle and ~40 minutes total per sample. ^{85}Rb was measured to correct for interfering ^{87}Rb, however, this correction was typically insignificant given column purification of Sr samples.

3.3 Results & Discussion

3.3.1 *Spike Calibration and Composition*

Direct measurement of the double mixed spike solution using the ELEMENT 2 HR-ICP-MS yielded the following isotopic composition: $^{42}Ca/^{44}Ca = 0.16178 \pm 0.0002$ (1σ SD; n = 3 replicate injections), $^{43}Ca/^{44}Ca = 16.42 \pm 0.05$, $^{48}Ca/^{44}Ca = 13.44 \pm 0.01$, $^{84}Sr/^{88}Sr = 2.33 \pm 0.01$ (n = 2), $^{86}Sr/^{88}Sr = 0.3658 \pm 0.0009$, and $^{87}Sr/^{88}Sr = 7.18 \pm 0.03$. With the exception of $^{86}Sr/^{88}Sr$, all measurements are within 4% of the optimized target values listed in Table 3.4. The measured $^{86}Sr/^{88}Sr$ ratio is over double (109% higher) that of the optimum blend. Given that ^{87}Sr and ^{84}Sr single spikes were used to create the double mixed spike solution and the < 4% relative difference between optimal and measured Sr isotope ratios in *all* other cases, this observed deviation is unlikely to be a result of weighing errors and potentially indicates a larger contamination/impurity of ^{86}Sr within the Oak Ridge single spike carbonates.

With these ICP-MS-derived spike values as initial inputs, inversion of the isotopic composition of the multiple spiked standard mixtures yielded the following isotopic composition for the double mixed spike solution: $^{40}Ca/^{44}Ca = 2.7278$, $^{42}Ca/^{44}Ca = 0.16177$, $^{43}Ca/^{44}Ca = 16.3876$, $^{48}Ca/^{44}Ca = 13.4125$, $^{84}Sr/^{88}Sr = 2.3321$, $^{86}Sr/^{88}Sr = 0.3650$, and $^{87}Sr/^{88}Sr = 7.2012$ (Table 3.6). Note that in this scheme, $^{46}Ca/^{44}Ca$ is assumed to be negligible given the trace abundance of ^{46}Ca in BSE (Russell et al., 1978). As shown in Figure 3.9, with these values as inputs into the spike inversion script, the average $\delta^{44/40}Ca$ of SRM 915a = -0.97 ± 0.07‰ (1σ external SD, n = 4 different X_{DS} mixtures), and the average $\delta^{44/40}Ca$ of IAPSO seawater = 1.12 ± 0.16‰ (1σ external SD, n = 4 different X_{DS} mixtures). For Sr, as shown in Figure 3.10, the average $\delta^{88/86}Sr$ of SRM 987 = -0.07 ± 0.03‰ (1σ external SD, n = 4 different X_{DS} mixtures), and the average $\delta^{88/86}Sr$ of SRM 987 = 0.330 ± 0.11‰ (1σ external SD, n = 4 different X_{DS}

mixtures). Analysis of the JCp-1 coral standard using SRM915a, SRM987, and IAPSO tuned values of spike composition allows for the tuning of the molar Sr/Ca ratio of the double mixed spike solution *and* provides an independent check on the isotope ratios of the spike solution. This analysis yielded a value of 0.13956 mol/mol for the Sr/Ca ratio of the spike when tuned to a $Sr/Ca_{JCp\text{-}1}$ (mol/mol) = 8.82 ± 0.04. The inverted stable Ca and Sr isotopic composition of JCp-1 at these tuned parameters were $\delta^{44/40}Ca_{JCp\text{-}1}$ = -0.11 ± 0.02‰ and $\delta^{88/86}Sr_{JCp\text{-}1}$ = 0.169 ± 0.005‰. Each of these values is in close agreement with previously published values for this standard, suggesting that the multi-standard numerical approach to spike design and calibration applied here is successful (Krabbenhöft et al., 2009; Hathorne et al., 2013; Elhamel, 2014; Mondal and Chakrabarti, 2018).

While the tuned values reproduce the isotopic composition of the standards quite well, it is possible that there are multiple solutions to the isotopic composition of the DMS solution (outside of the tuned values) that may produce inverted Sr/Ca_{sw} values of higher accuracy and/or precision. As part of a sensitivity analysis, I tested the impact of introducing uncertainty (ranging from 1 – 100% error) into each isotope ratio (while holding others constant) of the DMS solution on the precision and accuracy of the inverted Sr/Ca_{sw} ratio for any given sample. The results indicate that internal precision of ~120 ppm (1σ SD) on Sr/Ca_{sw} can be achieved across the whole tested range of accuracy errors in each spike isotope ratio. However, the propagation of this error in precision is more predictable for Ca isotopes (Figure 3.11) than for Sr isotopes (Figure 3.12). Furthermore, accuracy of the inverted Sr/Ca_{sw} (assuming those derived from the tuned spike values as "true") decreases the most rapidly as errors $^{43}Ca/^{44}Ca_{spk}$, $^{48}Ca/^{44}Ca_{spk}$, (Figure 3.13) and $^{87}Sr/^{88}Sr_{spk}$ (Figure 3.14) increase. Future experiments that involve designing a $^{43+48}Ca$ and $^{84+87}Sr$ double mixed spike solution may take this apparent sensitivity under

consideration when attempting to calibrate the composition of the spike for high-precision *and* accurate inversions of Sr/Ca ratios.

Table 3.6. Summary of optimized double mixed spike Sr and Ca isotope ratios for the solution calibrated for use during these experiments.

Isotope Ratio	**Calculated Composition in Double Mixed Spike Solution**
$^{40}Ca/^{44}Ca$	2.7278
$^{42}Ca/^{44}Ca$	0.16177
$^{43}Ca/^{44}Ca$	16.3876
$^{48}Ca/^{44}Ca$	13.4125
$^{84}Sr/^{88}Sr$	2.3321
$^{86}Sr/^{88}Sr$	0.3650
$^{87}Sr/^{88}Sr$	7.2012
Sr/Ca Ratio	0.13956

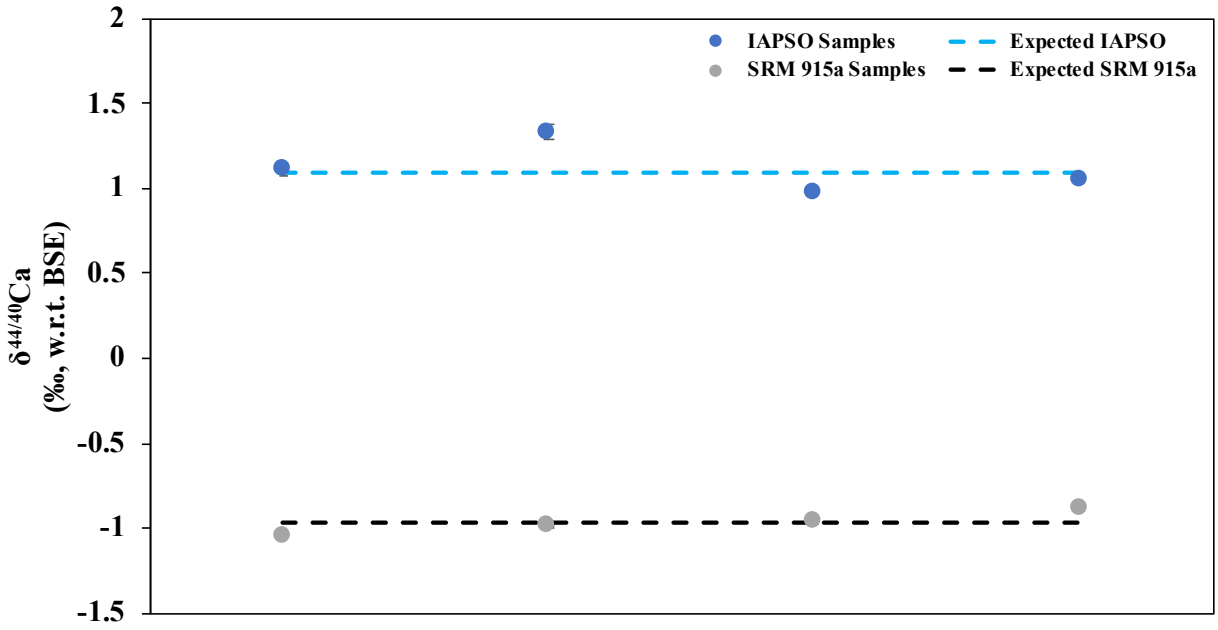

Figure 3.9. Inverted $\delta^{44/40}$Ca values (w.r.t. Bulk Silicate Earth) for the IAPSO and SRM 915a samples used during the spike calibration experiments relative to "true" accepted values for these standards (+1.1‰ for IAPSO and -0.97‰ for SRM 915a). Note that the composition of the double mixed spike solution was tuned such that sum of the square of the residuals between the points and the dashed references lines is minimized. Error bars indicate 1σ standard error internal precision of isotope ratio measurements across the 100 cycles for each individual measurement.

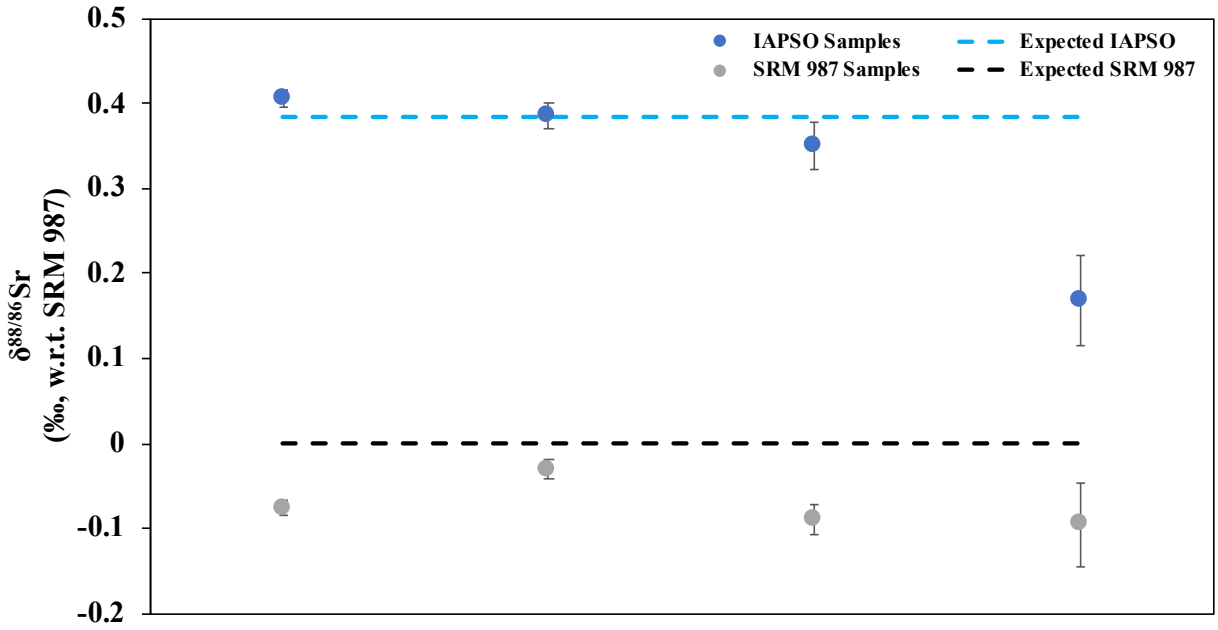

Figure 3.10. Inverted $\delta^{88/86}$Sr values (w.r.t. SRM 987) for the IAPSO and SRM 987 samples used during the spike calibration experiments relative to "true" accepted values for these standards (+0.386‰ for IAPSO and, by definition, 0‰ for SRM 987). Note that the composition of the double mixed spike solution was tuned such that sum of the square of the residuals between the points and the dashed references lines is minimized. Error bars indicate 1σ standard error internal precision of isotope ratio measurements across the 160 cycles for each individual measurement.

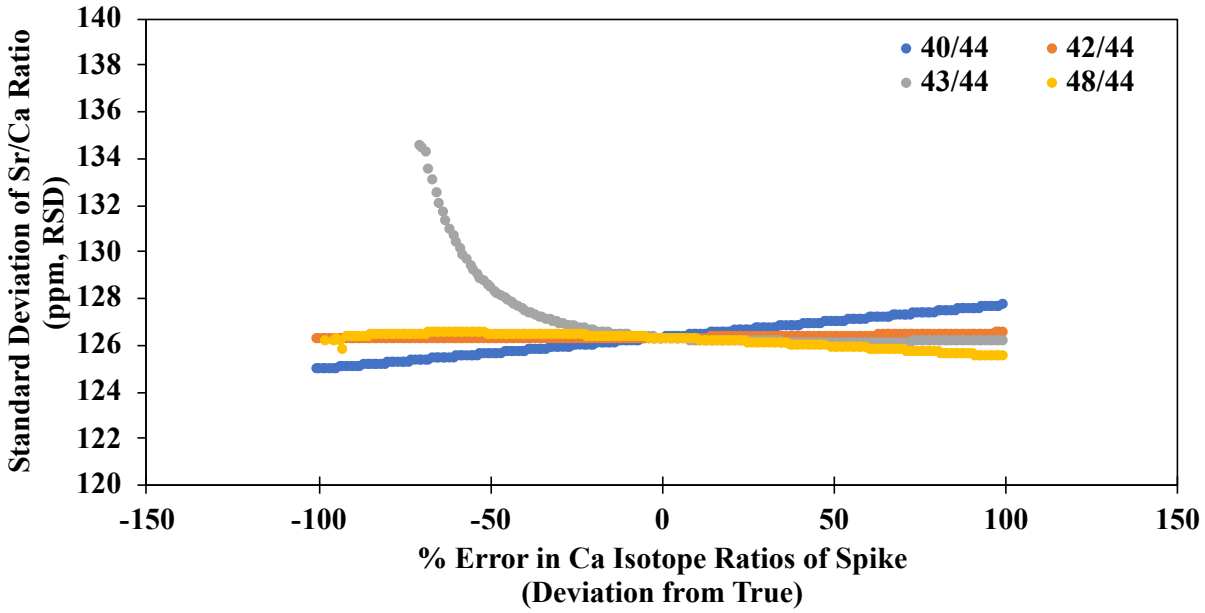

Figure 3.11. As error in the assumed value of each Ca isotope ratio of the double mixed spike solution increases from that of the "true" composition, internal precision on inverted Sr/Ca ratios is largely maintained (~120 ppm, 1σ RSD).

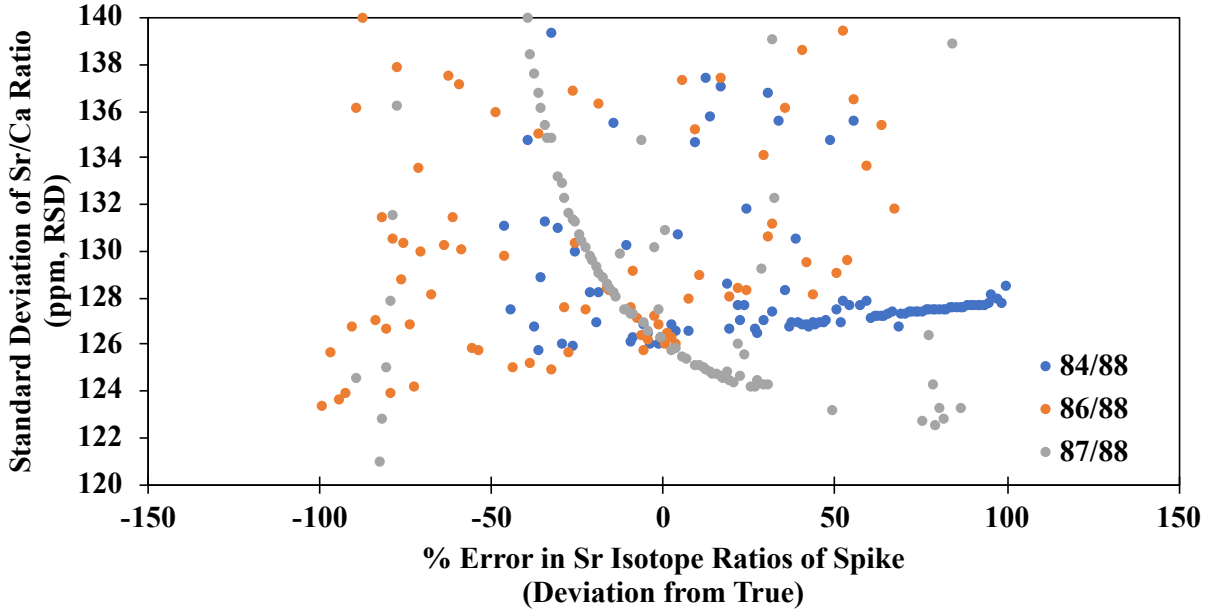

Figure 3.12. As error in the assumed value of each Sr isotope ratio of the double mixed spike solution increases from that of the "true" composition, internal precision of ~120 ppm (1σ RSD) can also be maintained; however, variability here is less predictable than for the Ca isotope system.

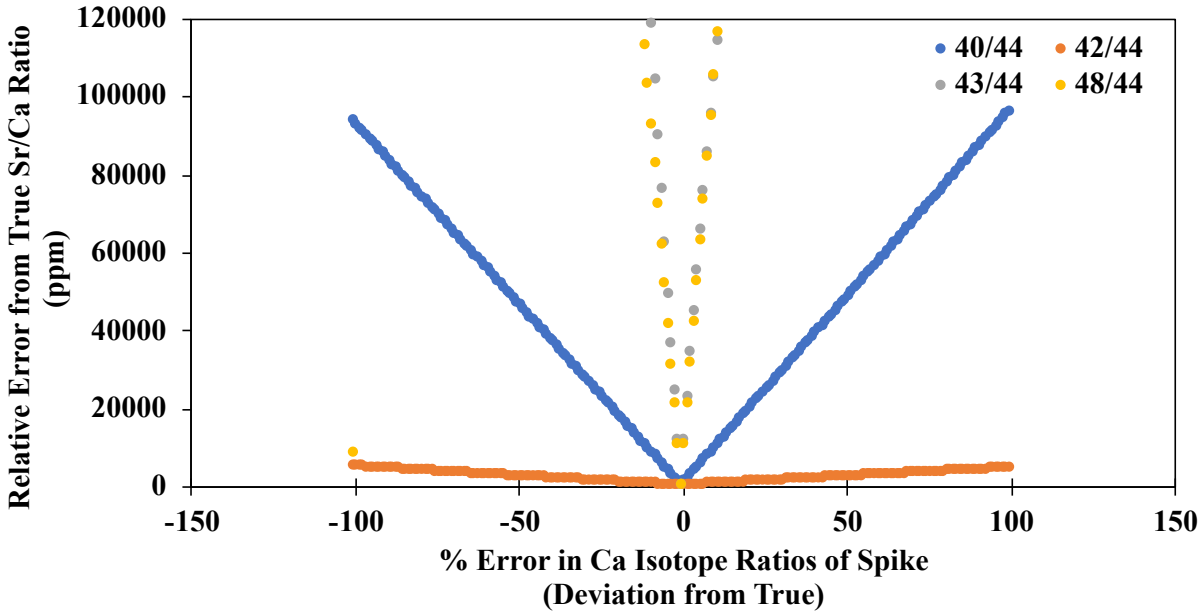

Figure 3.13. Errors in the assumed values of $^{43}Ca/^{44}Ca$ and $^{48}Ca/^{44}Ca$ of the double mixed spike solution (relative to the "true" composition) most rapidly increase accuracy errors in inverted molar Sr/Ca ratios. This is somewhat expected given the use of a $^{43+48}Ca$ double spike.

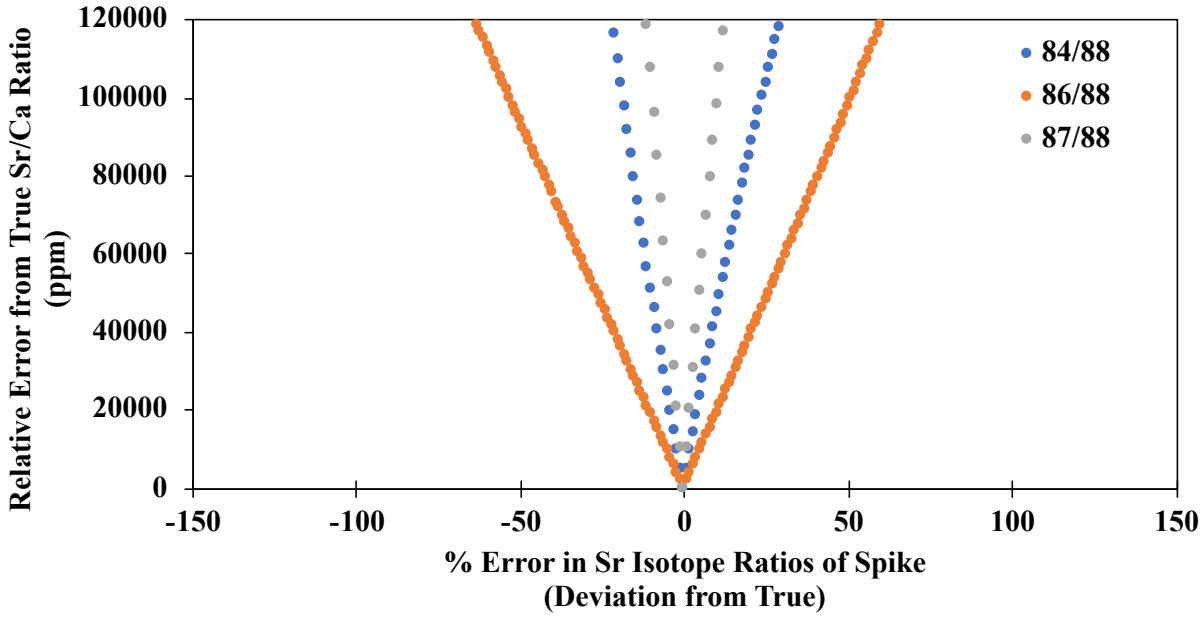

Figure 3.14. Errors in the assumed values of $^{87}Sr/^{88}Sr$ and $^{84}Sr/^{88}Sr$ of the double mixed spike solution (relative to the "true" composition) most rapidly increase accuracy errors in inverted molar Sr/Ca ratios. This is somewhat expected given the use of an $^{84+87}Sr$ double spike.

3.3.2 *Internal Precision of Isotope Ratios*

In practice, the composition of a double spike (and in this case, double *mixed* spike) solution is calibrated only once, and the composition from that calibration is applied in the inversion of any and all samples that have been spiked with it. Therefore, attempts to reduce uncertainty *during* an experiment should perhaps focus more on eliminating and/or reducing sources of internal error across measurement cycles of TIMS analysis. As mentioned in *Section 3.1.3*, this internal precision is a fundamental limit on external reproducibility of both isotope ratio measurements and inverted Sr/Ca ratio values. Visualizing the raw isotope data from a typical Reef Seawater Consistency Standard (RSCS) filament as a triple-isotope plot implies that IMF is a strong (up to 270 ppm RSE, 1σ) source of internal variability across individual cycles of both Ca and Sr isotope ratio measurements (Figure 3.15 and Figure 3.16). Recall, on plots such as these, a tight correlation around a linear relationship is indicative of a predictable mass-dependent fractionation of isotopes within the mass spectrometer (Equation 3.18; Dodson, 1963; Albarède and Beard, 2004; Rudge et al., 2009). Once subjected to the double mixed spike inversion script, however, internal precision on the $^{40}Ca/^{44}Ca$ ratio improved to an average 13 ppm across all RSCS samples (1σ RSE). Similarly, internal $^{86}Sr/^{88}Sr$ precision across these standards averaged 12 ppm (1σ RSE). Thus, the data reported here supports the use of double spike isotope dilution as a means to improve internal precision of isotope ratio measurements through TIMS; here, the application a DMS-ID-TIMS method improves internal precision by *at least* an order of magnitude over non-ID methods of TIMS.

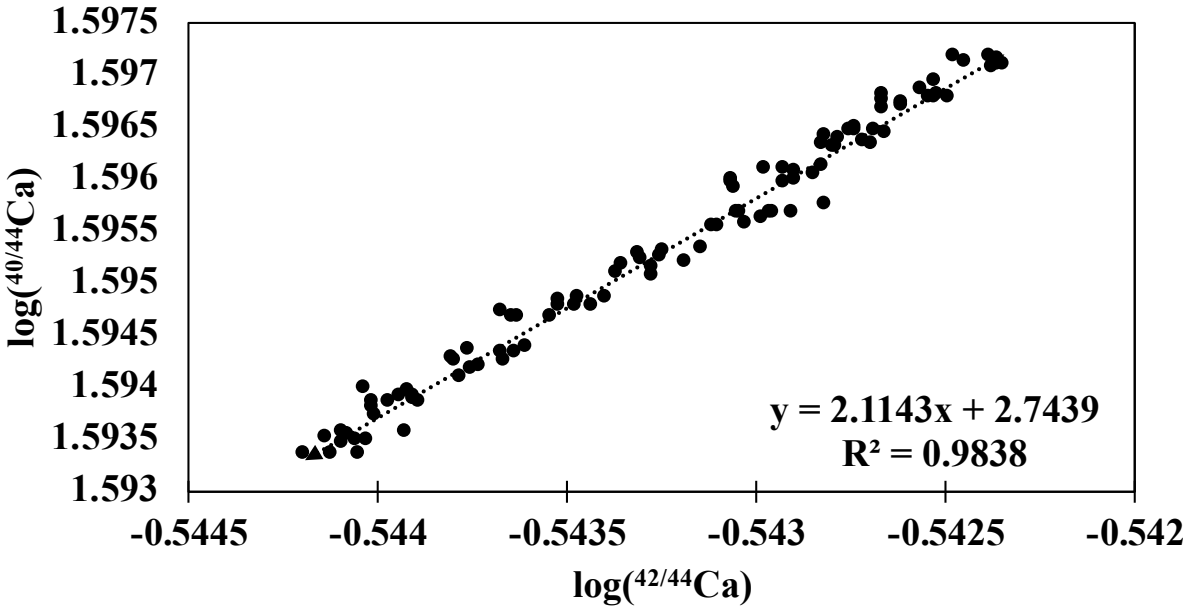

Figure 3.15. Ca triple isotope plot of raw measured $^{40/44}$Ca vs $^{42/44}$Ca from a typical Reef Seawater Consistency Standard is indicative of mass-dependent IMF being a major contributing source of internal error on measured Ca isotope ratio variability. 100 cycles of a single filament plotted.

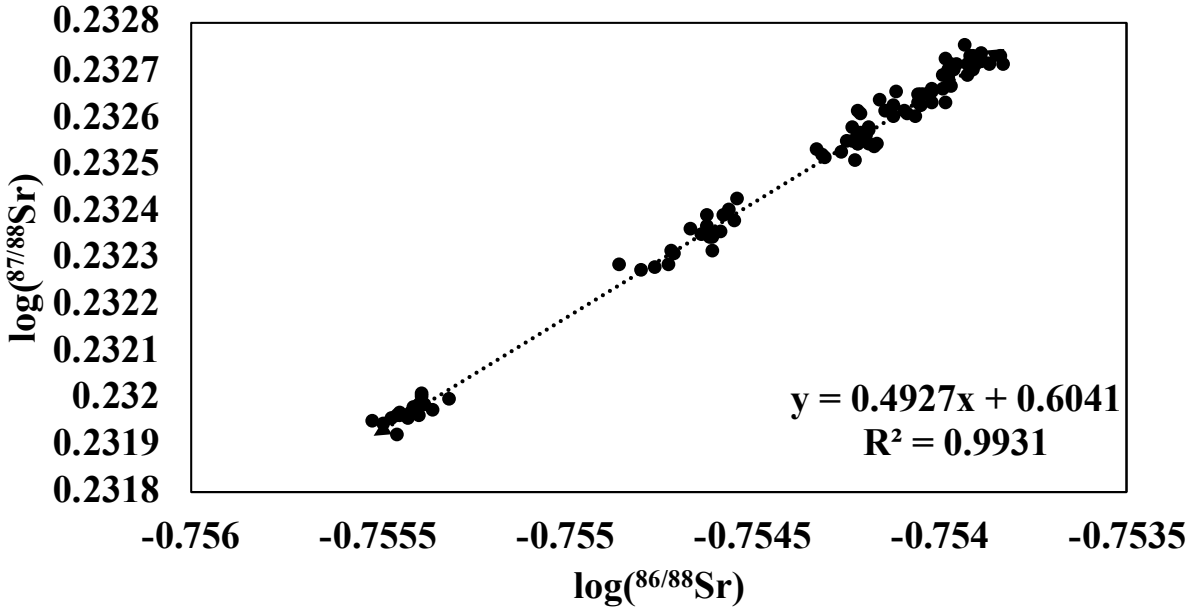

Figure 3.16. Sr triple isotope plot of raw measured $^{87/88}$Sr vs $^{86/88}$Sr from a typical Reef Seawater Consistency Standard is indicative of mass-dependent IMF being a major contributing

source of internal error on measured Sr isotope ratio variability. 160 cycles of a single filament plotted.

The typical raw filament data represented in Figures 3.15 and 3.16 further allow for an assessment of two key additional sources of internal error during mass spectrometry experiments: counting statistics (shot noise) and Johnson-Nyquist noise. Counting statistics describe the uncertainty inherent in approximating counts per unit time by measuring a finite number of randomly temporally-distributed ion detections within the TIMS Faraday cups (John and Adkins, 2010). The counting statistics error (σ_{CS}) on measurements of a single isotope ratio can be estimated by first converting the raw voltages across all cycles of each isotope into total counts (Equation 3.28):

$$Counts_a = \frac{Volts_a * C * t_m}{R} \qquad (3.28)$$

where C is equal to 1 Coulomb of charge (6.242 x 10^{18} elementary charges), R is the resistance in Ohms (10^{11}), and t_m is the integration time of the signal (40 seconds per cycle for Ca isotopes; 10 for Sr isotopes). σ_{CS} for a single isotope is set by the set by the standard deviation of the Poisson distribution (Equation 3.29):

$$\sigma_{CS,a} = \sqrt{Counts_a} \qquad (3.29)$$

Using the fundamental rules of error propagation, the relative internal error of the quotient of two isotopes (an isotope ratio, R_{ab}) is (Equation 3.30):

$$\sigma_{R_{ab}} = \sqrt{\frac{{\sigma_a}^2}{a^2} + \frac{{\sigma_b}^2}{b^2}} \qquad (3.30)$$

where a and b are the signal intensities of each isotope, and σ_a and σ_b are the errors in those quantities. Rewriting this equation such that the intensity of each isotope is expressed as total counts allows for the expression of σ_{CS} for an isotope ratio (Equation 3.31):

$$\sigma_{CS,R_{ab}} = \sqrt{\frac{Counts_a + Counts_b}{Counts_a * Counts_b}} \quad (3.31)$$

Equation 3.31 can be rewritten to define a new quantity that represents the *effective* number of total counts for each isotope (n_{eff}, Equation 3.32):

$$n_{eff} = \frac{Counts_a * Counts_b}{Counts_a + Counts_b} \quad (3.32)$$

This allows for the expression of Equation 3.31 in terms of n_{eff} (Equation 3.33):

$$\sigma_{CS,R_{ab}} = \frac{1}{\sqrt{n_{eff}}} \quad (3.33)$$

Johnson-Nyquist Noise is a product of the background voltage recorded by Faraday cups in the absence of an ion beam. Therefore, any measured voltage of a particular isotope is a sum of the true voltage of the signal and the background noise voltage (Equation 3.34):

$$Volts_{a-measured} = Volts_a + Volts_{JN} \quad (3.34)$$

The contribution of Johnson Noise, in volts, can be estimated from Equation 3.35 (Simpson, 1974):

$$Volts_{JN} = \sqrt{\frac{4 * k_b * R * T}{t_m}} \quad (3.35)$$

where k_B is the Boltzmann constant (1.381×10^{-23} $m^2 * kg * s^{-2} * K^{-1}$) and T is the absolute temperature of the resistor (310 K). Applying Equation 3.28 to convert volts to total counts, Equation 3.30 to express the combined error due to Johnson Noise for an isotope ratio ($\sigma_{JN, Rab}$), and Equation 3.32 to express total counts in terms of *effective* counts (n_{eff}) results in an expression for $\sigma_{JN, Rab}$ that is a function of n_{eff} (Equation 3.36):

$$\sigma_{JN, R_{ab}} = \frac{R_{ab}}{n_{eff} * (R_{ab} + 1)} * \sqrt{\left(\frac{Counts_{a-JN}}{R_{ab}}\right)^2 + \left(Counts_{b-JN}\right)^2} \quad (3.36)$$

Visualizing the impacts of counting statistics and Johnson Noise on a plot of $\log_{10}(\sigma)$ vs $\log_{10}(n_{eff})$ for a typical RSCS filament implies that isotope ratio precision of ideally-spiked

seawater samples are likely fundamentally limited by Johnson Noise of the Faraday cups rather than counting statistics (Figure 3.17). To confirm this, I designed an error propagation exercise using the measured isotope ratios of one of the spiked RSCS samples. I introduced errors of 0.001 - 1‰ RSD to a single measured ratio at a time, keeping all others constant. The Sr/Ca ratio was then calculated for each sample in a Monte Carlo fashion, with 100 different iterations per error per measured isotope ratio. The results of this analysis show that high internal precision (±0.05‰, 1σ RSD) on the measured $^{87}Sr/^{88}Sr$ of a sample is a particular target for when configuring the instrument to minimize error on inverted Sr/Ca_{sw} using the methods presented here (Figure 3.18 and Figure 3.19). That said, each of the samples presented as part of this analysis should not limited by internal error of the measured isotope ratios. As mentioned above, internal error of measured ratios across all cycles of any given sample (1σ SE) is on the order of single digits to 10's of ppm. Errors would need to be higher than this for even the most sensitive ratio to have an impact on inverted Sr/Ca ratio measurements. As a check on this line of reasoning, I re-processed the existing data using only the first half of the cycles for each Ca or Sr method. This change, reflecting a scenario in which the instrument collected only half as many counts for a particular sample, had a negligible impact on the external error for Sr/Ca_{sw} (~0.001 ppm). Taken in tandem, these results indicate the samples presented here are not count-limited and that the internal error of the method is minimized.

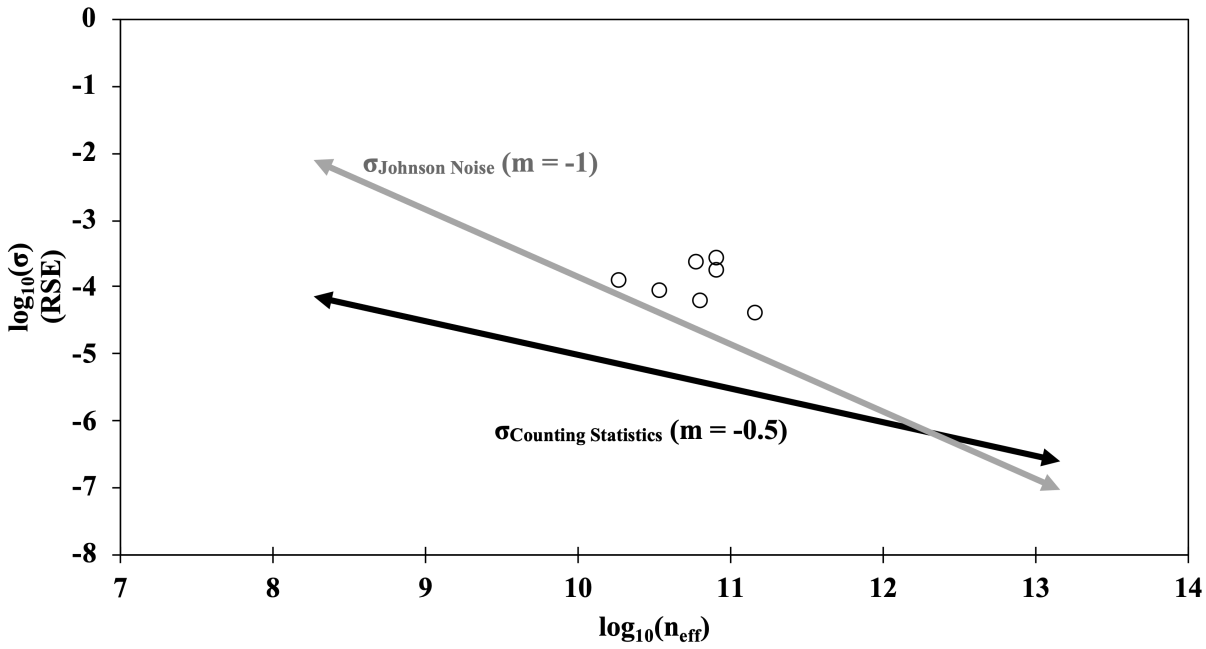

Figure 3.17. The errors (1σ RSE) in stable Sr (w.r.t. ^{88}Sr) and Ca (w.r.t ^{44}Ca) isotope ratios for a typical measurement of an ideally-spiked seawater sample are plotted with respect to predicted errors due to Johnson Noise (gray line) and counting statistics (black line). Signal intensity is given as the effective number of counts collected over this period (n_{eff}). The error due to counting statistics is based on theoretical calculations (slope = -0.5). The error due to Johnson noise is also based theoretical calculations of Johnson Noise (slope = -1).

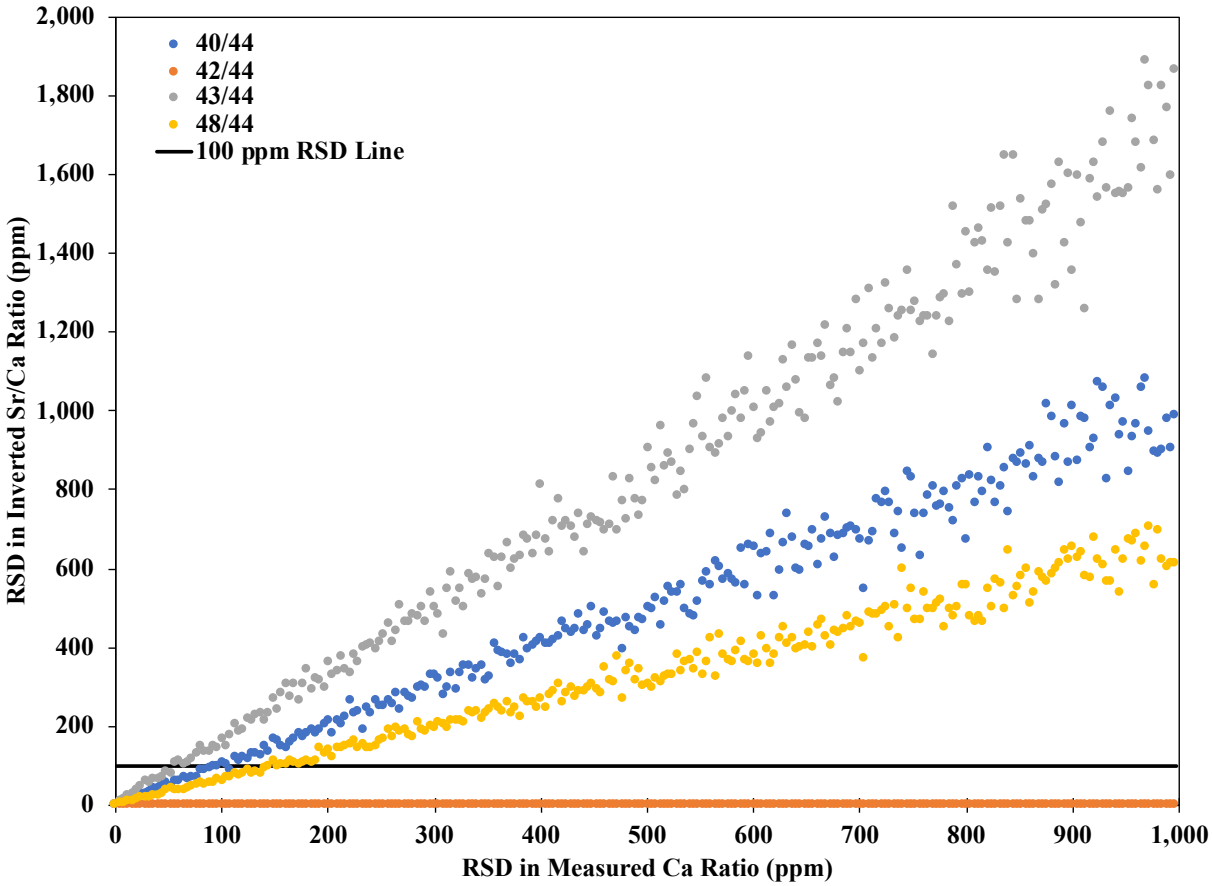

Figure 3.18. The impact of increasing error on measured (TIMS) $^{X/44}$Ca ratios of an ideally-spiked seawater sample using the DMS-ID-TIMS method detailed here scales linearly with the precision of the inverted Sr/Ca ratio (relative to a target 100 ppm RSD on Sr/Ca_{sw} – black line), with the internal precision of measured $^{43}Ca/^{44}Ca$ being the strictest control within the stable Ca isotope system.

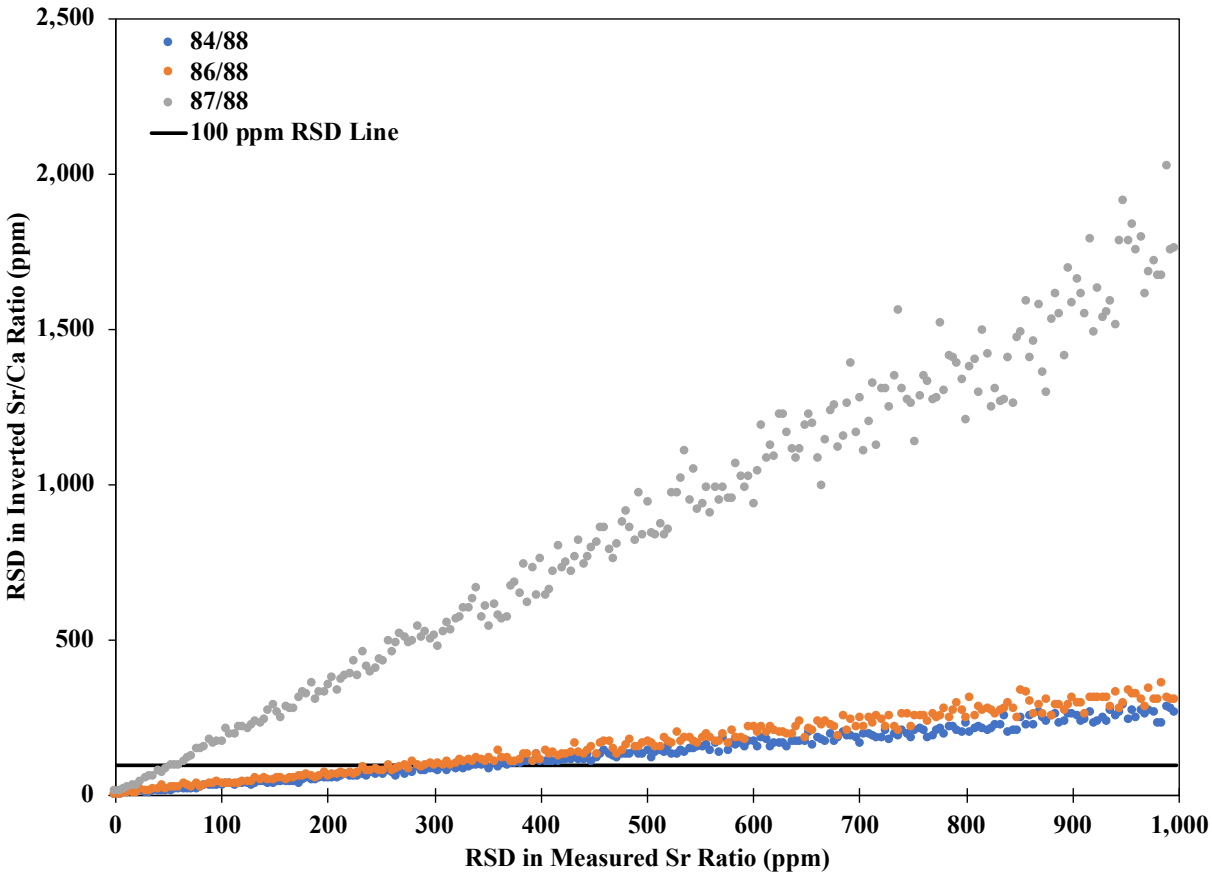

Figure 3.19. The impact of increasing error on measured (TIMS) $^{X/88}Sr$ ratios of an ideally-spiked seawater sample using the DMS-ID-TIMS method detailed here scales linearly with the precision of the inverted Sr/Ca ratio (relative to a target 100 ppm RSD on Sr/Ca_{sw} – black line), with the internal precision of measured $^{87}Sr/^{88}Sr$ being the strictest control within the stable Sr isotope system.

3.3.3 *External Precision of Isotope Ratios and Sr/Ca_{sw}*

To quantify the external reproducibility of this DMS-ID-TIMS method for determining Sr/Ca_{sw} measurements, eight aliquots of the Reef Seawater Consistency Standard (RSCS) solution were individually spiked at the optimal spike-to-sample ratio ($X_{DS} \cong 0.2$) and separately subjected to the column chemistry procedures detailed in *3.2.6 Column Chemistry*. These subsamples are all taken from the same homogeneous solution; thus, they should have identical Sr/Ca_{sw} values. Variability in the measured Sr/Ca_{sw} of these full procedural replicates is therefore

an indication of the reproducibility of the method (external error) due to factors like procedural blank and instrumental error. The average $\delta^{44/40}$Ca value was 0.93 ± 0.09‰ (1σ external SD, n = 8). For Sr, the average $\delta^{88/86}$Sr value was 0.38 ± 0.02‰ (1σ external SD, n = 8). Note – the external reproducibility of $\delta^{44/40}$Ca and $\delta^{88/86}$Sr through the DMS-ID-TIMS methods detailed here is on par with previously reported reproducibility of stable Ca and Sr isotopes based on repeated analyses of IAPSO seawater (Fietzke and Eisenhauer, 2006; Krabbenhöft et al., 2009; Liu et al., 2014). The trends in RSCS measurements can be observed in Figure 3.20, and these precision bounds on isotope ratios will be applied to future samples analyzed using the methods presented here. Furthermore, given that internal errors on measured isotope ratios is at least an order of magnitude lower than the observed external reproducibility on these RSCS samples (see *Section 3.3.2*), it is likely that the observed variability between RSCS samples reflects sample-to-sample procedural error (column recovery and/or procedural blank) rather than instrumental error.

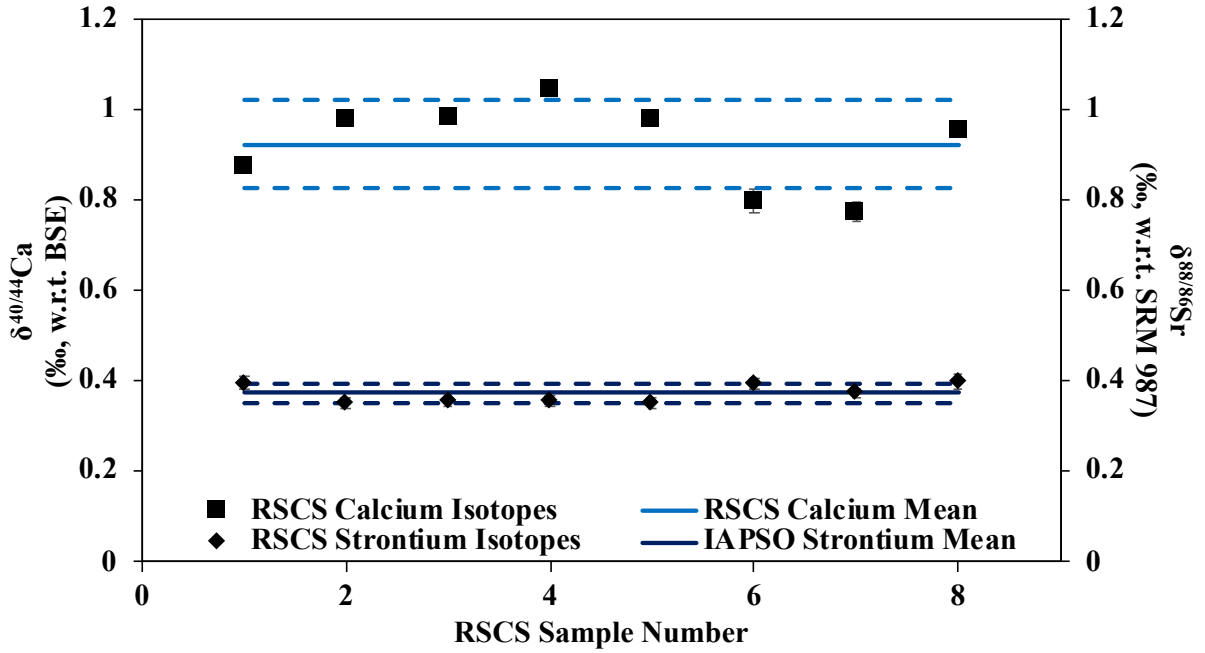

Figure 3.20. Reproducibility of repeated stable isotope ratio measurements of a homogenous reef seawater consistency standard. Inverted stable Ca (squares) and Sr (diamonds) isotope compositions of the Reef Seawater Consistency Standard (RSCS, n = 8) generally show good agreement with each other. Dashed lines represent the standard deviation of measured ratio values across the eight samples. Average $\delta^{44/40}Ca = 0.93 \pm 0.09‰$. Average $\delta^{88/86}Sr = 0.38 \pm 0.02‰$. Error bars on individual points indicate 1σ standard error internal precision of isotope ratio measurements across the multiple cycles for each individual measurement.

Inversion of the composition of these eight spiked RSCS samples also results in the determination of X_{DS}, which further allows for the calculation of the molar Sr/Ca_{sw} ratio and its external precision. As shown in Figure 3.21, the ID-DMS-TIMS method achieves an external 1σ RSD of 0.11% or 1.1‰ on molar Sr/Ca_{sw}. This is equivalent to a corresponding average RSCS $Sr/Ca_{sw} = 8.75 \pm 0.01$ mmol/mol (1σ external SD, n = 8). Again, based on the propagated "internal" error of each inverted Sr/Ca ratio measurement, it is likely that the observed variability between RSCS samples reflects issues arising from column and/or procedural blank (rather than instrumental error).

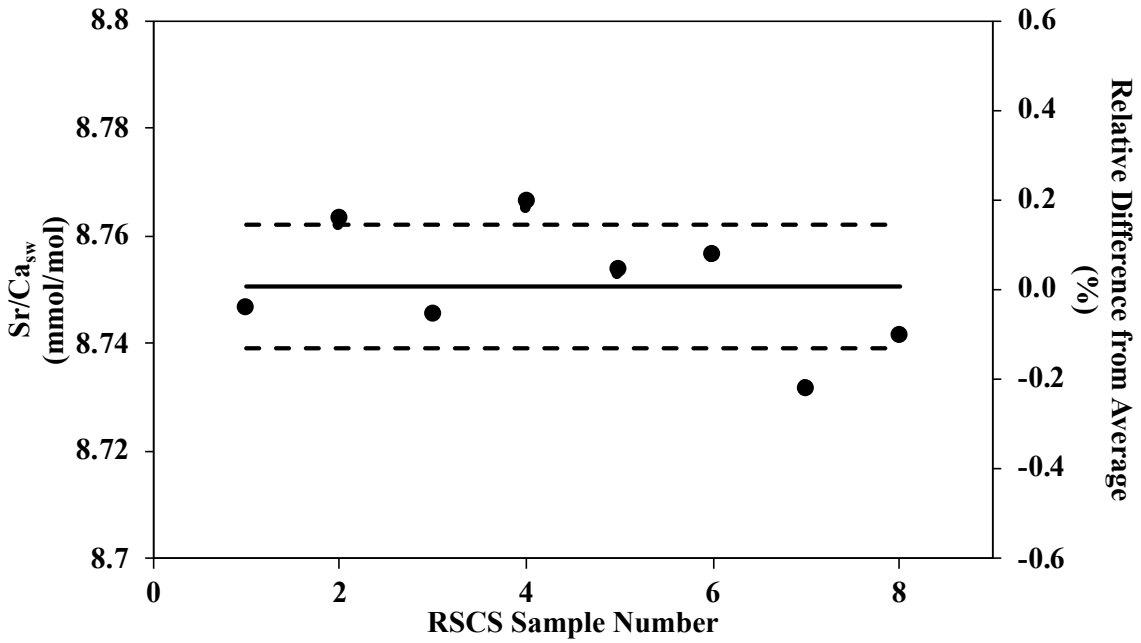

Figure 3.21. Reproducibility of Sr/Ca_{sw} measurements using the DMS-ID-TIMS method based on the repeated analysis of a Reef Seawater Consistency Standard (RSCS, n = 8). These samples provide the full procedural external reproducibility on Sr/Ca_{sw} of this method – 0.01 mmol/mol (0.11% 1σ RSD). Error bars on individual points indicate propagated 1σ standard error internal precision of Sr/Ca_{sw} measurements. Dashed lines indicate 1σ standard deviation across all eight inverted Sr/Ca_{sw} values.

Furthermore, as precise notes of sample and spike weights were kept throughout all experiments, Equation 3.24 can be used to calculate $[Ca]_{sw}$ and $[Sr]_{sw}$ for any given sample processed using the DMS-ID-TIMS method. Using this equation, the 0.11% relative external precision on Sr/Ca_{sw} translates to 0.9% (1σ RSD) precision on both $[Ca]_{sw}$ and $[Sr]_{sw}$. This reported external error is higher than the ~0.1% RSD reported for titration/complexation methods of determining $[Ca]_{sw}$ (Ringbom et al., 1958; Tsunogai, 1968; Krumgalz, 1982); however, it is lower than non-isotope dilution methods of ICP-MS and ICP-OES (Liu et al., 2014; Besson et al., 2014). As previously mentioned, this explicit calculation of concentrations includes external methodological errors that result from weighing variability; these errors are normalized by instead solving the mixed spike ID equation (Equation 3.23) for the molar Sr/Ca

ratio of a particular sample. Additionally, the tuning of the molar Sr/Ca ratio of the double mixed spike solution using JCp-1 means that the accuracy of any direct concentration inversions for $[Ca]_{sw}$ or $[Sr]_{sw}$ will be biased. JCp-1 is known to have impurities that skew its composition from that of pure $CaCO_3$; the weighing and dissolution of powders of the standard to make a stock solution assumed pure $CaCO_3$ for simplicity. Thus, while the precision of $[Ca]_{sw}$ and $[Sr]_{sw}$ is ± 0.9%, errors in accuracy could be ~5% (based on the reported composition of the standard, Okai et al., 2002).

de Villiers et al. (1994) was the first study to demonstrate that Sr/Ca_{sw} can vary significantly with biogenic cycling of Sr and Ca. Expanding on this concept, de Villiers (1999) used an ID-TIMS method to explore basin-scale variability in seawater Sr concentrations and Sr/Ca_{sw} as it related to biogeochemical cycling of elements and Quaternary paleoceanographic applications. Notably, that study reported a long-term external precision on Sr/Ca_{sw} measurements similar to those reported here (0.13%, 1σ RSD) based on replicate measurements of an internal standard over a two-year period. Additionally, de Villiers (199) found that duplicate measurements of seawater samples typically yielded differences less than 0.05%. Here, as seen in Figure 3.21, the external precision of the method is reported not in relation to repeated analyses of the *same* filament load of an internal standard, but as the 1σ RSD of multiple, separately spiked and purified loads of an internal standard. Furthermore, duplicate measurements of seawater samples using the methods detailed here yields unprecedented precision, with errors of less than 0.01%. This method also offers improves external precision on Sr/Ca_{sw} when compared to measurements using ICP-OES by a factor of at least 3x (Steiner et al., 2014; Steiner et al., 2018), while duplicate precision is improved by at least an order of magnitude (Lebrato et al., 2020). These improvements in precision lend themselves well to

current and future questions regarding the biogeochemical cycling of Ca and Sr in marine environments as it relates to ecological and paleoenvironmental changes. The timing of this method is particularly relevant given the recent suggestion that Sr/Ca_{sw} exhibits ~10% variability in the open ocean (higher variability observed coastal seas), which has considerable implications for reconstructions of ancient seawater chemistry using fossilized marine carbonates (Lebrato et al., 2020). The method designed here could potentially be used to reveal the degree to which this reported large, secular variability in Sr/Ca_{sw} is (1) reproducible and (2) itself temporally variable on seasonal to interannual timescales in the modern era.

3.3.4 *Temporal Variability in Sr/Ca_{sw} from Coral Reef Environments*

Recall, the ultimate goal of this DMS-ID-TIMS approach is the development of a method that can maintain external reproducibility of Sr/Ca_{sw} equal to 0.05 – 0.3% 1σ RSD for the application to measurements within and between coral reef environments. These precision targets were motivated by the results of the box model approach detailed in *Section 3.1.2.* and based on empirically-determined NEC fluxes from the March 2017 field campaign to Tetiaroa Atoll. The 0.11% external precision of the method reported here meets that analytical goal. Furthermore, if the observed temporal variability in Tetiaroa's Sr/Ca_{sw} samples is of similar magnitude to fluxes of alkalinity due to NEC, the external precision of the method should be capable of measuring calcite vs aragonite community-level contributions to NEC fluxes with *at least* a 26% minimum resolvable difference (Figure 3.3). Note - this resolvable difference should improve considerably if variability if NEC fluxes increase (or if dissolved Sr and/or Ca concentrations exhibit larger fluxes relative to alkalinity; see below).

Stable isotope analysis and double spike inversion of the reef seawater samples collected from Tetiaroa Atoll and One Tree Island indicate offsets of up to 0.08 mmol/mol between

daytime and nighttime values of salinity-normalized Sr/Ca_{sw} through use of the DMS-ID-TIMS method designed here (Table 3.7, Figure 3.22). On Tetiaroa, this variability is highest in the afternoon, when values display a maximum ~ -2% relative difference from the measured open ocean endmember (8.53 ± 0.01 mmol/mol, Table 3.7). Note – this measured Sr/Ca_{sw} value of open ocean waters between Tahiti and Tetiaroa is within external measurement error of the previously published value of 8.52 observed in South Pacific surface waters and used in *Section 3.1.2* (de Villiers et al., 1994; de Villiers, 1999). At night, this relative difference decreases to less than -1.5%, and between dawn and noon, the value of Sr/Ca_{sw} remains fairly constant (~ 8.42 ± 0.01 mmol/mol). On One Tree Island, the higher relative difference (0.5% from open ocean Sr/Ca_{sw}) is observed at dusk (18:10 local time), and the relatively lower value (-0.4%) is observed near dawn (05:00 local time). Furthermore, the precision of this method also implies quantifiable differences (~0.3‰) in Ca isotope fractionation within coral reef environments over diel timescales. However, there is no particular pattern tied to temporal variability in $\delta^{44/40}Ca$ compared to those observed in Sr/Ca_{sw}. Variability in $\delta^{88/86}Sr$ in all studied seawater samples is negligible in comparison to the external precision of the DMS-ID-TIMS method (Table 3.7).

Furthermore, the range in modeled diel Sr/Ca_{sw} variability from the exercise in *Section 3.1.2* is in line with the conclusions of de Villiers et al. (1994) for coral reef environments (±0.18% of 8.52 mmol/mol), but again depends on the magnitude of NEC fluxes and the calcifier community composition of the reef being studied. The 0.5% relative amplitude in measured diel variability in Sr/Ca_{sw} from Tetiaroa reported here exceeds that predicted by the variability in salinity-normalized alkalinity by an order of magnitude (Figure 3.1 and Figure 3.22). Diel variability in $[Ca]_{sw}$, calculated using tabulated sample and spike weights as inputs into Equation 3.24, implies a systematic pattern similar to calcification/dissolution; however, the amplitude of

this signal is also ~10x greater than that predicted by diel variability in nTA (Figure 3.23). Inclusive of error due to measurement precision (2σ), the amplitude deviation shrinks to ~2x greater than predicted from alkalinity variability. It is not immediately clear why or how Ca (or Sr) could become decoupled from measurements of total alkalinity, particularly after salinity-normalization, since the value for alkalinity includes conservative cations and anions (Equation 3.37):

$$nTA = n[Na^+] + 2 * n[Mg^{2+}] + n[K^+] + 2 * n[Ca^{2+}] + 2 * n[Sr^{2+}] + \cdots z * n[Conservative\ Cation^z] - n[Cl^-] - 2 * n[{SO_4}^{2-}] - n[{NO_3}^-] - z * n[Conservative\ Anion^z] \quad (3.37)$$

Note – the value represented by Equation 3.37 is also equal to the sum of anions that participate in acid/base equilibrium reactions minus the sum of cations that participate in acid/base equilibrium reactions (Equation 3.38):

$$nTA = n[{HCO_3}^-] + 2 * n[{CO_3}^{2-}] + n[HS^-] + n[OH^-] + \cdots z * n[Acid/Base\ Anion^z] - n[H^+] - n[{NH_4}^+] - z * n[Conservative\ Anion^z] \quad (3.38)$$

Therefore, in order for either $n[Ca]_{sw}$ or $n[Sr]_{sw}$ to increase/decrease with a smaller resultant change in nTA, there would need to be a simultaneous decrease/increase in conservative anions. For example, a decrease of 50 mmol*kg^{-1} Ca due to calcification would decrease alkalinity by 100 mmol*kg^{-1} unless $n[SO_4^{2-}]$, $n[NO_3^-]$, or another "conservative" anion simultaneously increased to reduce this delta in nTA. Given the observation of low concentrations of dissolved inorganic nitrogen on Tetiaroa in Chapter 2, it is unlikely that nitrogen cycling in these environments could account for the observed patterns in $n[Ca]_{sw}$. The extent to which other components of the total alkalinity expression can/cannot explain this shift should be the subject of future investigations in reef environments and could have significant implications for the

value of measuring $[Ca]_{sw}$ as a complementary (and perhaps more accurate) indicator of NEC within calcifying ecosystems.

Table 3.7. Summary of stable Ca and Sr isotope ratio data and Sr/Ca_{sw} offsets detected in the analyzed coral reef flat seawater samples from Tetiaroa Atoll, French Polynesia, One Tree Island, Great Barrier Reef (Australia), and the open ocean Pacific Ocean seawater sample. Errors on isotope and elemental ratios indicate 1σ standard deviation (external reproducibility) across multiple spiked samples of the Reef Seawater Consistency Standard (RSCS, n = 8).

	Salinity Normalized Alkalinity (μmol*kg^{-1})	Calculated $\delta^{44/40}$Ca (‰)	Calculated $\delta^{88/86}$Sr (‰)	Calculated Sal. Norm. Sr/Ca_{sw} (mmol/mol)
Tetiaroa Atoll				
12:00	2274	0.89 ± 0.09	0.28 ± 0.02	8.42 ± 0.01
18:00	2263	1.02 ± 0.09	0.36 ± 0.02	8.37 ± 0.01
22:00	2328	0.81 ± 0.09	0.35 ± 0.02	8.36 ± 0.01
02:00	2317	1.12 ± 0.09	0.40 ± 0.02	8.42 ± 0.01
06:00	2304	0.90 ± 0.09	0.34 ± 0.02	8.42 ± 0.01
08:00	2313	0.99 ± 0.09	0.39 ± 0.02	8.42 ± 0.01
12:00	2271	1.04 ± 0.09	0.35 ± 0.02	8.42 ± 0.01
One Tree Island				
05:00	2366	1.06 ± 0.09	0.36 ± 0.02	8.50 ± 0.01
18:10	2226	0.86 ± 0.09	0.38 ± 0.02	8.58 ± 0.01
Open Ocean Seawater	2332	1.08 ± 0.09	0.37 ± 0.02	8.53 ± 0.01

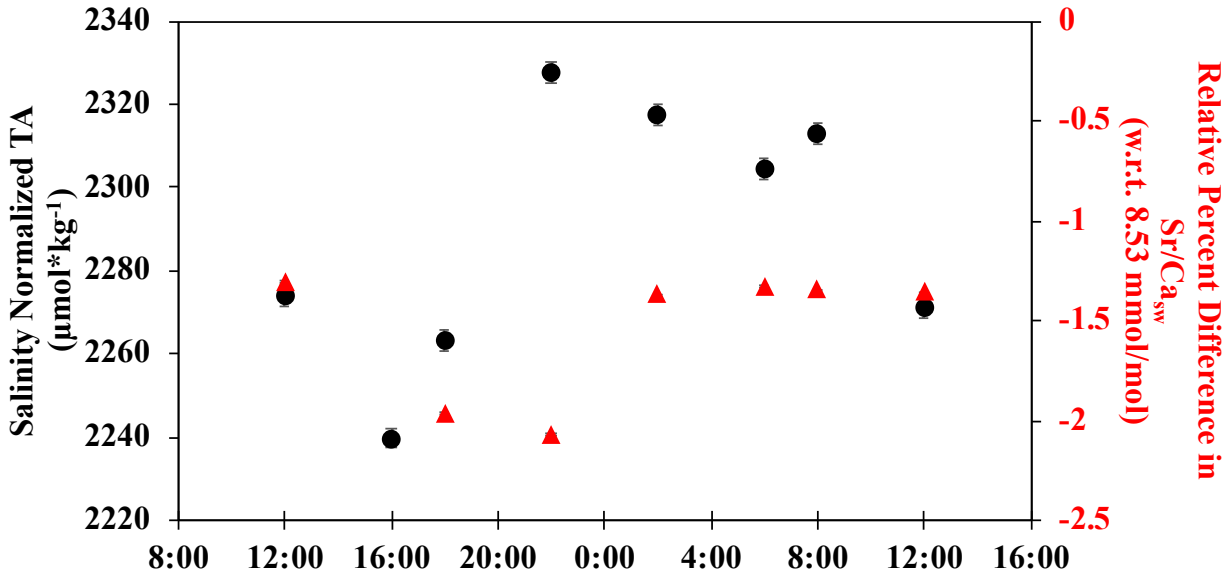

Figure 3.22. Diel measurements of salinity-normalized inverted Sr/Ca_{sw} values measured from Tetiaroa Atoll (March 2017, normalized to difference from open ocean seawater) indicate larger than predicted amplitudes of variability than that predicted from nTA. External error on individual $Sr/Ca_{sw} = \pm 0.11\%$

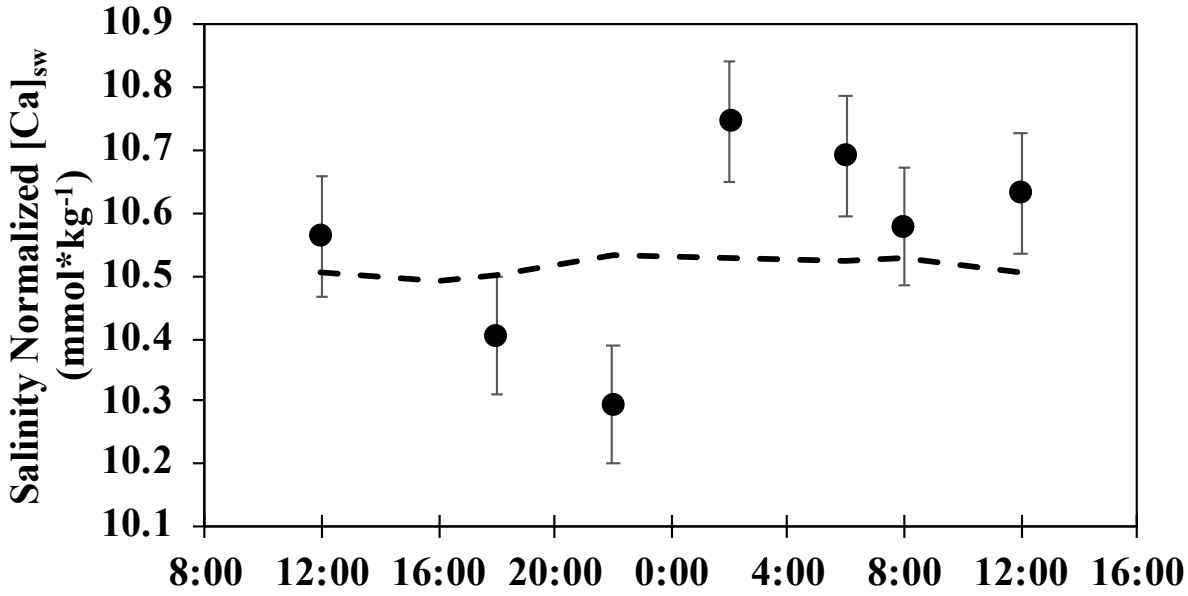

Figure 3.23. Diel variability in inverted $[Ca]_{sw}$ (black dots) shows patterns consistent with daily patterns in NEC; however, the amplitude of this variability exceeds that predicted from nTA variability (dashed line) by an order of magnitude. Error bars on $[Ca]_{sw} = \pm 0.9\%$ 1σ SD

external precision. Note – $[Ca]_{sw}$ may display ~5% accuracy error based on spike calibrations using JCp-1, a coral $CaCO_3$ standard.

3.3.5 *Rayleigh Implications for the Ecology of Coral Reef Ecosystems*

The observed diel trends in Sr/Ca_{sw} for both Tetiaroa and One Tree Island samples also allow for an application of the Rayleigh approach to isolating $K_{D\text{-}Net}$ detailed in *Section 3.1.2.* Applying Equations 3.10 – 3.13 to these samples implies partitioning behavior of Sr and Ca that is relatively consistent with the observed benthic coverage of calcifiers within each study location. When looking at the One Tree Island samples, the implied $K_{D\text{-}Net}$ value is 0.08 (Figure 3.24). Given the range of observed $K_{D\text{-}Sr}$ values reported in Table 3.1 as potential inputs into Equation 3.3, this observation implies 100% dominance of the study location by low-Mg calcite calcification/dissolution. As mentioned in *Section 3.2.3*, these One Tree Island samples were intentionally collected from a Perspex dome placed on top of a patch of the high-Mg calcite precipitating coralline alga *Porolithon onkodes*. Empirical studies of high-Mg calcite precipitating algae found values of $K_{D\text{-}Sr}$ ranging from 0.38 – 0.40 (Hetzinger et al., 2011), and it is not immediately clear why the inverted value is more similar to lower end of the scale of empirically-determined values of $K_{D\text{-}Sr}$ for calcite domination. However, due to tidal and logistical sampling constraints, only two samples were analyzed as part of the One Tree Island sample set – thus the ability to report statistics on this inverted $K_{D\text{-}Net}$ is limited. Furthermore, the magnitude of the relative observed daytime-nighttime differences in Sr/Ca_{sw} from One Tree Island is on the order of ~0.86%, which is slightly higher than the predicted value of 0.64% calculated from the numerical modeling exercise used to generate Figures 3.1 – 3.3 with the measured alkalinity deficit and $K_{D\text{-}Net} = 0.08$ as additional inputs (Table 3.7).

These findings imply (1) "leakiness" of the Perspex dome setup and significant influence of low-Mg calcite precipitation/dissolution on One Tree Island reef waters and/or (2) a $K_{D\text{-}Sr}$ value for *P. onkodes* that is << the 0.35 value assumed in *Section 3.1.2*. To this latter point, previous studies have investigated the extent to which crustose coralline algae like *P. onkodes* reprecipitate dolomite ($CaMg(CO_3)_2$), a more stable carbonate relative to calcite and aragonite, in the face of more acidic ocean conditions (Nash et al., 2011; Nash et al., 2013; Diaz-Pulido et al., 2014; Nash et al., 2015). If the organisms under the Perspex dome in One Tree Island were indeed building dolomitic skeletons, $K_{D\text{-}Sr}$ values could be expected to be on the order of 0.01 – 0.06 based on previous empirical measurements (Baker and Burns, 1985; Vahrenkamp and Swart, 1990). These values, though similar to the 0.08 value determined here, are also within the range of empirically-determined $K_{D\text{-}Sr}$ for low-Mg calcite organisms (Table 3.1). Without additional information (i.e. more sample points of Sr/Ca_{sw} and/or measurements of the molar Sr/Ca of benthic carbonates), conclusions about the ecological significance of the observed variability in the Sr/Ca_{sw} of One Tree Island samples cannot be drawn beyond the statement that trend in $K_{D\text{-}Sr}$ is consistent with dominance of calcifier communities with $K_{D\text{-}Sr} << 1$ – indicative of calcitic or dolomitic (rather than aragonitic) dominance of NEC fluxes.

The inverted $K_{D\text{-}Net}$ for Tetiaroa is 1.2 ± 0.04 (1σ SD of logarithmic regression slope), which is consistent with near 100% domination of calcification governed by aragonitic coral $K_{D\text{-}Sr}$ (Figure 3.25, Table 3.1). Notably, as mentioned in *Section 3.3.4*, the amplitude of daytime-nighttime variability in Sr/Ca_{sw} from Tetiaroa is roughly an order of magnitude higher than that predicted by the numerical modeling exercise used to generate Figures 3.1 – 3.3 with the measured alkalinity deficit and $K_{D\text{-}Net} = 1.2$ as additional inputs. Fortunately, in Rayleigh plots of $(Sr/Ca)_n/(Sr/Ca)_o$ vs Ca_n/Ca_o, increasing or decreasing the spread of Ca_n/Ca_o causes points to

move *along* the exponential regression curve without causing significant changes in the inverted $K_{D\text{-}Net}$. Said another way, scaling the Ca_n/Ca_o values such that the relative spacing between points is preserved but the overall axis spans an order of magnitude less range preserves the value of $K_{D\text{-}Net}$. This again is a result of using a double *mixed* spike to invert the molar Sr/Ca_{sw} ratio as an independent, more precise metric of seawater chemistry (Equation 3.23) compared to inversions of raw Ca or Sr concentrations alone (Equation 3.24).

In this context, it is also worth mentioning that the Rayleigh model approach outlined by Equations 3.10 – 3.13 *should* also be able to invert the same values for $K_{D\text{-}Net}$ with salinity-normalized $(Sr/TA)_n/(Sr/TA)_o$ and TA_n/TA_o ratios, since consumption of Sr and total alkalinity should covary with dissolution/precipitation of $CaCO_3$ (Steiner et al., 2014). However, when $K_{D\text{-}Net}$ is calculated in this way using One Tree Island data, the implied value is equal to -0.55, which is practically impossible given the constraints of potential values of K_D for polymorphs of $CaCO_3$ (Figure 3.26). With the full diel Tetiaroa data, this $K_{D\text{-}Net} = 0.977 \pm 0.9$, which, inclusive of error, spans the full range of calcite and aragonite components of the local calcifier community (Figure 3.27). Taken in tandem, these plots further highlight an apparent decoupling between $[Ca]_{sw}$, $[Sr]_{sw,}$ and total alkalinity within coral reef environments. Thus, though the Rayleigh method of resolving community calcifier dynamics in these environments does seem fruitful, I would indicate applying the method to Sr/Ca_{sw} variability (rather than Sr/TA_{sw} variability) at least for the sake of keeping the methods of analyte analysis internally consistent. As mentioned above, the degree to which the apparent observed temporal decoupling of $[Ca]_{sw}$, $[Sr]_{sw}$, and total alkalinity within coral reef environments is consistently observed and/or indicative of a novel biogeochemical process should be the subject of future investigations. Such

studies would greatly assist in reconciling the application of the Rayleigh approach to deciphering elemental partitioning within reef ecosystems.

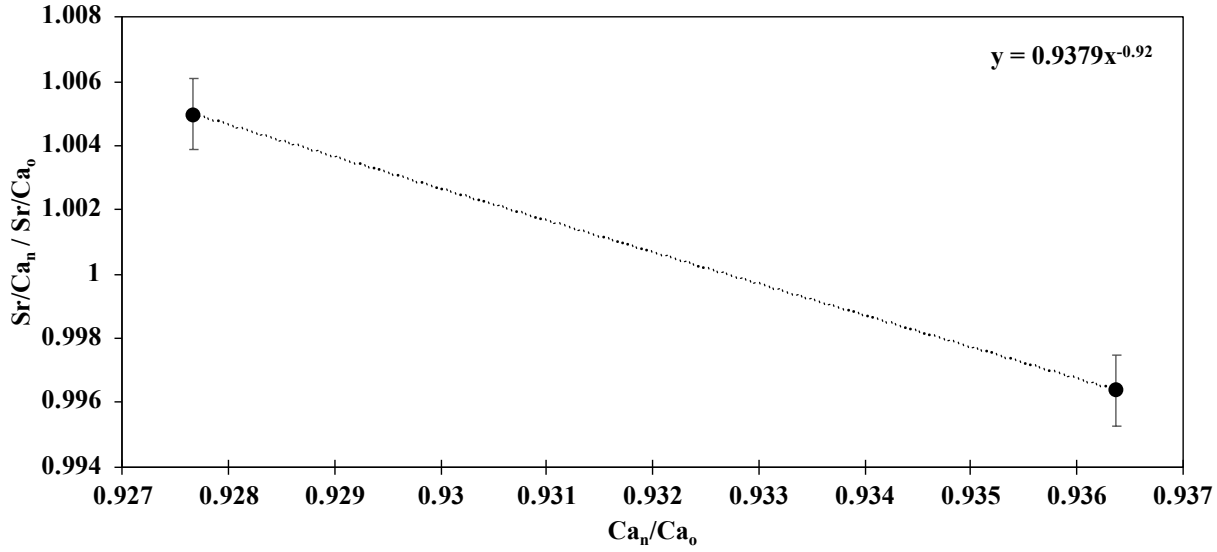

Figure 3.24. Rayleigh fractionation plot of the two One Tree Island samples collected from a crustose coralline algae dominated mesocosm implies Sr/Ca_{sw} partitioning consistent with 100% domination of NEC fluxes by low-Mg calcite values of $K_{D\text{-}Sr}$. $K_{D\text{-}Net} = 0.08$. In these plots, the relative Ca x-axis is calculated as follows: $Ca_n/Ca_o = (F_{Tot,\ Sample} / F_{Tot,\ Open\ Ocean}) * (V_{X,\ Open\ Ocean} / V_{S,\ Open\ Ocean}) * (V_{S,\ Sample} / V_{X,\ Sample})$. Error bars indicate propagated 1σ external SD on Sr/Ca_{sw} measurements.

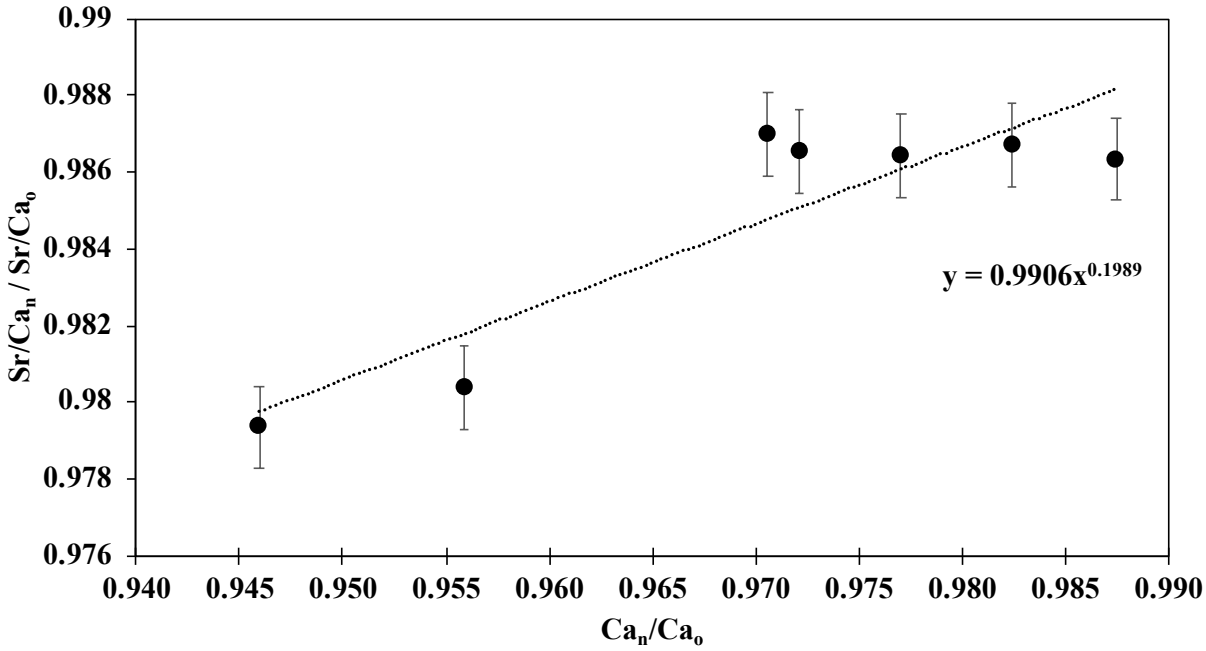

Figure 3.25. Rayleigh fractionation plot of the diel Tetiaroa Atoll reef flat samples implies Sr/Ca_{sw} partitioning consistent with near 100% domination of NEC fluxes by aragonite values of $K_{D\text{-}Sr}$. $K_{D\text{-}Net} = 1.20 \pm 0.04$ (1σ SD of logarithmic regression slope). In these plots, the relative Ca x-axis is calculated as follows: $Ca_n/Ca_o = (F_{Tot,\ Sample} / F_{Tot,\ Open\ Ocean}) * (V_{X,\ Open\ Ocean} / V_{S,\ Open\ Ocean}) * (V_{S,\ Sample} / V_{X,\ Sample})$. Error bars indicate propagated 1σ external SD on Sr/Ca_{sw} measurements.

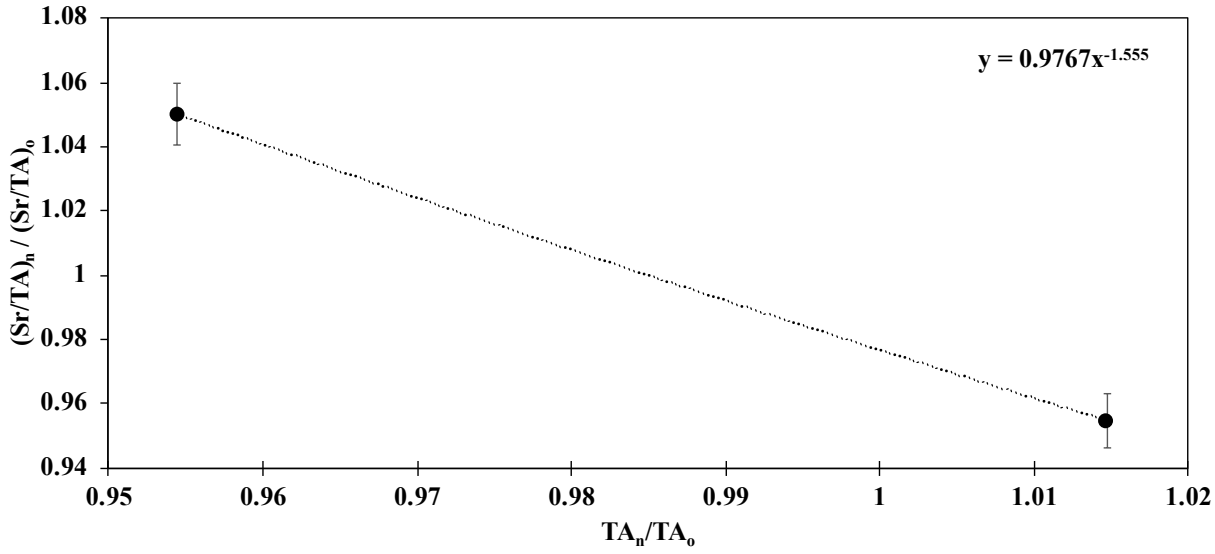

Figure 3.26. Compared to the Sr/Ca-based Rayleigh fractionation plot, a Sr/TA plot of the two One Tree Island samples collected from a crustose coralline algae dominated mesocosm

implies Sr/TA_{sw} partitioning that cannot be described with a two-member mixing model (Equation 3.13). $K_{D\text{-}Net}$ = -0.55. Error bars indicate propagated 1σ external SD on Sr/TA_{sw} measurements.

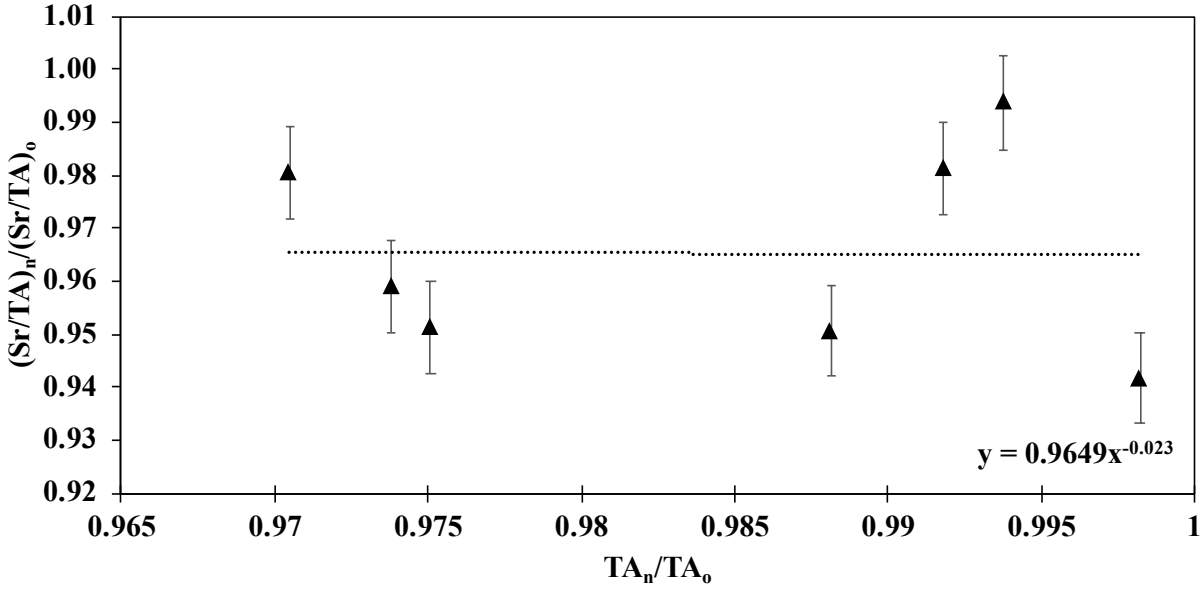

Figure 3.27. Compared to the Sr/Ca-based Rayleigh fractionation plot of the diel Tetiaroa Atoll reef flat samples, a Sr/TA plot implies Sr/TA_{sw} partitioning follows no coherent exponential fractionation relationship. $K_{D\text{-}Net}$ = 0.977 ± 0.9 (1σ SD of logarithmic regression slope). Error bars indicate propagated 1σ external SD on Sr/TA_{sw} measurements.

3.4 CONCLUSIONS

In this chapter, I outlined the fundamental principles that govern elemental Sr and Ca partitioning into $CaCO_3$ polymorphs within calcifying environments, such as coral reefs. I explored the implications of the magnitude of this partitioning in terms of the use Sr/Ca_{sw} as a tool to resolve differences in community calcifier composition within coral reef environments. With the knowledge that differences in Sr/Ca_{sw} could be on the order of 0.01 – 0.3% (1σ RSD from source seawater), I coupled isotope dilution (ID) double mixed spike (DMS) thermal ionization mass spectrometry (TIMS) to design a novel, high-precision (± 0.003% 1σ RSE Internal Error; ± 0.11% 1σ RSD, External Error; ± 0.03%, Replicate Error) method of

determining Sr/Ca_{sw}. This method also inverts the stable Ca ($\delta^{44/40}Ca$) and Sr ($\delta^{88/86}Sr$) composition of seawater samples at high precision (± 0.09% for Ca; ± 0.03% for Sr – 1σ RSD, External Error). I applied this method to samples of Sr/Ca_{sw}, collected over a diel cycle from two separate coral reef locations, and report the first dataset that captures the temporal evolution of Sr/Ca_{sw} (up to a 2% relative offset from open ocean source waters with a 0.5% diel signal amplitude) within these dynamic environments. To further explore the ecological significance of the observed Sr/Ca_{sw} variability, I derived and applied a single box, Rayleigh distillation model to calculate net community partition coefficients ($K_{D\text{-}Net}$) for measured Sr/Ca ratios from both sampling locations. While promising and internally consistent, this method reveals a potential decoupling between the magnitude of observed variability in Sr/Ca_{sw} and total alkalinity within coral reef environments that should be further investigated and/or reconciled.

To this end, the established 0.11% RSD external precision and 0.01% replicate error of the method developed in this chapter highlights the potential value added by sampling for Sr/Ca_{sw} and/or $[Ca]_{sw}$ to studies of net ecosystem calcification within reefs and other calcifying environments. To the extent that constraints on analytical and instrumental uncertainties will allow, variability in Sr/Ca_{sw} within a single reef ecosystem over a diel cycle may provide additional insights on instantaneous hourly fluxes of alkalinity due to calcification/dissolution of aragonitic vs calcitic organisms. Based on the results presented here, the method developed here will work best when applied to ecosystems with a large (≥ 60 $\mu mol*kg^{-1}$) temporal or spatial variability signal in salinity-normalized TA *and* empirically-determined endmember values of $K_{D\text{-}Sr}$ for local benthic carbonates. In addition to facilitating the calculation of daily calcification budgets from a community perspective, the level of detail provided by the Sr/Ca_{sw} proxy could also be used to reveal community-level nuances associated with the daily timing of carbonate

dissolution in the broader context of daily biogeochemical variability in reef pH, pCO_2, and Ω. Overall, this method allows for the assessment of spatiotemporal variability in a non-conservative geochemical ratio and further development of Sr/Ca_{sw} as a proxy for determining changes in community calcifier regimes on reefs, particularly under increasing environmental stressors like ocean acidification.

Chapter 4. $\Delta^{13}C_{DIC}$ IS A POTENTIAL INDICATOR OF ORGANIC MATTER FRACTIONATION AND PHOTOSYNTHETIC PLASTICITY WITHIN CORAL REEF ECOSYSTEMS

4.1 INTRODUCTION

Numerous studies have proposed that as environmental stressors (such as warming, ocean acidification, pollution, etc.) increase in reef environments, a pronounced shift from precipitation to dissolution of calcium carbonate ($CaCO_3$) substrates will induce the collapse of habitat-forming coral structures and lead to dominance of macroalgae (Fabricius et al., 2011; Andersson and Gledhill, 2013; Enochs et al., 2015; Agostini et al., 2018; Contreras-Silva et al., 2020). Such a trophic "phase" transition could have dramatic consequences for the biodiversity currently supported by these marine rainforests; therefore, novel forensic and analytical tools that complement traditional measurements of net ecosystem productivity (NEP) and calcification (NEC) and serve as leading indicators of trophic "phase" shifts within and between reef ecosystems are greatly needed. Such tools will be essential in capturing the nuanced, community-level biogeochemical fingerprints necessary to monitor, quantify, and mitigate the rate of detrimental impacts on coral reef ecosystems around the world.

To this end, the diversity of the macroalgal community that replaces corals in many ecosystems is itself hypothesized to be a function of the impacts of environmental stressors on ambient seawater chemistry. Although the direct diffusion of atmospheric CO_2 into cells drives photosynthesis for terrestrial plants, the natural buffering capacity of modern day seawater due to the high abundance of bicarbonate (HCO_3^-) ions translates to a diversity of observed carbon concentrating mechanisms (CCMs) amongst algae in the modern ocean (Raven, 1997; Raven et al., 2002; Falkowski and Raven, 2007; Hepburn et al., 2011; Carvalho et al., 2015; Cornwall et al., 2017). In organisms with CCMs, aqueous CO_2 can diffuse into cells and be converted to organic carbon *or* dissolved inorganic carbon (DIC, primarily HCO_3^-) can pass into cells and internally converted to CO_2 before being converted to organic carbon. A more nuanced characteristic of the coral-to-macroalgae "phase" transition for reefs, based on these works, is the idea that the diversity of the benthic macroalgae community will decline to favor a handful of species that exhibit flexible CCMs with affinities for CO_2 (Hepburn et al., 2011; Cornwall et al., 2017). In other words, modern reef ecosystems that average relatively alkaline pHs and low pCO_2 values can sustain a larger proportion of algal species that primarily rely on HCO_3^- for photosynthetic metabolism. However, increasing ambient seawater pCO_2 and decreasing pH from continued ocean acidification could lead to competition and benthic dominance of macroalgal species that prefer direct CO_2 assimilation.

A geochemical proxy that responds not only to the magnitude of productivity (NEP) but also to the diversity of algal inorganic carbon physiologies in a quantitative manner would provide a more informed and complementary record to observational transects and surveys of the benthic community in reefs. Additionally, macroalgae species in modern reefs can form mat-like turfs that cling to rocks, corals, and other benthic substrates *or* canopies of fleshy tissue that

could serve a habitat function for reef-dwelling organisms. Therefore, a method of identifying and tracking the dominant photosynthetic physiology of a reef ecosystem in conjunction with monitoring the relative abundances of turf and canopy-forming macroalgae would be impactful in investigations of the habitat suitability and function of future reef ecosystems. Such a method is particularly topical, since many algal species recently investigated in studies of benthic coverage on reefs are turf-forming and are hypothesized to have CCMs with high affinities for CO_2 (Hall-Spencer et al., 2008; Maliao et al., 2008; Hepburn et al., 2011; Cornwall et al., 2017; Stanca and Parsons, 2017).

The stable carbon isotope composition of DIC ($\delta^{13}C_{DIC}$) has the potential to make transformative progress towards a comprehensive productivity and community composition proxy in reef ecosystems. Early observational studies of the diel evolution of $\delta^{13}C_{DIC}$ in reef ecosystems noted up to a 2‰ magnitude shift between daytime and nighttime values (Weber and Woodhead, 1971). This variability is particularly significant in the context of a similar range of variability (-1 – 2‰) observed for the spatial distribution of $\delta^{13}C_{DIC}$ throughout the global ocean (Kroopnick, 1985). The source of the diel signal in reefs has largely been attributed to various community-level fractionation factors that are imparted onto surrounding seawater from processes of marine metabolism (productivity and calcification) and end-member mixing (Weber and Woodhead, 1971; Swart et al., 2005; Carvalho et al., 2015). The guiding motivation for many of these attribution studies has been a better understanding of the uses, limitations, and interpretations of $\delta^{13}C$ variability in biogenic carbonates from reefs as paleoenvironmental proxies (McConnaughey, 1989a; McConnaughey, 1989b; Swart et al., 1996; Sun et al., 2008; Swart et al., 2010; Dassié et al., 2013). However, less attention has been given toward how the smaller scale variability in $\delta^{13}C_{DIC}$ could serve as a biogeochemical indicator of ecosystem

transitions under current and future environmental stressors, such as ocean acidification and warming. Carvalho et al. (2015) is the first study to incorporate knowledge of variable inorganic carbon physiologies amongst primary producers to translate diel variability of $\delta^{13}C_{DIC}$ within coral reefs to variability in the integrated community fractionation factors (ε_{org}) associated with organic matter synthesis from ambient DIC. In this study, the authors explored a mixing model of carbon isotope fractionation processes associated with diffusive CO_2 uptake, facilitated diffusion of HCO_3^-, and active transport of HCO_3^- to establish analytical "floors" and "ceilings" of observed values of community ε_{org}. Koweek et al. (2019) further expanded on this ability to isolate ε_{org} from carbonate chemistry measurements on coral reefs and indicate that this factor *spatially* tracks differences between calcifier and macroalgae benthic coverage. Further studies of *temporal* variability in ε_{org} in relation to ambient carbonate chemistry within and between coral reef environments would elucidate the degree to which this factor may act as a leading indicator of benthic photosynthetic community composition and photosynthetic plasticity in a rapidly acidifying ocean.

In this chapter, I report diel variability in seawater $\delta^{13}C_{DIC}$, DIC, and total alkalinity (TA) on Tetiaroa Atoll, French Polynesia from two separate diel field campaigns in 2016 and 2017. I then use an analytical model framework to decompose the measured biogeochemical variability from each diel field campaign into steady-state estimates of empirically-determined community ε_{org}. I use this model to investigate the potential sources of observed temporal variability in values of ε_{org} between diel field campaigns, particularly with regard to the composition and physiological behaviors of the benthic photosynthetic community. Lastly, I comment on the application of tandem discrete measurements of carbonate chemistry and stable carbon isotopes

in other reef locations to develop and calibrate ε_{org} as a geochemical indicator of shifts in community productivity dynamics in reefs under stress.

4.2 METHODS

4.2.1 *Study Site*

Sampling campaigns were conducted in January 2016 and March 2017 from the reef flat of Motu Onetahi, Tetiaroa Atoll, French Polynesia (17.0ºS, 149.5ºW, Figure 2.2). See *2.2.1. Study Site* for more information about the sampling location. Recent evaluations of benthic coverage at the 10 meter isobath on Tetiaroa indicate the atoll's reefs are ≥ 80% crustose coralline algae, algal turf, and bare carbonate sands (CTB) and ~ 10% large macroalgae (Edmunds et al., 2016). Algal coverage near the sampling site could vary seasonally due to local nutrient inputs.

4.2.2 *Sampling*

During each field campaign, samples for DIC, TA, and $\delta^{13}C_{DIC}$ analyses were collected at a frequency of 2 hours for a duration of 24-36 hours using hand-triggered Niskin bottles. Carbonate chemistry sampling followed the standard operating procedures of Dickson et al. (2007). Briefly, samples were transferred from the Niskin bottle without exposure to the atmosphere into two separate 300 mL borosilicate glass BOD bottles. One bottle sample was used for DIC and TA analyses, while the other was subjected to $\delta^{13}C_{DIC}$ analysis. All water samples were poisoned onsite with 150 µL of a saturated solution of the biocide mercuric chloride ($HgCl_2$) and stoppered with greased glass caps for later offsite analyses. Temperature (± 0.005ºC) and salinity (± 0.005) at the sampling site were obtained for each diel cycle at 15-30 minute resolution using an SBE 16plus V2 SeaCAT CTD Recorder.

4.2.3 *DIC and TA Analyses*

Analyses of DIC and TA followed the methods and errors reported in *2.2.3. DIC and TA Analyses*.

4.2.4 *$\delta^{13}C_{DIC}$ Analyses*

Due to logistical constraints, only four samples from each diel cycle, inclusive of pre-dusk and pre-dawn chemical conditions on the reef flat, were analyzed as part of this study. For each sample, the $^{13}C/^{12}C$ ratio of DIC (in the form of CO_2) extracted from the seawater was measured via mass spectrometry according to the procedure described in Quay et al. (1992). The $^{13}C/^{12}C$ ratio of any sample is expressed in del (δ) notation in per mil (‰) units relative to a standard (Equation 4.1):

$$\delta^{13}C\ (‰) = \left(\frac{\left[\frac{^{13}C}{^{12}C} \right]_{Sample}}{\left[\frac{^{13}C}{^{12}C} \right]_{Standard}} - 1 \right) * 1000 \quad (4.1)$$

All values of $\delta^{13}C_{DIC}$ are calculated with reference to Vienna Pee Dee Belemnite (VPDB), which is defined to have a $\delta^{13}C$ value equal to 0 and an absolute $^{13}C/^{12}C$ ratio equal to 0.0112372 (Allison et al., 1995). The reproducibility of all $\delta^{13}C_{DIC}$ values based on replicate internal seawater standard measurements is ±0.1‰.

4.2.5 *Modeling Approach to Isolating ε_{org}*

Decomposing discrete temporal variability of DIC, TA, and $\delta^{13}C_{DIC}$ into values of net community ε_{org} requires a biogeochemical modeling framework. In Chapter 2, I explored three different model geometries to decompose chemical measurements into metabolic fluxes of NEP and NEC: a single box model, a non-dispersive flow model, and an Eulerian inverse model

(Bolden et al., 2019). The results indicate that, inclusive of analytical and instrumental uncertainties, these different biogeochemical model topologies yield similar estimates of metabolism on the reef flat of this location. I therefore proceed with designing a simple algebraic modeling approach to isolating ε_{org} by treating Tetiaroa's reef flat as a single, well-mixed box.

In this model, the governing differential equations for the time rate of change evolution of DIC and TA concentrations on the reef are similar to Equations 2.1 and 2.2; however, because of the importance of isolating the pure, photosynthetic fractionation of organic matter in this study, these equations have been modified and expanded to incorporate the influences of *gross* productivity/calcification (GPP/GCC) and net respiration/dissolution (NR/ND, Equations 4.2 – 4.3):

$$\frac{d[DIC]}{dt} = \frac{1}{\tau}([DIC]_{sw} - [DIC]_M) + \frac{GPP_{DIC}}{z\rho} + \frac{NR_{DIC}}{z\rho} + \frac{GCC_{DIC}}{z\rho} + \frac{ND_{DIC}}{z\rho} + \frac{k_{CO2}}{z}([CO_2]_{sat} - [CO_2]_M) \quad (4.2)$$

$$\frac{d[TA]}{dt} = \frac{1}{\tau}([TA]_{sw} - [TA]_M) + 2\frac{GCC_{DIC}}{z\rho} + 2\frac{ND_{DIC}}{z\rho} \quad (4.3)$$

The quantities $[DIC]_M$ and $[TA]_M$ represent the measured values of DIC and TA for any given sample. The values of $[DIC]_{sw}$ and $[TA]_{sw}$, 1978 µmol/kg DIC and 2332 µmol/kg TA, represent the concentrations of DIC and TA of open ocean seawater that is advected onto the reef through swell and wind-driven waves over a characteristic residence time (τ, in hours) and is set by our direct sampling of nearby offshore waters along with data from the CLIVAR Repeat Section P16 hydrography cruises (Talley et al., 2015; Cross et al., 2017). Repeat occupations of this region indicate seasonal variability in offshore DIC and TA on the order of ±12 and ±17 µmol/kg, respectively (Feely et al., 2006). NEP and NEC are the area-normalized fluxes of carbon (in $\mu mol*m^{-2}*hr^{-1}$) due to productivity and calcification, respectively. The parameter z is the ratio of the box volume to the benthic surface area and is effectively equivalent to the average depth of

the box, which is set to 1 m. The term ρ is an assumed average seawater density of 1025 kg/m^3. Actual densities at the field location ranged between 1022 – 1024 kg/m^3. Air/sea gas exchange of CO_2 influences DIC concentrations and follows a gas-specific piston velocity, k_{CO2}, in m*hr^{-1}. However, I actually assume this component of Equation 4.2 is negligible based on previously observed hourly gas exchange fluxes on Tetiaroa being up to 2 orders of magnitude lower than simultaneous fluxes of productivity, calcification, and advection (Bolden et al., 2019). I further use our calculated hourly pCO_2 values as inputs in an empirical relationship between carbonate sediment dissolution rate and pCO_2, determined by Cyronak et al. (2013) for Heron Island in the Great Barrier Reef. With this relationship, I conclude that fluxes of DIC and TA due to dissolution are often 1% or less of the gross calcification fluxes (see Supplementary Materials). I therefore redefine Equations 4.2 – 4.3 as (Equation 4.2a – 4.3a):

$$\frac{d[DIC]}{dt} = \frac{1}{\tau}([DIC]_{sw} - [DIC]_M) + \frac{GPP_{DIC}}{z\rho} + \frac{NR_{DIC}}{z\rho} + \frac{GCC_{DIC}}{z\rho} \quad (4.2a)$$

$$\frac{d[TA]}{dt} = \frac{1}{\tau}([TA]_{sw} - [TA]_M) + 2\frac{GCC_{DIC}}{z\rho} \quad (4.3a)$$

Similarly, the time evolution of the ^{13}C component of DIC can be estimated by expanding Equation 4.2a to account for the stable carbon isotope fractionation factors associated with productivity and calcification as well as the $^{13}C/^{12}C$ ratio of open ocean seawater (Equation 4.4):

$$\frac{d[DIC,13C]}{dt} = \frac{1}{\tau}\left(\frac{R_s[DIC]_{sw}}{R_s+1} - \frac{R_m[DIC]_M}{R_m+1}\right) + \frac{GPP_{DIC}}{z\rho}\left(\frac{R_m\alpha_{org}}{R_m\alpha_{org}+1}\right) + \frac{NR_{DIC}}{z\rho}\left(\frac{R_{org}}{R_{org}+1}\right) + \frac{GCC_{DIC}}{z\rho}\left(\frac{R_m\alpha_{calc}}{R_m\alpha_{calc}+1}\right) \quad (4.4)$$

R_m is equal to the $^{13}C/^{12}C$ ratio of any measured sample. R_s is defined as the $^{13}C/^{12}C$ ratio of open ocean seawater DIC advected onto the reef and is estimated to be 0.01125237 (1.35‰) from measurements of surface waters in the region collected during the 2013 GEOTRACES EPZT cruise (Quay, 2017). R_{org} is the mean $^{13}C/^{12}C$ ratio of organic matter that is produced/respired on

the reef flat and is estimated from the intercept of the regression line between measured $\delta^{13}C_{DIC}$ and $1/[DIC]_M$ for each diel cycle (Keeling et al., 1980; Karlsson et al., 2007; Carvalho et al., 2015). α_{org} is defined as the fractionation factor between organic matter and DIC that is imparted onto DIC during photosynthesis and should reflect the dominant inorganic carbon physiology being used by primary producers (Equation 4.5):

$$\alpha_{org} = \frac{\left[\frac{^{13}C}{^{12}C}_{Organic}\right]}{\left[\frac{^{13}C}{^{12}C}_{DIC}\right]} \quad (4.5)$$

Similarly, α_{calc} is defined as the fractionation factor between inorganic $CaCO_3$ and DIC that is imparted onto DIC during calcification. Recall, in isotope systems, ε values are per mil transformations of α values (Equation 4.6):

$$\varepsilon_{org}\ or\ \varepsilon_{calc}(‰) = 1000\left(\alpha_{org}\ or\ \alpha_{calc}\ - 1\right) \quad (4.6)$$

Discretely sampling DIC, TA, and $\delta^{13}C_{DIC}$ at frequency of 2 hours over diel cycles allows us to sufficiently characterize the periodic biogeochemical "heartbeat" of the reef ecosystem (Shamberger et al., 2011; Hofmann et al., 2011; Koweek, Dunbar, Monismith, et al., 2015; Koweek, Dunbar, Rogers, et al., 2015; Gruber et al., 2017; Cyronak et al., 2018; Bolden et al., 2019). That is, at this sampling frequency, I expect that our measurements span relative maxima and minima in all measured constituents. This method allows us to apply a steady-state assumption (d[DIC]/dt = d[DIC, 13C]/dt = d[TA]/dt = 0) to combine Equations 4.2a, 4.3, and 4.4 for measurements taken at relative minima and maxima over a diel cycle and also eliminate the influences of GCC. I make a further assumption that the abundance of ^{13}C in DIC is approximately equal to R_m because $R_m <<< 1$ (Equation 4.7):

$$\frac{R_m}{R_m+1} \approx R_m \quad (4.7)$$

Together, these assumptions allow us to construct an equation to solve for steady-state (dusk and dawn) community diel α_{org} (and by extension, ε_{org}) in the sample datasets (Equation 4.8):

$$0 = \frac{1}{\tau}\left(\frac{R_s[DIC]_{sw}}{R_s+1} - \frac{R_m[DIC]_M}{R_m+1}\right) + \frac{GPP_{DIC}}{z\rho}\left(\frac{R_m\alpha_{org}}{R_m\alpha_{org}+1}\right) + \frac{NR_{DIC}}{z\rho}\left(\frac{R_{org}}{R_{org}+1}\right) - \frac{1}{2\tau}([TA]_{sw} - [TA]_M)\left(\frac{R_m\alpha_{calc}}{R_m\alpha_{calc}+1}\right) \quad (4.8)$$

Dusk and dawn values for hourly GPP_{DIC} and NR_{DIC} were estimated using the single box modeling framework and residence times derived using the salinity-anomaly method detailed in Chapter 2 and Bolden et al. (2019). Using these methods, I estimate residence times (τ) of 11.5 hours for the January 2016 field campaign and 5.8 hours for the March 2017 field campaign. NR_{DIC} fluxes were calculated as the average residual between total d[DIC]/dt and advective plus calcification fluxes during nighttime hours (~18:00 to ~06:00 local time). I further assumed that this average respiratory flux applied during daytime hours, allowing us to solve for hourly GPP_{DIC} as the residual between total d[DIC]/dt and advective, calcification, and respiratory fluxes during daytime hours (~06:00 to ~18:00 local time).

Measured and source water values of DIC and TA, Keeling plot-determined R_{org}, and the $^{13}C/^{12}C$ ratio, GPP_{DIC}, and NR_{DIC} at times of implied steady-state behavior are used as inputs into a MATLAB optimization function (fminsearchbnd, a version of fminsearch that allows the user to specify bounds on output) that iteratively solves for the value of α_{org} and α_{calc} by minimizing the sum of the square of the residuals between measured values of R_s/R_m and those calculated within the function itself (D'Errico, 2020). This optimization is inclusive of a Monte Carlo simulation of 10,000 iterations that explore the impacts of analytical errors associated with measurements of DIC, TA, $\delta^{13}C_{DIC}$, and the Keeling plot intercept. Additionally, while I allow the optimization function to explore infinite bounds for isolating α_{org}, I acknowledge the large

body of literature that seeks to investigate kinetic and equilibrium fractionation mechanisms during calcification within biogenic carbonates (Swart, 1983; McConnaughey, 1989a; McConnaughey, 1989b; McConnaughey, 2003; Sun et al., 2008). To this end, I explored the range $0.985 \leq \alpha_{calc} \leq 1.003$ during the optimization.

4.3 RESULTS

4.3.1 *Diel Trends in Carbonate Chemistry and $\delta^{13}C_{DIC}$*

Data for diel variability in DIC and TA for the March 2017 field campaign has been discussed in Chapter 2 and Bolden et al. (2019). I expand this dataset with the addition of the January 2016 field campaign and the analyses of stable carbon isotopes. DIC and TA data from the January 2016 field campaign shows similar characteristics to the diel cycles presented in Chapter 2, where minima are observed in the late afternoon (near dusk) and maxima are observed in the early morning (near dawn, Figure 4.1). This variability is consistent with the influences of daytime net photosynthesis sequestering CO_2 into organic carbon, light-enhanced precipitation of $CaCO_3$, and nighttime net respiration consuming organic carbon and producing CO_2. The amplitude of the diel cycle in DIC and TA are similar between the January 2016 and March 2017 field campaigns, averaging ~180 µmol/kg (DIC) and ~110 µmol/kg (TA). The differences within each campaign dataset could be attributed to error in residence time constraints and/or differences in daily or seasonal productivity due to insolation, cloud coverage, etc.

Hourly measurements of $\delta^{13}C_{DIC}$ across all diel field campaigns indicate up to a 2‰ range of values over a diel cycle (Figure 4.1). This observation is consistent with previously published values of $\delta^{13}C_{DIC}$ from coral reefs and is again significant given the -1 – 2‰ spatial range of variability observed across the global surface ocean (Weber and Woodhead, 1971;

Kroopnick, 1985; Swart et al., 2005; Carvalho et al., 2015). Furthermore, this diel variability in $\delta^{13}C_{DIC}$ is inversely related to variability in TA and DIC. This pattern implies $\delta^{13}C_{DIC}$ reaches a relative maximum over a diel cycle near dusk (when DIC and TA are at their lowest), while a relative minimum is reached near dawn (when DIC and TA are at their highest). Given the relative diel magnitudes of diel DIC versus TA, I hypothesize that productivity (rather than calcification) is the dominant metabolic process driving diel cycles in carbonate chemistry on the Tetiaroa reef flat (Bolden et al., 2019). That being the case, I indicate that the observed inverse relationship between $\delta^{13}C_{DIC}$ and DIC is a result of the strong carbon isotope discriminations associated with photosynthesis (rather than calcification) on the reef flat (Raven et al., 1994; Raven, 1997; Raven et al., 2002; Hepburn et al., 2011). More detailed discussion of these isotope fractionation pathways can be found in Section 4.4.1.

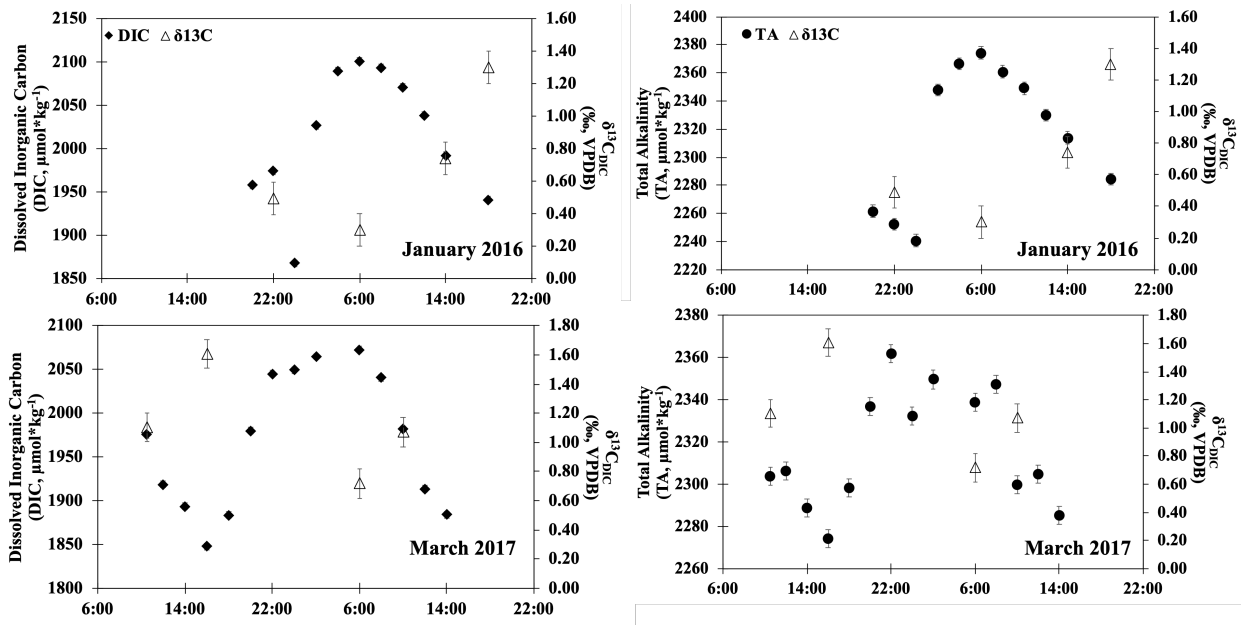

Figure 4.1. Diel variability in DIC, TA and $\delta^{13}C_{DIC}$ for January 2016 (top row) and March 2017 (bottom row). DIC and TA are tightly coupled across all sampling campaigns, indicative of the impact of carbonate precipitation/dissolution on the local carbonate system. TA also appears to be influenced by light-enhanced calcification during the day across both diel cycles. DIC and TA show an inversely related diel pattern with $\delta^{13}C_{DIC}$.

4.3.2 *Keeling Plots*

Keeling plots were generated using the four measurements of $\delta^{13}C_{DIC}$ and their corresponding measurements of DIC during each field campaign (Figure 4.2). Recall, on these plots, the y-intercept of the regression line between measured seawater $\delta^{13}C_{DIC}$ and $1/[DIC]_M$ is equal to the mean $\delta^{13}C$ value of the organic matter contributing to any observed variability in $\delta^{13}C_{DIC}$. Regression statistics on the Keeling plots generated from this dataset indicate a mean $\delta^{13}C_{organic}$ = -9.0 ± 4.5‰ for January 2016 and -6.0 ± 0.3‰ for March 2017. These values and their associated errors were converted into raw $^{13}C/^{12}C$ ratios using the absolute ratio of VPDB; they were further used as inputs into the numerical inversion and error exploration detailed in *4.2.5 Modeling Approach to Isolating* ε_{org}.

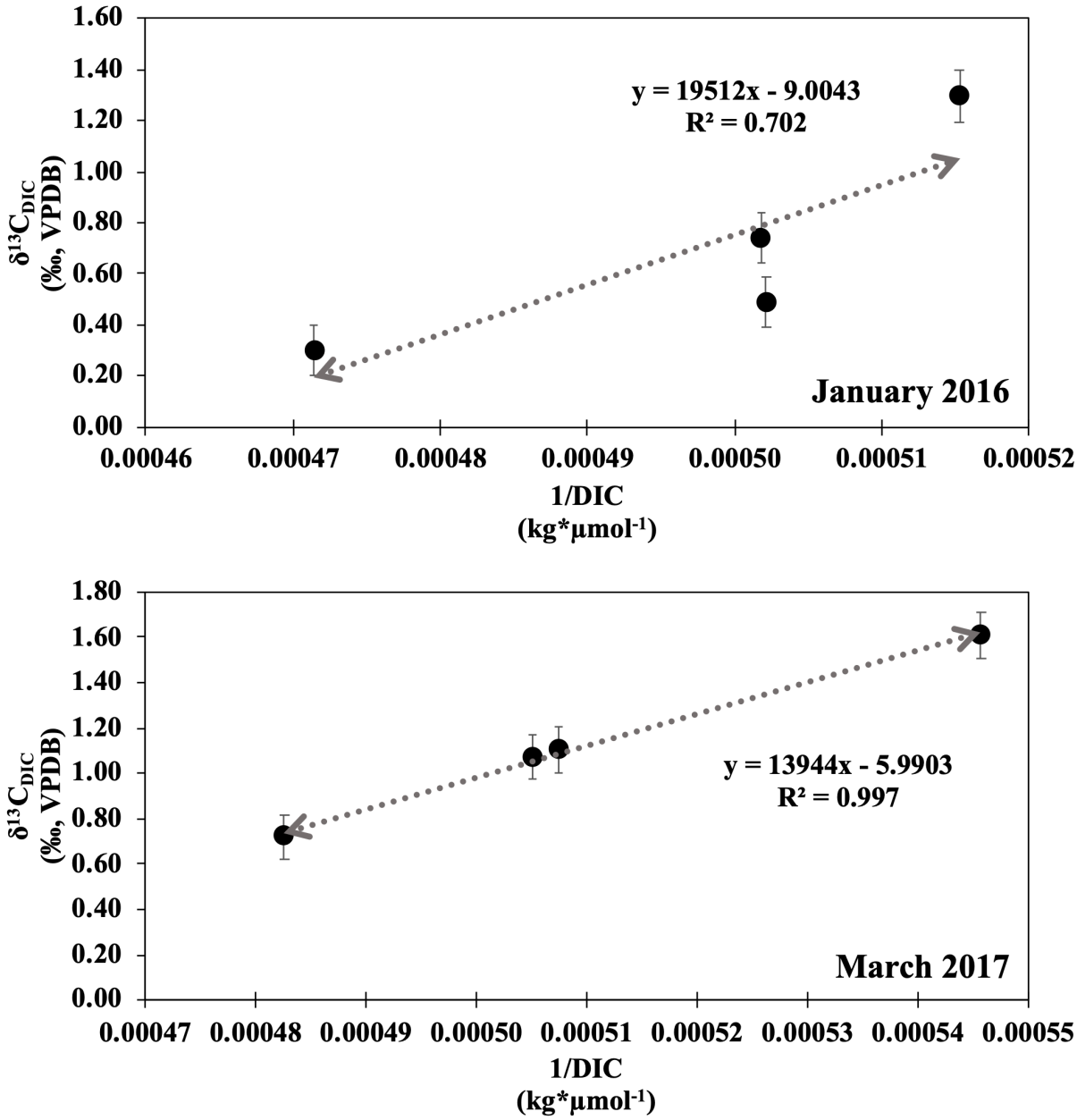

Figure 4.2. Keeling plots for January 2016 (top) and March 2017 (bottom) built using measured DIC and stable isotope data from Tetiaroa. Black dots are individual measurements and gray stippled lines are linear regression fits. Error bars indicate the long-term precision in $\delta^{13}C_{DIC}$ measurements (0.1‰).

4.3.3 *Variability in Steady-State ε_{org} and ε_{calc}*

Steady-state values for ε_{org} and ε_{calc} were effectively optimized for the mid-afternoon and early-morning samples of the January 2016 and March 2017 campaign datasets. Inclusive of the analytical errors and Monte Carlo simulations detailed in Section 4.2.5, these values ranged from $-8.6 \pm 0.6‰ \leq$ Steady State $\varepsilon_{org} \leq -4.1 \pm 5.9‰$ and $-7.5 \pm 2.2‰ \leq$ Steady State $\varepsilon_{calc} \leq 1.6 \pm 0.7‰$ (Table 4.1). Despite the larger error envelopes in inverted ε values observed in the January 2016 dataset, hourly steady-state values of ε_{org} indicate lower (more negative) values occur near dawn and more positive values occur near dusk (Table 4.1). Optimized values for steady state ε_{calc} span a larger range, and inclusive of error, no trends can be observed *between* datasets. *Within* the March 2017 campaign (which has tighter error on inverted values of ε_{calc}), the more positive value is observed near dusk, while the lower value occurs near dawn. It is worth stating that our small sample size of inverted values of ε_{org} and ε_{calc} (n = 4 for both) may limit our interpretations of any observed differences between dusk-dawn values of these fractionation factors.

Table 4.1. Summary of diel ranges of measured constituents and steady-state hourly community ε_{org} and ε_{calc} values for the field campaigns conducted on Tetiaroa Atoll. Recall, analytical errors on all reported DIC measurements is 3.7 µmol*kg^{-1} (2σ std. dev.), error on TA measurements is 4.3 µmol*kg^{-1} (2σ std. dev.), and error on $\delta^{13}C_{DIC}$ measurements is 0.1‰ (1σ std. dev.). pH and pCO_2 data were calculated using measured values of DIC and TA as inputs into CO2SYS v2.1 for Microsoft Excel. Errors (1σ std. dev.) on calculated values of ε are presented alongside each estimate and include the impacts of a Monte Carlo error propagation of 10,000 iterations utilizing the analytical uncertainties on DIC, TA, and $\delta^{13}C_{DIC}$.

	January 2016	March 2017
Diel Range in DIC (µmol*kg^{-1})	1867 – 2101	1848 – 2072
Mean Diel DIC (µmol*kg^{-1})	2028	1979
Diel Range in TA (µmol*kg^{-1})	2240 – 2374	2274 – 2362
Mean Diel TA (µmol*kg^{-1})	2316	2319
Diel Range in $\delta^{13}C_{DIC}$ (‰)	0.30 – 1.30	0.72 – 1.61
Diel Range in pCO_2 (µatm)	325 – 546	287 – 566
Mean Diel pCO_2 (µatm)	470	426
Diel Range in pH	7.927 – 8.087	7.918 – 8.139
Mean Diel pH	7.977	8.029
Dawn Community ε_{org} (‰)	-6.5 ± 6.1	-8.6 ± 0.5
Dusk Community ε_{org} (‰)	-4.1 ± 5.9	-6.5 ± 0.5
Dawn Community ε_{calc} (‰)	1.6 ± 1.8	-7.5 ± 2.2
Dusk Community ε_{calc} (‰)	-1.9 ± 3.5	1.6 ± 0.7

4.4 DISCUSSION

4.4.1 *Interpreting Diel Variability in $\delta^{13}C_{DIC}$*

$\delta^{13}C_{DIC}$ on coral reefs is hypothesized to evolve as a function of the rates of NEP, NEC, and mixing between water parcels as well as the α or ε values associated with each of those processes (Weber and Woodhead, 1971; Swart et al., 2005; Carvalho et al., 2015). The largest of these fractionation factors is the α_{org} associated with RuBisCO-driven photosynthesis, which results in the $\delta^{13}C$ of organic matter produced during primary productivity to be isotopically depleted (relative to surrounding seawater) by ~30‰ ($\alpha_{RuBisCO} \cong 1.030$; Raven et al., 1994). Note – RuBisCO fractionation of stable carbon isotopes has been shown to vary across a variety of photosynthetic taxa (particularly within species of cyanobacteria, Table 4.2). Here, I assume an average $\alpha_{RuBisCO}$ value of 1.030 based on the previous observation that eukaryotic algae and bryophytes have similar RuBisCO fractionation factors as flowering plants (such as spinach; $\alpha_{RuBisCO} \cong 1.029 – 1.030$, Guy et al., 1993; Raven et al., 1994). Additionally, observations of the $\delta^{13}C$ of a variety of marine primary producers implies a large range of variability from seawater DIC ($-35‰ \leq \delta^{13}C_{tissue} \leq -3‰$), with both "leaky," non-quantitative fixation of inorganic carbon and the existence of CCM pathways that fix organic carbon using HCO_3^- and CO_2 suggested as intricate mechanisms driving this scatter (Raven et al., 2002). As mentioned in Section 4.2.5, there is much ongoing discussion on the magnitude of stable carbon isotope fractionation that occurs during calcification (α_{calc}). These discussions stem from observations that the skeletal $\delta^{13}C$ of corals and other marine calcifiers often strays on the negative side from values that would be predicted from isotope equilibrium models of mineral and aqueous phases ($\varepsilon_{calc\text{-}eq}$ 2 - 3‰; Swart, 1983; McConnaughey, 1989a; McConnaughey, 1989b; McConnaughey, 2003; Sun et al., 2008). This depletion from equilibrium is attributed to a kinetic isotope effect (KIE) of ~ -

10‰ associated with the hydration/hydroxylation of intracellular CO_2 within the calcifying space of these organisms (McConnaughey, 1989a; McConnaughey, 1989b).

Table 4.2. Reproduced from Raven et al., 1994. *In vivo* estimates of the RuBisCO fractionation factors for stable carbon isotopes ($\alpha_{RuBisCO}$, shown below as α_c) for a variety of lower order photolithotrophs.

Organism	α_c	Reference
Cyanobacteria[1,2]		From literature analysis by
Agmanellum quadruplicatum	1·016	Raven & Johnston (1991)
Agmanellum quadruplicatum	1·022	
Agmanellum quadruplicatum	1·024	
Anabaena azollae	1·025	
Coccochloris elebens	1·012	
Coccochloris elebens	1·020	
Coccochloris elebens	1·022	
Oscillatoria willionsii	1·017	
Microcoleus chthonoplastes	1·017	
Schizothrix calciocola	1·013	
Synechococcus lividus	1·013	
Synechococcus lividus	1·011	
Chlorophyceae[1,2]		From literature analysis by
Chlamydomonas reinhardtii	1·028	Raven & Johnston (1991)
Chlorella ellipsoidea	1·026	
Chlorella emersonii	1·025	
Chlorella pyrenoidosa	1·026	
Chlorella sorokiniana	1·026	
Bacillariophyceae[1]		Rounick & James (1984)
Melosira sp.	1·024	
Phaeophyceae[1,3]		From data in Wiencke & Fischer (1990)
Desmarestia anceps	1·023	
Desmarestia antarctica	1·023	
Himantothallus grandifolius	1·025	
Himantothallus grandifolius	1·026	
Laminaria digitata	1·024	
Laminaria digitata	1·028	
Laminaria solidungula	1·022	
Laminaria solidungula	1·029	
Rhodophyta[1,4]		From data in MacFarlane & Raven (1990)
Lemanea mamillosa	1·031	
Lemanea mamillosa	1·032	
Bryophyta[1,5]		From data in Table 2 of Raven (1987)
Fontinalis antipyretica	1·025	
Fontinalis antipyretica	1·029	
Fontinalis antipyretica	1·030	
Fontinalis antipyretica	1·033	

My estimations of ε_{calc} indicate KIEs associated with calcification have a limited influence on observed variability in $\delta^{13}C_{DIC}$ (estimates are typically near hypothesized equilibrium values). Given the magnitude differences in estimates of ε_{calc} and ε_{org} presented here and strong previously published evidence that photosynthesis carries the largest fractionation

factor for stable carbon isotopes in tropical marine environments, I conclude that the magnitude of diel variability in $\delta^{13}C_{DIC}$ observed on Tetiaroa's reef flat is mostly associated with cyclical patterns in primary productivity. Thus, the difference between near-dawn maxima and near-dusk minima in $\delta^{13}C_{DIC}$ in Figure 4.1 is accurately capturing a fingerprint of the extent of organic matter fractionation during primary productivity.

4.4.2 *Interpreting Variability in ε_{org}*

There have been a number of studies that have approached assessments of inorganic carbon physiologies (i.e. CO_2 diffusion, high-affinity CO_2 CCMs, low-affinity CO_2 CCMs) in macroalgae using a single-box model analysis of $\delta^{13}C$ variability observed in sample tissues (e.g. Figure 4.3, Carvalho et al., 2015; Cornwall et al., 2017; Hepburn et al., 2011). Here, I apply a similar model to our interpretations of net daily community ε_{org}. This model first assumes a 10‰ depletion in ^{13}C in aqueous CO_2 when compared to HCO_3^- (or broadly DIC). There is no assumed fractionation associated with either the active transport of HCO_3^- nor the conversion of HCO_3^- to CO_2, which must happen before RuBisCO can catalyze photosynthesis. Thus, if an organism primarily utilizes HCO_3^-, observed fractionation during organic matter synthesis should range from -30‰ ("leaky") to 0‰ (purely quantitative – all HCO_3^- is converted and catalyzed). Conversely, should an organism utilize CO_2, the fractionation during organic matter synthesis should range from -40‰ ("leaky") to -10‰ (purely quantitative – all CO_2 is catalyzed). In other words, calculated values of net daily community $\varepsilon_{org} < -30‰$ indicate a large contribution to observed productivity from those producers without CCMs *or* with high-affinity CO_2 CCMs, $-30‰ \leq \varepsilon_{org} \leq -10‰$ indicates a primary producer community with diverse inorganic carbon physiologies (contribution from species with and without CCMs), and $-10‰ \leq \varepsilon_{org} \leq 0‰$ indicates that the benthic community is primarily composed of organisms with low-affinity CO_2

CCMs. It is also worth noting that a vast majority of extant algal species have evolved CCMs with high and low affinities for CO_2 use (Raven et al., 2012). Therefore, any observed temporal variability in isolated values of ε_{org} within marine environments could be a result of behavioral plasticity within the existing algal community *or* the addition/expansion of opportunistic species of algae that are more adapted to *in situ* chemical conditions.

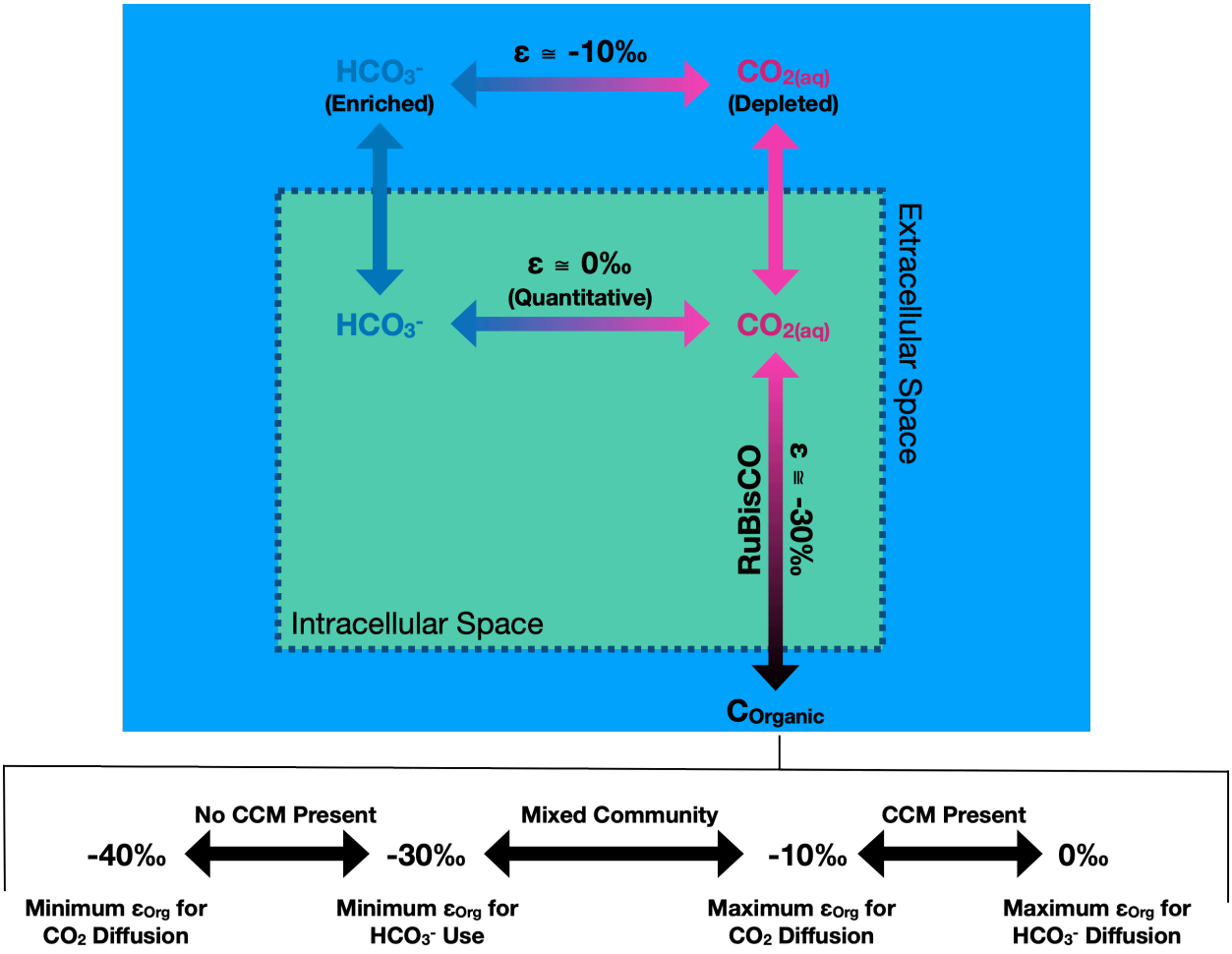

Figure 4.3. Adapted from logic of Carvalho et al. (2015) and Cornwall et al. (2017). Model of intracellular ^{13}C fractionation mechanisms in photosynthetic organisms and their impact on observed $\delta^{13}C$ of the organic material produced.

I use this interpretive framework to unravel the variability in steady-state values of hourly community ε_{org} observed across all diel field campaigns. Our results indicate that the benthic

algae community on Tetiaroa's reef flat is composed of a variety of species that utilize flexible CCMs with low affinities for CO_2 use (recall, $-8.6 \pm 0.6‰ \leq$ Steady State $\varepsilon_{org} \leq -4.1 \pm 5.9‰$, Table 4.1). This observation is consistent with anecdotal and previously published evidence of *Halimeda* spp. (a green calcifying alga common to reef environments), being an integral component to the benthic composition reefs in this region *and* having a $\delta^{13}C_{tissue}$ indicative of low-affinity CO_2 CCM usage ($-11 \leq \delta^{13}C_{tissue} \leq -7$; Raven et al., 2002; Edmunds et al., 2016). The trends in ε_{org} within and between the two diel field campaigns implies that some component of this community, either the community itself of the plasticity of the CCMs, is variable on Tetiaroa's reef flat over diel and possibly seasonal timescales. Near dawn estimates of ε_{org} in both datasets are the more negative values, and these values appear to trend more positive as the day goes on (Table 4.1; Figure 4.3). This observation could be an indication of a mixed community of primary producers utilizing a variety of CCMs with different affinities for CO_2. Additionally, as it is unlikely that the entire photosynthetic community can shift on the order of hours on reefs, the observed trends imply that ε_{org} on reefs captures *plasticity* in the inorganic carbon physiologies of local photosynthesizers on diel timescales.

4.4.3 *Implications of Variability in ε_{org} for Coral Reef Environments*

The source of observed variability in ε_{org} warrants further investigation and has the potential to be an incredibly useful metric for monitoring trophic transitions in coral reef ecosystems as environmental stressors compound. As previously stated, the results from numerous ecosystem-scale studies and simulations of coral reef environments point towards a coral-to-macroalgae transition that will accompany increasing ambient seawater pCO_2 and decreasing pH (Fabricius et al., 2011; Andersson and Gledhill, 2013; Enochs et al., 2015; Agostini et al., 2018; Contreras-Silva et al., 2020). Cornwall et al. (2017) expanded on this

hypothesis by linking the ability of macroalgae to adapt to rising pCO_2/low pH conditions to their inorganic carbon physiology during photosynthesis, showing that species with CCMs capable of taking advantage of more abundant CO_2 increased in abundance near a volcanic seep site in the Mediterranean; those without such a mechanism declined in abundance. The ability to isolate the biogeochemical fingerprint of inorganic carbon physiology from tandem measurements of DIC, TA, and $\delta^{13}C_{DIC}$ provides a proxy for monitoring and mitigating the rate and magnitude of the impending phase transition within and between reefs around the world.

Additionally, our observation of potential temporal variability in ε_{org} within a particular reef location warrants further investigation. While I do not have discrete measurements of benthic coverage to complement our geochemical observations, it is noteworthy that our observed minima (most negative values) in ε_{org} occur near dawn, when pCO_2 is at its highest during a diel cycle and pH is at its lowest (Figure 4.4). This observation is seemingly consistent with the hypothesis that algal inorganic carbon uptake mechanisms may behave plastically in response to ambient seawater carbonate chemistry. However, the data presented here implies that this response does not necessarily scale linearly with either pH or pCO_2 and instead may be linked to threshold conditions in ambient carbonate chemistry. This observation, if shown to be consistent on Tetiaroa and/or within other reef ecosystems, is significant as it implies that the benthic composition and physiological behavior of macroalgae in coral reef ecosystems will not only be sensitive to "top-down" influences on carbonate chemistry (such as ocean acidification), but also the internal biogeochemical "heartbeat" of carbonate chemistry of the ecosystem relative to its mean state.

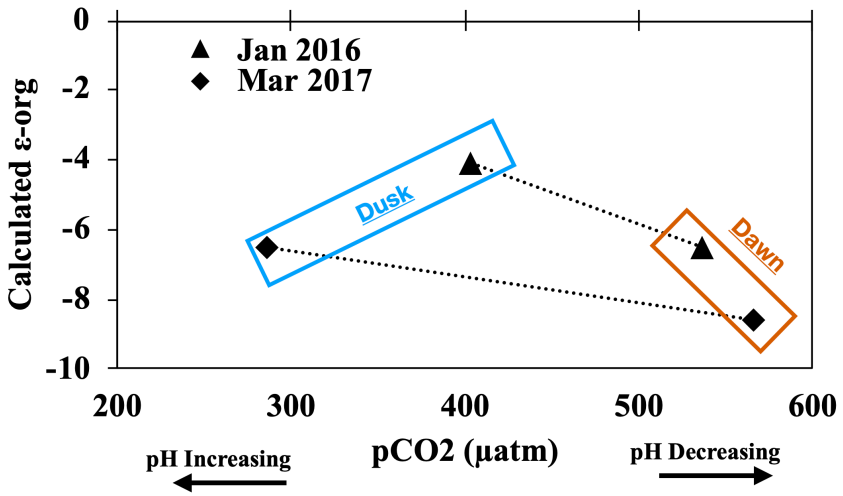

Figure 4.4. Scatter plot of isolated hourly estimates of ε_{org} vs pCO_2 indicate that carbonate chemistry may be a control on the inorganic carbon physiology utilized by reef-dwelling algal communities. More data is needed at high pHs/low pCO_2 to further validate this hypothesis.

Continued investigations of diel and/or seasonal variability of DIC, TA, $\delta^{13}C_{DIC}$, and ε_{org} on Tetiaroa would be worthwhile to establish a sense of how predictable the variability presented here is of this location. Similar investigations on other reef ecosystems, preferably accompanied by traditional surveys of benthic coverage, would greatly assist in continuing to calibrate ε_{org} as a proxy for benthic community composition for primary producers. Future investigations would be particularly impactful in the Florida Keys and broader Caribbean region, where reefs have been experiencing a rapid shift from coral cover to macroalgae dominance in recent decades. Some reports indicate that this region of reefs is a representative analogue for the ultimate community "phase shift" expected to occur on reefs as environmental stressors accumulate (e.g. Maliao et al., 2008). Additionally, the prevalence of fleshy green macroalgae species without CCMs (e.g. *Udotea* spp.) and those with CCMs with a high affinity for CO_2 (e.g. *Dictyota* spp.) has been a defining characteristic of portions of the Florida Keys National Marine Sanctuary (Maliao et al., 2008; Cornwall et al., 2017; Stanca and Parsons, 2017). Exploring the natural variability of ε_{org} as it relates to carbonate chemistry in this region would provide further insight toward the

relationship between ambient carbonate chemistry conditions and the inorganic carbon physiology community utilized by the local macroalgae community.

4.5 CONCLUSIONS

This study provides coral reef biogeochemists with a method of isolating estimates of net community organic matter fractionation factors associated with photosynthesis and calcification from temporal variability in carbonate chemistry and the stable carbon isotope composition of dissolved inorganic carbon within coral reef ecosystems. Our results, though limited in sample size, are consistent with previously published hypotheses that indicate that macroalgae inhabiting rapidly acidifying environments can and will adapt their photosynthetic physiologies to take advantage of changes to ambient seawater chemistry. In the context of ocean acidification and other environmental stressors impacting modern coral reef ecosystems, our method provides a tool for tracking the observed coral-to-macroalgae dominance transition believed to impact a majority of global coral reefs by the end of the century. Additionally, this tool can be used to elucidate degrees of natural variability in photosynthetic communities on reefs over diel, seasonal, and interannual timescales.

Chapter 5. DISSERTATION SUMMARY

The investigations explored in this dissertation will contribute to a growing body of explorations of reef biogeochemistry that aim to understand ecosystem level responses to environmental stressors. My research attempts to harness the potential of the geochemical fingerprints of natural variability within reef ecosystems to better understand and develop novel proxies for monitoring the health of these dynamic environments. With submission of the research prepared for this dissertation, I will have developed a quantitative decomposition model

of processes contributing to reef biogeochemistry on varying temporal scales, used this model to investigate assumptions of important metabolic ratios within reefs, and developed/applied methods for determining subtle, yet important nuances in community level calcification and productivity dynamics on coral reefs. Each of these tools contributes a small yet salient piece to the much larger puzzle of understanding biogeochemical cycling in the world's most diverse marine ecosystems. I will leverage the power of this toolkit to provide ecosystem managers with methods that inform adaptation and mitigation decisions in response to anthropogenic stressors in coral reef ecosystems.

BIBLIOGRAPHY

Agostini S., Harvey B. P., Wada S., Kon K., Milazzo M., Inaba K. and Hall-Spencer J. M. (2018) Ocean acidification drives community shifts towards simplified non-calcified habitats in a subtropical−temperate transition zone. *Sci. Rep.* **8**, 5–10.

Albarède F., Albalat E. and Télouk P. (2015) Instrumental isotope fractionation in multiple-collector icp-ms. *J. Anal. At. Spectrom.* **30**, 1736–1742. Available at: http://xlink.rsc.org/?DOI=C5JA00188A.

Albarède F. and Beard B. (2004) Analytical Methods for Non-Traditional Isotopes. *Rev. Mineral. Geochemistry* **55**, 113–152. Available at: http://rimg.geoscienceworld.org/cgi/doi/10.2138/gsrmg.55.1.113.

Albright R., Langdon C. and Anthony K. R. N. (2013) Dynamics of seawater carbonate chemistry, production, and calcification of a coral reef flat, Central Great Barrier Reef. *Biogeosciences Discuss.* **10**, 7641–7676. Available at: http://www.biogeosciences-discuss.net/10/7641/2013/.

Albright R., Takeshita Y., Koweek D. A., Ninokawa A., Wolfe K., Rivlin T., Nebuchina Y., Young J. and Caldeira K. (2018) Carbon dioxide addition to coral reef waters suppresses net community calcification. *Nature* **555**, 516–519. Available at: http://www.nature.com/doifinder/10.1038/nature25968.

Allison C. E., Francey R. J. and Meijer H. A. J. (1995) *Recommendations for the reporting of stable isotope measurements of carbon and oxygen in CO2 gas*., International Atomic Energy Agency (IAEA). Available at: http://inis.iaea.org/search/search.aspx?orig_q=RN:27021343.

Alongi D. (1989) The role of soft-bottom benthic communities in tropical mangroves and coral

reef ecosystems. *Rev. Aquat. Sci.* **1**, 243–280.

Altieri A. H., Harrison S. B., Seemann J., Collin R., Diaz R. J. and Knowlton N. (2017) Tropical dead zones and mass mortalities on coral reefs. *Proc. Natl. Acad. Sci.* **114**, 3660–3665. Available at: http://www.pnas.org/lookup/doi/10.1073/pnas.1621517114.

Andersson A. J. and Gledhill D. (2013) Ocean Acidification and Coral Reefs: Effects on Breakdown, Dissolution, and Net Ecosystem Calcification. *Ann. Rev. Mar. Sci.* **5**, 321–348. Available at: http://www.annualreviews.org/doi/10.1146/annurev-marine-121211-172241.

Andersson A. J., Mackenzie F. and Bates N. (2008) Life on the margin: implications of ocean acidification on Mg-calcite, high latitude and cold-water marine calcifiers. *Mar. Ecol. Prog. Ser.* **373**, 265–273. Available at: http://www.int-res.com/abstracts/meps/v373/p265-273/.

Andersson A. J., Yeakel K. L., Bates N. R. and de Putron S. J. (2014) Partial offsets in ocean acidification from changing coral reef biogeochemistry. *Nat. Clim. Chang.* **4**, 56–61. Available at: http://www.nature.com/doifinder/10.1038/nclimate2050.

Atkinson M. J. and Grigg R. W. (1984) Model of a coral reef ecosystem. *Coral Reefs* **3**, 13–22. Available at: https://doi.org/10.1007/BF00306136.

Baird A. H., Keith S. A., Woolsey E., Yoshida R. and Naruse T. (2018) Rapid coral mortality following unusually calm and hot conditions on Iriomote, Japan. *F1000Research* **6**, 1728. Available at: https://f1000research.com/articles/6-1728/v2.

Baker P. A. and Burns S. J. (1985) Occurrence and Formation of Dolomite in Organic-Rich Continental Margin Sediments. *Am. Assoc. Pet. Geol. Bull.* **69**, 1917–1930. Available at: http://search.datapages.com/data/doi/10.1306/94885570-1704-11D7-8645000102C1865D.

Barnes D. J. (1983) Profiling coral reef productivity and calcification using pH and oxygen electrodes. *J. Exp. Mar. Bio. Ecol.* **66**, 149–161. Available at:

http://linkinghub.elsevier.com/retrieve/pii/0022098183900369.

Barnes D. J. and Lazar B. (1993) Metabolic performance of a shallow reef patch near Eilat on the Red Sea. *J. Exp. Mar. Bio. Ecol.* **174**, 1–13. Available at: http://linkinghub.elsevier.com/retrieve/pii/002209819390248M.

Bastviken D. (2009) Methane. *Encycl. Inl. Waters*, 783–805. Available at: http://www.sciencedirect.com/science/article/pii/B9780123706263001174.

Bates N. R. (2002) Seasonal variability of the effect of coral reefs on seawater CO2 and air–sea CO2 exchange. *Limnol. Oceanogr.* **47**, 43–52.

Besson P., Degboe J., Berge B., Chavagnac V., Fabre S. and Berger G. (2014) Calcium, Na, K and Mg Concentrations in Seawater by Inductively Coupled Plasma-Atomic Emission Spectrometry: Applications to IAPSO Seawater Reference Material, Hydrothermal Fluids and Synthetic Seawater Solutions. *Geostand. Geoanalytical Res.* **38**, 355–362. Available at: http://doi.wiley.com/10.1111/j.1751-908X.2013.00269.x.

Bolden I. W., Sachs J. P. and Gagnon A. C. (2019) Temporally-variable productivity quotients on a coral atoll: Implications for estimates of reef metabolism. *Mar. Chem.* **217**, 103707. Available at: https://linkinghub.elsevier.com/retrieve/pii/S0304420319302142.

Bouman H. A., Platt T., Doblin M., Figueiras F. G., Gudmundsson K., Gudfinnsson H. G., Huang B., Hickman A., Hiscock M., Jackson T., Lutz V. A., Mélin F., Rey F., Pepin P., Segura V., Tilstone G. H., van Dongen-Vogels V. and Sathyendranath S. (2018) Photosynthesis–irradiance parameters of marine phytoplankton: synthesis of a global data set. *Earth Syst. Sci. Data* **10**, 251–266. Available at: https://www.earth-syst-sci-data.net/10/251/2018/.

Bryant D., Burke L., McManus J. and Spalding M. (1998) *Reefs at Risk: A Map-Based Indicator*

of Threats to the World's Coral Reefs., World Resources Institute, Washington, DC. Available at: http://www.ncbi.nlm.nih.gov/pubmed/24825660.

Burton E. A. and Walter L. M. (1987) Relative precipitation rates of aragonite and Mg calcite from seawater: temperature or carbonate ion control? *Geology* **15**, 111–114.

Camp E. F., Nitschke M. R., Rodolfo-Metalpa R., Houlbreque F., Gardner S. G., Smith D. J., Zampighi M. and Suggett D. J. (2017) Reef-building corals thrive within hot-acidified and deoxygenated waters. *Sci. Rep.* **7**, 2434. Available at: http://www.nature.com/articles/s41598-017-02383-y.

Carlson R. W. (2014) Thermal Ionization Mass Spectrometry. In *Treatise on Geochemistry* Elsevier. pp. 337–354. Available at: http://dx.doi.org/10.1016/B978-0-08-095975-7.01427-3.

Carpenter R. C. and Williams S. L. (2007) Mass transfer limitation of photosynthesis of coral reef algal turfs. *Mar. Biol.* **151**, 435–450.

Carpenter S. J. and Lohmann K. C. (1992) Ratios of modern marine calcite: Empirical indicators of ocean chemistry and precipitation rate. *Geochim. Cosmochim. Acta* **56**, 1837–1849. Available at: https://linkinghub.elsevier.com/retrieve/pii/0016703792903149.

Carvalho M. C., Santos I. R., Maher D. T., Cyronak T., McMahon A., Schulz K. G. and Eyre B. D. (2015) Drivers of carbon isotopic fractionation in a coral reef lagoon: Predominance of demand over supply. *Geochim. Cosmochim. Acta* **153**, 105–115. Available at: http://dx.doi.org/10.1016/j.gca.2015.01.012.

Coath C. D., Elliott T. and Hin R. C. (2017) Double-spike inversion for three-isotope systems. *Chem. Geol.* **451**, 78–89. Available at: http://linkinghub.elsevier.com/retrieve/pii/S0009254116306854.

Cohen I., Dubinsky Z. and Erez J. (2016) Light Enhanced Calcification in Hermatypic Corals: New Insights from Light Spectral Responses. *Front. Mar. Sci.* **2**, 1–12. Available at: http://journal.frontiersin.org/Article/10.3389/fmars.2015.00122/abstract.

Cole J. J. and Caraco N. F. (1998) Atmospheric exchange of carbon dioxide in a low-wind oligotrophic lake measured by the addition of SF 6. *Limnol. Oceanogr.* **43**, 647–656. Available at: http://doi.wiley.com/10.4319/lo.1998.43.4.0647.

Contreras-Silva A. I., Tilstra A., Migani V., Thiel A., Pérez-Cervantes E., Estrada-Saldívar N., Elias-Ilosvay X., Mott C., Alvarez-Filip L. and Wild C. (2020) A meta-analysis to assess long-term spatiotemporal changes of benthic coral and macroalgae cover in the Mexican Caribbean. *Sci. Rep.* **10**.

Cooper T. F., Uthicke S., Humphrey C. and Fabricius K. E. (2007) Gradients in water column nutrients, sediment parameters, irradiance and coral reef development in the Whitsunday Region, central Great Barrier Reef. *Estuar. Coast. Shelf Sci.* **74**, 458–470. Available at: https://linkinghub.elsevier.com/retrieve/pii/S0272771407001412.

Cornwall C. E., Revill A. T., Hall-Spencer J. M., Milazzo M., Raven J. A. and Hurd C. L. (2017) Inorganic carbon physiology underpins macroalgal responses to elevated CO2. *Sci. Rep.* **7**, 1–12. Available at: http://dx.doi.org/10.1038/srep46297.

Cross J., Macdonald A. M., Alin S. R., Wanninkhof R., Dickson A. G., Carlson C. A., Johnson G. C., Baringer M. O., Mordy C., Langdon C., Key R. M., McNichol A., Bullister J. L., Jenkins W. J. and Nelson N. (2017) Carbon Dioxide, Hydrographic, and Chemical Data Obtained During NOAA Ship Ronald H. Brown Repeat Hydrography Cruises in the Pacific Ocean: GO-SHIP Section P16N_2015, Legs 1 and 2 (EXPOCODEs 33RO20150410 and 33RO20150525), (10 April - 27 June, 2015) (NCEI .

Cyronak T., Andersson A. J., Langdon C., Albright R., Bates N. R., Caldeira K., Carlton R., Corredor J. E., Dunbar R. B., Enochs I., Erez J., Eyre B. D., Gattuso J.-P., Gledhill D., Kayanne H., Kline D. I., Koweek D. A., Lantz C., Lazar B., Manzello D., McMahon A., Meléndez M., Page H. N., Santos I. R., Schulz K. G., Shaw E., Silverman J., Suzuki A., Teneva L., Watanabe A. and Yamamoto S. (2018) Taking the metabolic pulse of the world's coral reefs ed. C. R. Voolstra. *PLoS One* **13**, e0190872. Available at: https://correspondent.afp.com/covering-refugee-crisis.

Cyronak T., Santos I. R. and Eyre B. D. (2013) Permeable coral reef sediment dissolution driven by elevated p CO 2 and pore water advection. *Geophys. Res. Lett.* **40**, 4876–4881. Available at: https://onlinelibrary.wiley.com/doi/abs/10.1002/grl.50948.

D'Errico J. (2020) fminsearchbnd, fminsearchcon. Available at: https://www.mathworks.com/matlabcentral/fileexchange/8277-fminsearchbnd-fminsearchcon.

Dassié E. P., Lemley G. M. and Linsley B. K. (2013) The Suess effect in Fiji coral δ13C and its potential as a tracer of anthropogenic CO2 uptake. *Palaeogeogr. Palaeoclimatol. Palaeoecol.* **370**, 30–40. Available at: http://dx.doi.org/10.1016/j.palaeo.2012.11.012.

DeCarlo T. M., Cohen A. L., Wong G. T. F., Shiah F., Lentz S. J., Davis K. A., Shamberger K. E. F. and Lohmann P. (2017) Community production modulates coral reef pH and the sensitivity of ecosystem calcification to ocean acidification. *J. Geophys. Res. Ocean.* **122**, 745–761. Available at: http://doi.wiley.com/10.1002/2016JC012326.

DePaolo D. J. (2004) Calcium Isotopic Variations Produced by Biological, Kinetic, Radiogenic and Nucleosynthetic Processes. *Rev. Mineral. Geochemistry* **55**, 255–288. Available at: https://pubs.geoscienceworld.org/rimg/article/55/1/255-288/87511.

Diaz-Pulido G., Nash M. C., Anthony K. R. N., Bender D., Opdyke B. N., Reyes-Nivia C. and Troitzsch U. (2014) Greenhouse conditions induce mineralogical changes and dolomite accumulation in coralline algae on tropical reefs. *Nat. Commun.* **5**, 1–9. Available at: http://www.nature.com/doifinder/10.1038/ncomms4310.

Dickson A. G. (1990) Thermodynamics of the dissociation of boric acid in synthetic seawater from 273.15 to 318.15 K. *Deep Sea Res. Part A. Oceanogr. Res. Pap.* **37**, 755–766. Available at: http://linkinghub.elsevier.com/retrieve/pii/019801499090004F.

Dickson A. G. and Millero F. J. (1987) A comparison of the equilibrium constants for the dissociation of carbonic acid in seawater media. *Deep Sea Res. Part A. Oceanogr. Res. Pap.* **34**, 1733–1743. Available at: http://linkinghub.elsevier.com/retrieve/pii/0198014987900215.

Dickson A. G., Sabine C. L. and Christian J. R. (2007) *Guide to best practices for ocean CO2 measurements*.,

Dietzel M., Gussone N. and Eisenhauer A. (2004) Co-precipitation of Sr2+ and Ba2+ with aragonite by membrane diffusion of CO2 between 10 and 50 °C. *Chem. Geol.* **203**, 139–151. Available at: http://linkinghub.elsevier.com/retrieve/pii/S0009254103003073.

Dodson M. H. (1963) A theoretical study of the use of internal standards for precise isotopic analysis by the surface ionization technique: Part I - General first-order algebraic solutions. *J. Sci. Instrum.* **40**, 289–295. Available at: http://stacks.iop.org/0950-7671/40/i=6/a=307?key=crossref.717fd3ff5f0dd92051e7cdc198a35eaf.

Doney S. C., Fabry V. J., Feely R. a and Kleypas J. a (2009) Ocean Acidification: The Other CO 2 Problem. *Ann. Rev. Mar. Sci.* **1**, 169–192. Available at: http://www.ncbi.nlm.nih.gov/pubmed/21141034 [Accessed May 24, 2014].

Drupp P. S., De Carlo E. H., Mackenzie F. T., Sabine C. L., Feely R. A. and Shamberger K. E. (2013) Comparison of CO2 Dynamics and Air-Sea Gas Exchange in Differing Tropical Reef Environments. *Aquat. Geochemistry* **19**, 371–397.

Edmunds P. J., Leichter J. J., Johnston E. C., Tong E. J. and Toonen R. J. (2016) Ecological and genetic variation in reef-building corals on four Society Islands. *Limnol. Oceanogr.* **61**, 543–557. Available at: http://doi.wiley.com/10.1002/lno.10231.

Egilsdottir H., Olafsson J. and Martin S. (2016) Photosynthesis and calcification in the articulated coralline alga Ellisolandia elongata (Corallinales, Rhodophyta) from intertidal rock pools. *Eur. J. Phycol.* **51**, 59–70. Available at: http://www.tandfonline.com/doi/full/10.1080/09670262.2015.1101165.

Elderfield H., Bertram C. J. and Erez J. (1996) A biomineralization model for the incorporation of trace elements into foraminiferal calcium carbonate. *Earth Planet. Sci. Lett.* **142**, 409–423. Available at: https://linkinghub.elsevier.com/retrieve/pii/0012821X96001057.

Elderfield H., Cooper M. and Ganssen G. (2000) Sr/Ca in multiple species of planktonic foraminifera: Implications for reconstructions of seawater Sr/Ca. *Geochemistry, Geophys. Geosystems* **1**, n/a-n/a. Available at: http://doi.wiley.com/10.1029/1999GC000031.

Elhamel N. (2014) The Development of an Analytical Technique to Measure Stable and Radiogenic Strontium Isotope Ratios Using Thermal Ionization Mass Spectrometry with the Double Spike Method. University of Calgary. Available at: http://hdl.handle.net/11023/1553.

Emerson S. R. and Hedges J. I. (2008) *Chemical Oceanography and the Marine Carbon Cycle*. 1st ed., Cambridge University Press, New York.

Enochs I. C., Manzello D. P., Donham E. M., Kolodziej G., Okano R., Johnston L., Young C.,

Iguel J., Edwards C. B., Fox M. D., Valentino L., Johnson S., Benavente D., Clark S. J., Carlton R., Burton T., Eynaud Y. and Price N. N. (2015) Shift from coral to macroalgae dominance on a volcanically acidified reef. *Nat. Clim. Chang.* **5**, 1–9. Available at: http://www.nature.com/doifinder/10.1038/nclimate2758.

Entsch B., Boto K. G., Sim R. G. and Wellington J. T. (1983) Phosphorus and nitrogen in coral reef sediments. *Limnol. Oceanogr.* **28**, 465–476. Available at: http://doi.wiley.com/10.4319/lo.1983.28.3.0465.

Erler D. V., Santos I. R. and Eyre B. D. (2014) Inorganic nitrogen transformations within permeable carbonate sands. *Cont. Shelf Res.* **77**, 69–80. Available at: http://dx.doi.org/10.1016/j.csr.2014.02.002.

Eyre B. D., Cyronak T., Drupp P., De Carlo E. H., Sachs J. P. and Andersson A. J. (2018) Coral reefs will transition to net dissolving before end of century. *Science (80-.).* **359**, 908–911. Available at: http://www.sciencemag.org/lookup/doi/10.1126/science.aao1118.

Fabricius K. E., Langdon C., Uthicke S., Humphrey C., Noonan S., De'ath G., Okazaki R., Muehllehner N., Glas M. S. and Lough J. M. (2011) Losers and winners in coral reefs acclimatized to elevated carbon dioxide concentrations. *Nat. Clim. Chang.* **1**, 165–169. Available at: http://dx.doi.org/10.1038/nclimate1122.

Falkowski P. G. (1998) Biogeochemical Controls and Feedbacks on Ocean Primary Production. *Science (80-.).* **281**, 200–206. Available at: http://www.sciencemag.org/cgi/doi/10.1126/science.281.5374.200.

Falkowski P. G., Dubinsky Z., Muscatine L. and Porter J. W. (1984) Light and the Bioenergetics of a Symbiotic Coral. *Bioscience* **34**, 705–709. Available at: https://academic.oup.com/bioscience/article-lookup/doi/10.2307/1309663.

Falkowski P. G. and Raven J. A. (2007) *Aquatic Photosynthesis*. STU-Stud., Princeton University Press. Available at: http://www.jstor.org/stable/j.ctt4cgbxs.

Falter J. L., Atkinson M. J. and Merrifield M. A. (2004) Mass-transfer limitation of nutrient uptake by a wave-dominated reef flat community. *Limnol. Oceanogr.* **49**, 1820–1831. Available at: http://doi.wiley.com/10.4319/lo.2004.49.5.1820.

Falter J. L., Lowe R. J., Atkinson M. J. and Cuet P. (2012) Seasonal coupling and de-coupling of net calcification rates from coral reef metabolism and carbonate chemistry at Ningaloo Reef, Western Australia. *J. Geophys. Res. Ocean.* **117**, 1–14.

Falter J. L., Lowe R. J., Atkinson M. J., Monismith S. G. and Schar D. W. (2008) Continuous measurements of net production over a shallow reef community using a modified Eulerian approach. *J. Geophys. Res. Ocean.* **113**, 1–14.

Falter J. L., Lowe R. J., Zhang Z. and McCulloch M. (2013) Physical and Biological Controls on the Carbonate Chemistry of Coral Reef Waters: Effects of Metabolism, Wave Forcing, Sea Level, and Geomorphology ed. I. Álvarez. *PLoS One* **8**, e53303. Available at: http://dx.plos.org/10.1371/journal.pone.0053303.

Fassbender A. J., Sabine C. L., Lawrence-Slavas N., De Carlo E. H., Meinig C. and Maenner Jones S. (2015) Robust Sensor for Extended Autonomous Measurements of Surface Ocean Dissolved Inorganic Carbon. *Environ. Sci. Technol.* **49**, 3628–3635. Available at: http://pubs.acs.org/doi/abs/10.1021/es5047183.

Fassett J. D. and Paulsen P. J. (1989) Isotope dilution mass spectrometry for accurate elemental analysis. *Anal. Chem.* **61**, 643A-[649A]. Available at: http://pubs.acs.org/doi/abs/10.1021/ac00185a001.

Feely R. A., Sabine C. L., Millero F. J., Wanninkhof R. and Hansell D. (2006) Carbon Dioxide,

Hydrographic, and Chemical Data Obtained During the R/V Thomas Thompson Cruise in the Pacific Ocean on CLIVAR Repeat Hydrography Sections P16N_2006 (Feb. 14 - Mar. 30, 2006). , 1–79.

Fietzke J. and Eisenhauer A. (2006) Determination of temperature-dependent stable strontium isotope (88 Sr/ 86 Sr) fractionation via bracketing standard MC-ICP-MS. *Geochemistry, Geophys. Geosystems* **7**, n/a-n/a. Available at: http://doi.wiley.com/10.1029/2006GC001243.

Frankignoulle M., Gattuso J. P., Biondo R., Bourge I., Copin-Montégut G. and Pichon M. (1996) Carbon fluxes in coral reefs. II. Eulerian study of inorganic carbon dynamics and measurement of air-sea CO2 exchanges. *Mar. Ecol. Prog. Ser.* **145**, 123–132. Available at: www.jstor.org/stable/24857321.

Gaetani G. a. and Cohen A. L. (2006) Element partitioning during precipitation of aragonite from seawater: A framework for understanding paleoproxies. *Geochim. Cosmochim. Acta* **70**, 4617–4634.

Gagnon A. C. (2010) Geochemical mechanisms of biomineralization from analysis of deep-sea and laboratory cultured corals. California Institute of Technology. Available at: http://resolver.caltech.edu/CaltechTHESIS:05102010-102555148.

Gagnon A. C., Adkins J. F., Erez J., Eiler J. M. and Guan Y. (2013) Sr/Ca sensitivity to aragonite saturation state in cultured subsamples from a single colony of coral: Mechanism of biomineralization during ocean acidification. *Geochim. Cosmochim. Acta* **105**, 240–254. Available at: http://dx.doi.org/10.1016/j.gca.2012.11.038.

Gagnon A. C., Adkins J. F., Fernandez D. P. and Robinson L. F. (2007) Sr/Ca and Mg/Ca vital effects correlated with skeletal architecture in a scleractinian deep-sea coral and the role of

Rayleigh fractionation. *Earth Planet. Sci. Lett.* **261**, 280–295.

Gattuso J.-P., Allemand D. and Frankignoulle M. (1999) Photosynthesis and Calcification at Cellular, Organismal and Community Levels in Coral Reefs: A Review on Interactions and Control by Carbonate Chemistry. *Am. Zool.* **39**, 160–183. Available at: https://academic.oup.com/icb/article-lookup/doi/10.1093/icb/39.1.160.

Gattuso J.-P., Frankignoulle M. and Smith S. V (1999) Measurement of community metabolism and significance in the coral reef CO2 source-sink debate. *Proc. Natl. Acad. Sci. U. S. A.* **96**, 13017–13022.

Gattuso J.-P., Payri C. E., Pichon M., Delesalle B. and Frankignoulle M. (1997) PRIMARY PRODUCTION, CALCIFICATION, AND AIR-SEA CO2 FLUXES OF A MACROALGAL-DOMINATED CORAL REEF COMMUNITY (MOOREA, FRENCH POLYNESIA). *J. Phycol.* **33**, 729–738. Available at: http://doi.wiley.com/10.1111/j.0022-3646.1997.00729.x.

Gattuso J.-P., Pichon M., Delesalle B., Canon C. and Frankignoulle M. (1996) Carbon fluxes in coral reefs. I. Lagrangian measurement of community metabolism and resulting air-sea CO2 disequilibrium. *Mar. Ecol. Prog. Ser.* **145**, 109–121. Available at: http://www.int-res.com/abstracts/meps/v145/p109-121/.

Gattuso J.-P., Pichon M., Delesalle B. and Frankignoulle M. (1993) Community metabolism and air-sea C02 fluxes in a coral reef ecosystem (Moorea, French Polynesia). *Mar. Ecol. Prog. Ser.* **96**, 259–267. Available at: http://www.int-res.com/articles/meps/96/m096p259.pdf.

Gray S. E. C., DeGrandpre M. D., Langdon C. and Corredor J. E. (2012) Short-term and seasonal pH, p CO 2 and saturation state variability in a coral-reef ecosystem. *Global Biogeochem. Cycles* **26**, 1–13. Available at: http://doi.wiley.com/10.1029/2011GB004114.

Gruber R. K., Lowe R. J. and Falter J. L. (2017) Metabolism of a tide-dominated reef platform subject to extreme diel temperature and oxygen variations. *Limnol. Oceanogr.* **62**, 1701–1717.

Guy R. D., Fogel M. L. and Berry J. A. (1993) Photosynthetic Fractionation of the Stable Isotopes of Oxygen and Carbon. *Plant Physiol.* **101**, 37–47. Available at: http://www.plantphysiol.org/lookup/doi/10.1104/pp.101.1.37.

Hall-Spencer J. M., Rodolfo-Metalpa R., Martin S., Ransome E., Fine M., Turner S. M., Rowley S. J., Tedesco D. and Buia M. C. (2008) Volcanic carbon dioxide vents show ecosystem effects of ocean acidification. *Nature* **454**, 96–99.

Hamylton S. (2014) Will Coral Islands Maintain Their Growth over the Next Century? A Deterministic Model of Sediment Availability at Lady Elliot Island, Great Barrier Reef ed. I. Álvarez. *PLoS One* **9**, e94067. Available at: https://dx.plos.org/10.1371/journal.pone.0094067.

Hathorne E. C., Gagnon A., Felis T., Adkins J., Asami R., Boer W., Caillon N., Case D., Cobb K. M., Douville E., DeMenocal P., Eisenhauer A., Garbe-Schönberg D., Geibert W., Goldstein S., Hughen K., Inoue M., Kawahata H., Kölling M., Cornec F. L., Linsley B. K., McGregor H. V., Montagna P., Nurhati I. S., Quinn T. M., Raddatz J., Rebaubier H., Robinson L., Sadekov A., Sherrell R., Sinclair D., Tudhope A. W., Wei G., Wong H., Wu H. C. and You C.-F. (2013) Interlaboratory study for coral Sr/Ca and other element/Ca ratio measurements. *Geochemistry, Geophys. Geosystems* **14**, 3730–3750. Available at: http://doi.wiley.com/10.1002/ggge.20230.

Hedges J. I., Baldock J. A., Gélinas Y., Lee C., Peterson M. L. and Wakeham S. G. (2002) The biochemical and elemental compositions of marine plankton: A NMR perspective. *Mar.*

Chem. **78**, 47–63.

Hepburn C. D., Pritchard D. W., Cornwall C. E., Mcleod R. J., Beardall J., Raven J. A. and Hurd C. L. (2011) Diversity of carbon use strategies in a kelp forest community: Implications for a high CO2ocean. *Glob. Chang. Biol.* **17**, 2488–2497.

Hetzinger S., Halfar J., Zack T., Gamboa G., Jacob D. E., Kunz B. E., Kronz A., Adey W., Lebednik P. A. and Steneck R. S. (2011) High-resolution analysis of trace elements in crustose coralline algae from the North Atlantic and North Pacific by laser ablation ICP-MS. *Palaeogeogr. Palaeoclimatol. Palaeoecol.* **302**, 81–94. Available at: http://dx.doi.org/10.1016/j.palaeo.2010.06.004.

Heumann K. G. (1992) Isotope dilution mass spectrometry. *Int. J. Mass Spectrom. Ion Process.* **118**–**119**, 575–592. Available at: http://linkinghub.elsevier.com/retrieve/pii/016811769285076C.

Heuser A., Eisenhauer A., Gussone N., Bock B., Hansen B. T. and Nägler T. F. (2002) Measurement of calcium isotopes (δ44Ca) using a multicollector TIMS technique. *Int. J. Mass Spectrom.* **220**, 385–397. Available at: http://linkinghub.elsevier.com/retrieve/pii/S1387380602008382.

Ho D. T., De Carlo E. H. and Schlosser P. (2018) Air-Sea Gas Exchange and CO 2 Fluxes in a Tropical Coral Reef Lagoon. *J. Geophys. Res. Ocean.* **123**, 8701–8713. Available at: http://doi.wiley.com/10.1029/2018JC014423.

Ho D. T., Coffineau N., Hickman B., Chow N., Koffman T. and Schlosser P. (2016) Influence of current velocity and wind speed on air-water gas exchange in a mangrove estuary. *Geophys. Res. Lett.* **43**, 3813–3821. Available at: http://doi.wiley.com/10.1002/2016GL068727.

Ho D. T., Law C. S., Smith M. J., Schlosser P., Harvey M. and Hill P. (2006) Measurements of

air-sea gas exchange at high wind speeds in the Southern Ocean: Implications for global parameterizations. *Geophys. Res. Lett.* **33**, L16611. Available at: http://doi.wiley.com/10.1029/2006GL026817.

Ho D. T., Schlosser P. and Orton P. M. (2011) On Factors Controlling Air–Water Gas Exchange in a Large Tidal River. *Estuaries and Coasts* **34**, 1103–1116. Available at: http://link.springer.com/10.1007/s12237-011-9396-4.

Hoegh-Guldberg O., Mumby P. J., Hooten A. J., Steneck R. S., Greenfield P., Gomez E., Harvell C. D., Sale P. F., Edwards A. J., Caldeira K., Knowlton N., Eakin C. M., Iglesias-Prieto R., Muthiga N., Bradbury R. H., Dubi A. and Hatziolos M. E. (2007) Coral reefs under rapid climate change and ocean acidification. *Science* **318**, 1737–1742. Available at: http://www.sciencemag.org/cgi/doi/10.1126/science.1152509 [Accessed July 15, 2014].

Hoeke R., Gove J., Smith E., Fisher-Pool P., Lammers M., Merritt D., Vetter O., Young C., Wong K. and Brainard R. (2009) Coral reef ecosystem integrated observing system: In-situ oceanographic observations at the US Pacific islands and atolls. *J. Oper. Oceanogr.* **2**, 3–14. Available at: https://www.tandfonline.com/doi/full/10.1080/1755876X.2009.12027737.

Hofmann G. E., Smith J. E., Johnson K. S., Send U., Levin L. A., Micheli F., Paytan A., Price N. N., Peterson B., Takeshita Y., Matson P. G., Crook E. D., Kroeker K. J., Gambi M. C., Rivest E. B., Frieder C. A., Yu P. C. and Martz T. R. (2011) High-Frequency Dynamics of Ocean pH: A Multi-Ecosystem Comparison ed. W.-C. Chin. *PLoS One* **6**, e28983. Available at: https://dx.plos.org/10.1371/journal.pone.0028983.

Howard E. M., Forbrich I., Giblin A. E., Lott D. E., Cahill K. L. and Stanley R. H. R. (2018) Using Noble Gases to Compare Parameterizations of Air-Water Gas Exchange and to Constrain Oxygen Losses by Ebullition in a Shallow Aquatic Environment. *J. Geophys.*

Res. Biogeosciences **123**, 2711–2726.

Jeanson M., Anthony E. J., Etienne S. and Dolique F. (2014) Morphodynamic characterization of beaches on a Pacific atoll island: Tetiaroa, French Polynesia. *J. Coast. Res.* **70**, 176–181. Available at: http://www.bioone.org/doi/10.2112/SI70-030.1.

John S. G. (2012) Optimizing sample and spike concentrations for isotopic analysis by double-spike ICPMS. *J. Anal. At. Spectrom.* **27**, 2123. Available at: http://pubs.rsc.org.offcampus.lib.washington.edu/-/content/articlepdf/2012/ja/c2ja30215b [Accessed January 7, 2018].

John S. G. and Adkins J. F. (2010) Analysis of dissolved iron isotopes in seawater. *Mar. Chem.* **119**, 65–76. Available at: http://dx.doi.org/10.1016/j.marchem.2010.01.001.

Karlsson J., Jansson M. and Jonsson A. (2007) Respiration of allochthonous organic carbon in unproductive forest lakes determined by the Keeling plot method. *Limnol. Oceanogr.* **52**, 603–608. Available at: http://doi.wiley.com/10.4319/lo.2007.52.2.0603.

Kealoha A. K. (2019) CORAL REEF ECOSYSTEM HEALTH IN RESPONSE TO CLIMATE CHANGE AND ENVIRONMENTAL STRESSORS. Texas A&M University.

Kealoha A. K., Doyle S., Shamberger K., Sylvan J., Hetland R. and DiMarco S. (2019) Localized hypoxia drives coral reef mortality at the Flower Garden Banks. *Coral Reefs*. Available at: https://doi.org/10.1007/s00338-019-01883-9.

Keeling C. D., Bacastow R. B. and Tans P. P. (1980) Predicted shift in the 13 C / 12 C ratio of atmospheric carbon dioxide. *Geophys. Res. Lett.* **7**, 505–508. Available at: http://doi.wiley.com/10.1029/GL007i007p00505.

Kinsey D. W. (1979) Carbon Turnover and Accumulation by Coral Reefs. University of Hawaii. Available at: http://hdl.handle.net/10125/10015.

Kinsey D. W. (1985) Metabolism, calcification and carbon production: systems level studies. In *The Fifth International Coral Reef Congress* pp. 505–526.

Kinsman D. J. J. and Holland H. . (1969) The co-precipitation of cations with CaCO3—IV. The co-precipitation of Sr2+ with aragonite between 16° and 96°C. *Geochim. Cosmochim. Acta* **33**, 1–17. Available at: https://linkinghub.elsevier.com/retrieve/pii/0016703769900891.

Kohn A. J. and Helfrich P. (1957) Primary Organic Productivity of a Hawaiian Coral Reef. *Limnol. Oceanogr.* **2**, 241–251. Available at: http://doi.wiley.com/10.1002/lno.1957.2.3.0241.

Koschorreck M., Hentschel I. and Boehrer B. (2017) Oxygen Ebullition From Lakes. *Geophys. Res. Lett.* **44**, 9372–9378. Available at: http://doi.wiley.com/10.1002/2017GL074591.

Koweek D. A., Dunbar R. B., Monismith S. G., Mucciarone D. A., Woodson C. B. and Samuel L. (2015) High-resolution physical and biogeochemical variability from a shallow back reef on Ofu, American Samoa: an end-member perspective. *Coral Reefs* **34**, 979–991.

Koweek D. A., Dunbar R. B., Rogers J. S., Williams G. J., Price N., Mucciarone D. and Teneva L. (2015) Environmental and ecological controls of coral community metabolism on Palmyra Atoll. *Coral Reefs* **34**, 339–351. Available at: http://link.springer.com/10.1007/s00338-014-1217-3.

Koweek D. A., Forden A., Albright R., Takeshita Y., Mucciarone D. A., Ninokawa A. and Caldeira K. (2019) Carbon Isotopic Fractionation in Organic Matter Production Consistent With Benthic Community Composition Across a Coral Reef Flat. *Front. Mar. Sci.* **5**.

Krabbenhöft A., Fietzke J., Eisenhauer A., Liebetrau V., Böhm F. and Vollstaedt H. (2009) Determination of radiogenic and stable strontium isotope ratios (87Sr/86Sr; δ88/86Sr) by thermal ionization mass spectrometry applying an 87Sr/84Sr double spike. *J. Anal. At.*

Spectrom. **24**, 1267. Available at: http://xlink.rsc.org/?DOI=b906292k.

Kroopnick P. M. (1985) The distribution of delta13C of ΣCO2 in the world oceans. *Deep Sea Res. Part A, Oceanogr. Res. Pap.* **32**, 57–84. Available at: http://www.scopus.com/inward/record.url?eid=2-s2.0-0021860461&partnerID=40&md5=120fca7c8642e49f94f67f3ca4d42c8b.

Krumgalz B. S. (1982) Calcium distribution in the world ocean waters. *Oceanol. Acta* **5**, 121–128.

Kuffner I. B., Andersson A. J., Jokiel P. L., Rodgers K. S. and Mackenzie F. T. (2008) Decreased abundance of crustose coralline algae due to ocean acidification. *Nat. Geosci.* **1**, 114–117. Available at: http://www.nature.com/articles/ngeo100.

Langdon C. and Atkinson M. J. (2005) Effect of elevated pCO 2 on photosynthesis and calcification of corals and interactions with seasonal change in temperature/irradiance and nutrient enrichment. *J. Geophys. Res.* **110**, C09S07. Available at: http://doi.wiley.com/10.1029/2004JC002576.

Laws E. A. (1991) Photosynthetic quotients, new production and net community production in the open ocean. *Deep Sea Res. Part A, Oceanogr. Res. Pap.* **38**, 143–167. Available at: http://linkinghub.elsevier.com/retrieve/pii/019801499190059O.

Lebrato M., Garbe-Schönberg D., Müller M. N., Blanco-Ameijeiras S., Feely R. A., Lorenzoni L., Molinero J. C., Bremer K., Jones D. O. B., Iglesias-Rodriguez D., Greeley D., Lamare M. D., Paulmier A., Graco M., Cartes J., Barcelos e Ramos J., de Lara A., Sanchez-Leal R., Jimenez P., Paparazzo F. E., Hartman S. E., Westernströer U., Küter M., Benavides R., da Silva A. F., Bell S., Payne C., Olafsdottir S., Robinson K., Jantunen L. M., Korablev A., Webster R. J., Jones E. M., Gilg O., du Bois P. B., Beldowski J., Ashjian C., Yahia N. D.,

Twining B., Chen X. G., Tseng L. C., Hwang J. S., Dahms H. U. and Oschlies A. (2020) Global variability in seawater Mg:Ca and Sr:Ca ratios in the modern ocean. *Proc. Natl. Acad. Sci. U. S. A.* **117**, 22281–22292.

Liu H. C., You C. F., Cai W. J., Chung C. H., Huang K. F., Chen B. S. and Li Y. (2014) Precise determination of seawater calcium using isotope dilution inductively coupled plasma mass spectrometry. *Analyst* **139**, 734–741.

Long M. H., Berg P., de Beer D. and Zieman J. C. (2013) In Situ Coral Reef Oxygen Metabolism: An Eddy Correlation Study ed. A. Davies. *PLoS One* **8**, e58581. Available at: https://dx.plos.org/10.1371/journal.pone.0058581.

Lowe R. J., Falter J. L., Monismith S. G. and Atkinson M. J. (2009) A numerical study of circulation in a coastal reef-lagoon system. *J. Geophys. Res.* **114**, C06022. Available at: http://doi.wiley.com/10.1029/2008JC005081.

Maliao R. J., Turingan R. G. and Lin J. (2008) Phase-shift in coral reef communities in the Florida Keys National Marine Sanctuary (FKNMS), USA. *Mar. Biol.* **154**, 841–853.

Manzello D. P., Enochs I. C., Melo N., Gledhill D. K. and Johns E. M. (2012) Ocean Acidification Refugia of the Florida Reef Tract ed. R. K. F. Unsworth. *PLoS One* **7**, 1–10. Available at: https://dx.plos.org/10.1371/journal.pone.0041715.

Martini M., Butman B. and Mickelson M. J. (2007) Long-Term Performance of Aanderaa Optodes and Sea-Bird SBE-43 Dissolved-Oxygen Sensors Bottom Mounted at 32 m in Massachusetts Bay. *J. Atmos. Ocean. Technol.* **24**, 1924–1935. Available at: http://journals.ametsoc.org/doi/abs/10.1175/JTECH2078.1.

Martz T. R., Carr J. J., French C. R. and DeGrandpre M. D. (2003) A Submersible Autonomous Sensor for Spectrophotometric pH Measurements of Natural Waters. *Anal. Chem.* **75**, 1844–

1850. Available at: http://pubs.acs.org/doi/abs/10.1021/ac020568l.

McConnaughey T. (1989a) 13C and 18O isotopic disequilibrium in biological carbonates: I. Patterns. *Geochim. Cosmochim. Acta* **53**, 151–162. Available at: http://linkinghub.elsevier.com/retrieve/pii/0016703789902822.

McConnaughey T. (1989b) 13C and 18O isotopic disequilibrium in biological carbonates: II. In vitro simulation of kinetic isotope effects. *Geochim. Cosmochim. Acta* **53**, 163–171. Available at: http://linkinghub.elsevier.com/retrieve/pii/0016703789902822.

McConnaughey T. A. (2003) Sub-equilibrium oxygen-18 and carbon-13 levels in biological carbonates: carbonate and kinetic models. *Coral Reefs* **22**, 316–327. Available at: http://link.springer.com/10.1007/s00338-003-0325-2.

McMahon A., Santos I. R., Schulz K. G., Cyronak T. and Maher D. T. (2018) Determining coral reef calcification and primary production using automated alkalinity, pH and pCO2 measurements at high temporal resolution. *Estuar. Coast. Shelf Sci.* **209**, 80–88. Available at: https://doi.org/10.1016/j.ecss.2018.04.041.

Mehrbach C., Culberson C. H., Hawley J. E. and Pytkowicx R. M. (1973) MEASUREMENT OF THE APPARENT DISSOCIATION CONSTANTS OF CARBONIC ACID IN SEAWATER AT ATMOSPHERIC PRESSURE. *Limnol. Oceanogr.* **18**, 897–907. Available at: http://doi.wiley.com/10.4319/lo.1973.18.6.0897.

Mondal S. and Chakrabarti R. (2018) A novel sample loading method and protocol for monitoring sample fractionation for high precision Ca stable isotope ratio measurements using double-spike TIMS. *J. Anal. At. Spectrom.* **33**, 141–150. Available at: http://xlink.rsc.org/?DOI=C7JA00322F.

Monismith S. G. (2007) Hydrodynamics of Coral Reefs. *Annu. Rev. Fluid Mech.* **39**, 37–55.

Available at: http://www.annualreviews.org/doi/10.1146/annurev.fluid.38.050304.092125.

Monsen N. E., Cloern J. E., Lucas L. V. and Monismith S. G. (2002) A comment on the use of flushing time, residence time, and age as transport time scales. *Limnol. Oceanogr.* **47**, 1545–1553. Available at: http://doi.wiley.com/10.4319/lo.2002.47.5.1545.

Morse J. W. and Bender M. L. (1990) Partition coefficients in calcite: Examination of factors influencing the validity of experimental results and their application to natural systems. *Chem. Geol.* **82**, 265–277. Available at: https://linkinghub.elsevier.com/retrieve/pii/000925419090085L.

Müller M. N., Lebrato M., Riebesell U., Barcelos e Ramos J., Schulz K. G., Blanco-Ameijeiras S., Sett S., Eisenhauer A. and Stoll H. M. (2014) Influence of temperature and CO2 on the strontium and magnesium composition of coccolithophore calcite. *Biogeosciences* **11**, 1065–1075. Available at: https://bg.copernicus.org/articles/11/1065/2014/.

Muscatine L., R. McCloskey L. and E. Marian R. (1981) Estimating the daily contribution of carbon from zooxanthellae to coral animal respiration1. *Limnol. Oceanogr.* **26**, 601–611. Available at: http://doi.wiley.com/10.4319/lo.1981.26.4.0601.

Nash M. C., Opdyke B. N., Troitzsch U., Russell B. D., Adey W. H., Kato a., Diaz-Pulido G., Brent C., Gardner M., Prichard J. and Kline D. I. (2013) Dolomite-rich coralline algae in reefs resist dissolution in acidified conditions. *Nat. Clim. Chang.* **3**, 268–272. Available at: http://www.nature.com/doifinder/10.1038/nclimate1760.

Nash M. C., Troitzsch U., Opdyke B. N., Trafford J. M., Russell B. D. and Kline D. I. (2011) First discovery of dolomite and magnesite in living coralline algae and its geobiological implications. *Biogeosciences* **8**, 3331–3340.

Nash M. C., Uthicke S., Negri A. P. and Cantin N. E. (2015) Ocean acidification does not affect

magnesium composition or dolomite formation in living crustose coralline algae, Porolithon onkodes in an experimental system. *Biogeosciences* **12**, 5247–5260.

Nayar K. G., Sharqawy M. H., Banchik L. D. and Lienhard V J. H. (2016) Thermophysical properties of seawater: A review and new correlations that include pressure dependence. *Desalination* **390**, 1–24. Available at: http://dx.doi.org/10.1016/j.desal.2016.02.024.

Nielsen L. C., Druhan J. L., Yang W., Brown S. T. and DePaolo D. J. (2012) Calcium Isotopes as Tracers of Biogeochemical Processes. In *Handbook of Environmental Isotope Geochemistry* Springer Berlin Heidelberg, Berlin, Heidelberg. pp. 105–124. Available at: http://link.springer.com/10.1007/978-3-642-10637-8_7.

Odum H. T. and Odum E. P. (1955) Trophic Structure and Productivity of a Windward Coral Reef Community on Eniwetok Atoll. *Ecol. Monogr.* **25**, 291–320. Available at: http://doi.wiley.com/10.2307/1943285.

Okai T., Suzuki A., Kawahata H., Terashima S. and Imai N. (2002) Preparation of a New Geological Survey of Japan Geochemical Reference Material: Coral JCp-1. *Geostand. Geoanalytical Res.* **26**, 95–99. Available at: http://doi.wiley.com/10.1111/j.1751-908X.2002.tb00627.x.

Pandolfi J. M. (2003) Global Trajectories of the Long-Term Decline of Coral Reef Ecosystems. *Science (80-.).* **301**, 955–958. Available at: http://www.sciencemag.org/cgi/doi/10.1126/science.1085706.

Pandolfi J. M., Connolly S. R., Marshall D. J. and Cohen A. L. (2011) Projecting coral reef futures under global warming and ocean acidification. *Science* **333**, 418–22. Available at: http://www.ncbi.nlm.nih.gov/pubmed/21778392 [Accessed May 22, 2013].

Platt T., Gallegos C. L. and Harrison W. G. (1980) Photoinhibition of photosynthesis in natural

assemblages of marine phytoplankton. *J. Mar. Res.* **38**, 687–701.

Price N. N., Martz T. R., Brainard R. E. and Smith J. E. (2012) Diel Variability in Seawater pH Relates to Calcification and Benthic Community Structure on Coral Reefs. *PLoS One* **7**, 1–9.

Quay P. D. (2017) The 13C/12C stable carbon isotopic ratio of the dissolved inorganic carbon from samples collected on the GEOTRACES EPZT cruise (R/V Thomas G. Thompson TN303) in the Eastern Tropical South Pacific from October to December 2013.

Quay P. D., Tilbrook B. and Wong C. S. (1992) Oceanic Uptake of Fossil Fuel CO2: Carbon-13 Evidence. *Science* **256**, 74–79.

Raddatz J., Liebetrau V., Rüggeberg A., Hathorne E., Krabbenhöft A., Eisenhauer A., Böhm F., Vollstaedt H., Fietzke J., López Correa M., Freiwald A. and Dullo W.-C. (2013) Stable Sr-isotope, Sr/Ca, Mg/Ca, Li/Ca and Mg/Li ratios in the scleractinian cold-water coral Lophelia pertusa. *Chem. Geol.* **352**, 143–152. Available at: http://dx.doi.org/10.1016/j.chemgeo.2013.06.013.

Rädecker N., Pogoreutz C., Voolstra C. R., Wiedenmann J. and Wild C. (2015) Nitrogen cycling in corals: the key to understanding holobiont functioning? *Trends Microbiol.* **23**, 490–497. Available at: http://linkinghub.elsevier.com/retrieve/pii/S0966842X1500075X.

Raven J. (1997) Inorganic Carbon Acquisition by Marine Autotrophs. *Adv. Bot. Res.*, 85–209. Available at: https://linkinghub.elsevier.com/retrieve/pii/S0065229608602815.

Raven J. A., Giordano M., Beardall J. and Maberly S. C. (2012) Algal evolution in relation to atmospheric CO 2 : carboxylases, carbon-concentrating mechanisms and carbon oxidation cycles. *Philos. Trans. R. Soc. B Biol. Sci.* **367**, 493–507. Available at: https://royalsocietypublishing.org/doi/10.1098/rstb.2011.0212.

Raven J. A., Johnston A. M., Kübler J. E., Korb R., Mcinroy S. G., Handley L. L., Scrimgeour C. M. and Walker D. I. (2002) Mechanistic Interpretation of Carbon Discrimination by Marine Macroalgae and Seagrasses. *Funct. Plant Biol. Contin. Aust. J. Plant Physiol.* **29**, 355–378.

Raven J. A., Johnston A. M., Newman J. R. and Scrimgeour C. M. (1994) Inorganic Carbon Acquisition by Aquatic Photolithotrophs of the Dighty Burn, Angus, U.K.: Uses and Limitations of Natural Abundance Measurements of Carbon Isotopes. *New Phytol.* **127**, 271–286. Available at: http://www.jstor.org/stable/2558027.

Redfield A. C., Ketchum B. H. and Richards F. A. (1963) The Influence of Organisms on the Composition of Sea Water. In *The Sea* (ed. M. N. Hill). John Wiley, New York. pp. 26–77.

Ries J. B. (2010) Review: geological and experimental evidence for secular variation in seawater Mg/Ca (calcite-aragonite seas) and its effects on marine biological calcification. *Biogeosciences* **7**, 2795–2849. Available at: http://www.biogeosciences.net/7/2795/2010/.

Ringbom A., Pensar G. and Wänninen E. (1958) A complexometric titration method for determining calcium in the presence of magnesium. *Anal. Chim. Acta* **19**, 525–531. Available at: https://linkinghub.elsevier.com/retrieve/pii/S0003267000882136.

Rosenheim B. E., Swart P. K. and Thorrold S. R. (2005) Minor and trace elements in sclerosponge Ceratoporella nicholsoni: Biogenic aragonite near the inorganic endmember? *Palaeogeogr. Palaeoclimatol. Palaeoecol.* **228**, 109–129. Available at: http://linkinghub.elsevier.com/retrieve/pii/S0031018205002786 [Accessed July 4, 2013].

Rudge J. F., Reynolds B. C. and Bourdon B. (2009) The double spike toolbox. *Chem. Geol.* **265**, 420–431. Available at: http://dx.doi.org/10.1016/j.chemgeo.2009.05.010.

Russell R. D. (1971) The systematics of double spiking. *J. Geophys. Res.* **76**, 4949–4955. Available at: http://doi.wiley.com/10.1029/JB076i020p04949.

Russell W. A., Papanastassiou D. A. and Tombrello T. A. (1978) Ca isotope fractionation on the Earth and other solar system materials. *Geochim. Cosmochim. Acta* **42**, 1075–1090. Available at: http://linkinghub.elsevier.com/retrieve/pii/0016703778901059.

Santos I. R., Eyre B. D. and Glud R. N. (2012) Influence of porewater advection on denitrification in carbonate sands: Evidence from repacked sediment column experiments. *Geochim. Cosmochim. Acta* **96**, 247–258. Available at: http://dx.doi.org/10.1016/j.gca.2012.08.018.

Sargent M. C. and Austin T. S. (1954) *Biologic economy of coral reefs*.,

Sargent M. C. and Austin T. S. (1949) Organic productivity of an Atoll. *Trans. Am. Geophys. Union* **30**, 245. Available at: http://doi.wiley.com/10.1029/TR030i002p00245.

Seidel M. P., DeGrandpre M. D. and Dickson A. G. (2008) A sensor for in situ indicator-based measurements of seawater pH. *Mar. Chem.* **109**, 18–28.

Shamberger K. E. F., Feely R. A., Sabine C. L., Atkinson M. J., DeCarlo E. H., Mackenzie F. T., Drupp P. S. and Butterfield D. A. (2011) Calcification and organic production on a Hawaiian coral reef. *Mar. Chem.* **127**, 64–75.

Sharqawy M. H., Lienhard J. H. and Zubair S. M. (2010) Thermophysical properties of seawater: a review of existing correlations and data. *Desalin. Water Treat.* **16**, 354–380. Available at: http://www.tandfonline.com/doi/abs/10.5004/dwt.2010.1079.

Shen C.-C., Lee T., Chen C.-Y., Wang C.-H., Dai C.-F. and Li L.-A. (1996) The calibration of D[Sr/Ca]versus sea surface temperature relationship for Porites corals. *Geochim. Cosmochim. Acta* **60**, 3849–3858. Available at: https://linkinghub.elsevier.com/retrieve/pii/0016703796002050.

Siboni N., Ben-Dov E., Sivan A. and Kushmaro A. (2008) Global distribution and diversity of

coral-associated Archaea and their possible role in the coral holobiont nitrogen cycle. *Environ. Microbiol.* **10**, 2979–2990. Available at: http://doi.wiley.com/10.1111/j.1462-2920.2008.01718.x.

Silverman J., Kline D. I., Johnson L., Rivlin T., Schneider K., Erez J., Lazar B. and Caldeira K. (2012) Carbon turnover rates in the One Tree Island reef: A 40-year perspective. *J. Geophys. Res. Biogeosciences* **117**, 1–16. Available at: http://doi.wiley.com/10.1029/2012JG001974.

Silverman J., Lazar B., Cao L., Caldeira K. and Erez J. (2009) Coral reefs may start dissolving when atmospheric CO 2 doubles. *Geophys. Res. Lett.* **36**, 1–5. Available at: http://doi.wiley.com/10.1029/2008GL036282.

Silverman J., Lazar B. and Erez J. (2007) Community metabolism of a coral reef exposed to naturally varying dissolved inorganic nutrient loads. *Biogeochemistry* **84**, 67–82. Available at: http://link.springer.com/10.1007/s10533-007-9075-5.

Silverman J., Schneider K., Kline D. I., Rivlin T., Rivlin A., Hamylton S., Lazar B., Erez J. and Caldeira K. (2014) Community calcification in Lizard Island, Great Barrier Reef: A 33 year perspective. *Geochim. Cosmochim. Acta* **144**, 72–81. Available at: http://dx.doi.org/10.1016/j.gca.2014.09.011.

Simpson R. E. (1974) *Introductory Electronics for Scientists and Engineers*., Allyn and Bacon. Available at: https://books.google.com/books?id=pxUyAAAAMAAJ.

Smith S. V and Marsh J. A. (1973) ORGANIC CARBON PRODUCTION ON THE WINDWARD REEF FLAT OF ENIWETOK ATOLL. *Limnol. Oceanogr.* **18**, 953–961. Available at: http://doi.wiley.com/10.4319/lo.1973.18.6.0953.

Søndergaard J., Asmund G. and Larsen M. M. (2015) Trace elements determination in seawater

by ICP-MS with on-line pre-concentration on a Chelex-100 column using a 'standard' instrument setup. *MethodsX* **2**, 323–330. Available at: https://linkinghub.elsevier.com/retrieve/pii/S2215016115000382.

Spaulding R. S., DeGrandpre M. D., Beck J. C., Hart R. D., Peterson B., De Carlo E. H., Drupp P. S. and Hammar T. R. (2014) Autonomous in Situ Measurements of Seawater Alkalinity. *Environ. Sci. Technol.* **48**, 9573–9581. Available at: http://pubs.acs.org/doi/abs/10.1021/es501615x.

Stanca E. and Parsons M. L. (2017) Phytoplankton diversity along spatial and temporal gradients in the Florida Keys. *J. Plankton Res.* **39**, 531–549. Available at: http://academic.oup.com/plankt/article/39/3/531/3052905/Phytoplankton-diversity-along-spatial-and-temporal.

Steiner Z., Erez J., Shemesh A., Yam R., Katz A. and Lazar B. (2014) Basin-scale estimates of pelagic and coral reef calcification in the Red Sea and Western Indian Ocean. *Proc. Natl. Acad. Sci.* **111**, 16303–16308. Available at: http://www.pnas.org/content/111/46/16303.abstract.

Steiner Z., Turchyn A. V., Harpaz E. and Silverman J. (2018) Water chemistry reveals a significant decline in coral calcification rates in the southern Red Sea. *Nat. Commun.* **9**, 3615. Available at: http://www.nature.com/articles/s41467-018-06030-6.

Stoll H. M., Rosenthal Y. and Falkowski P. (2002) Climate proxies from Sr/Ca of coccolith calcite: calibrations from continuous culture of Emiliania huxleyi. *Geochim. Cosmochim. Acta* **66**, 927–936. Available at: https://linkinghub.elsevier.com/retrieve/pii/S0016703701008365.

Sun D., Su R., McConnaughey T. A. and Bloemendal J. (2008) Variability of skeletal growth

and δ13C in massive corals from the South China Sea: Effects of photosynthesis, respiration and human activities. *Chem. Geol.* **255**, 414–425.

Swart P., Dodge R. and Hudson H. (1996) A 240-Year Stable Oxygen and Carbon Isotopic Record in a Coral from South Florida: Implications for the Prediction of Precipitation in Southern Florida. *Palaios* **11**, 362–375. Available at: http://www.jstor.org/stable/10.2307/3515246 [Accessed December 14, 2013].

Swart P. K. (1983) Carbon and oxygen isotope fractionation in scleractinian corals: a review. *Earth-Science Rev.* **19**, 51–80. Available at: https://linkinghub.elsevier.com/retrieve/pii/0012825283900764.

Swart P. K., Greer L., Rosenheim B. E., Moses C. S., Waite A. J., Winter A., Dodge R. E. and Helmle K. (2010) The 13 C Suess effect in scleractinian corals mirror changes in the anthropogenic CO 2 inventory of the surface oceans. *Geophys. Res. Lett.* **37**, n/a-n/a. Available at: http://doi.wiley.com/10.1029/2009GL041397.

Swart P. K., Szmant A., Porter J. W., Dodge R. E., Tougas J. I. and Southam J. R. (2005) The isotopic composition of respired carbon dioxide in scleractinian corals: Implications for cycling of organic carbon in corals. *Geochim. Cosmochim. Acta* **69**, 1495–1509.

Taddei D., Cuet P., Frouin P., Esbelin C. and Clavier J. (2008) Low community photosynthetic quotient in coral reef sediments. *Comptes Rendus - Biol.* **331**, 668–677.

Takahashi T., Broecker W. S. and Langer S. (1985) Redfield ratio based on chemical data from isopycnal surfaces. *J. Geophys. Res.* **90**, 6907–6924. Available at: http://doi.wiley.com/10.1029/JC090iC04p06907.

Takeshita Y., McGillis W., Briggs E. M., Carter A. L., Donham E. M., Martz T. R., Price N. N. and Smith J. E. (2016) Assessment of net community production and calcification of a coral

reef using a boundary layer approach. *J. Geophys. Res. Ocean.* **121**, 5655–5671. Available at: http://doi.wiley.com/10.1002/2016JC011886.

Talley L. D., Feely R. A., Dickson A. G., Swift J. H., Carlson C. A., Warner M. J., McNichol A., Key R. M. and Schlosser P. (2015) Carbon Dioxide, Hydrographic, and Chemical Data Obtained During the RVIB Nathaniel B. Palmer Repeat Hydrography Cruises in the Pacific Ocean: GO-SHIP Sections P16S_2014 (20 March - 5 May, 2014). Available at: http://cdiac.ess-dive.lbl.gov/ftp/oceans/CLIVAR/P16S_2014/.

Tang J., Köhler S. J. and Dietzel M. (2008) Sr2+/Ca2+ and 44Ca/40Ca fractionation during inorganic calcite formation: I. Sr incorporation. *Geochim. Cosmochim. Acta* **72**, 3718–3732. Available at: https://linkinghub.elsevier.com/retrieve/pii/S0016703708002895.

Terlouw G. J., Knor L. A. C. M., De Carlo E. H., Drupp P. S., Mackenzie F. T., Li Y. H., Sutton A. J., Plueddemann A. J. and Sabine C. L. (2019) Hawaii Coastal Seawater CO2 Network: A Statistical Evaluation of a Decade of Observations on Tropical Coral Reefs. *Front. Mar. Sci.* **6**, 1–18. Available at: https://www.frontiersin.org/article/10.3389/fmars.2019.00226/full.

Thomson J. (2012) Wave Breaking Dissipation Observed with “SWIFT” Drifters. *J. Atmos. Ocean. Technol.* **29**, 1866–1882. Available at: http://journals.ametsoc.org/doi/abs/10.1175/JTECH-D-12-00018.1.

Tropical Rainfall Measuring Mission (2011) TRMM (TMPA) Rainfall Estimate L3 3 hour 0.25 degree x 0.25 degree V7. Available at: https://disc.gsfc.nasa.gov/datasets/TRMM_3B42_V7/summary.

Tsunogai S. (1968) Complexometric titration of calcium in the presence of larger amounts of magnesium. *Talanta* **15**, 385–390. Available at:

https://linkinghub.elsevier.com/retrieve/pii/0039914068802474.

UNESCO (1982) *Comparing Coral reef survey methods*.,

Uppström L. R. (1974) The boron/chlorinity ratio of deep-sea water from the Pacific Ocean. *Deep Sea Res. Oceanogr. Abstr.* **21**, 161–162. Available at: http://linkinghub.elsevier.com/retrieve/pii/0011747174900746.

Vahrenkamp V. C. and Swart P. K. (1990) New distribution coefficient for the incorporation of strontium into dolomite and its implications for the formation of ancient dolomites. *Geology* **18**, 387. Available at: https://pubs.geoscienceworld.org/geology/article/18/5/387-391/189009.

de Villiers S. (1999) Seawater strontium and Sr/Ca variability in the Atlantic and Pacific oceans. *Earth Planet. Sci. Lett.* **171**, 623–634. Available at: https://linkinghub.elsevier.com/retrieve/pii/S0012821X99001740.

de Villiers S., Shen G. T. and Nelson B. K. (1994) The Sr Ca-temperature relationship in coralline aragonite: Influence of variability in (Sr Ca)seawater and skeletal growth parameters. *Geochim. Cosmochim. Acta* **58**, 197–208.

Voet D. and Voet J. G. (2011) *Biochemistry*. 4th ed., John Wiley & Sons, New York.

Wanninkhof R. (1992) Relationship Between Wind Speed and Gas Exchange. *J. Geophys. Res.* **97**, 7373–7382.

Wanninkhof R. (2014) Relationship between wind speed and gas exchange over the ocean revisited. *Limnol. Oceanogr. Methods* **12**, 351–362. Available at: http://doi.wiley.com/10.4319/lom.2014.12.351.

Weber J. N. (1973) Incorporation of strontium into reef coral skeletal carbonate. *Geochim. Cosmochim. Acta* **37**, 2173–2190. Available at:

https://linkinghub.elsevier.com/retrieve/pii/001670377390015X [Accessed January 23, 2020].

Weber J. N. and Woodhead P. M. J. (1971) Diurnal variations in the isotopic composition of dissolved inorganic carbon in seawater from coral reef environments. *Geochim. Cosmochim. Acta* **35**, 891–902. Available at: http://linkinghub.elsevier.com/retrieve/pii/0016703771900032.

Wei G. J., McCulloch M. T., Mortimer G., Deng W. F. and Xie L. H. (2009) Evidence for ocean acidification in the Great Barrier Reef of Australia. *Geochim. Cosmochim. Acta* **73**, 2332–2346.

Wild C., Rasheed M., Werner U., Franke U., Johnstone R. and Huettel M. (2004) Degradation and mineralization of coral mucus in reef environments. *Mar. Ecol. Prog. Ser.* **267**, 159–171. Available at: http://www.int-res.com/abstracts/meps/v267/p159-171/.

Wilschefski S. and Baxter M. (2019) Inductively Coupled Plasma Mass Spectrometry: Introduction to Analytical Aspects. *Clin. Biochem. Rev.* **40**, 115–133. Available at: https://www.aacb.asn.au/clinical-biochemist-reviews/area?command=record&id=308&cid=109.

Zhang Z., Falter J., Lowe R. and Ivey G. (2012) The combined influence of hydrodynamic forcing and calcification on the spatial distribution of alkalinity in a coral reef system. *J. Geophys. Res. Ocean.* **117**, 1–18.

Zhong S. and Mucci A. (1989) Calcite and aragonite precipitation from seawater solutions of various salinities: Precipitation rates and overgrowth compositions. *Chem. Geol.* **78**, 283–299.

APPENDIX A: SUPPLEMENTARY MATERIALS FOR CHAPTER 2

A1. SATELLITE IMAGE ANALYSIS OF SAMPLING LOCATION

In the absence of continuous benthic survey data spanning all diel field campaigns presented in the main text, we conducted a color analysis of pixels to get a rough estimate of coral coverage on the sampled portion of Tetiaroa's reef flat (Figure A1.0.1). A Google Earth satellite image of Tetiaroa was imported into the web-based Image Color Summarizer (© 2006 – 2019, Martin Krzywinski) and partitioned into three color tag classes: (1) "paradise," (2) "gulf stream," and (3) "imprint." The 3rd category, "imprint," is the darkest color class and was used as an indicator of coral coverage. Based on this output and interpretation (detailed in RGB and HSV histograms below), the coverage of the survey area is ~21.25% coral coverage:

Figure A1.0.1. Google Earth image of Tetiaroa Atoll, French Polynesia. Marked location indicates sampling site for biogeochemical investigations explored in the main text.

IMAGE COLOR SUMMARIZER

RGB, HSV, LCH & Lab image color statistics and clustering—simple and easy

HOME ANALYZE EXAMPLES API DOWNLOAD FAQ NEWS

IMAGE COLOR SUMMARY

THE IMAGE IN WORDS

bay bounce breaker copper cutty cyan dark desaturated green gulf imprint juniper kumutoto neptune odyssey paradise patina sark scaramanga stream thor william

COLOR CLUSTERS

Colors in the image were clustered into 3 groups (k-means). The average color of the colors for each cluster is shown. The name is the closest named color and its distance is shown using ΔE. The tags are the set of words formed by all named neighbours within ΔE ≤ 5. The list of words above is the set of all unique words in this set of words.

Cluster colors, sized by number of pixels:

cluster	pixels	name	HEX	RGB	HSV	LCH	Lab	tags
	41.25%	106,156,149 paradise ΔE=2.8	#66958F	102 149 143	173 31 59	58 17 187	58 −17 −2	bounce cyan desaturated juniper paradise patina
	37.49%	128,179,174 gulf stream ΔE=2.0	#80B7B3	128 183 179	175 30 72	71 19 191	71 −19 −4	gulf kumutoto neptune stream
	21.25%	92,118,112 imprint ΔE=2.2	#5A7972	90 121 114	167 26 47	48 13 180	48 −13 0	dark bay breaker copper cutty imprint odyssey sark scaramanga thor william green

IMAGE CLUSTER PARTITIONS

Pixels of the image assigned to each cluster. The border is the color of the cluster as calculated by the average value of its pixels.

RGB HISTOGRAM

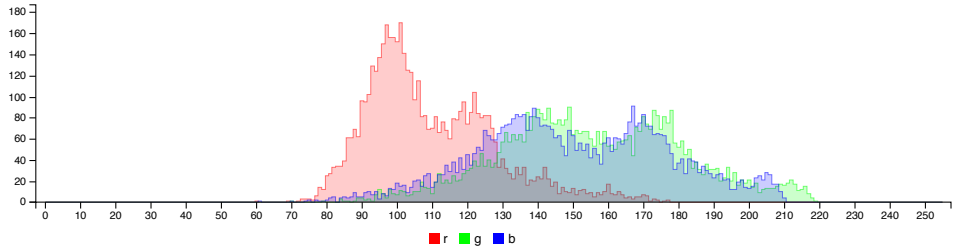

HSV HISTOGRAMS

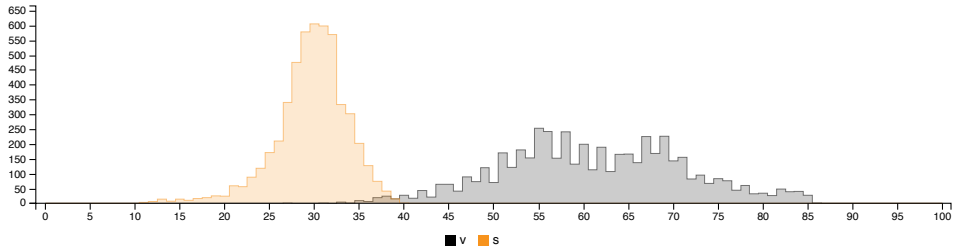

A2. RAIN & SALINITY

Time-series data of salinity-anomalies associated with rainfall (interpreted with the NASA Tropical Rainfall Measuring Mission data product) were compiled, and the maximum/minimum values of salinity associated with these events were used as inputs in Equation A1.1 to solve for residence time:

$$Sal(t) = e^{\frac{-t}{\tau}}\left(Sal_o - Sal_{final}\right) + Sal_{final} \quad \text{(A1.1)}$$

Where possible, if a month recorded multiple salinity excursions associated with rainfall, the residence times of these events were averaged to create a "mean" residence time for that particular month (± 1σ std. dev.). For excursions associated with data presented in the main text, the impact of evaporation on salinity recovery events and residence time estimates was found to be negligible on diel timescales and was estimated using evaporative heat flux of vaporization estimates from local temperature and salinity measurements in accordance with the hfbulktc.m MATLAB script (ver. 2.0, 1999) and the MIT Thermophysical Properties of Seawater function toolbox for MATLAB (Sharqawy et al., 2010; Nayar et al., 2016). A summary table of data related to this method of estimating residence times is presented below (Table A2.0.1):

Table A2.0.1. Summary of residence times recovered from the rainfall-associated salinity anomaly method. Error on residence time represents ± 1σ std. dev. for multiple averaged rain events in a particular month (where reported).

Diel Field Campaign	Salinity Minimum	Salinity Maximum	Estimated Residence Time (Hours)	Estimated Rainfall (mm)
May 2014	35.3447	35.7614	8.75 ± 6	20.3
November 2014	35.3381	35.5663	3.58 ± 2	18.3
October 2015	34.8859	35.5893	2.75	19.1
March 2017	35.6522	35.7914	5.83	15.1

A3. SUMMARY OF TUNED PARAMETERS OF EULERIAN INVERSE MODEL

A summary of the tuned parameters governing Equations 14, 15, and 16 presented in the main text is presented below (Table A3.0.1):

Table A3.0.1: Tunable parameters for the multi-box Eulerian inverse model that result in the minimization of the sum of the square of residuals between measured data (nO_2, nDIC, and nTA) and modeled data for each of the four explored field campaigns presented in the main text.

	Mixing Rate (m * hr-1)	α-PR (mol O2 or DIC * m-2 *hr-1 * µmol photons-1 * m-2 * sec-1)	PmaxO2 (mol O2 * m-2 * hr-1)	RO2 (mol O2 * m-2 * hr-1)	PmaxDIC (mol O2 * m-2 * hr-1)	RDIC (mol O2 * m-2 * hr-1)	Cmax (mol CaCO3 * m-2 * hr-1)	α-CD (mol CaCO3 * m-2 *hr-1 * µmol photons-1 * m-2 * sec-1)	C (mol CaCO3 * m-2 * hr-1)
May 14	350	0.0001	0.02	0.006	-0.022	0.005	0.0030	0.00005	0.0004
Nov 14	770	0.0001	0.03	0.0085	-0.038	0.030	0.0065	0.00005	-0.0005
Oct 15	880	0.0001	0.016	0.0045	-0.025	0.017	0.005	0.00005	0.0005
Mar 17	530	0.0001	0.043	0.014	-0.042	0.015	0.010	0.00005	-0.0002

A4. EXPLORATION OF PIECEWISE DECOMPOSITIONS OF Q

This exercise explores the impact of decomposing fluxes of nDIC, nTA, and nO_2 into hourly and net daily values of Q if piecewise rates of change (corresponding to particular periods of the day where nDIC, nTA, and nO_2 follow similar slopes) are used instead of point-by-point rate of change. This approach is done in the single box model framework. For each field campaign dataset, the total rate of change in nDIC, nTA, and nO_2 is calculated piecewise as the average over multiple time points where these constituents followed a particular slope (for example: 11 AM – 5 PM, 5 PM – 11 PM, 11 PM – 5 AM, and 7 AM – 11 AM in the May 2014 dataset). The instantaneous hourly advection and gas exchange fluxes are calculated in accordance with equations in the main text. In decomposing the remaining flux contributions due to photosynthesis/respiration and calcification/dissolution, which is interpreted as the residual of the total rate of change in nDIC, nTA, nO_2 after corrections for other processes, the total rate of change applied is specific to the timing of the particular measurement (all samples taken between 11 AM – 5 PM will have the same d[nDIC]/dt to account for, for example). In times where a sample overlaps with multiple rate of change brackets (like 5 PM), the total rate of change is taken as the average of adjacent brackets. A summary of table of the results of this exercise is presented below (Table A4.0.1):

Table A4.0.1. Summary of piecewise decomposition of Q

	Average Q (dO2/dDIC)	
March 2014	Prod.	Net Daily Q (11 - 11)
11 AM - 5 PM	-0.85	-1.08
5 PM - 11 PM	-1.15	
11 PM - 5 AM	-1.21	
7 AM - 11 AM	-4.43	
November 2014		Net Daily Q (8-8)
8 AM - 2 PM	0.44	-0.51
4 PM - 10 PM	-0.84	
10 PM - 2 AM	-1.29	
4 AM - 8 AM	-0.97	
October 2015		Net Daily Q (6-6)
6 AM - 10 AM	-0.85	-0.56
12 PM - 6 PM	-1.15	
10 PM - 6 AM	-0.33	
March 2017		Net Daily Q (12 - 12)
12 PM - 4 PM	-0.51	-1.01
4 PM - 10 PM	-1.22	
10 PM - 6 AM	-0.80	
6 AM - 12 PM	-1.20	

A5. O_2 GRADIENT EVIDENCE

This section contains the O_2 evolution gradient data collected on kayak and handheld O_2 probe (ThermoScientific ORION A329) on Tetiaroa's reef flat on 02 April 2017 between 2 PM and 4 PM local time. A heatmap of the distribution of this data near the sampling location is provided as a summary figure (Figure A5.0.1). The data represented in this figure served as the motivation for the multi-box Eulerian inverse model approach to biogeochemical decomposition.

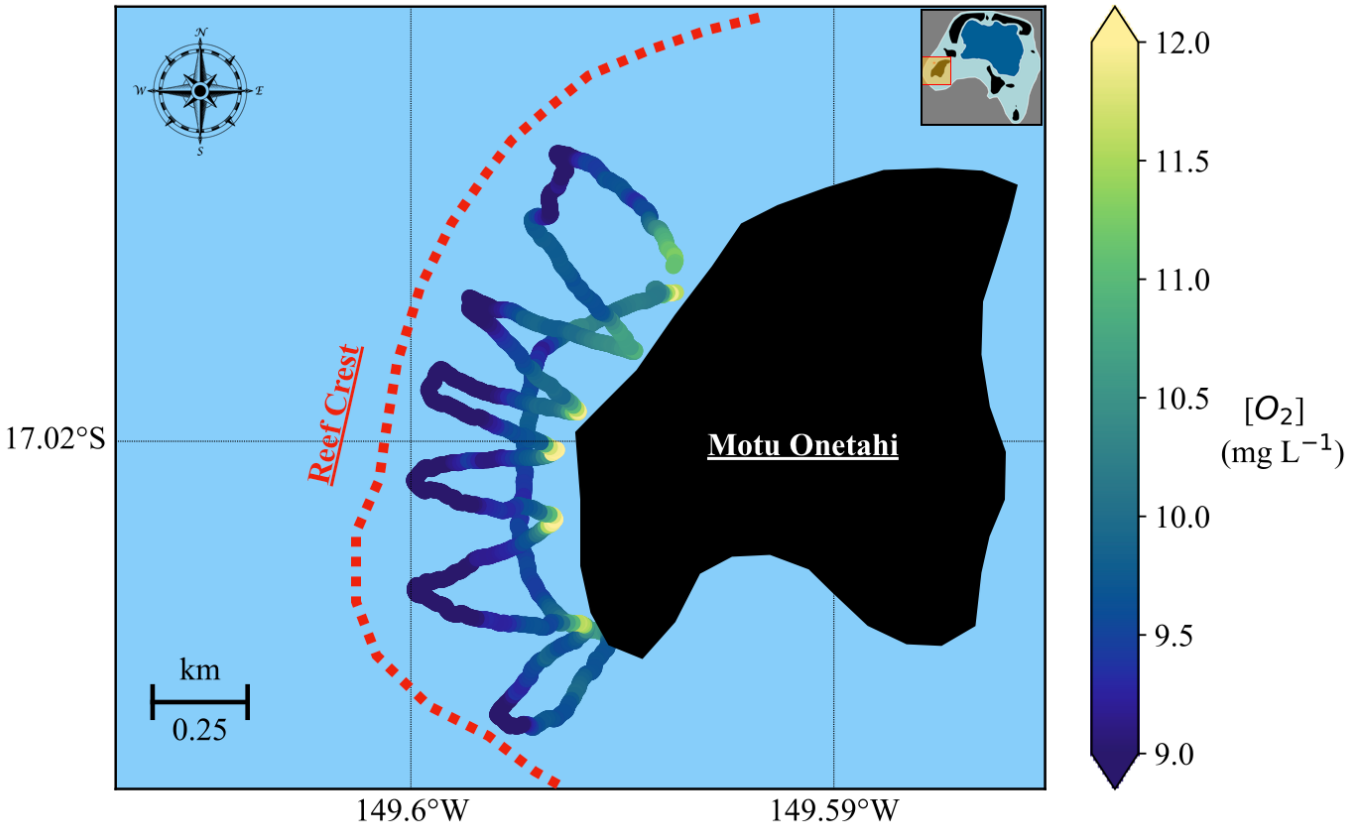

Figure A5.0.1. High spatial-resolution (~10 m) dissolved O_2 measurements from the Tetiaroa reef flat, taken by kayak between 2 PM and 4 PM on 02 April 2017, when productivity fluxes are the largest and thus easiest to observe, revealed a strong chemical gradient with concentrations generally increasing from the reef crest toward the shore. A multi-box Eulerian inverse model that faithfully reproduces both the trend in the mapped spatial gradient in dissolved oxygen and diel chemistry was used to test whether Q still differs from canonical or assumed values in a more realistic model.

A6. EXPLICIT TESTING OF ANALYTICAL UNCERTAINTY AND GAS EXCHANGE ON TEMPORAL VARIABILITY OF Q

Though observed signal-to-noise ratios for nO_2, nDIC, and nTA are quite high, the impact of their associated measurement uncertainties on measurements of Q were still of interest. A Monte Carlo propagation of just analytical uncertainty on per hour measurements of DIC, O_2, and TA reveals a slope uncertainty range of $0.002 \leq 2\sigma$ std. dev. ≤ 0.016 for all slopes presented in in the main text (Table S6.1). This error envelope is quite small given the other potential sources of error described in detail throughout the manuscript and cannot explain the observed Q_{net} deviations from canonically assumed values of O_2/DIC NEP stoichiometry alone.

Additionally, as mentioned in the main text, there is much discussion surrounding the appropriate parameterization of gas exchange in shallow, coastal reef environments, with slight nuances between different approaches, such as variability in constants used in equations and specific considerations of surface rugosity, potentially resulting in significant differences in wind speed-derived piston velocities (Wanninkhof, 1992; Cole and Caraco, 1998; Ho et al., 2006; Wanninkhof, 2014; Ho et al., 2016). Empirically-measured wind speeds for the field campaigns presented here ranged from 3 – 7 m/s. Differences in calculated piston velocities (k_{600} in $m*hr^{-1}$) for many parameterizations at these wind speeds are provided in Figure A6.0.1:

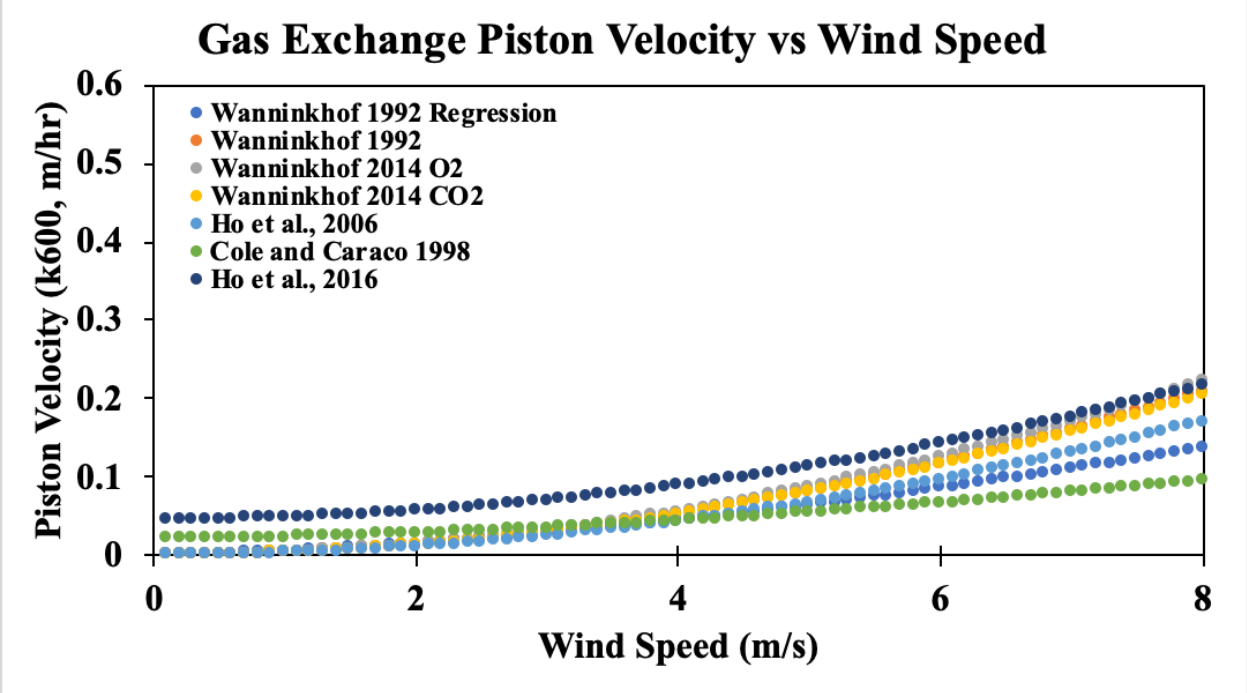

Figure A6.0.1. Calculated piston velocities (k_{600}) for O_2 and CO_2 based on wind speeds explored for many previously published parameterizations of gas exchange in marine ecosystems.

Note that, generally, differences in piston velocities between models are small in this explored range. For instance, the largest difference between models at the highest windspeed is a factor of ~ 2. However, as many parametrizations treat piston velocity as a function of wind speed exponentially, these differences are magnified as wind speed increases. Nonetheless, as a component of the hypothesis-testing exercise explored in the Monte Carlo experiment from the main text, we explored a range of piston velocities (0 – 0.6 $m*hr^{-1}$) to truly test the extent to which we could reject the null hypothesis that piston velocity differences (due either to inaccurate wind speeds or variable model parameters) could drive the observed changes in Q within and between datasets.

We further conducted a simple sensitivity analysis using the single box model where we increase piston velocities for each discrete measurement across all field campaigns by 4x their estimated amount (from local wind speeds) and subjected them to the analytical uncertainties of nDIC, nTA, and nO_2 measurements. Table A6.0.2 summarizes the key findings that per-hour Q is still highly variable, and $-1.52 \leq$ Daily $Q_{net} \leq -0.71$. The $Q_{net} = -1.52$ value (March 2017), although closer to that predicted for Redfield-like stoichiometry, implies sustained windspeeds in excess of 12 m/s throughout the day, which is inconsistent with measured wind speed data. This result implies that reasonable uncertainties in gas exchange errors alone cannot explain the deviation from canonical Redfield stoichiometric closing of metabolic carbon and oxygen budgets observed and reported on in the main text.

Table A6.0.1. Summary of error envelopes associated with analytical uncertainties on decomposition of Q

Time	Observed Q_{net}	Error
May 2014	-0.74	0.002
November 2014	-0.77	0.013
October 2015	-0.57	0.015
March 2017	-0.86	0.016

Table A6.0.2. Summary of gas exchange variability (k's increased 4x) on decomposition of Q

May 2014 Campaign

Time	**Q**
11:00	-1.13
13:00	-1.29
15:00	-1.24
17:00	-3.17
19:00	1.64
21:00	-0.63
23:00	-0.80
1:00	1.70
3:00	-6.13
5:00	-1.29

7:00	-2.88
9:00	-0.76
Daily Qnet	**-0.95**

November 2014 Campaign

Time	**Q (Single Box Model)**
6:00	0.12
8:00	-4.43
10:00	-3.12
12:00	-3.90
16:00	0.92
18:00	-0.05
22:00	-0.34
0:00	-0.35
2:00	-0.46
4:00	-0.37
Daily Q_{net}	**-0.92**

October 2015 Campaign

Time	**Q (Single Box Model)**
6:15	-0.11
8:00	-1.34
10:00	-1.90
12:00	-1.31
14:00	-1.43
16:00	-2.05
17:45	0.03
22:00	-0.52
0:04	-0.44
2:04	-0.41
4:00	-0.40
Daily Q_{net}	**-0.71**

March 2017 Campaign

Time	**Q (Single Box Model)**
12:00	-3.31
14:00	-2.53
16:00	-7.64
18:00	1.26
20:00	-0.54
22:00	-1.52
0:00	-1.96
2:00	-1.82

6:00	17.19
8:00	0.13
10:00	-1.18
Daily Q_{net}	**-1.52**

A7. MONTE CARLO EXPLORATION PLOTS FOR REMAINING FIELD DATASETS

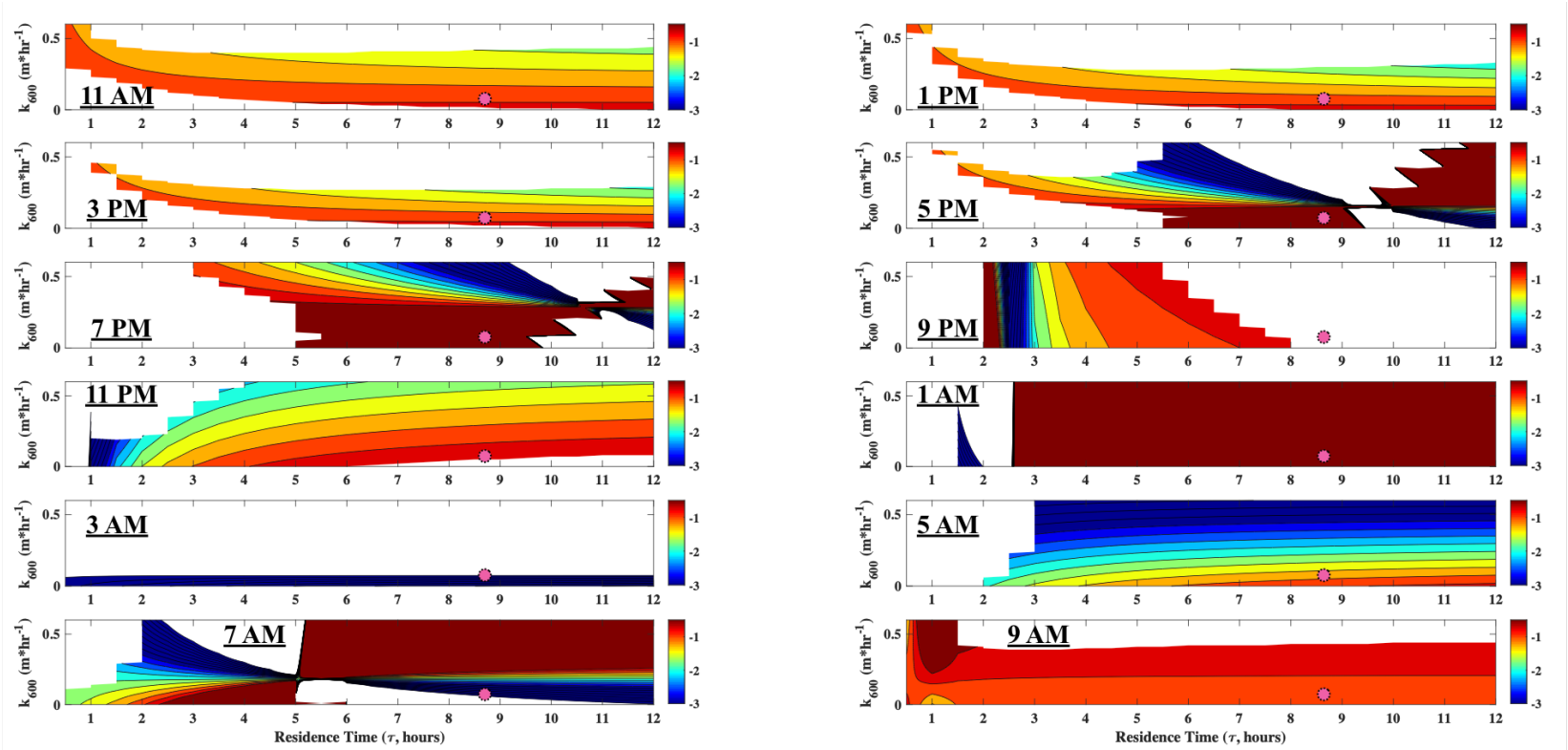

Figure A7.0.1. Single box model error propagation analysis of hourly values of Q explored over a range of residence times (12 hours at 0.5 hour resolution) and gas exchange piston velocities (k_{600} for wind speeds = 0 - 20 m/s) for Tetiaroa's reef flat (May 2014). Gas exchange parameterization followed results of Wanninkhof, 1992. Contours within each panel represent values of Q calculated at each time point from empirically measured DIC, TA, and O_2. Shaded regions correspond to values of Q where a value of -1 cannot be statistically excluded at 95% C.I. when considering analytical uncertainty on DIC, TA, and O_2 measurements errors over 5000 Monte Carlo iterations of Q inversions. In contrast, the unshaded white regions within each plot indicate locations where Q = -1 can be excluded at the 95% C.I. The position of the pink circle in each plot is indicative of the value of Q at that time point that is consistent with empirical measurements of piston velocity and precipitation + salinity anomaly-derived residence times.

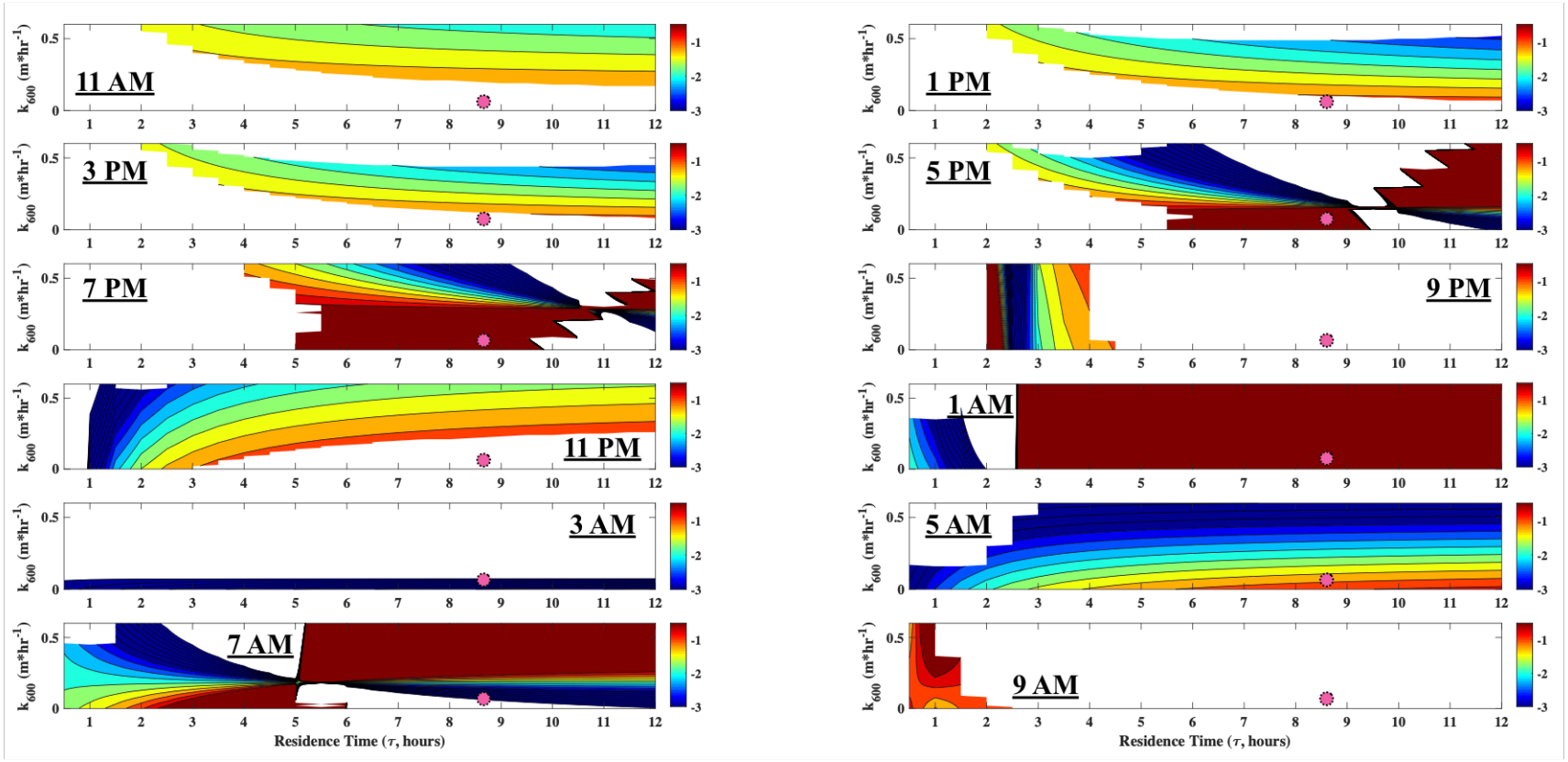

Figure A7.0.2. Single box model error propagation analysis of hourly values of Q explored over a range of residence times (12 hours at 0.5 hour resolution) and gas exchange piston velocities (k_{600} for wind speeds = 0 - 20 m/s) for Tetiaroa's reef flat (May 2014). Gas exchange parameterization followed results of Wanninkhof, 1992. Contours within each panel represent values of Q calculated at each time point from empirically measured DIC, TA, and O_2. Shaded regions correspond to values of Q where a value of -1.45 cannot be statistically excluded at 95% C.I. when considering analytical uncertainty on DIC, TA, and O_2 measurements errors over 5000 Monte Carlo iterations of Q inversions. In contrast, the unshaded white regions within each plot indicate locations where Q = -1.45 can be excluded at the 95% C.I. The position of the pink circle in each plot is indicative of the value of Q at that time point that is consistent with empirical measurements of piston velocity and precipitation + salinity anomaly-derived residence times.

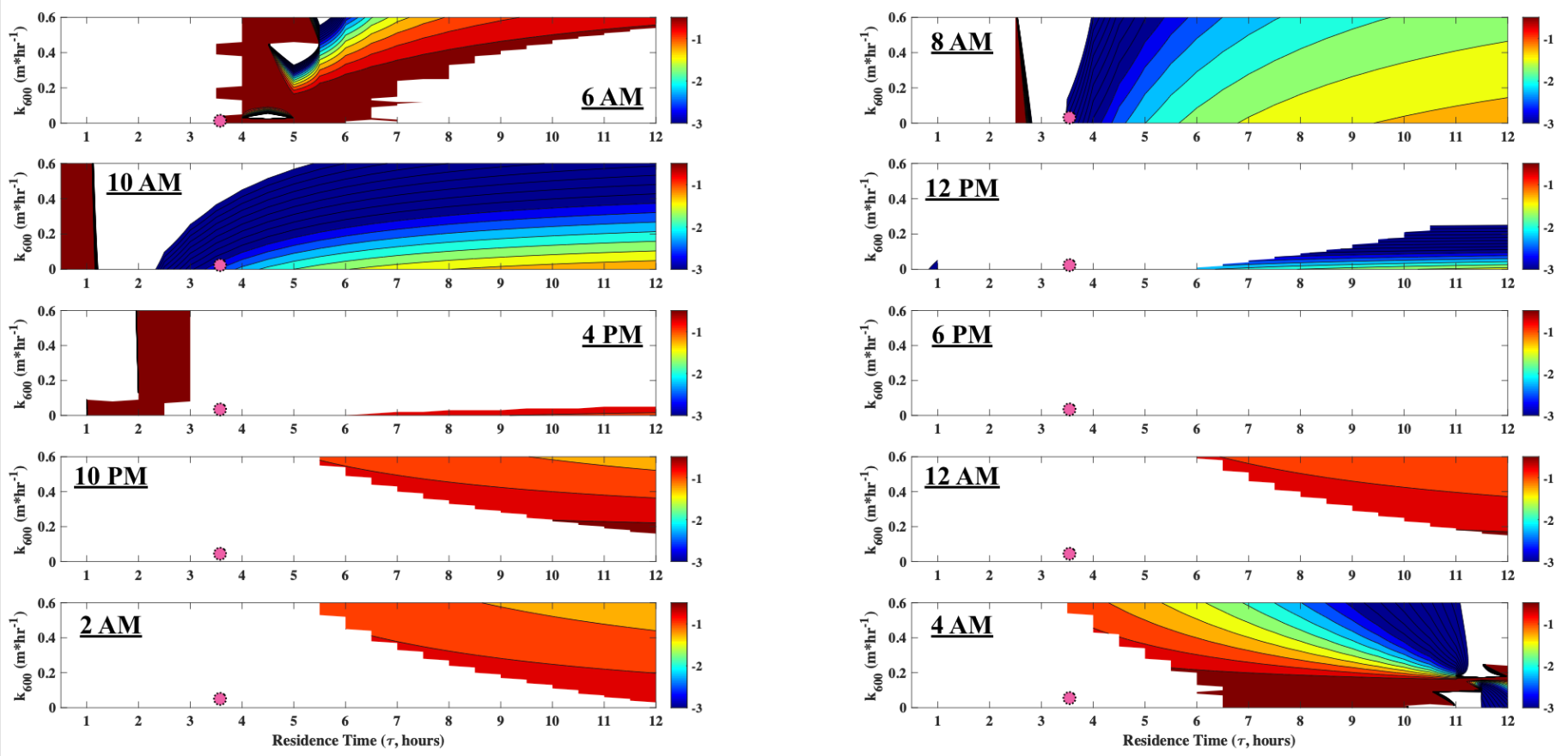

Figure A7.0.3. Single box model error propagation analysis of hourly values of Q explored over a range of residence times (12 hours at 0.5 hour resolution) and gas exchange piston velocities (k_{600} for wind speeds = 0 - 20 m/s) for Tetiaroa's reef flat (November 2014). Gas exchange parameterization followed results of Wanninkhof, 1992. Contours within each panel represent values of Q calculated at each time point from empirically measured DIC, TA, and O_2. Shaded regions correspond to values of Q where a value of -1 cannot be statistically excluded at 95% C.I. when considering analytical uncertainty on DIC, TA, and O_2 measurements errors over 5000 Monte Carlo iterations of Q inversions. In contrast, the unshaded white regions within each plot indicate locations where Q = -1 can be excluded at the 95% C.I. The position of the pink circle in each plot is indicative of the value of Q at that time point that is consistent with empirical measurements of piston velocity and precipitation + salinity anomaly-derived residence times.

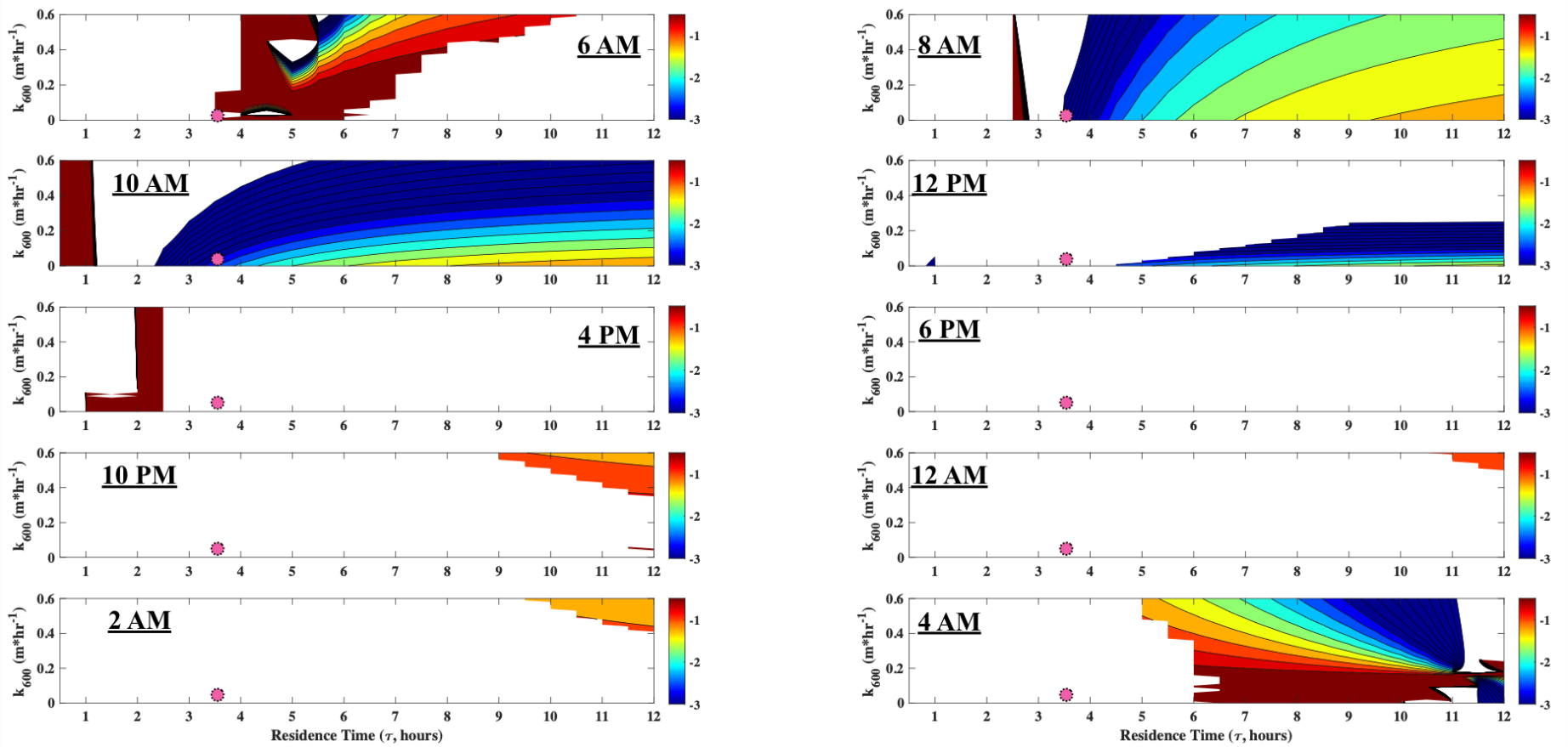

Figure A7.0.4. Single box model error propagation analysis of hourly values of Q explored over a range of residence times (12 hours at 0.5 hour resolution) and gas exchange piston velocities (k_{600} for wind speeds = 0 - 20 m/s) for Tetiaroa's reef flat (November 2014). Gas exchange parameterization followed results of Wanninkhof, 1992. Contours within each panel represent values of Q calculated at each time point from empirically measured DIC, TA, and O_2. Shaded regions correspond to values of Q where a value of -1.45 cannot be statistically excluded at 95% C.I. when considering analytical uncertainty on DIC, TA, and O_2 measurements errors over 5000 Monte Carlo iterations of Q inversions. In contrast, the unshaded white regions within each plot indicate locations where Q = -1.45 can be excluded at the 95% C.I. The position of the pink circle in each plot is indicative of the value of Q at that time point that is consistent with empirical measurements of piston velocity and precipitation + salinity anomaly-derived residence times.

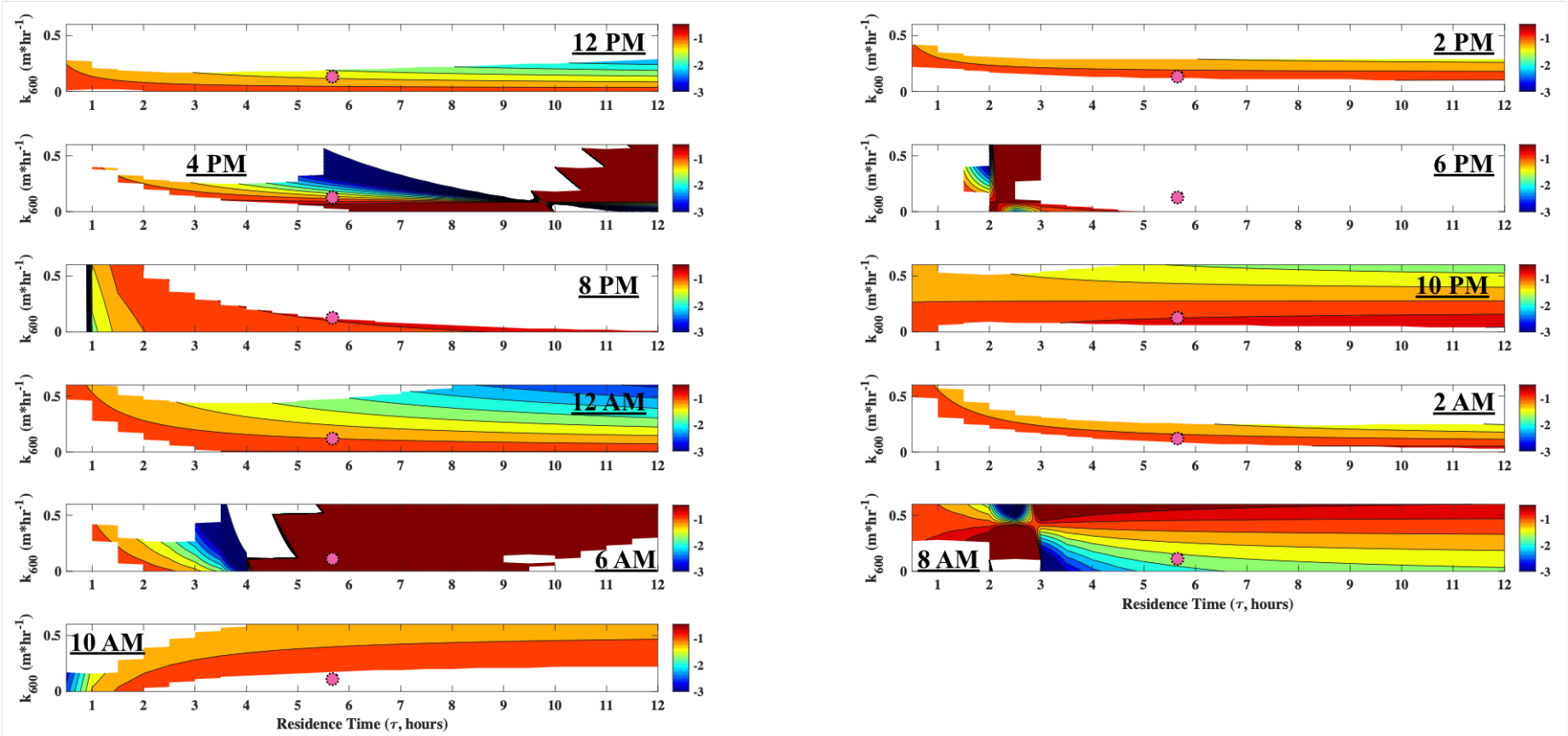

Figure A7.0.5. Single box model error propagation analysis of hourly values of Q explored over a range of residence times (12 hours at 0.5 hour resolution) and gas exchange piston velocities (k_{600} for wind speeds = 0 - 20 m/s) for Tetiaroa's reef flat (March 2017). Gas exchange parameterization followed results of Wanninkhof, 1992. Contours within each panel represent values of Q calculated at each time point from empirically measured DIC, TA, and O_2. Shaded regions correspond to values of Q where a value of -1 cannot be statistically excluded at 95% C.I. when considering analytical uncertainty on DIC, TA, and O_2 measurements errors over 5000 Monte Carlo iterations of Q inversions. In contrast, the unshaded white regions within each plot indicate locations where Q = -1 can be excluded at the 95% C.I. The position of the pink circle in each plot is indicative of the value of Q at that time point that is consistent with empirical measurements of piston velocity and precipitation + salinity anomaly-derived residence times.

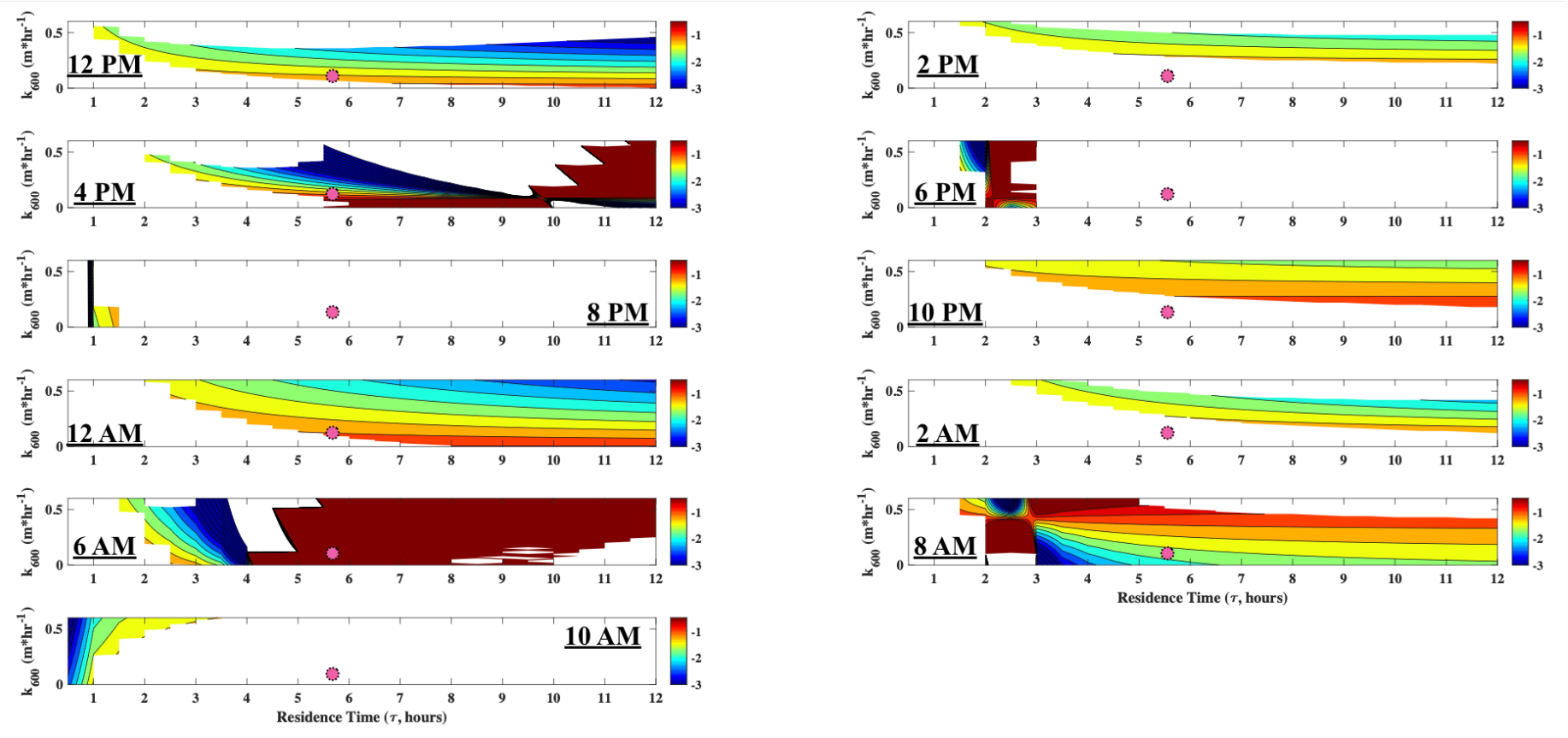

Figure A7.0.6. Single box model error propagation analysis of hourly values of Q explored over a range of residence times (12 hours at 0.5 hour resolution) and gas exchange piston velocities (k_{600} for wind speeds = 0 - 20 m/s) for Tetiaroa's reef flat (March 2017). Gas exchange parameterization followed results of Wanninkhof, 1992. Contours within each panel represent values of Q calculated at each time point from empirically measured DIC, TA, and O_2. Shaded regions correspond to values of Q where a value of -1.45 cannot be statistically excluded at 95% C.I. when considering analytical uncertainty on DIC, TA, and O_2 measurements errors over 5000 Monte Carlo iterations of Q inversions. In contrast, the unshaded white regions within each plot indicate locations where Q = -1.45 can be excluded at the 95% C.I. The position of the pink circle in each plot is indicative of the value of Q at that time point that is consistent with empirical measurements of piston velocity and precipitation + salinity anomaly-derived residence times.

A8. APPLICATION OF THE BARNES (1983) METHOD OF METABOLIC DECOMPOSITION ON REEFS

Here, we tested the impact of using an assumed Q to infer estimates of NEP and NEC for each diel dataset of nO_2, nDIC, and nTA measurements. The impact of variable values of Q on estimates of daily NEP and NEC was investigated using the data generated from the Eulerian inverse model, which is the most conservative dataset because this model architecture results in empirical Q values that are the closest to the canonical value. NEP_{DIC} is calculated by integrating the fluxes of NEP_{O2} and multiplying by Q = -1 or Q = -1.45. NEC estimates employed the analytical scheme described graphically in Fig. 1 in the main text and are algebraically identical to the approach of Barnes (1983), which itself has been applied in more recent reef metabolism investigations that relied on coupled pH and O_2 measurements (Equation A8.1, Gattuso et al., 1999b; Takeshita et al., 2016):

$$NEC = \frac{NEP_{O2} * Q + (K - K_o) * nTA_o - K * (BA + HA) + K_o * (BA_o + HA_o)}{(K - 0.5)} \quad \text{(A8.1)}$$

where "K" is an expression equivalent to the ratio of carbonate alkalinity to DIC, "BA" is borate alkalinity, "HA" is hydroxyl alkalinity, and subscript "o" denotes values of each parameter at an initial time point. K, BA, and HA are all pH dependent and can be solved independently of knowledge of DIC and/or total alkalinity. A summary table of the error associated with these assumptions is provided below, where NEC and NEP_{DIC} that resulted from measurements of nDIC and nTA are assumed to be "truth" (Table A8.0.1).

Table A8.0.1. Summary of NEP and NEC errors associated with applying Barnes (1983) methods to the Tetiaroa datasets

Time	NEP_{DIC} True (mmol C * m^{-2} * day^{-1})	NEP_{DIC} Q = -1 (mmol C * m^{-2} * day^{-1})	% Error in NEP_{DIC} (Q = -1)	NEP_{DIC} Q = -1.45 (mmol C * m^{-2} * day^{-1})	% Error in NEP_{DIC} (Q = -1.45)	NEC True (mmol $CaCO_3$ * m^{-2} * day^{-1})	NEC Q = -1 (mmol $CaCO_3$ * m^{-2} * day^{-1})	% Error in NEC (Q = -1)	NEC Q = -1.45 (mmol $CaCO_3$ * m^{-2} * day^{-1})	% Error in NEC (Q = -1.45)
May 2014	-110	-69	38	-47	57	44	-3	107	5	88
Nov. 2014	292	-142	149	-98	133	66	-90	235	-73	210
October 2015	131	-80	161	-55	142	66	25	62	28	57
March 2017	-49	-82	66	-57	15	74	15	80	6	92

A9. INVESTIGATION OF EBULLITION AS A MECHANISM TO EXPLAIN VARIABILITY IN Q

This exercise explores the daily evolution of a missing O_2 flux that would have to be accounted for in each diel dataset if Redfield-Hedges stoichiometry is regulating photosynthetic/respiratory fluxes. It also explores the extent to which standing bubble formation/dissolution/evasion can explain trends in this missing flux. For each diel campaign dataset, hourly fluxes of gas exchange, mixing, productivity, and calcification are calculated for nDIC in accordance with parameterizations used in the single box model framework. Fluxes of gas exchange and mixing are calculated similarly for O_2, but hourly NEP_{O2} is set to be equal to $-1.45*NEP_{DIC}$. The single box model then subtracts the sum of hourly productivity, mixing, and gas exchange fluxes from the total $d[nO_2]/dt$ to produce a residual, which is considered to be the implied missing flux of O_2. The 2σ standard deviation values associated with these missing fluxes are the result of a Monte Carlo error propagation of 5000 iterations using random, normally-distributed numbers around the instrumental uncertainties of DIC (± 3.7 µmol*kg^{-1}), TA (± 4.3 µmol*kg^{-1}), and O_2 (± 4 µmol*kg^{-1}) analysis. In exploring the impact of standing bubbles, calculations involved calculating pressure of a bubble at depth (P_B), which is equal to the pressure of the atmosphere at the surface of the ocean + hydrostatic pressure. The pressure of O_2 inside the bubble can be expressed as:

$$P_{O2} = (P_B - P_{H2O}) * X_{O2}$$

where P_{H2O} is the partial pressure of water vapor and X_{O2} is the mole fraction of O_2 in the bubble. Using Henry's Law, $P_{O2}*K_{H,O2} = [O_2]_{aq}$. So, $(P_B - P_{H2O}) * X_{O2} = P_{O2} = [O_2]_{aq} / K_{H,O2}$…or:

$$X_{O2} = \frac{[O_2]_{aq}}{K_{H,O2} * (P_B - P_{H2O})}$$

The number of moles of total gas in bubbles can be expressed as $n_{gas} = n_{O2\ Missing} / X_{O2}$. We then use the ideal gas law, PV = nRT, to solve for volume of bubbles needed to explain the missing O_2 fluxes. We also assume the bubbles have an average diameter of 4 mm and generally follow the shape of a sphere ($V = 4/3\pi r^3$). A summary of the parameters used in the bubble exploration and the associated errors are provided in Table A9.0.1. This summary is meant to accompany Figures 2.7 and 2.8 in the main text.

Table A9.0.1. Summary of bubble parameters and missing O_2 flux behavior assuming canonical Redfield stoichiometry.

Let kH O2 (µmol*kg-1*atm-1)	981
Let kH CO2 (µmol*kg-1*atm-1)	32782
Let pH2O (atm)	0.0379
Let pB (atm @ 1 m depth)	1.1
Let R (L*atm*K-1*mol-1)	0.08205

Let Average *Porites* polyp size (mm)	4
Polyp Bubble Volume (mm3)	33.51
Polyp Bubble Volume (L)	3.351E-05

May 2014 Campaign

Time	Implied Missing O2 Flux (µmol*kg-1*hr-1)	Error in Flux (2sig, based on instrumental error)
11:00	-13.10	9.30
13:00	-10.70	9.35
15:00	-12.53	9.32
17:00	-8.32	9.36
19:00	-9.48	9.30
21:00	17.07	9.32
23:00	12.24	9.30
1:00	-13.09	9.30
3:00	-3.59	9.31
5:00	4.39	9.35
7:00	6.41	9.36
9:00	-9.38	9.36
11:00	9.56	

November 2014 Campaign

Time	Implied Missing O2 Flux (µmol*kg-1*hr-1)	Error in Flux (2sig, based on instrumental error)
6:00	8.60	8.06
8:00	13.02	8.06
10:00	9.36	8.06
12:00	10.26	3.71

16:00	16.50	8.06
18:00	29.04	3.70
22:00	33.87	8.13
0:00	35.93	8.09
2:00	37.12	8.09
4:00	27.48	8.10
6:00	26.24	

October 2015 Campaign

Time	Implied Missing O2 Flux (µmol*kg-1*hr-1)	Error in Flux (2sig, based on instrumental error)
6:00	4.279397623	8.976843625
8:00	-1.933686287	7.565587405
10:00	0.333297136	7.628113533
12:00	-4.919880566	7.68834091
14:00	-2.896943674	7.695982667
16:00	-0.970814681	8.969439616
17:45	12.11043001	3.937574661
22:00	17.06838885	7.319006208
0:04	26.25052575	7.656055354
2:04	22.56020188	7.986900907
4:00	24.52742729	7.684216052
6:00	18.89073139	

March 2017 Campaign

Time	Implied Missing O2 Flux (µmol*kg-1*hr-1)	Error in Flux (2sig, based on instrumental error)
12:00	0.469335275	8.865146958

14:00	-13.49045987	8.808223233
16:00	4.586612338	8.818821538
18:00	27.28014311	8.84560634
20:00	17.37674905	8.799736399
22:00	10.90895533	8.814475613
0:00	5.329258471	8.795983134
2:00	7.566690236	3.846972148
6:00	-13.50196859	8.828170851
8:00	-0.555892242	8.781302491
10:00	-22.12584993	8.780223386
12:00	-3.057549453	

APPENDIX B: SUPPLEMENTARY MATERIALS FOR CHAPTER 3

B1. SR/CA DOUBLE MIXED SPIKE SCRIPT (FOR MATLAB)

Double Mixed Isotope Spike Inversion Script (for Sr/Ca ratios)

Table of Contents

Isaiah W. Bolden, School of Oceanography - University of Washington. Fall 2018

Introduction

The interactive impacts of environmental stressors within coral reef environments could translate to large reductions in rates of net ecosystem calcification (NEC), which will only be intensified by ocean acidification. While corals themselves are negatively impacted by the decreasing saturation state of carbonate ion (CO32-) that is associated with increasing seawater pCO2, acidified environments have a range of effects on the calcification of other marine organisms within a reef ecosystem, like calcitic coralline algae (Ries et al., 2009). The future impact of ocean acidification at this community level is still unclear. Should highly sensitive coral species be replaced by more acid-tolerant coral species as acidification increases, then future reef ecosystems may behave similarly to current reefs. Conversely, if ocean acidification leads to the replacement of corals by non-reef building communities, then the loss of coral could destabilize the entire reef ecosystem. New tools that detect potential trophic-level regime shifts from corals to other calcifiers could dramatically increase our ability to identify the early signs of this transition, quantify the rate of this shift where it occurs and help manage the impacts of ocean acidification in reef ecosystems.

Conventional measurements of TA and DIC quantify the amount of calcification/dissolution on reef ecosystems without identifying what is calcifying. The signature of calcifying organisms is recorded in seawater, however, making it theoretically possible to distinguish the organisms undergoing calcification or dissolution through their distinct geochemical fingerprints. Specifically, the partition coefficient of strontium (DSr), is different for coral aragonite (DSr ~ 1.1 - 1.2) as compared to high-Mg calcite organisms like coralline algae (DSr ~ 0.28 - 0.45), which is an incredibly useful piece of information for monitoring trophic level calcification dynamics (Dietzel et al., 2004; Gaetani and Cohen, 2006; Gagnon, 2010; Gagnon et al., 2007; Hetzinger et al., 2011; Zhong and Mucci, 1989). This concept has been applied to Sr/Casw as means to separate the calcification signals of coral from pelagic algae on a basin-wide scale in the Red Sea, a unique location where very large spatial gradients in calcification are observed (Steiner et al., 2014). If this technique were adapted to detect the subtler changes in Sr/Casw within and between coral reef environments, it could complement carbonate chemistry estimates of NEC across diel and seasonal cycles by quantifying community percent contributions to calcification budgets. Additionally, Sr/Casw could then be used as a tool from which to monitor the rate at which calcification regimes may change with time as ambient acidity increases. This would be particularly useful given that the high-Mg calcites of coralline algae have been shown to be much more sensitive to ocean acidification than the aragonites

of scleractinian corals (Andersson et al., 2008; Burton and Walter, 1987; Ries, 2010). However, simple single-box model estimates of alkalinity fluxes attributed to calcification/dissolution using diel data from Tetiaroa suggests that variability in reef Sr/Casw can be quite small in magnitude, with a maximum offset from open ocean seawater on the order of 100 ppm if all calcification was from aragonite precipitation and 160 permil offset if all calcification was due to coralline algae precipitation. An analytical technique capable of determining these extremely subtle changes in Sr/Casw with high precision and accuracy warrants development if this tool is to have any truly practical applications.

Thermal ionization mass spectrometry (TIMS) has historically been used to obtain Sr/Ca ratios from solutions of coral skeletons with demonstrated precision of up to ± 0.03% (2 sigma), a level unmatchable by inductively coupled plasma (ICP) methods of mass or optical emission spectrometry (Beck et al., 1992; Schrag, 1999). Additionally, isotope dilution (ID) has been coupled with mass spectrometry measurements of both seawater Sr and Ca to obtain total elemental concentrations at the precision and accuracy levels of isotope ratios (> 0.5%, Bernat et al., 1972; Liu et al., 2014). Analyses of Sr/Ca in solid carbonates that have been enriched with less abundant isotopes of Sr and Ca (mixed spike) have been shown to carry precisions of up to 0.4% (2 sigma), with magnetic sector ICP-MS as the instrument of choice (Fernandez et al., 2010). Combining the mixed spike isotope dilution technique with the high precision and control of TIMS may result in unprecedented levels of precision with which small temporal variations in Sr/Casw can be distinguished. Furthermore, as both strontium and calcium have four or more naturally occurring isotopes, TIMS measurements of Sr/Casw can be corrected for instrumental mass fractionation within the mass spectrometer through spiking the sample with two enriched isotopes of Sr and Ca (double spike), providing an additional constraint on analytical precision (Dodson, 1963; Rudge et al., 2009).

Goals

We aim to use double mixed spike isotope dilution thermal ionization mass spectrometry (DMS-ID-TIMS) to develop a method for detecting minute variability in Sr/Casw. We will make repeated measurements of a stock seawater solution and assess the level of precision obtained by this technique in comparison with the precision needed to draw valid conclusions from observed variability in discrete diel samples of Sr/Casw from coral reefs.

Double spike experiments not only require analytes of interest to have more than three isotopes (three independent isotope ratios must be used in the inversion of a system of equations to solve for concentrations), but the ratio of single spikes in the double spike mixture and the double spike to sample mixing ratio must be optimized as well to minimize error in any inverted variables.

Typically, double spike isotope dilution experiments are designed such that error on natural or instrumental fractionation factors (alpha or beta, respectively) or a particular isotope ratio of interest is minimized. However, in this case, the isotope dilution method is part of a double *mixed* spike (where isotopes of both Sr and Ca will be enriched in the spike) for the ultimate determination of relative Sr/Ca ratios of any given sample. The ratio of moles of reference isotope in the sample compared to the spike can be expressed as:

(1 - chi-ds) / chi-ds = "F" (for either Sr or Ca)...

...where "chi-ds" is the proportion of double spike solution in the double spike + sample mixture. Eventually, for any given sample, F-Sr will be divided by the corresponding F-Ca to yield a measure of the Sr/Ca ratio of the sample with reference to a natural standard (and defined in terms of 88Sr and 44Ca). Therefore, minimizing the error on inversions of "F" as a function of both the single spikes in the double spike mixture and overall double spike to sample ratio will be essential in the application of isotope dilution here.

This script iteratively optimizes the best choice of single isotope spikes in the double spike mixture for both Sr and Ca, and it further optimizes the overall double spike to sample mixing ratio in the final mixture that is run through a mass spectrometer. The user is given a list of respective mixing ratios that minimize errors in their choice of alpha, beta, isotope ratio, or "F."

Summary of Results

We find that, for an 84-87Sr + 43-48Ca double spike (using Oak Ridge National Laboratory certified single element spikes), the error-minimizing mixing ratios are (focusing on sample-to-spike moles of reference isotope):

0.27 moles 84Sr single spike to 0.73 moles 87Sr single spike and 0.58 moles 43Ca single spike to 0.42 moles 48Ca single spike in the overall double mixed spike mixture...

0.22 moles of the 84-87Sr double spike to 0.78 moles sample -AND-

0.19 moles of the 43-48Ca double spike to 0.81 moles sample...

...though the error minimizing trough actually spans a range of potential mixing ratios, giving the user some range of allowable uncertainty while still capturing greater than 100 ppm precision. For example, mean relative error on "F" across all double spike-to-sample mixing ratios is below 20 ppm for the 0.15 to 0.59 range of ORNL 84Sr single spike proportions in the double mixture (Fig. 1A). At the "ideal" 84Sr proportion (0.27), better than 10 ppm relative error in "F" is observed for the 0.08 - 0.74 range of Sr double spike to sample ratios (Fig. 2A). In the Ca system, mean relative error on "F" is below 100 ppm across all ORNL 43Ca single spike proportions in the double spike mixture and better than 20 ppm in the range 0.22 - 0.92 (Fig. 3A). At the "ideal" 43Ca proportion (0.58), better than 10 ppm relative error in F is observed for the 0.06 - 0.50 range of Ca double spike to sample ratios (Fig. 4A).

These *ideal* values of mixing ratios will be used in a separate script (**Double Mixed Isotope Spike Calibration Script**) that will numerically calibrate the composition of spike, which is needed as an input in the overall double spike inversion.

Run Code: Construct Reference Matrices for both Ca and Sr.

Begin a runtime clock, clear the cache and workspace of any previous variables, and build reference Ca and Sr matrices that will house "global" Ca and Sr atomic masses, abundances, standard compositions, and spike compositions.

```
tic

clear all
format long

load Ca_Ref
load Sr_Ref
```

Both Ca_Ref and Sr_Ref are formatted with rows corresponding to isotopes (40, 42, 43, 44, 46, and 48 for Ca and 84, 86, 87, and 88 for Sr) and columns corresponding to [Isotope Atomic_Mass Standard_Comp Enriched_Spike_1...Enriched_Spike_n]. All experiments here assume a 43Ca-48Ca double spike (columns 6 and 9 of Ca_Ref) and an 84Sr-87Sr double spike (columns 4 and 6 of Sr_Ref).

Run Code: Calculate "typical" Beam CPS for Major Ca and Sr Ion Beams.

This conversion of beam voltages to counts per second (cps) will allow for better estimates of the errors associated with counting statistics and shot noise on overall Ca and Sr isotope ratios.

```
cps_Ca = zeros(6,3);
SN_RelErr_Ca = zeros(6,1);
cps_Sr = zeros(4,3);
SN_RelErr_Sr = zeros(4,1);
```

After pre-allocating the necessary arrays, prescribe a value for the 40Ca and 88Sr beam voltages (V_40 and V_88) on the MS instrument. A value of 20 volts for 40Ca and 2 volts for 88Sr (Compston et al. 1965) has been pre-assigned based on October 2018 calibration run data. Use V = I*R to calculate the respective currents (I, in amps) of each beam using a 1E11 ohm resistor (R). The value of 1 Coulomb in electrons will be necessary in the final conversion of all isotope currents to counts per second, so that constant is also prescribed here.

```
V_40 = 20;
R = 1E11;
I_40 = V_40 / R;

Coulomb = 6.242E18;

V_88 = 2;
I_88 = V_88 / R;
```

Run Code: Run the Inversion Script on Synthetic Sr Mixtures

First, the script will iterate through combinations of single-spikes in the double spike mixture, combinations of double spike to sample, and error due to counting stats/shot noise to optimize the single-spike ratio that gives the minimizes relative error in multiple variables of interest.

The isotopes of any given sample are fractionated with respect to a standard (whole mean Earth or otherwise) in accordance with the exponential law:

Rsmp = RNat * (MW_a / MW_b)^(alpha) ... where MW_a and MW_b are the exact masses of isotopes a and b of an element.

The same can be said for a spiked sample which, when run through a mass spectrometer, will be further fractionated from its "isotope" composition:

Rmeasured = RMixture * (MW_a / MW_b)^(beta).

Note that in both equations, the respective quantities (MW_a / MW_b)^(alpha) and (MW_a / MW_b)^(beta) are equivalent the relative "ratio of ratios" in each case. Relative (permil or otherwise) deviations between "sample" vs "natural" and "measured" vs "true" can be expressed using this notation. To make a synthetic mixture that will be used in the double spike inversion, first prescribe values for alpha and beta.

```
Alpha = 0.01;
Beta = -0.07;
```

Build arrays to hold the overall output of 84-87 proportions in the double spike mixture (chi-84 and chi-87), double spike to sample proportions (chi-ds), inverted isotope ratios, and inverted solutions to alpha, beta, and the double spike to sample mixing ratio (chi-ds).

```
S_SingleSpk_DblSpk = zeros(length(0.01:0.01:0.99),
 length(0.01:0.01:0.99), 9);
S_DblSpk_Sample = zeros(length(0.01:0.01:0.99),9);
```

```
S_Mean_Err = zeros(length(0.01:0.01:0.99),2);
S_Mean_PerMil_Dev = zeros(length(0.01:0.01:0.99),5);
S_Mean_Invert_Vector = zeros(length(0.01:0.01:0.99),4);

ii = 1;
```

The iteration steps are as follows: 1). Choose a chi-84. Note - chi-87 = 1 - chi-84.

```
for Chi_SingleSpk1_Sr = 0.01:0.01:0.99

        Chi_SingleSpk2_Sr = 1 - Chi_SingleSpk1_Sr;
        jj = 1;
```

2). For that chosen chi-84 and chi-87, choose a chi-ds. Note that chi-sample = 1 - chi-ds.

```
    for Chi_Sr_DblSpk = 0.01:0.01:0.99
```

3). Create a mixture of a synthetic sample and double spike using the preset values for alpha and beta, the chosen mixing ratios, and the data from the Sr_Ref global values. RNat are the values of the isotope abundances in the natural standard referenced to 88Sr. RDbl_Spk are the isotope abundances in the double spike mixture referenced to 88Sr. RMixture represents the "true" isotope ratios of the sample+spike mixture, whereas Rmixture represents the measured value after the sample was subjected to some amount of instrumental mass fractionation inside of the mass spectrometer. Abundances of isotopes are used in the calculation of chi-84 and chi-87, while all ratios, chi-ds, and chi-sample values are with respect to 88Sr.

```
        R_Nat_Sr = Sr_Ref(:,3) ./ Sr_Ref(4,3);
        Abd_DblSpk_Sr = (Chi_SingleSpk1_Sr .* Sr_Ref(:,4)) +
 (Chi_SingleSpk2_Sr .* Sr_Ref(:,6));
        R_DblSpk_Sr = Abd_DblSpk_Sr ./ Abd_DblSpk_Sr(4,1);

        MW_Sr = Sr_Ref(:,2) ./ Sr_Ref(4,2);
        rSample_Sr = R_Nat_Sr .* (MW_Sr) .^ (Alpha);
        rMixture_Sr = Chi_Sr_DblSpk .* R_DblSpk_Sr + (1 -
 Chi_Sr_DblSpk) .* rSample_Sr;
        rmixture_Sr = rMixture_Sr .* (MW_Sr) .^ (Beta);
```

4). Calculate the cps of each Sr isotope given the supplied voltage of the 88Sr ion beam. Calculate the total counts of each isotope using these values and a total collection time of 10 minutes. Compute the relative error (Poisson Stats) in total counts of each isotope with respect to 88Sr.

```
        cps_88 = I_88 * Coulomb;
        cps_84 = cps_88 * (rmixture_Sr(1,1) / rmixture_Sr(4,1));
        cps_86 = cps_88 * (rmixture_Sr(2,1) / rmixture_Sr(4,1));
        cps_87 = cps_88 * (rmixture_Sr(3,1) / rmixture_Sr(4,1));

        cps_Sr(1,1) = cps_84;
        cps_Sr(2,1) = cps_86;
        cps_Sr(3,1) = cps_87;
        cps_Sr(4,1) = cps_88;

        cps_Sr(:,2) = cps_Sr(:,1) .* 60 .* 10;

        cps_Sr(1,3) = sqrt(cps_Sr(1,2)) / cps_Sr(1,2);
        cps_Sr(2,3) = sqrt(cps_Sr(2,2)) / cps_Sr(2,2);
        cps_Sr(3,3) = sqrt(cps_Sr(3,2)) / cps_Sr(3,2);
```

```
cps_Sr(4,3) = sqrt(cps_Sr(4,2)) / cps_Sr(4,2);

SN_RelErr_Sr(1,1) = sqrt((cps_Sr(1,3))^2 + (cps_Sr(4,3))^2);
SN_RelErr_Sr(2,1) = sqrt((cps_Sr(2,3))^2 + (cps_Sr(4,3))^2);
SN_RelErr_Sr(3,1) = sqrt((cps_Sr(3,3))^2 + (cps_Sr(4,3))^2);
SN_RelErr_Sr(4,1) = sqrt((cps_Sr(4,3))^2 + (cps_Sr(4,3))^2);
```

5). Incorporate this error as Counting Statistics (Shot Noise) to the measured Rmixture values using a Monte Carlo simulation of 1000 iterations of normally-distributed random values around a mean of the counting stats relative error of each isotope ratio.

```
k = 1000;
num_iterations_Sr = k;
rm_Sr_matrix = zeros(size(rmixture_Sr,1), size(rmixture_Sr,2),
num_iterations_Sr);
invert_vector_Sr_err = zeros(num_iterations_Sr, 3);
permil_dev_Sr = zeros(size(rmixture_Sr,1), num_iterations_Sr);
F_s_Sr = zeros(num_iterations_Sr, 1);
initial_guess_Sr = [0.001, 0.001, 0.2];
```

6). For each Monte Carlo iteration, an optimization function will use these new values of Rmixture with error together with true values of RNat, RDbl_Spk, and the ratio of isotope weights to invert the values of alpha, beta, and chi-ds using no additional information. The optimization function uses an initial guess of alpha, beta, and chi-ds to create synthetic mixtures using similar logic as step 2 above, reporting the values of alpha, beta, and chi-ds that correspond with the minima in the sum of the square of the residuals between the calculated Rmixture inside of the optimization function and the true values of Rmixture with error from counting statistics.

7). Because of the importance of F-Sr (and F-Ca), pre-allocated arrays are designed to hold its values at each iteration.

8). The inverted vector of alpha, beta, and chi-ds for each Monte Carlo iteration is used in a subsequent function that uses that information along with true values of RNat, RDbl_Spk, and the ratio of isotope weights to calculate an empirical RSample, RMixture, and Rmixture. The permil deviations of the empirical Rmixture from the true Rmixture values are also computed.

```
for i = 1:num_iterations_Sr
    Sr_Rand = rmixture_Sr .* (1 + SN_RelErr_Sr .*
randn(size(rmixture_Sr,1),1));
    rmixture_Sr_err = Sr_Rand;

    fun_pass_rm_Sr = @(x)RMTESTfn_search_Sr(x,
rmixture_Sr_err, R_Nat_Sr, R_DblSpk_Sr, MW_Sr);
    options =
optimset('TolFun',1e-15,'TolX',1e-9,'MaxIter',1000000,'MaxFunEvals',5000);
    invert_vector_Sr =
fminsearch(fun_pass_rm_Sr,initial_guess_Sr,options);

    initial_guess_Sr = invert_vector_Sr;
    invert_vector_Sr_err(i,:) = invert_vector_Sr;
    Chi_i = invert_vector_Sr(3);
    F_s_Sr(i) = (1 - Chi_i) / Chi_i;
    [Solved_Out_Sr] = RMTESTfn_Sr(invert_vector_Sr(1),
invert_vector_Sr(2), invert_vector_Sr(3), R_Nat_Sr, R_DblSpk_Sr,
MW_Sr);
```

```
            rm_Sr_matrix(:,:,i) = Solved_Out_Sr(:,3);
            permil_dev_Sr(:,i) = ((Solved_Out_Sr(:,3) ./ rmixture_Sr)
 - 1) * 1E3;
        end
```

9). Calculate the relative error in F-Sr values and the mean values of permil deviations between empirical and true Rmixture for this particular choice of chi-ds. Collapse all permil deviations for each isotope ratio, empirical alphas, betas, and chi-ds's into averages across all Monte Carlo iterations. Continue iterating through steps 2-8 until all data for the final value of chi-ds at this given chi-84 and chi-87 has been allocated.

```
        relerrFsample_Sr = std(F_s_Sr) / mean(F_s_Sr);
        S_DblSpk_Sample(jj,:) = [Chi_Sr_DblSpk relerrFsample_Sr
 mean(permil_dev_Sr(1,:)) mean(permil_dev_Sr(2,:))
 mean(permil_dev_Sr(3,:)) mean(permil_dev_Sr(4,:))
 mean(invert_vector_Sr_err(:,1)) mean(invert_vector_Sr_err(:,2))
 mean(invert_vector_Sr_err(:,3))];
        jj = jj + 1;

    end
```

10). For any given chi-84, collapse all output from the chi-ds loop into averages across all chi-ds iterations. Repeat steps 1-9 until data for all chi-84's has been allocated.

```
    mean_relerrFsample_Sr = mean(S_DblSpk_Sample(:,2));
    S_Mean_Err(ii,:) = [Chi_SingleSpk1_Sr mean_relerrFsample_Sr];

    mean_permil_dev_84 = mean(S_DblSpk_Sample(:,3));
    mean_permil_dev_86 = mean(S_DblSpk_Sample(:,4));
    mean_permil_dev_87 = mean(S_DblSpk_Sample(:,5));
    mean_permil_dev_88 = mean(S_DblSpk_Sample(:,6));

    mean_alpha_Sr_err = mean(S_DblSpk_Sample(:,7));
    mean_beta_Sr_err = mean(S_DblSpk_Sample(:,8));
    mean_Chi_Sr_err = mean(S_DblSpk_Sample(:,9));


    S_Mean_Invert_Vector(ii,:) = [Chi_SingleSpk1_Sr mean_alpha_Sr_err
 mean_beta_Sr_err mean_Chi_Sr_err];
    S_Mean_PerMil_Dev(ii,:) = [Chi_SingleSpk1_Sr mean_permil_dev_84
 mean_permil_dev_86 mean_permil_dev_87 mean_permil_dev_88];
    S_SingleSpk_DblSpk(ii,:,:) = S_DblSpk_Sample;
    ii = ii + 1;

end
```

Run Code: Find the Error-Minimizing Mixing Ratios & Plot the Distribution of Error - Strontium

11). Find the values of chi-84 across all chi-ds that correspond with respective minima in relative error in F-Sr, permil deviations in 86/88Sr ratios, empirical alpha's and beta's.

```
tmp1 = S_Mean_Err(:,2);
idx1 = find(tmp1 == min(tmp1));
Chi_84Sr_Opt_FSr = S_Mean_Err(idx1,1)

tmp1_isotopes = S_Mean_PerMil_Dev(:,3);
idx1_isotopes = find(tmp1_isotopes == min(tmp1_isotopes));
Chi_84Sr_Opt_8688 = S_Mean_PerMil_Dev(idx1_isotopes,1)

tmp1_alpha = abs(S_Mean_Invert_Vector(:,2) - Alpha);
idx1_alpha = find(tmp1_alpha == min(tmp1_alpha));
Chi_84Sr_Opt_Alpha = S_Mean_Invert_Vector(idx1_alpha,1)

tmp1_beta = abs(S_Mean_Invert_Vector(:,3) - Beta);
idx1_beta = find(tmp1_beta == min(tmp1_beta));
Chi_84Sr_Opt_Beta = S_Mean_Invert_Vector(idx1_beta,1)
```

```
Chi_84Sr_Opt_FSr =

   0.220000000000000


Chi_84Sr_Opt_8688 =

   0.010000000000000


Chi_84Sr_Opt_Alpha =

   0.150000000000000


Chi_84Sr_Opt_Beta =

   0.590000000000000
```

12). Plot the distribution of errors in F-Sr, permil deviations in 86/88Sr ratios, empirical alphas and betas vs chi-84s. Use 100 ppm relative error as a key threshold.

```
figure(1)
clf
subplot(2,2,1)
plot(S_Mean_Err(:,1),S_Mean_Err(:,2),'ro')
xlabel('Single Spike Chi_8_4_S_r');
ylabel('Mean Relative Error in F-Sample_S_r');
xlim([0 1]);
ylim([0 0.001]);
hold on
plot(0.01:0.01:0.99,ones(size(0.01:0.01:0.99)) .* 0.0001, 'k-')

subplot(2,2,2)
plot(S_Mean_PerMil_Dev(:,1), S_Mean_PerMil_Dev(:,3), 'ro')
xlabel('Single Spike Chi_8_4_S_r');
```

```
ylabel('Mean Permil Deviation in ^8^6^/^8^8Sr Ratio of Sample');
hold on
plot(0.01:0.01:0.99,ones(size(0.01:0.01:0.99)) .* 0.01, 'k-')

subplot(2,2,3)
plot(S_Mean_Invert_Vector(:,1),S_Mean_Invert_Vector(:,2), 'ro')
xlabel('Single Spike Chi_8_4_S_r');
ylabel('Mean Inverted Alpha Value');
hold on
plot(0.01:0.01:0.99,ones(size(0.01:0.01:0.99)) .* Alpha, 'k-')

subplot(2,2,4)
plot(S_Mean_Invert_Vector(:,1),S_Mean_Invert_Vector(:,3), 'ro')
xlabel('Single Spike Chi_8_4_S_r');
ylabel('Mean Inverted Beta Value');
hold on
plot(0.01:0.01:0.99,ones(size(0.01:0.01:0.99)) .* Beta, 'k-')
```

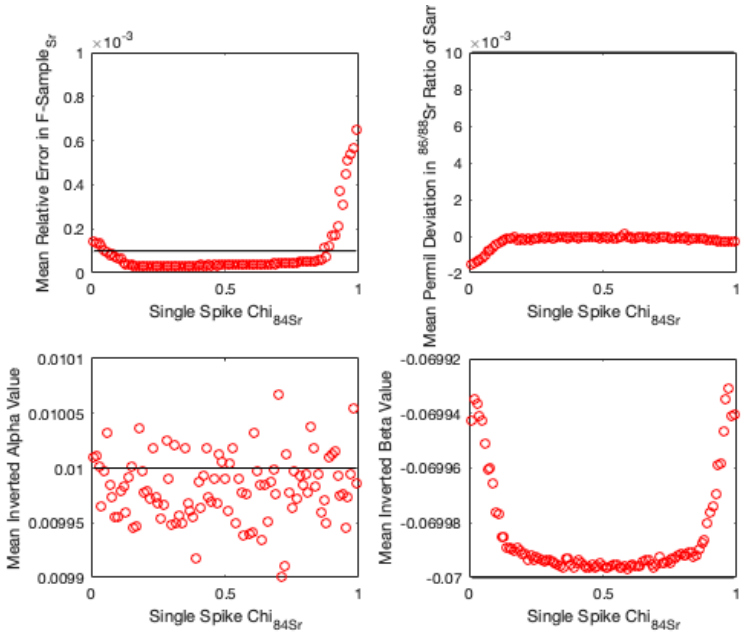

13). Find the values of chi-ds at the optimum chi-84 that correspond with respective minima in relative error in F-Sr, permil deviations in 86/88Sr ratios, empirical alphas and betas.

```
tmp2 = S_SingleSpk_DblSpk(idx1,:,2)';
idx2 = find(tmp2 == min(tmp2));
Chi_DblSpk_Sr_Opt_FSr = S_SingleSpk_DblSpk(idx1, idx2, 1)

tmp2_isotopes = S_SingleSpk_DblSpk(idx1,:,4)';
idx2_isotopes = find(tmp2_isotopes == min(tmp2_isotopes));
```

```
Chi_DblSpk_Sr_Opt_8688 = S_SingleSpk_DblSpk(idx1,idx2_isotopes,1)

tmp2_alpha = abs(S_SingleSpk_DblSpk(idx1,:,7) - Alpha)';
idx2_alpha = find(tmp1_alpha == min(tmp1_alpha));
Chi_DblSpk_Opt_Sr_Alpha = S_SingleSpk_DblSpk(idx1,idx2_alpha,1)

tmp2_beta = abs(S_SingleSpk_DblSpk(idx1,:,8) - Beta)';
idx2_beta = find(tmp2_beta == min(tmp2_beta));
Chi_DblSpk_Opt_Sr_Beta = S_SingleSpk_DblSpk(idx1,idx2_beta,1)


Chi_DblSpk_Sr_Opt_FSr =

   0.190000000000000


Chi_DblSpk_Sr_Opt_8688 =

   0.020000000000000


Chi_DblSpk_Opt_Sr_Alpha =

   0.150000000000000


Chi_DblSpk_Opt_Sr_Beta =

   0.090000000000000
```

14). Plot the distribution of errors in F-Sr, permil deviations in 86/88Sr ratios, empirical alphas and betas vs chi-ds at the optimal chi-84. Use 100 ppm relative error as a key threshold.

```
figure(2)
clf
subplot(2,2,1)
plot(S_SingleSpk_DblSpk(idx1,:,1),S_SingleSpk_DblSpk(idx1,:,2),'ro')
xlabel('Double Spike Chi_S_r');
ylabel('Relative Error in F-Sample_S_r');
xlim([0 1]);
ylim([0 0.001]);
hold on
plot(0.01:0.01:0.99,ones(size(0.01:0.01:0.99)) .* 0.0001, 'k-')

subplot(2,2,2)
plot(S_SingleSpk_DblSpk(idx1,:,1), S_SingleSpk_DblSpk(idx1,:,4), 'ro')
xlabel('Double Spike Chi_S_r');
ylabel('Mean Permil Deviation in ^8^6^/^8^8Sr Ratio of Sample');
hold on
plot(0.01:0.01:0.99,ones(size(0.01:0.01:0.99)) .* 0.01, 'k-')

subplot(2,2,3)
plot(S_SingleSpk_DblSpk(idx1,:,1),S_SingleSpk_DblSpk(idx1,:,7), 'ro')
xlabel('Double Spike Chi_S_r');
```

```
ylabel('Mean Inverted Alpha Value');
hold on
plot(0.01:0.01:0.99,ones(size(0.01:0.01:0.99)) .* Alpha, 'k-')

subplot(2,2,4)
plot(S_SingleSpk_DblSpk(idx1,:,1),S_SingleSpk_DblSpk(idx1,:,8), 'ro')
xlabel('Double Spike Chi_S_r');
ylabel('Mean Inverted Beta Value');
hold on
plot(0.01:0.01:0.99,ones(size(0.01:0.01:0.99)) .* Beta, 'k-')
```

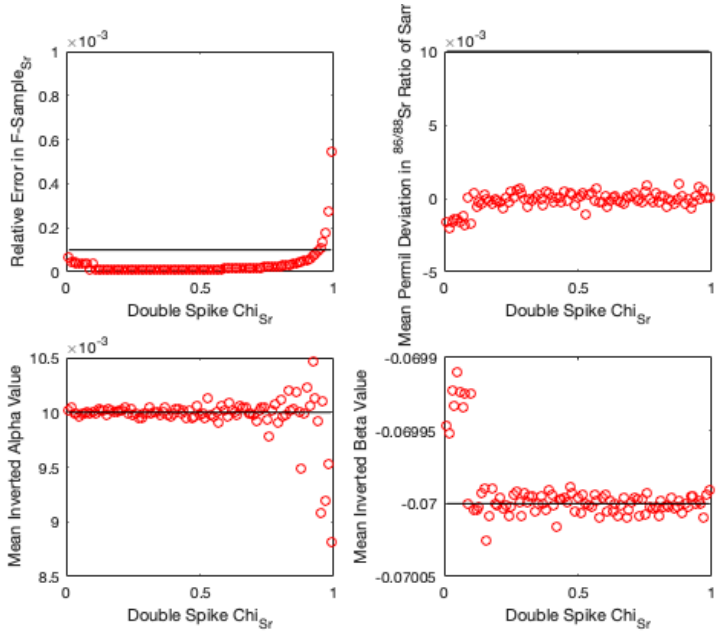

Run Code: Run the Inversion Script on Synthetic Ca Mixtures.

The Ca system inversion works similarly to the Sr system; follow those steps as a template.

```
Alpha = 0.01;
Beta = -0.07;
```

Pre-construct arrays to hold the overall output of 43-48 proportions in the double spike mixture (chi-43 and chi-48), double spike to sample proportions (chi-ds), inverted isotope ratios, and inverted solutions to alpha, beta, and the double spike to sample mixing ratio (chi-ds).

```
C_SingleSpk_DblSpk = zeros(length(0.01:0.01:0.99),
 length(0.01:0.01:0.99), 11);
```

```
C_DblSpk_Sample = zeros(length(0.01:0.01:0.99),11);
C_Mean_Err = zeros(length(0.01:0.01:0.99),2);
C_Mean_PerMil_Dev = zeros(length(0.01:0.01:0.99),7);
C_Mean_Invert_Vector = zeros(length(0.01:0.01:0.99),4);

kk = 1;
```

15). Choose a chi-43. Note - chi-48 = 1 - chi-43.

```
for Chi_SingleSpk1_Ca = 0.01:0.01:0.99

        Chi_SingleSpk2_Ca = 1 - Chi_SingleSpk1_Ca;
        ll = 1;
```

16). For that chosen chi-43 and chi-48, choose a chi-ds. Note that chi-sample = 1 - chi-ds.

```
    for Chi_Ca_DblSpk = 0.01:0.01:0.99
```

17). Create a mixture of a synthetic sample and double spike using the preset values for alpha and beta, the chosen mixing ratios, and the data from the Ca_Ref global values. RNat are the values of the isotope abundances in the natural standard referenced to 44Ca. RDbl_Spk are the isotope abundances in the double spike mixture referenced to 44Ca. RMixture represents the "true" isotope ratios of the sample+spike mixture, whereas Rmixture represents the measured value after the sample was subjected to some amount of instrumental mass fractionation inside of the mass spectrometer. Abundances of isotopes are used in the calculation of chi-43 and chi-48, while all ratios, chi-ds, and chi-sample values are with respect to 44Ca.

```
        R_Nat_Ca = Ca_Ref(:,3) ./ Ca_Ref(4,3);
        Abd_DblSpk_Ca = (Chi_SingleSpk1_Ca .* Ca_Ref(:,6)) +
 (Chi_SingleSpk2_Ca .* Ca_Ref(:,9));
        R_DblSpk_Ca = Abd_DblSpk_Ca ./ Abd_DblSpk_Ca(4,1);

        MW_Ca = Ca_Ref(:,2) ./ Ca_Ref(4,2);

        rSample_Ca = R_Nat_Ca .* (MW_Ca) .^ (Alpha);
        rMixture_Ca = Chi_Ca_DblSpk .* R_DblSpk_Ca + (1 -
 Chi_Ca_DblSpk) .* rSample_Ca;
        rmixture_Ca = rMixture_Ca .* (MW_Ca) .^ (Beta);
```

18). Calculate the cps of each Ca isotope given the supplied voltage of the 40Ca ion beam. Calculate the total counts of each isotope using these values and a total collection time of 10 minutes. Compute the relative error in total counts of each isotope with respect to 44Ca.

```
        cps_40 = I_40 * Coulomb;
        cps_42 = cps_40 * (rmixture_Ca(2,1) / rmixture_Ca(1,1));
        cps_43 = cps_40 * (rmixture_Ca(3,1) / rmixture_Ca(1,1));
        cps_44 = cps_40 * (rmixture_Ca(4,1) / rmixture_Ca(1,1));
        cps_46 = cps_40 * (rmixture_Ca(5,1) / rmixture_Ca(1,1));
        cps_48 = cps_40 * (rmixture_Ca(6,1) / rmixture_Ca(1,1));

        cps_Ca(1,1) = cps_40;
        cps_Ca(2,1) = cps_42;
        cps_Ca(3,1) = cps_43;
        cps_Ca(4,1) = cps_44;
        cps_Ca(5,1) = cps_46;
        cps_Ca(6,1) = cps_48;
```

```
cps_Ca(:,2) = cps_Ca(:,1) .* 60 .* 10;

cps_Ca(1,3) = sqrt(cps_Ca(1,2)) / cps_Ca(1,2);
cps_Ca(2,3) = sqrt(cps_Ca(2,2)) / cps_Ca(2,2);
cps_Ca(3,3) = sqrt(cps_Ca(3,2)) / cps_Ca(3,2);
cps_Ca(4,3) = sqrt(cps_Ca(4,2)) / cps_Ca(4,2);
cps_Ca(5,3) = sqrt(cps_Ca(5,2)) / cps_Ca(5,2);
cps_Ca(6,3) = sqrt(cps_Ca(6,2)) / cps_Ca(6,2);

SN_RelErr_Ca(1,1) = sqrt((cps_Ca(1,3))^2 + (cps_Ca(4,3))^2);
SN_RelErr_Ca(2,1) = sqrt((cps_Ca(2,3))^2 + (cps_Ca(4,3))^2);
SN_RelErr_Ca(3,1) = sqrt((cps_Ca(3,3))^2 + (cps_Ca(4,3))^2);
SN_RelErr_Ca(4,1) = sqrt((cps_Ca(4,3))^2 + (cps_Ca(4,3))^2);
SN_RelErr_Ca(5,1) = sqrt((cps_Ca(5,3))^2 + (cps_Ca(4,3))^2);
SN_RelErr_Ca(6,1) = sqrt((cps_Ca(6,3))^2 + (cps_Ca(4,3))^2);
```

19). For each Monte Carlo iteration, an optimization function will use these new values of Rmixture with error together with true values of RNat, RDbl_Spk, and the ratio of isotope weights to invert the values of alpha, beta, and chi-ds using no additional information. The optimization function uses an initial guess of alpha, beta, and chi-ds to create synthetic mixtures using similar logic as step 2 above, reporting the values of alpha, beta, and chi-ds that correspond with the minima in the sum of the square of the residuals between the calculated Rmixture inside of the optimization function and the true values of Rmixture with error from counting statistics.

20). Calculate F-Ca (see discussion on F-Sr):

(1 - chi-ds) / chi-ds = F-Ca

21). The inverted vector of alpha, beta, and chi-ds for each Monte Carlo iteration is used in a subsequent function that uses that information along with true values of RNat, RDbl_Spk, and the ratio of isotope weights to calculate an empirical RSample, RMixture, and Rmixture. The permil deviations of the empirical Rmixture from the true Rmixture values are also computed.

```
k = 1000;
num_iterations_Ca = k;
rm_Ca_matrix = zeros(size(rmixture_Ca,1), size(rmixture_Ca,2),
num_iterations_Ca);
invert_vector_Ca_err = zeros(num_iterations_Ca, 3);
permil_dev_Ca = zeros(size(rmixture_Ca,1), num_iterations_Ca);
F_s_Ca = zeros(num_iterations_Ca,1);
initial_guess_Ca = [0.001 0.001 0.2];

for l = 1:num_iterations_Ca
    Ca_Rand = rmixture_Ca .* (1 + SN_RelErr_Ca .*
randn(size(rmixture_Ca,1),1));
    rmixture_Ca_err = Ca_Rand;

    fun_pass_rm_Ca = @(x)RMTESTfn_search_Ca(x,
rmixture_Ca_err, R_Nat_Ca, R_DblSpk_Ca, MW_Ca);
    options =
optimset('TolFun',1e-15,'TolX',1e-9,'MaxIter',1000000,'MaxFunEvals',5000);
    invert_vector_Ca =
fminsearch(fun_pass_rm_Ca,initial_guess_Ca,options);

    initial_guess_Ca = invert_vector_Ca;
```

```
            invert_vector_Ca_err(l,:) = invert_vector_Ca;
            Chi_l = invert_vector_Ca(3);
            F_s_Ca(l) = (1 - Chi_l) / Chi_l;
            [Solved_Out_Ca] = RMTESTfn_Ca(invert_vector_Ca(1),
invert_vector_Ca(2), invert_vector_Ca(3), R_Nat_Ca, R_DblSpk_Ca,
MW_Ca);

            rm_Ca_matrix(:,:,l) = Solved_Out_Ca(:,3);
            permil_dev_Ca(:,l) = ((Solved_Out_Ca(:,3) ./ rmixture_Ca)
- 1) * 1E3;
        end
```

22). Calculate the relative error in F-Ca values and the mean values of permil deviations between empirical and true Rmixture for this particular choice of chi-ds. Collapse all permil deviations for each isotope ratio, empirical alpha's, beta's, and chi-ds's into averages across all Monte Carlo iterations. Continue iterating through steps 15-21 until all data for the final value of chi-ds at this given chi-43 and chi-48 has been allocated.

```
        relerrFsample_Ca = std(F_s_Ca) / mean(F_s_Ca);
        C_DblSpk_Sample(ll,:) = [Chi_Ca_DblSpk relerrFsample_Ca
 mean(permil_dev_Ca(1,:)) mean(permil_dev_Ca(2,:))
 mean(permil_dev_Ca(3,:)) mean(permil_dev_Ca(4,:))
 mean(permil_dev_Ca(5,:)) mean(permil_dev_Ca(6,:))
 mean(invert_vector_Ca_err(:,1)) mean(invert_vector_Ca_err(:,2))
 mean(invert_vector_Ca_err(:,3))];
        ll = ll + 1;

    end
```

23). For any given chi-43, collapse all output from the chi-ds loop into averages across all chi-ds iterations. Repeat steps 14-22 until data for all chi-43's has been allocated.

```
    mean_relerrFsample_Ca = mean(C_DblSpk_Sample(:,2));
    C_Mean_Err(kk,:) = [Chi_SingleSpk1_Ca mean_relerrFsample_Ca];

    mean_permil_dev_40 = mean(C_DblSpk_Sample(:,3));
    mean_permil_dev_42 = mean(C_DblSpk_Sample(:,4));
    mean_permil_dev_43 = mean(C_DblSpk_Sample(:,5));
    mean_permil_dev_44 = mean(C_DblSpk_Sample(:,6));
    mean_permil_dev_46 = mean(C_DblSpk_Sample(:,7));
    mean_permil_dev_48 = mean(C_DblSpk_Sample(:,8));

    mean_alpha_Ca_err = mean(C_DblSpk_Sample(:,9));
    mean_beta_Ca_err = mean(C_DblSpk_Sample(:,10));
    mean_Chi_Ca_err = mean(C_DblSpk_Sample(:,11));

    C_Mean_PerMil_Dev(kk,:) = [Chi_SingleSpk1_Ca mean_permil_dev_40
 mean_permil_dev_42 mean_permil_dev_43 mean_permil_dev_44
 mean_permil_dev_46 mean_permil_dev_48];
    C_Mean_Invert_Vector(kk,:) = [Chi_SingleSpk1_Ca mean_alpha_Ca_err
 mean_beta_Ca_err mean_Chi_Ca_err];
    C_SingleSpk_DblSpk(kk,:,:) = C_DblSpk_Sample;
    kk = kk + 1;

end
```

Run Code: Find the Error-Minimizing Mixing Ratios & Plot the Distribution of Error - Calcium

24). Find the values of chi-43 across all chi-ds that correspond with respective minima in relative error in F-Ca, permil deviations in 40/44Ca ratios, empirical alphas and betas.

```
tmp3 = C_Mean_Err(:,2);
idx3 = find(tmp3 == min(tmp3));
Chi_43Ca_Opt_FCa = C_Mean_Err(idx3,1)

tmp3_isotopes = C_Mean_PerMil_Dev(:,2);
idx3_isotopes = find(tmp1_isotopes == min(tmp1_isotopes));
Chi_43Ca_Opt_4044 = C_Mean_PerMil_Dev(idx3_isotopes,1)

tmp3_alpha = abs(C_Mean_Invert_Vector(:,2) - Alpha);
idx3_alpha = find(tmp3_alpha == min(tmp3_alpha));
Chi_43Ca_Opt_Alpha = C_Mean_Invert_Vector(idx3_alpha,1)

tmp3_beta = abs(C_Mean_Invert_Vector(:,3) - Beta);
idx3_beta = find(tmp3_beta == min(tmp3_beta));
Chi_43Ca_Opt_Beta = C_Mean_Invert_Vector(idx3_beta,1)
```

```
Chi_43Ca_Opt_FCa =

   0.620000000000000


Chi_43Ca_Opt_4044 =

   0.010000000000000


Chi_43Ca_Opt_Alpha =

   0.030000000000000


Chi_43Ca_Opt_Beta =

   0.120000000000000
```

25). Plot the distribution of errors in F-Ca, permil deviations in 40/44Ca ratios, empirical alphas and betas vs chi-43. Use 100 ppm relative error as a key threshold.

```
figure(3)
clf
subplot(2,2,1)
plot(C_Mean_Err(:,1),C_Mean_Err(:,2),'bo')
xlabel('Single Spike Chi_4_3_C_a');
```

```
ylabel('Mean Relative Error in F-Sample_C_a');
xlim([0 1]);
ylim([0 0.001]);
hold on
plot(0.01:0.01:0.99,ones(size(0.01:0.01:0.99)) .* 0.0001, 'k-')

subplot(2,2,2)
plot(C_Mean_PerMil_Dev(:,1), C_Mean_PerMil_Dev(:,2), 'bo')
xlabel('Single Spike Chi_4_3_C_a');
ylabel('Mean Permil Deviation in ^4^0^/^4^4Ca Ratio of Sample');
hold on
plot(0.01:0.01:0.99,ones(size(0.01:0.01:0.99)) .* 0.01, 'k-')

subplot(2,2,3)
plot(C_Mean_Invert_Vector(:,1),C_Mean_Invert_Vector(:,2), 'bo')
xlabel('Single Spike Chi_4_3_C_a');
ylabel('Mean Inverted Alpha Value');
hold on
plot(0.01:0.01:0.99,ones(size(0.01:0.01:0.99)) .* Alpha, 'k-')

subplot(2,2,4)
plot(C_Mean_Invert_Vector(:,1),C_Mean_Invert_Vector(:,3), 'bo')
xlabel('Single Spike Chi_4_3_C_a');
ylabel('Mean Inverted Beta Value');
hold on
plot(0.01:0.01:0.99,ones(size(0.01:0.01:0.99)) .* Beta, 'k-')
```

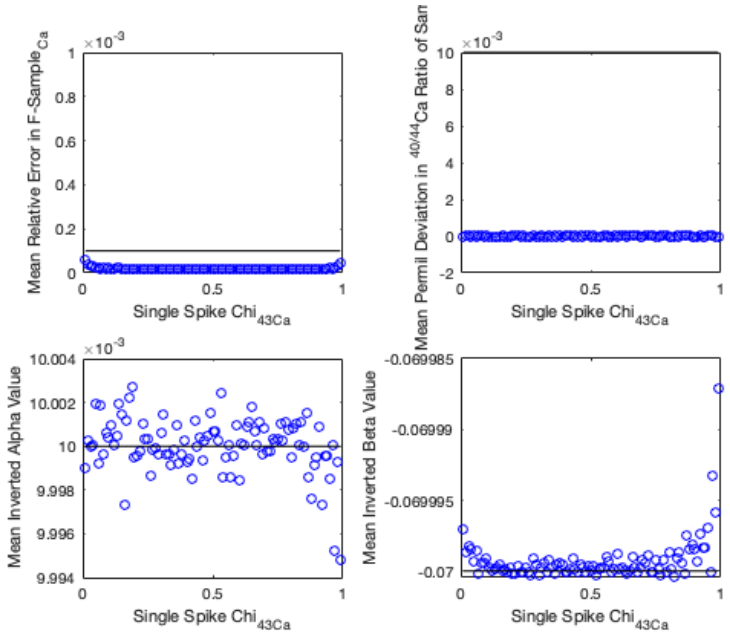

26). Find the values of chi-ds at the optimum chi-43 that correspond with respective minima in relative error in F-Ca, permil deviations in 40/44Ca ratios, empirical alphas and betas.

```
tmp4 = C_SingleSpk_DblSpk(idx3,:,2)';
idx4 = find(tmp4 == min(tmp4));
Chi_DblSpk_Ca_Opt = C_SingleSpk_DblSpk(idx3, idx4, 1)

tmp4_isotopes = C_SingleSpk_DblSpk(idx3,:,3)';
idx4_isotopes = find(tmp4_isotopes == min(tmp4_isotopes));
Chi_DblSpk_Ca_Opt_4044 = C_SingleSpk_DblSpk(idx1,idx4_isotopes,1)

tmp4_alpha = abs(C_SingleSpk_DblSpk(idx3,:,9) - Alpha)';
idx4_alpha = find(tmp4_alpha == min(tmp4_alpha));
Chi_DblSpk_Opt_Ca_Alpha = C_SingleSpk_DblSpk(idx1,idx4_alpha,1)

tmp4_beta = abs(C_SingleSpk_DblSpk(idx3,:,10) - Beta)';
idx4_beta = find(tmp4_beta == min(tmp4_beta));
Chi_DblSpk_Opt_Ca_Beta = C_SingleSpk_DblSpk(idx3,idx4_beta,1)
```

```
Chi_DblSpk_Ca_Opt =

   0.210000000000000


Chi_DblSpk_Ca_Opt_4044 =

   0.670000000000000


Chi_DblSpk_Opt_Ca_Alpha =

   0.800000000000000


Chi_DblSpk_Opt_Ca_Beta =

   0.690000000000000
```

27). Plot the distribution of errors in F-Ca, permil deviations in 40/44Ca ratios, empirical alphas and betas vs chi-ds at the optimal chi-43. Use 100 ppm relative error as a key threshold.

```
figure(4)
clf
subplot(2,2,1)
plot(C_SingleSpk_DblSpk(idx3,:,1),C_SingleSpk_DblSpk(idx3,:,2),'bo')
xlabel('Double Spike Chi_C_a');
ylabel('Relative Error in F-Sample_C_a');
xlim([0 1]);
ylim([0 0.001]);
hold on
plot(0.01:0.01:0.99,ones(size(0.01:0.01:0.99)) .* 0.0001, 'k-')

subplot(2,2,2)
```

```
plot(C_SingleSpk_DblSpk(idx3,:,1), C_SingleSpk_DblSpk(idx3,:,3), 'bo')
xlabel('Double Spike Chi_C_a');
ylabel('Mean Permil Deviation in ^4^0^/^4^4Ca Ratio of Sample');
hold on
plot(0.01:0.01:0.99,ones(size(0.01:0.01:0.99)) .* 0.01, 'k-')

subplot(2,2,3)
plot(C_SingleSpk_DblSpk(idx3,:,1),C_SingleSpk_DblSpk(idx3,:,9), 'bo')
xlabel('Double Spike Chi_C_a');
ylabel('Mean Inverted Alpha Value');
hold on
plot(0.01:0.01:0.99,ones(size(0.01:0.01:0.99)) .* Alpha, 'k-')

subplot(2,2,4)
plot(C_SingleSpk_DblSpk(idx3,:,1),C_SingleSpk_DblSpk(idx3,:,10), 'bo')
xlabel('Double Spike Chi_C_a');
ylabel('Mean Inverted Beta Value');
hold on
plot(0.01:0.01:0.99,ones(size(0.01:0.01:0.99)) .* Beta, 'k-')

toc
```

Elapsed time is 47855.424276 seconds.

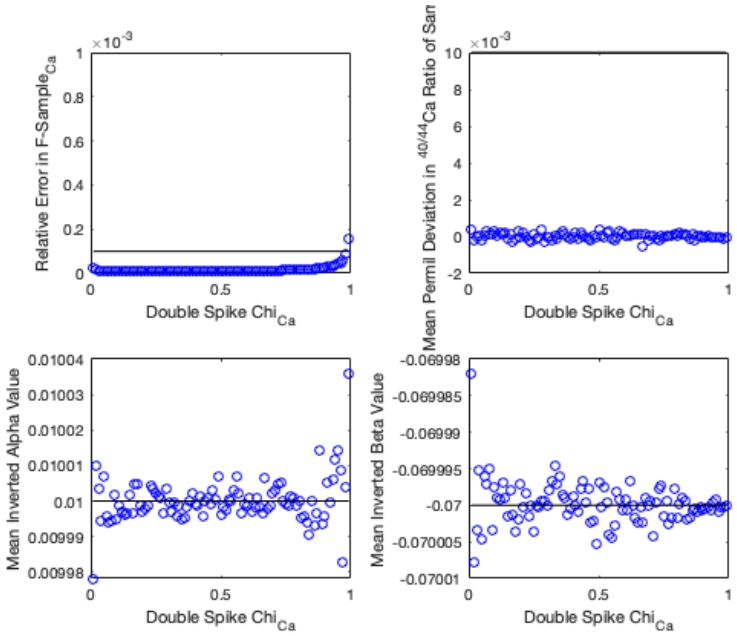

Published with MATLAB® R2018a

VITA

ISAIAH WESLEY BOLDEN

CAMPUS BOX 357940, 1501 NE BOAT ST., SEATTLE, WA 98195

PHONE: (+1) 615.983.0726 EMAIL: IBOLDEN[AT]UW[DOT]EDU

EDUCATION

University of Washington (Seattle, WA): Ph.D. Oceanography (Expected December 2020)
Advisor: Alexander C. Gagnon
Thesis Title: "Constructing a Toolbox of Geochemical Indicators of Stress-Induced Community Composition Shifts in Coral Reef Ecosystems."
University of Washington: M.S. Oceanography (July 2017)
Advisor: Alexander C. Gagnon
Bowdoin College (Brunswick, ME): B.A. with Departmental Honors (August 2011 – May 2015)
Major – Earth & Oceanographic Science, Minor – Chemistry
Advisor: Michèle LaVigne
Thesis Title: "Anomalous Seasonal Oscillations in the Ba/Ca Ratios from a Floridian Surface Coral."

PROFESSIONAL APPOINTMENTS

Academic Pathways Postdoctoral Fellow, Department of Earth and Environmental Sciences – Vanderbilt University (Nashville, TN). Primary Advisor: Jessica L. Oster	Beginning Jan. 2021

RESEARCH EXPERIENCE

Graduate Research Fellow, School of Oceanography – University of Washington (Seattle, WA). Primary Advisor: Alexander C. Gagnon	September 2015 - Present
Ernest F. Hollings Scholar, Ocean Acidification Program, National Oceanic and Atmospheric Administration (Silver Spring, MD). Primary Advisor: Dwight K. Gledhill	March 2013 – May 2015
Research Assistant, Department of Earth & Oceanographic Science – Bowdoin College (Brunswick, ME). Primary Advisor: Michèle LaVigne	June 2013 – May 2015

Summer Student Fellow, Department of Marine Chemistry & Geochemistry – Woods Hole Oceanographic Institution, Woods Hole, MA. Primary Advisor: Matthew A. Charette	June – August 2012
Research Assistant, Marine Biology Research Division – Scripps Institution of Oceanography, La Jolla, CA. Primary Advisor: Michael I. Latz	June – August 2011
Research Assistant, Vanderbilt University Institute for Energy and the Environment, Nashville, TN. Primary Advisor(s): George Hornberger and Christopher P. Vanags	May 2010 – May 2011
Research Assistant, Department of Microbiology and Immunology, Vanderbilt University (Nashville, TN). Primary Advisor: Louise A. Rollins-Smith	January 2010 – May 2011

PUBLICATIONS

Bolden, I.W. and Gagnon, A.C. "Diel Variability in $\delta^{13}C$ of Seawater Dissolved Inorganic Carbon as a Proxy for Coral Reef Productivity Dynamics." *In prep.*

Bolden, I.W., Satkoski, A., Lassiter, J.C., and Gagnon, A.C. "High-Precision Determination of Sr/Ca Ratios in Carbonates and Seawater through Double Mixed Spike Isotope Dilution Thermal Ionization Mass Spectrometry (DMS-ID-TIMS)." *In prep.*

Bolden, I.W., Sachs, J.P., and Gagnon, A.C. (2019) "Temporally-Variable Productivity Quotients on a Coral Atoll: Implications for Estimates of Reef Metabolism." *Marine Chemistry*. 217 (103707), 1-13.

Bolden, I.W., Seroy, S.K., Roberts, E.A., Schmeisser, L., Koehn, J.Z., Rilometo, C.H., Odango, E.L., Barros, C., Sachs, J.P., and Klinger, T. (2018) "Climate-related Community Knowledge Networks as a Tool to Increase Learning in the Context of Environmental Change." *Climate Risk Management*. 21, 1-16.

Bolden, I.W. (2016) "Reconstructing Tropical Climates with Coral Reefs: Links to Local Precipitation and Primary Productivity." *Mellon Mays Undergraduate Research Journal* 20, 12-16.

INVITED PRESENTATIONS

Invited Webinar Speaker – "Building Resilient, Adaptive, and Inclusive Coastal Communities through Marine Science: Lessons Learned with Plenty Left to Do," Coastal & Estuarine Research Federation (September 2020).

Departmental Seminar – Earth & Atmospheric Sciences, Georgia Institute of Technology. Atlanta, GA (January 2020).

Departmental Seminar – Jackson School of Geosciences, University of Texas at Austin. Austin, TX (January 2020).

Departmental Seminar – Earth & Environmental Sciences, Vanderbilt University. Nashville, TN (September 2019).

Guest Lecturer – "Coral Reefs & Climate Change," Marine Biology (BIOL 3650), Seattle University, Seattle, WA (April 2019).

Guest Lecturer – "Repurposing a Paleo-Proxy: The Sr/Ca Ratio," Research in Oceanography – Topics in Paleoceanography (EOS 3515), Bowdoin College, Brunswick, ME (November 2018).

Guest Lecturer – "Topics in Climate Change," Patriots Debate Institute – George Mason University, Fairfax, VA (July 2014).

Departmental Seminar – Marine Chemistry & Geochemistry, Woods Hole Oceanographic Institution, Woods Hole, MA (August 2012).

CONFERENCE & SYMPOSIA PRESENTATIONS

Boysen, A.K., Baker, C., **Bolden, I.W.**, and McLachlan, R. (2019) "A phenomenon-based climate science curriculum for middle-school classrooms: Harmful Algal Blooms, Society, and Climate Change." 2019 Earth Educators Rendezvous. Nashville, TN. *Poster*.

Bolden, I.W., Sachs, J.P., and Gagnon, A.C. (2018) "Spatial & Temporal Variability in the Biogeochemical 'Heartbeat' of Tetiaroa Atoll, French Polynesia – An Exploration of Productivity Quotients." 2018 Ocean Sciences Meeting. Portland, OR. *Oral.*

Bolden, I.W., Gagnon, A.C., and Sachs, J.P. (2017) "Quantitative Decomposition of the Biogeochemical 'Heartbeat' of a French Polynesian Atoll." Goldschmidt Geochemistry Conference. Paris, France. *Poster*

Bolden, I.W., Brandkamp, L.K., Gregersen, J.A., Gagnon, A.C., and Sachs, J.P. (2016) "Quantifying Chemical Changes in the 'Heartbeat' of a Coral Reef on Tetiaroa Atoll, French Polynesia." 13th International Coral Reef Symposium. Honolulu, HI. *Poster*

Bolden, I.W., DeLong, K, and LaVigne, M. (2015) "Anomalous Seasonal Oscillations in the Ba/Ca Ratios from a Floridian Surface Coral." Geological Society of Maine Spring Meeting. Colby College, Waterville, ME. *Poster*

Bolden, I.W. (2014) "Ocean Acidification in the Public Eye – OA in the NE." Annual Meeting of the Geological Society of America (GSA), Vancouver, BC, Canada. *Oral*

Bolden, I.W. (2013) "Corals, Coasts, and Climate Change." Mellon-Mays Undergraduate Summer Research Symposium – Bowdoin College, Brunswick, ME. *Oral*

TEACHING & OUTREACH EXPERIENCE

Lecturer and Program Director (with A.R. Rupan), Autonomous & Robotic Observations of Marine Ecosystems in Australia (Ocean 499), University of Washington and Queensland University of Technology, Brisbane, Australia	June – July 2019
Workshop Leader (with A.C. Gagnon, S.K. Seroy, and T. Burns) – "All I Need to Understand Climate Science I Learned in High School Chemistry," UW Oceanography & Northwest Educational Service District (ESD) 189, Marysville and Bellingham, WA	March 2019
Outreach Volunteer (Marine Ecology), Seattle MESA	September 2017 - Present
Graduate Mentor, Marine Research in Puget Sound for Community College STEM Students (NSF Award #1358835)	March – June 2017
Outreach Volunteer, University of Washington Program on Climate Change.	September 2016 - Present
Teaching Assistant, Indigenous Science (Ocean 497/Anthro 369), University of Washington.	September 2016 – December 2016
Workshop Leader (with S.K. Seroy) – "ENSO Impacts on Water Resource Management," University of Washington & Pacific Resources for Education and Learning, Pohnpei, Federated States of Micronesia	September 2016
Virtual Panelist, Upward Bound Summer Program – Bowdoin College, Brunswick, ME	July 2016
Lead Mentor, Bowdoin Science Experience – Bowdoin College, Brunswick, ME	August 2013 - September 2014

HONORS/AWARDS

Mellon Mays Undergraduate Fellows Travel and Research Grant (Woodrow Wilson National Fellowship Foundation) – Awarded $4,235 for assistance in the progression of dissertation research and fieldwork.	April 2019
SSRC Graduate Studies Enhancement Grant (SSRC-GSE) – Awarded $1,500 for travel, equipment, and software related to dissertation research.	August 2016
NSF Graduate Research Fellowship (NSF-GRFP) – Awarded $138,000 for 3 years of graduate support (5 years total tenure).	April 2016

Achievement Rewards for College Scientists Fellowship (ARCS) – Awarded $17,500 for three years of additional graduate support. May 2015

IGERT Program on Ocean Change Fellowship (NSF & University of Washington) – Awarded $60,000 for two years of graduate research support plus tuition remission and interdisciplinary research opportunities. May 2015

Grua/O'Connell Research Award (Bowdoin College) – Awarded $3,000 for undergraduate research expenses. October 2014

Ernest F. Hollings Undergraduate Scholarship (NOAA, US Dept. of Commerce) – Awarded $16,000 for 2 years of undergraduate tuition support and a salaried summer internship at NOAA HQ. March 2013

Mellon Mays Undergraduate Fellowship (Andrew W. Mellon Foundation) – Awarded $9,600 for 2 years of undergraduate research support and travel funds. An additional $10,000 of support to be used for undergraduate loan forgiveness following completion of Ph.D. March 2013

AFFILIATIONS & MEMBERSHIPS

Geochemical Society	2017-Present
Society for the Advancement of Chicanos and Native Americans in Science	2017-Present
International Society for Reef Studies	2016-Present
Geological Society of America	2012-Present